Universidad de Granada

Monte Carlo Models of the Dust Environment of a Sample of Comets from the Oort Cloud to the Outer Main Asteroid Belt

A Ph.D. dissertation presented by:

Francisco José Pozuelos Romero

Instituto de Astrofísica de Andalucía (CSIC)

Supervisor:

Dr. Fernando Moreno Danvila

Granada, July 2014

A mis padres, Dolo y Paco,
y a Silvia

Agradecimientos

Es difícil escribir unos agradecimientos. A uno le vienen a la memoria muchas caras y recuerdos, y cuesta centrarse en ser breve. Un día señalado para mí fue el 10 de septiembre de 2010. Fecha en la que me incorporé al Instituto de Astrofísica de Andalucía (IAA-CSIC), gracias a la oportunidad que me ofrecieron en aquel momento Fernando Moreno, mi director de tesis, y Olga Muñoz. Es a ellos a los primeros a quienes quiero transmitir mi más sincero agradecimiento. Gracias, por la confianza que depositaron en mi, por la paciencia (mucha) y por saber enseñarme tantas y tantas cosas.

Si miro con detenimiento hacia atrás recuerdo mi Punta Umbría, en especial, el verano de 1997, cuando tenía 14 años, y pasaba las noches en la playa con mis amigos de la infancia, hablando de los asuntos cotidianos de esas edades. En esas noches, mirábamos al cielo más sorprendidos que nunca, aparecía allí, majestuoso, el Hale Bopp. Todas las mañanas leía el periódico en busca de alguna información, ¿qué era?, ¿de dónde venía?, ¿volverá otra vez?, demasiadas preguntas, que escasamente veían respuesta, en una era donde la información no estaba a un click de distancia. Quién me iba a decir, que mi tesis doctoral trataría, precisamente, de responder esas cuestiones...

Quiero agradecer a mis amigos de Punta Umbría, en especial a Raúl Contreras, Cristina Martín, Rocío Pedreira, Emanuel Caron-Cot, Urbano Flores, Raquel León, Jose Carlos Rodríguez y Javier Domínguez, por recordarme que, aunque me fui de allí hace ya 12 años, ese siempre será mi pueblo. De igual forma, mi agradecimiento a mis amigos de Cádiz, con los que he compartido los inolvidables años universitarios, Daniel Guerrero, Daniel Díaz, Daniel Jurado, José Ramón Manzano, y Borja Rosado, porque a pesar de los kilómetros, siempre encontramos algún momento para reunirnos y pasar una noche de charla, recordando tiempos en los que vivíamos en una Sevilla que se nos antojaba eterna, fueron buenos años. Cómo no, a mis amigos de la carrera, compañeros de batalla, en especial, a Cristóbal Tornay, Jose M. Escalante, Miguel A. Tenor e Israel García, parecía que nunca se acabaría, pero todo llega... Quiero agradecer también a Rubén Herrero, Rubén López y Haritz Saizar por los buenos ratos que pasamos juntos, viviendo rápido, riendo siempre, desgranando Granada... fue un primer año inolvidable... También a mis amigos y amigas que han compartido conmigo estos años en Granada, Sol Molina, Zaira Modroño, Carolina Casadio, Andrea Aleotti, Gabriel López, Francesco Costagliola y Federica Costa por los buenos ratos, los cafés, las barbacoas, los días de playa y noches de labradores, por ser mi familia en Granada. A esos compañeros, que son amigos, que hacen que el día a día sea menos duro, que ir a trabajar no sea ir al trabajo, a Juanma Mayén, Jose Ramón Rodón, Alberto Molino, David Perez, Lorena Hernández, Alba Fernández, Darío Díaz, Marta González, Alícia Benítez, Laura Sampedro, Rafa Lopez, William Schoenell, Pablo Ramírez, Iker Requerey, María Passas, Mónica Blanco, Fran Parra, Estela Fernández...

A los miembros del departamento de Sistema Solar del IAA, que hacen que este campo sea tan apasionante, a los miembros del Centro de Cálculo, sin quienes la informática ya me habría matado a disgustos hace tiempo, y a todo el personal del OSN, por su dedicación y ayuda durante las campañas de observación. A Julio Castellano y Esteban Reina, así como a toda la red de observadores de Cometas-Obs, quienes pasan las noches, pacientes, entre telescopios y tazas de café, y

sin cuyos esfuerzos, esta tesis hubiese sido muy distinta.

No sería justo por mi parte, si no le diera las gracias al profesor que más me influyó en la carrera, Dr. Manuel García León, con quien estaré siempre agradecido por su confianza, paciencia y apoyo, ojalá hubiese más profesores como él en las aulas.

A mi familia, en especial mis primos Antonio, Rodrigo y Manuel, mi tía Julia y mi tío Antonio, quienes estando lejos, tienen la virtud de hacerte sentir que están cerca, aunque sea desde Madrid, aunque sea desde Chile. Siempre seremos esos cuatro que crecieron entre los naranjos y limoneros de casa de los abuelos.

Quiero también agradecer a Celestino, Luisa, Adrián y Fredy el haberme acogido, desde el primer momento, como uno más de la familia y hacerme sentir siempre como en casa cuando voy a Cantillana.

Dejo para el final los más importantes. A Silvia, porque nos queda mucha vida por vivir, mucho por recorrer, mucho por hacer, porque sin su paciencia, su risa y sus ganas, su forma de ver la vida y su forma de vivirla, este trabajo habría sido gris. Gracias por estar a mi lado.

Y a mis padres, porque sé que puedo contar con ellos pase lo que pase, llueva lo que llueva, siempre. Han visto pasar mi vida, estando ahí en cada momento, ni un consejo sin razón, haciéndome sentir siempre envuelto en compresión para contar lo que cualquier hijo esconde, han sabido hacer de mi el hombre que soy. Nunca tendré suficientes palabras para poder expresar lo mucho que los quiero y los necesito.

Special mention

I want to express my deepest gratitude to Dr. Louis Fayard and Dr. Francesco Polci from the CNRS who tutored me in my first step as a researcher in 2009 during in my last year as an undergraduate student at the University of Paris XI. It was with their help, support and encouragement when I decided that my future would be in the research field. I would like to thank them for all the advice and opportunities they gave me. This experience was a turning point in my life.

"La noche está estrellada,
y tiritan, azules, los astros, a lo lejos".
Pablo Neruda (1904-1973)

Resumen

La principal labor investigadora desarrollada en esta tesis doctoral consiste en la caracterización del polvo ambiental generado en los cometas como consecuencia de su actividad a lo largo de su órbita. Estos estudios han sido implementados para varios cometas, de diferentes familias, usando un código de Monte Carlo. Este programa computacional, que ha sido desarrollado íntegramente en el Departamento de Sistema Solar del Instituto de Astrofísica de Andalucía (IAA) (véase Moreno 2009), permite la generación de imágenes sintéticas que pueden ser directamente comparadas con las observaciones cometarias. El código ha sido usado, entre otras muchas aplicaciones, en la caracterización del polvo del cometa 67P/Churyumov-Gerasimenko, para el instrumento GIADA (Grain Impact and Dust Accumulator) de la misión Rosetta (el llamado "Granada model", ver Fulle et al. 2010), y permite inferir, en función de la distancia heliocéntrica, la tasa de producción de polvo, las velocidades terminales de las partículas, la función de distribución de tamaños y las propiedades de anisotropía de la emisión. Desafortunadamente, al ser un problema con múltiples parámetros de entrada, la solución no es única, en el sentido de que podría encontrarse más de un conjunto de parámetros de entrada que generasen un mismo resultado. Ahora bien, si el número de observaciones cometarias es lo suficientemente amplio, la degeneración de las soluciones disminuye considerablemente. Por ello, en nuestros estudios, usamos el mayor número de ellas, intentando cubrir la mayor parte del arco orbital.

Los resultados obtenidos se muestran agrupados en distintos artículos, atendiendo a las diferentes familias cometarias. En primer lugar, el código ha sido usado para la caracterización de una muestra de once cometas de la Familia de Júpiter. Para dichos estudios, hemos usado generalmente observaciones realizadas en el Observatorio de Sierra Nevada con el telescopio de 1.52 m. Además, con objeto de aumentar la información disponible para cada cometa, hemos usado medidas del parámetro $Af\rho$ realizadas por distintos miembros de la asociación astrónoma amateur *Cometas-Obs*. En este trabajo, además de la caracterización en términos de polvo, hemos estudiado la historia dinámica de cada cometa, haciendo uso del integrador numérico híbrido implementado por Chambers (1999) en su código Mercury. Los resultados de estos estudios se muestran en los artículos I, II y III, en donde, para cada cometa, se proporciona una detallada caracterización del polvo ambiental en función de la distancia heliocéntrica y un análisis dinámico que cubre los últimos 15 millones de años, de donde deducimos cuáles han sido las regiones más visitadas y cuánto tiempo llevan formando parte de la Familia de Júpiter. El resultado global más relevante que hemos encontrado es que existe una cierta relación entre la cantidad de polvo emitido anualmente y la edad en la Familia de Júpiter, siendo los cometas más activos los más jóvenes.

También han sido analizados los cometas del Cinturón Principal P/2012 T1 (PANSTARRS) y P/2013 P5 (PANSTARRS). Estos objetos forman parte de una familia cometaria que ha sido descubierta recientemente, en donde los objetos tienen tanto rasgos cometarios (cola de polvo) como características asteroidales (parámetros orbitales). De esta nueva población apenas se conocen once miembros, siendo el mayor interrogante el mecanismo que los activa. Los resultados se presentan en los artículos IV y V. En ellos determinamos como causas más probables de activación la sublimación de hielos, en el caso de P/2012 T1, y la ruptura rotacional, en el caso de P/2013 P5.

En el artículo VI, presentamos un amplio estudio llevado a cabo sobre el cometa de largo periodo C/2012 S1 (ISON), perteneciente a la Nube de Oort. Este trabajo ha sido realizado usando telescopios de diferentes observatorios (Observatorio de Sierra Nevada, Observatorio de Calar Alto y el Solar and Heliospheric Observatory) en diferentes épocas, y medidas de $Af\rho$ en función de la distancia heliocéntrica llevadas a cabo por *Cometas-Obs*. Esto nos permitió tener información observacional desde su descubrimiento, a ~6 Unidades Astronómicas, hasta su casi completa destrucción tras su paso por el perihelio. La evolución de los parámetros de polvo derivados de estas observaciones muestran un comportamiento altamente complejo, en donde cabe destacar la ruptura del núcleo y los fenómenos de vaporización y fragmentación sufridos por las partículas, que dan como resultado la destrucción casi completa del cometa, quedando como producto final, tan sólo, una nube de pequeñas partículas.

Se exponen también unas aportaciones aún no publicadas, aunque en proceso de finalización. Estos estudios están dedicados a la caracterización de la evolución de los parámetros de polvo de los cometas 217P/Linear y P/2010 H2 (Vales), los cuales, en un momento determinado de su órbita, experimentaron una explosión de actividad. De esta forma, proponemos una caracterización completa antes, durante y después del estallido, pudiendo así cuantificar la cantidad de polvo emitida y el tiempo de recuperación tras estos eventos.

Finalmente, hacemos un breve resumen de los proyectos, que se encuentran en desarrollo, y que conforman nuestro trabajo futuro. En este sentido, y en relación con los cometas de corto periodo, realizaremos una amplia campaña observacional sobre el cometa 67P/Churyumov-Gerasimenko determinando en tiempo real la evolución de parámetros de polvo. Los resultados podrán ser comparados directamente con los obtenidos por la misión espacial Rosetta, así como con los presentados en los artículos I, II, y III. En el caso de los cometas del cinturón principal, continuaremos con el programa de "Target of Opportunity" en el OSN y la colaboración IAA-IAC, con observaciones con el Gran Telescopio Canarias, para la rápida observación de estos cuerpos cuando se activen. Sobre la familia de cometas de largo periodo, contamos con observaciones ya realizadas de una muestra de cometas, cuyos resultados podrán ser comparados directamente con los obtenidos en el artículo VI, además de una colaboración entre el IAA y el Complejo Astronómico el Leoncito (CASLEO) para monitorizar el fuerte acercamiento entre el cometa C/2013 A1 (Siding Spring) y Marte, que tendrá lugar en Octubre de 2014.

Contents

Chapter 1

Introduction

1.1 Historical background

The word "comet" comes from the Greek "kometes", which means "long-haired star", but the earliest observations of these bodies are from ancient China in 1000 BC. Comets were observed in the sky with curiosity and expectation as well as fear and dread. Due to their enigmatic nature, and their unpredictable appearances, they were considered messengers of gods, mostly as bad omens. In his *Meteorology* (ca. $\sim$ 330 BC), Aristotle described the comets as "dry and warm exhalations" in the atmosphere, and they were relegated to the lowest sphere in his spherical shell description of the sky. For a long time, Aristotle's influence was very strong, until 1433, when Toscanelli started observing several comets. These observations continued until 1472 and focused in particular on comet 1P/Halley in 1456. This period inaugurated the renaissance of European observational astronomy. Between 1570 and 1600 the comets were located far from the Earth, and this raised the question of how they move. In 1610, the amateur astronomer Lower Bradley et al. (1833) suggested that the comet orbits could be highly elongated ellipses. Later in 1680, Dörffel was the first to explain the motion of comet C/1680 V1 along a parabola with the Sun as its focus. The comet was observed twice, before and after its perihelion passage, thus providing an explanation for the general fact that many comets were observed in pairs. It was Newton in his *Principia* (1687) who determined that the orbit of comet C/1680 V1 was elliptical, albeit almost parabolic, and concluded that the comet passed only 0.00154 AU above the surface of the Sun, starting at this point, a new era in the determination of comet motion. Halley in 1705 computed the orbits of a dozen comets based on Newton's theory, and demonstrated the periodic nature of the most famous comet, 1P/1682 Q1, the so called Halley's Comet. Cometary astronomy gradually improved due to orbital computation techniques during the eighteenth century, when astronomers began to get a picture of the existence of different types of comets, realizing that some comets presented low inclinations and aphelia close to Jupiter's orbit while others did not. Despite this advance, the nature of comets was still uncertain. In 1835, due to the extensive work carried out by Herschel, Bessel, and Struve to study comet 1P/Halley, the first analysis of a comet was made, where the presence of jets, cones, and streamers was described. Bessel in the 1830's was the first to suggest that the ejected particles from the comets in the sunward direction were repelled back to the tail

by an unknown repulsive force. Bond in 1862 proved that the scattered light was essentially solar, from observations of comet C/1858 L1 (Donatti). The first spectroscopic observations of comets were performed by Donatti. He was followed by Huggins in 1868, who compared the spectra of comets C/1864 N1 (Temple) and 55P/1865 Y1 (Temple-Tuttle) with a flame, and determined that the bands seen in the comets and the flame were similar. In addition, Huggins identified the presence of a broad continuum due to the reflected sunlight. A bit later, in 1866 and 1867, Schiaparelli linked meteors and comets thanks to the observation that the Perseid and Leonid meteor streams coincided with the orbits of comets 109P/Swift-Tuttle and 55P/Temple-Tuttle respectively. This proved that comets were indeed losing solid particles. Some years later, Arrhenius (1900) solved the problem described by the Bessel model in 1862, where an unknown repulsive force was responsible for the development of the comets tails. Arrhenius identified that force as the pressure exerted by sunlight, which is what we call radiation pressure. In 1926, Baldet published a wide catalog of the spectra of 40 comets observed from 1864, and a complete bibliography of all those comets observed by spectroscopy. Five years later, Nicolas Bobrovnikoff (1931) published an extensive work about the 1910 appearance of comet 1P/Halley. Both Baldet and Bobrovnikoff provided the first two comprehensive papers on cometary physics published in the twentieth century. From the first observations and references to comets until this point, cometary science had improved and was highly developed, but the major evolution took place in 1950-1951, when three very important ideas were formulated within a short time span: First, the icy-conglomerate ("dirty-snowball") model proposed by Whipple (1950) to describe the cometary nucleus. Second, the dynamical studies of the distribution of semimajor axes of comets carried out by Oort (1950), which allowed him to identify a distant population of comets, now known as the Oort Cloud. Third, Biermann (1951) gave the correct explanation for the motions of features in cometary plasma tails as due to the interaction between charged particles emanating from the Sun's surface (i.e., the solar wind) and the ionized cometary atoms and molecules. These three ideas determined a new era in cometary science, where the physics and nature of comets combined with the existence of a family of celestial bodies were suddenly revealed at the same time. In the following subsections we develop these three important ideas more extensively.

The Icy-Conglomerate model of the nucleus

Whipple based his icy-conglomerate model on previous studies. He tried to unify some ideas in an attempt to explain all of the facts known about cometary nuclei, and tried to explain some unsolved questions. For example, from 1932 until 1943, some studies of Wurm and Swings revealed that the molecules observed in the cometary comae were not chemically stable, and that these species must be created by photochemistry of more stable molecules residing in the nucleus. Then the concepts of "parent" molecules, and "daughter" species, created in the coma by photochemistry were born. However, it was unclear how molecules were stored in the cometary material. Another unsolved important problem was the delay in the perihelion passages observed in some comets, mainly in 2P/Encke. This problem was studied by Bessel in 1936, who suggested for the first time, a solid body hidden in the brightness of the coma, which by asymmetric outflows of gases produced non-gravitational effects that influenced the comet's motion. This idea was not accepted until Whipple (1950, 1951) formulated the modern model of a solid nucleus a century later, based on the previous

studies of Laplace in 1813 and Bessel (1836). The nucleus was described as a mixture of ices (mainly: water-ice, ammonia, methane, and carbon dioxide), from which the gases observed in the coma are produced by sublimation when the comet approaches the Sun and the surface temperature of the nucleus rises. When the ices evaporated, the gases dragged the embedded meteoritic dust. This simple description of a cometary nucleus was accepted rapidly by the science community because it explained successfully many observed cometary phenomena such as the observed jet-like structures in the coma, the non-gravitational effect produced by outflows of gases which by means of the momentum transfer produce a deviation in the orbital motion of the nucleus, and the survival of the comets that passed extremely close to the Sun. Despite general acceptance, Whipple described some controversial points in his model, such as the large differences among the latent heat of vaporization of the gases that he thought might be trapped in the nucleus. This model was validated in 1986, when Giotto mission visited comet 1P/Halley and obtained the first images showing a nucleus with jets emerging from it.

The Oort cloud

During the first decades of the twentieth century, extensive studies of cometary dynamics were carried out, and a wide understanding of the matter was reached. However, some questions still remained unanswered, for example, the existence of comets with original hyperbolic orbits, which would mean that they were not members of the Solar System. A bit later, mainly based on the work of Stroemgren (1947), it was demonstrated that these were not comets with original hyperbolic orbits, it was the influence of planets, chiefly Jupiter, which perturbed the original states. Thus, comets were not coming from interstellar space.

Oort based his studies on the list of 21 comets with long period listed in Sinding (1937), and the work of van Woerkom (1948). Oort (1950) deduced the existence of a cometary population residing in the outer region of the solar system by studying the actual distribution of the semimajor axes of 19 observed comets. He explained that while comets can remain in stable orbits until 200,000 AU, some of them were perturbed by passing stars, and were launched towards the inner solar system. Oort estimated the numbers of members of the cloud at around 2×10^{11} comets to explain the discovery rate of new comets each year. Considering a mean cometary mass of 10^{13} kg, the total of mass of the cloud was concluded to be 10^{24} kg, or $\sim 0.3 M_{Earth}$.

In the early stages of the long term dynamics of the Oort cloud, the passing stars were considered to be the main cause of the comets perturbation, which provided new comets to the inner solar system from the outer part of the cloud. However, during the last decades, the theory evolved and currently the most accepted mechanism is the tidal effects of the galaxy as a whole. In addition, recent simulations established the numbers of comets in the Oort cloud as $1\text{-}2\times10^{12}$ (Heisler 1990; Weissman 1996), and the bulk of them were formed in the Saturn-Uranus region, being transferred from the outer planets region to the Oort cloud.

Ion tails and the Solar wind

The relationship, observed by Carrington (1859), between solar flares and variation of the magnetic activity on Earth, established the first clues of the possible existence of an electrically charged

stream of particles from the Sun, which could be responsible for the excitation of molecules and ions observed in cometary comae. It was Biermann (1951) who identified this relationship when (Hoffmeister 1943) made observations of a comet where the angle between gas tail and the anti-solar direction was $\sim 6°$. That electrically charged stream of particles (mainly hydrogen and helium ions) approximately radially outward from the Sun, was determined as the Solar Wind, whose particles reach velocities of several hundred kilometers per second, depending on the heliographic latitude, solar cycle and interaction regions within the solar wind flow. It was also found that the ion tails are developed closer to the Sun than the dust tail. The cometary ion tails serve as a laboratory for plasma phenomena, which cannot be simulated properly in a laboratory on Earth. The current picture of the Solar Wind was confirmed by the *in situ* spacecrafts ICE and Giotto, when they were visiting comets P/Giacobini-Zinner, P/Halley, and P/Grigg-Skejellerup. Despite being a very good physical phenomena to study the Solar Wind, ion tails do not show large differences when different conditions lead the Solar Wind.

1.2 Comets taxonomies

Historically, the classification of comets has been made according to their orbital properties, i.e., a classification based on their reservoir at the present time. Thus, comets are classified into two large groups: new or not periodic comets, where the orbits are quasi-parabolic, the so-called Long-Period Comets (LPCs), and periodic comets, with elliptic orbits, called Short-Period Comets (SPCs). In the second group (SPCs), two sub-groups are identified depending on their orbital period P : Halley-type Comets (HCs), where the $P \sim 200$ yr, and Jupiter Family Comets (JFCs), with $P \leq 30$ yr. These categories are diffuse, and recently a new population with intermediate values of P between HCs and JFCs, i.e., $30 < P < 200$ (Horner et al. 2003) has been proposed.

The modern dynamical classification is based on the Tisserand parameter with respect to Jupiter T_J (Levison 1996). This parameter is an approximation of the Jacobi constant, which is an integral of motion in the three-body problem. The three bodies involved in our context are the Sun, Jupiter and the comet. Therefore, T_J is a measure of the influence of the biggest giant planet on the dynamics of the comets. It is formulated as follows:

$$T_J = \frac{a_J}{a} + 2\left[(1-e^2)\frac{a}{a_J}\right]^{1/2} \cos i \,, \tag{1.1}$$

where a_J is Jupiter's semimajor axis, and a, e, and i refer to the object's semimajor axis, eccentricity, and inclination, respectively. In addition, this parameter it is also related to the relative velocity v_{rel} between the comet and Jupiter during close encounters:

$$v_{rel} = v_c(3 - T_J)^{1/2} \,, \tag{1.2}$$

where v_c is Jupiter's velocity about the Sun. In this scheme, comets with $T_J < 2$ are designated as *nearly isotropic*, and it is believed that they are mainly comets from the Oort cloud (Oort 1950), reflecting their inclination distribution (Dones et al. 2004). On the other hand, comets with $T_J > 2$ are designated as *ecliptic*, which have small inclinations. These objects most likely originated

at the Kuiper belt (Edgeworth 1949; Kuiper 1951; Fernandez 1980; Duncan et al. 1988) or at the Scattered Disk (Torbett 1989; Duncan & Levison 1997). The *ecliptic* comets can be further subdivided into three groups. Comets with $2 < T_J < 3$ are on Jupiter-crossing orbits, which are dynamically dominated by that planet. This group is called JFCs. Comets with $T_J > 3$ are not on Jupiter-crossing orbits, and can be subdivided according to their semimajor axis a. If $a < a_J$, it is designated *Encke-type*, and if $a > a_J$, it is *Chiron-type* or *Centaur*.

The dynamical classifications described here are the most extended. Despite this, in recent years, the emergence of accurate measurements about volatiles in the coma (from multiple spectral regions) have shown H_2O as the volatile dominant, with large number of parent species (HCH, CH_3CN, CH_3OH, CO, CH_4, C_2H_2, C_2H_6, etc.) with abundance varying from comet to comet. This has triggered a new taxonomic classification based on the chemical composition, but it is beyond the scope of this work.

1.3 The dynamics of comets

1.3.1 General cometary equations of motion

The general equation of motion of comets, in a heliocentric frame, should include the gravity of the Sun, gravitational perturbations from planets and larger minor planets, relativistic effects, and the jet forces caused by gases leaving the nucleus, i.e., accelerations due to non-gravitational effects. Thus, the equation of motion can be written as:

$$\frac{d^2\vec{r}}{dt^2} = -\frac{k^2\vec{r}}{r^3} + k^2 \sum_j m_j \left[\frac{(\vec{r}_j - \vec{r})}{|r_j - r|^3} - \frac{\vec{r}_j}{r_j^3} \right] + \frac{k^2}{c^2 r^3} \left[\frac{4k^2\vec{r}}{r} - (\dot{\vec{r}}\cdot\dot{\vec{r}})\vec{r} + 4(\vec{r}\cdot\dot{\vec{r}})\dot{\vec{r}} \right] + \vec{J} \tag{1.3}$$

Where c is the speed of light given in AU day^{-1}; k is the Gaussian Gravitational constant $k \approx 0.017202$ AU$^{3/2}$ day^{-1} M$_\odot^{-1/2}$; m_j are the masses of planets and the minor planets Ceres, Vesta, and Pallas; $\vec{r}$ and r are the heliocentric position vector and distance of the comet; $\dot{\vec{r}}$ are the accelerations given in AU (ephemeris day)$^{-2}$; r_j are the planetary distances from the Sun. The first term in the right-hand side of the equation is the solar acceleration where the Sun's mass is taken as unit (Marsden et al. 1973). The second term represents both the direct effects of the perturbing bodies on the comet, which are the planets plus the three most massive minor planets, and the indirect effects of the perturbing bodies upon the Sun. The third term represents the relativistic effects (Anderson et al. 1975). These effects affect objects with small semimajor axes and large eccentricities introducing a non-negligible radial acceleration toward the Sun (Sitarski 1983, 1992). Finally, the fourth term in the equation, $\vec{J}$, represents the non-gravitational effects due to outgassing owing to ice sublimation on the nucleus surface. We discuss the nature and the influence of the non-gravitational forces in the cometary motion in the next subsection.

Non-gravitational forces

In 1819, the German astronomer Johann Franz Encke, discovered that the comet 2P/Encke experienced a shortening in its orbital period at a rate of about 2.5 hours per orbit. That deviation from the pure gravitational motion was also observed in comets 3D/Biela and 16P/Brooks. In principle, those delays were attributed to the presence of a resisting medium crossed by the comets in their motion, but this interpretation did not explain the secular increase of periods observed in some comets like 8P/Tuttle, or the increase and decrease shown by 21P/Giacobini-Zinner. It was 1836, when the astronomer Friedrich Wilhelm Bessel, suggested that the variations in the orbital motions were caused by the material expelled predominantly in the sunward direction, which produced a recoil force on the comet nucleus. This idea was ignored for more than a century due to the lack of information about the nature of comets. In 1950, Fred Whipple reintroduced Bessel's idea, introducing the non-gravitational forces as a consequence of the jets produced by the non-isotropic sublimation of gases from the comet nucleus. According to Whipple, due to the thermal inertia in a rotating nucleus, the outgassing region produced a net force $\vec{J}$ deviated from the radial direction of the Sun (see Fig 1.1). This net force has three non-gravitational components acting on the comet nucleus: radial J_r, transverse J_t, and normal J_n. The acceleration or deceleration of the comet's motion is caused by the transverse component, depending on whether it is directed along the motion or in the opposite direction. The detection of non-gravitational forces in the case of the periodic comets is based on the delay or advance in the time of the perihelion passage in respect to the prediction of the pure gravitational motion, and this corresponds to a change of ΔP in the orbital period P. For example, in the case of comet 1P/Halley, the average delay is $\Delta P \simeq 4.1$ days. The change ΔP can be expressed as a function of the radial and transverse non-gravitational components by means of the planetary equations under the Gauss form, which leads to:

$$\Delta P = \frac{6\pi}{n^2 a} \int_0^P \left[\frac{e \ \sin f}{(1-e^2)^{1/2}} J_r + \frac{a(1-e^2)^{1/2}}{r} J_t \right] \, dt \ , \tag{1.4}$$

where n is the mean motion given by $n = 2\pi/P$, e is the eccentricity, and f is the true anomaly.

The standard model of the non-gravitational forces establishes the values for the three components as:

$$J_r = A_1 g(r) = \Gamma \ g(r) \cos\lambda \ , \tag{1.5}$$

$$J_t = A_2 g(r) = \Gamma \ g(r) \sin\lambda \ , \tag{1.6}$$

$$J_n = A_3 g(r) = 0 \ , \tag{1.7}$$

where Γ is the magnitude of the non-gravitational force at 1 AU from the Sun, λ is the lag angle, and the $g(r)$ is the variation law with the heliocentric distance. A_1, A_2, and A_3 are the standard non-gravitational parameters, where $A = (A_1^2 + A_2^2 + A_3^2)^{1/2}$. The non-gravitational acceleration is generally given in terms of these parameters, which are expressed in units of 10^{-8} AU day^{-2}.

Therefore, the equation of motion defined in equation 1.3 becomes:

$$\frac{d^2\vec{r}}{dt^2} = -\frac{k^2\vec{r}}{r^3} + k^2 \sum_j m_j \left[\frac{(\vec{r}_j - \vec{r})}{|r_j - r|^3} - \frac{\vec{r}_j}{r_j^3} \right] + \frac{k^2}{c^2 r^3} \left[\frac{4k^2\vec{r}}{r} - (\dot{\vec{r}} \cdot \dot{\vec{r}})\vec{r} + 4(\vec{r} \cdot \dot{\vec{r}})\dot{\vec{r}} \right] + A_1 g(r) \frac{\vec{r}}{r} + A_2 g(r) \vec{t} \tag{1.8}$$

The $g(r)$ variation law was established by Marsden et al. (1973) from a fit of the sublimation rate of water-ice given by Delsemme & Miller (1971) as:

$$g(r) = \alpha \left(\frac{r}{r_o} \right)^{-m} \left[1 + \left(\frac{r}{r_o} \right)^n \right]^{-k} , \tag{1.9}$$

where $\alpha = 0.1113$ is a normalization factor such that $g(1) = 1$, $m = 2.15$, $n = 5.093$, $k = 4.6142$, and $r_o = 2.808$ AU.

The component J_r may become dominant when moderate to high asymmetric outgassing with respect to perihelion is produced. In contrast, if the outgassing is symmetric, ΔP will depend only on the transverse component, J_t. The acceleration component normal to the orbit plane J_n, is also present for the most active comets, and will affect the longitude of the ascending node and the orbital inclination, but it is not secular, and in general it is poorly determined. Thus, the solution for A_3 is generally not useful.

The evaluation of the non-gravitational forces is, in general, more difficult for LPCs than for SPCs, since these have not been observed in a second (or further) appearance, which allow us to determine the advance or delay in the time of perihelion passage. Despite this fact, non-gravitational terms have been fitted to the equation of motion of some LPCs, where they show values of A_1 and A_2 one or two order of magnitude larger than for period comets.

Although it has an important role in the accurate determination of the cometary motion, the non-gravitational force is relatively small, and is mainly used to link periodic comet appearances during long time intervals and when discussing models of thermophysical behavior of cometary nuclei. Thus, in the large-scale evolution of cometary orbits, it is rarely of importance, being in general neglected for these kinds of studies.

1.3.2 Comet reservoirs and transfer mechanisms

The physical and dynamical lifetime of comets is short compared to the age of the solar system. Comets must be coming from some regions, which have the role of reservoirs that leak out the comets to the inner regions where they can be detected. These reservoirs should be stable enough to retain a significant number of objects for billions of years, and they should have active mechanisms to transport comets into other regions. Currently, there are three recognized comet reservoirs: (1) The Oort Cloud, which is the source of the LPCs, postulated by Oort in 1950 (Oort 1950). (2) The Transneptunian region, which is "traditionally" subdivided into two populations: The Kuiper Belt,

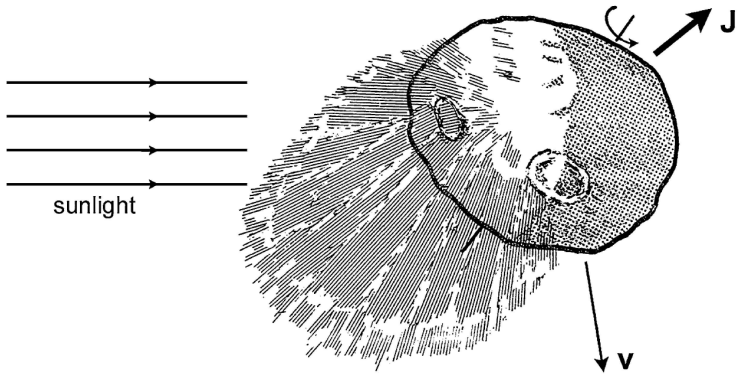

Figure 1.1: Action of non-gravitational forces on comets. $\vec{V}$ is the orbital velocity. The sunlight produces the sublimation of ices, which causes a net force $\vec{J}$ in the opposite direction to the maximum outgassing. Due to the thermal inertia, the region of maximum outgassing of the rotating nucleus will lag with respect to subsolar point. Extracted from Fernández (2005).

which was discovered in 1992 (Jewitt & Luu 1993), and entailed a huge step in the understanding of how the solar system works, and the Scattered Disk, which is an extended disk of highly eccentric objects with their semimajor axes outside the orbit of Neptune. This population was proposed by Fernandez (1980) and Torbett (1989). (3) The main Asteroid Belt. The active asteroids in the Main-Belt constitute a new class of objects. The prototype for them is comet 133P/Elst-Pizarro, the first member of this class discovered (Hsieh et al. 2004).

Oort cloud

In 1950, Jan Hendrik Oort identified a family of comets with random inclinations of their orbits, with semimajor axes clustered at large values. Those comets were the first to be determined as LPCs, coming from a spherical bubble located in the outermost region of the solar system. This spherical cloud was formed by the ejection of bodies from the giant planets region. The primitive first explanation of the Oort Cloud formation, does not take into account effects like galactic tide, Dones et al. (2005) carried out simulations of the Oort cloud dynamics using the following assumptions: (1) The distribution of the planetesimal were distributed in the 4-40 AU zone with small eccentricities and inclinations. (2) The giant planets were assumed to be in their current orbits. (3) The migration of the planetesimal because the late bombardment was neglected. (4) The evolution of the planetesimals were under the influence of the gravitational force of the 4 giant planets, the galactic tide, and passing stars. The result of this simulation showed that in early times the cloud was empty, and the region of giant planet was filled with small solid bodies ("icy planetesimals"). After some encounters of these objects with Neptune, the planetesimals were scattered to larger semimajor axes, while keeping their perihelion distances in the planets region. After 700 Myr, the random walk produced an enhancement of the semimajor axis up to $\sim 10^4$ AU, and then the galactic tide started to be effective moving the perihelion distance to 45 AU. In this phase, the influence of Neptune is negligible, and the major changes in the semimajor axis are due to distant stellar encounters. At $t = 1$ Gyr, there were some perturbations which produce important variations in their

inclination relative to the galactic plane $\tilde{\imath}$, and when $\tilde{\imath} = 65°$, the effect of the tide started to be more pronounced, causing an increase in perihelion distance and inclination (up to $\sim$ 1000 AU, $\sim 80°$) at $t = 1.7$ Gyr. The planetesimal with the argument to perihelion, $\tilde{\omega}$, (also refered to the galactic plane, not be confused with one relative to solar system plane, ω) in the range of 90° to 180° (or symmetrically, between 270° to 360°) had their e decreased. This fact produced an enhancement in the perihelion distances, carrying them beyond the planets' reach, so the planetesimals could not be scattered any more, and they became Oort cloud objects. In principle, this process is reversible, and the perihelion distances and $\tilde{\imath}$ should decrease, and bring the planetesimals into the planetary regions again, but the reversibility is broken by the encounters with distant stars, making a stable situation in the Oort Cloud, which is breaking under hazardous perturbations. Not all the particles in the simulations followed the same evolution. Some that interact closely with Jupiter and Saturn were mostly ejected from the solar system. The formation process of the Oort Cloud dominated until 840 Myr, when the population peaks its maximum value. The erosion process became dominant afterwards, and the total mass in the cloud decreased by $\sim 5.5\%$. The final picture of the Oort Cloud presents a radial distribution given by $N(r)dr \propto 1/r^3$. About 5-9% of the planetesimal from the Uranus-Neptune-transneptunian region remains in the Oort Cloud at the end of the simulation. However, just 2% of the ones from the Jupiter-Saturn region do so. It seems that the scattering action is too strong in this region.

The mechanism of how LPCs become observable, i.e., the comets travelling from the Oort Cloud to inner part of the solar system where they could be heated by the Sun, was explained by Oort as a perturbation due to distant passing stars. Currently, two additional perturbers have been recognized: (1) Gas Molecular Clouds (GMCs) in the galaxy, proposed for the first time in 1970 and later reported by Biermann (1978) and Clube & Napier (1982); (2) Galactic gravitational field itself, in particular the tidal field of the galactic disk (Byl 1983, 1986; Harrington 1985; Heisler & Tremaine 1986). Passing stars can eject some comets and perturb the orbits of others (Hills 1981). A $1M_\odot$ star passing at a speed of $\sim$ 20 km s^{-1} could perturb comets within a radius of $\sim$ 450 AU. Weissman (1980) estimated that over the history of the solar system, passing stars have ejected about 10% of the Oort Cloud population. The GMCs encounters are very rare, actually occurring each 3-4$\times 10^8$ yr, but they can produce the major perturbations in the comets orbital motion in the Oort Cloud. Some studies have determined (Hut & Tremaine 1985) that the perturbation suffered by the Oort Cloud, due to effect of GMCs, is roughly equal to that produced by stellar passages. The third mechanism to perturb the comets of the Oort Cloud is the overall gravitational field resulting from the mass distribution in the galaxy, i.e., the galactic tide. The galaxy can be considered as a disk-like structure, with the Sun out of the center. In this case the galactic tide has both "disk" (F_z) and "radial" (F_x and F_y) force components given by:

$$F_x = \Omega_o^2 x \tag{1.10}$$

$$F_y = -\Omega_o^2 y \tag{1.11}$$

$$F_z = -4\pi G \rho_o^2 z \tag{1.12}$$

where Ω_o is the frequency of revolution of the Sun around the galaxy, ρ_o is the mass density in the solar neighborhood, and G is the gravitational constant (Heisler & Tremaine 1986). The disk component dominates over the radial component by a factor 8-10, and for this reason $F_{x,y}$ are typically neglected. The disk tide preserves the semimajor axes, a, and the z-component of the angular momentum of the comet , $H_z = \sqrt{1-e^2}\cos\tilde{\imath}$, while e and $\tilde{\imath}$ change with the precession of $\tilde{\omega}$. This behavior causes that under the effect of the tide, when a comet has high inclination relative to the galactic plane , $\tilde{\imath}$, its e increases, and consequently its perihelion decreases. So, the comet becomes a planet-crosser. When perihelion decreases from beyond 10 AU to less than ~ 3 AU within half of an orbital period, the comet is called "new comet", and is active during its first entrance into the inner region of the solar system. This perturbation is larger for orbits with their line of apsides at galactic latitudes of $\pm 45°$ and becomes null at the galactic equator and poles.

In summary, the galactic tide is established as the major perturber of the Oort Cloud at most times (Harrington 1985; Byl 1983, 1986; Heisler & Tremaine 1986; Delsemme 1987). However, GMCs and passing stars still play an important role as perturbation mechanisms.

Transneptunian populations: Kuiper Belt and Scattered disk

Edgeworth and Kuiper developed the idea of the existence of a belt of small bodies beyond Neptune, between 30-50 AU, where planetesimals conserved their pristine conditions of the protoplanetary disk. However, their picture of the frozen disk of objects was incorrect, because it has been affected by processes that altered its original structure.

The study on the transneptunian objects may provide us with the necessary clues to understand how the giant planets were formed , and as a domino effect, how the terrestrial planets were formed, in short, what occurred during the primordial ages in the outer solar system.

The population in the belt beyond Neptune is divided into two subpopulations: Kuiper Belt Objects (KBOs) and the Scattered Disk (SD). The definition of both subpopulations is somewhat diffuse. Here we discuss a categorization based on the dynamical properties of the objects. The KBOs have low eccentricities, their orbits are quasi circular with semimajor axes between 35-50 AU. In 1993, Jewitt & Luu (1993) reported the discovery of the first KBO candidate 1992 QB1. They are very stable objects, which can be subdivided into two populations: The *resonant population* and the *classical belt*. The former corresponds to objects located in the major mean-motion resonances with Neptune (essentially the 3:4, 2:3 and 1:2). These resonances offer a protection mechanism against close encounters and orbital perturbations. However, the classical belt objects are not in any resonance configuration. KBOs region can not be populated by bodies after suffering encounters with Neptune. Therefore, their eccentricities and inclinations can not be explained by the scattering action of the planet. This point to a some excitation mechanism in the past. The Scattered Disk region is populated by bodies that have encountered Neptune within the influence of Hill's radius [1] at least once during their dynamical evolution. They are unstable, with very elliptical orbits with perihelion distances in the region of 30-40 AU. Therefore, their orbits can evolve due

[1] The Hill's radius is defined by $R_H = a_p(m_p/3)^{1/3}$, where m_p is the planet's mass relative to the mass of the Sun, and a_p is the planet's semi major axis. It corresponds roughly to the distance from the planet to the Lagrange equilibrium points L_1 and L_2.

to encounters with Neptune. The current theories suggest this population as the origin of the Centaurs, whose semimajor axes are in 10-30 AU region. Consequently, they are under the influence of giant planets, and their half-lifes are short, in the range of 1-100 Myr. The gravitational interaction with giant planets, basically Jupiter, can perturb their orbits injecting these comets into the Jupiter Family region. Nowadays, there are around 200 Centaurs cataloged, some of which are Chiron, Cariklo, Echecleus, and 29P/Schwassmann-Wachmann (29P/S-W). Dynamical simulations show that roughly 30% of the Centaurs can evolve into JFCs. In addition, some Centaurs show activity, as Chiron and 29P/S-W, though what drives their activity is still not completely understood. CO sublimation and cryovolcanism are invoked as possible mechanisms.

Main Asteroid Belt

The Main Asteroid Belt is located between the orbits of Mars and Jupiter, and has been historically populated by (inactive) asteroids. However, in 1996, a comet-like object was discovered: It had dust coma and tail, but with orbital parameters typical of asteroids from the Main-Belt. This object was 133P/Elst-Pizarro. It was supposed that its activation was triggered by a collisional event, but the reappearance of its activity in 2003 during its perihelion passage implied another explanation. This was the first Main-Belt Comet (MBC) discovered. From that date, at the time of writing, there are 14 MBCs identified. The orbits of this population of objects are decoupled from Mars and Jupiter, and it seems that they are dynamically stable on billion year timescales (as the asteroids that occupy the same region) (Hsieh & Jewitt 2006) . The current dynamical studies of this population reveal that there is not any mechanism which could inject comets into the MBC-like orbits, so they are native to this region. What drives their activity is still unclear. Three mechanisms have been proposed: (1) Water ice sublimation. Water ice is the only volatile expected to survive in the outer part of the Main-Belt, and in addition, in the case of the 133P/Elst-Pizarro the mass loss has been observed at consecutive perihelia but not in between, which is the typical behavior of sublimation activity (Hsieh et al. 2004) (2) Collisional activation. It was identified as the driver in the case of (596) Sheila (Moreno et al. 2011b). (3) Rotational disruption. Dust particles can be ejected by the centrifugal force from the surface if the rotational period is short enough (Jewitt et al. 2013; Moreno et al. 2014).

Of these three driving mechanisms of the MBCs activity, it seems that the most likely is water-ice sublimation, and an attempt to link this fact with the Earth's oceans has been established. In early times, Earth was too hot to trap much water, so it is widely accepted that an external source of water was required. One possible source are comets, but the measurements of the isotope ratios of deuterium to hydrogen (D/H ratio) have shown that it is implausible because this ratio is approximately double in comets than in the oceanic water. Just in one comet, 103P/Hartley 2 (which is a member of the JFCs), this ratio was found to be the same as Earth's oceans. The existence of water in the Main-Belt should not be a surprise. Actually, some meteorites show evidence of clay minerals and serpentines, proving that they have been bathed in liquid water at temperatures close to triple point. In addition, half of the outer belt asteroids show absorption features, which can be attributed to the presence of hydrated minerals.

In order to determine if MBCs are the source of water on Earth, there is an expert committee preparing a European space Mission called Castalia, which is an *in situ* mission whose spacecraft

will visit the best known MBC at this moment, 133P/Elst-Pizarro. The specific science goals of Castalia will try to answer three key questions: (1) What is the nature of the MBCs and what triggers their activity?. (2) Is water present in MBCs and does it drive the activity?. (3) Is the water in the asteroidal belt related to terrestrial water? (see e.g. Hilchenbach 2013; Snodgrass & Castalia mission science Team 2013).

1.3.3 Introduction to numerical integration codes

Newton's Law of Universal Gravity describes the force F between two bodies of masses m_i and m_j as:

$$\vec{F}_{ij} = k^2 \frac{m_i m_j}{\rho_{ij}^2} \frac{\vec{r}_i - \vec{r}_j}{\rho_{ij}} \,, \tag{1.13}$$

where $\vec{r}_i$ and $\vec{r}_j$ are the position vectors in an inertial frame, ρ_{ij} is the scalar distances between particles, and k is the Gaussian constant. For more than two bodies, the so-called N-body problem, the resulting system of differential equations can only be solved by numerical techniques. However, due to the huge progress in the computing field during the last decades, many powerful algorithms have been developed which allow us to solve many problems with reasonable CPU/memory requirements, giving accurate results. In this subsection we give an introduction to the most commonly used methods to solve the N-body gravitational problem, namely the Gauss-Radau quadratures, the Burlish-Stoer method, and the symplectic integrators. In addition, we introduce the Mercury6 FORTRAN package, developed by Chambers (1999), which contains the implementation of all of those methods, and where the author incorporates his Hybrid symplectic algorithm, which is the one used by us in our dynamical studies.

Gauss-Radau quadratures

The main idea is that the integral of a given function can be estimated by a sum of functional evaluations at arbitrary points (nodes), being multiplied by certain coefficients or weights. The method establishes, at the beginning of the integration interval, one fixed abscissa point, and the rest of the points and the weights coefficients are selected to maximize the degree of accuracy of the interpolation. This method can integrate polynomials of an order that is related to the abscissa number of nodes up to the precision of the machine. The major drawback of this algorithm concerns the recalculation of the optimal abscissa and weights when the order of the integration changes, which is very inefficient. Everhart was one of the first to apply this algorithm to astrodynamical problems (Everhart 1974).

Bulirsch-Stoer method

This algorithm (Stoer & Bulirsch 1980) to solve ordinary differential equations, is a clever mixture of two separate ideas: (1) an extrapolation method via the rotational function in Richardson-type applications, where the step-size is an unknown analytic function, computing the numerical integrations for various values of the step-size, and (2) the modified midpoint method, which itself

is a second-order method, to achieve numerical solutions with high accuracy and small computational effort compared to most second-order algorithms. This algorithm is one of the most effective methods, thanks to the variable step-size integration and the cost-effectiveness concerning the CPU time.

Symplectic Integrators

The symplectic integrators are algorithms to compute differential equations related to classical mechanics under non-dissipative phenomena, which are often modeled by the numerical solution of Hamilton's equations. In the symplectic theory, these conservative phenomena have certain geometrical properties which are time invariant. These integrators are widely used in discrete element methods, molecular dynamics, and celestial mechanics as well.

The MERCURY package and the Hybrid symplectic integrator

This software package is designed to calculate the orbital evolution of objects moving under the influence of a gravitational field generated by a large central body. In our case, we use it to study the orbital evolution of comets around the Sun, taking into account the presence of the eight planets of the solar system. In addition, one can introduce the non-gravitational acceleration parameters A_1, A_2, and A_3 to compute the non-gravitational forces in the problem. This package includes five different N-body integrators:

- *MVS*. This is a second-order-mixed-variable symplectic algorithm. It is a very fast integrator, but unable to control close encounters.
- *BS*. This is a general Bulirsch-Stoer algorithm. It is generally very accurate, but demands large CPU time.
- *BS2*. It is a conservative Bulirsch-Stoer algorithm, twice as fast as the general BS routine, but only applicable to conservative systems.
- *RADAU*. It is a Gauss-Radau quadrature, 2-3 times faster than general BS. Usually gives good results, but fails for very close encounters or very eccentric orbits.
- *Hybrid*. It is a MVS+BS algorithm. It is a very fast integrator and is capable of dealing with close encounters, although it is only moderately accurate.

The package can be downloaded from: `http://star.arm.ac.uk/~jec/home.html`. For our purposes, we used the Hybrid symplectic algorithm (see Chambers 1999), which is an integrator specially suited to the field of celestial mechanics. This technique uses the symplectic theory in combination with the Burlirsch-Stoer method, in order to obtain a fast integrator with the capability to work under situations where the symplectic theory is violated, as in the case of close encounters between bodies. However, as anticipated, its accuracy is only moderate, which produces some spurious results. In order to solve this problem, we performed a statistical study of the orbital evolution of each comet, as it was first made by Levison & Duncan (1994), who also

reported on the chaotic nature of each individual orbit. We follow the procedure of the authors, who were the first to study the dynamical evolution of a sample of comets using a set of long-term integrations. They computed backward and forward integrations, up to 10 Myr, for 160 SPCs. To carry out the statistical study, they used three clones for each comet with offsets in the positions along the x, y, and z directions of +0.01 AU, resulting a total of 640 test particles. From those studies, the authors concluded that the integrations are statistically equivalent either forward or backward in time. In addition, they obtained that $\sim$ 98% of the particles were removed from the integration via ejection from the solar system ($\sim$ 92%) or becoming Sun-grazers ($\sim$ 6%). They derived the median lifetime of those comets in the JFCs as 3.25×10^5 yr. In a later study (Levison & Duncan 1997), they extended this value to the range of $(3 - 25) \times 10^3$ yr, where the most likely value was found as $12{\times}10^3$ yr. In our work, our aim is to reproduce their studies for a sample of eleven comets, in order to determine statistically the orbital evolution of each one. To perform this task, we generated 99 clones having 2σ dispersion in three orbital elements: semimajor axis a, eccentricity e, and inclination i, where σ is the uncertainty of each parameter extracted from the JPL Horizons on-line solar system data (see `ssd.pjl.nasa.gov/?horizons`). This means for each comet 100 massless test particles. It is important to note that for these long integrations, the non-gravitational forces can be neglected. To justify this estimation, we followed Lacerda (2013), who assumed that the change rate of the semimajor axis da/dt is generated by a non-gravitational acceleration T, produced by a single sublimation jet tangential to the comet's motion, and acting until the total evaporation of the nucleus t_{sub}. This process is formulated as follows:

$$\frac{da}{dt} = \frac{2Va^2T}{GM_\odot} \tag{1.14}$$

$$T = \frac{dM_d}{dt} \times \frac{v_d}{m_{nuc}} \tag{1.15}$$

$$t_{sub} = m_{nuc} \times \left(\frac{dM_d}{dt}\right)^{-1} \tag{1.16}$$

Therefore, the total deviation of the semimajor axis D would be:

$$D = \frac{da}{dt} \times t_{sub} \tag{1.17}$$

where dM_d/dt is the dust mass loss rate, V is the orbital velocity, a is the semimajor axis, G is the gravitational constant, $M_\odot$ is the Sun mass, v_d is the dust velocity, and m_{nuc} is the mass of the nucleus. These equations were solved by Lacerda (2013), where the author found $D = 0.42$ AU, which agrees with our highest value $D = 0.33$ AU. Those values demonstrate that the non-gravitational forces can be neglected, due to their small contribution to the cometary orbital motion in a long-integration problem. This is described in detail in papers II and III.

From the analysis of the dynamical history of SPCs, we expect to verify the previous studies of Levison & Duncan (1994) and Levison & Duncan (1997), to determine the most likely recent past of the comets of the sample, where it is expected that they came from the Centaur or Transneptunian region, and derive, with a 90% confidence level (CL), the time spent by them in the region of the JFCs. The results are shown in chapter 4, papers II and III.

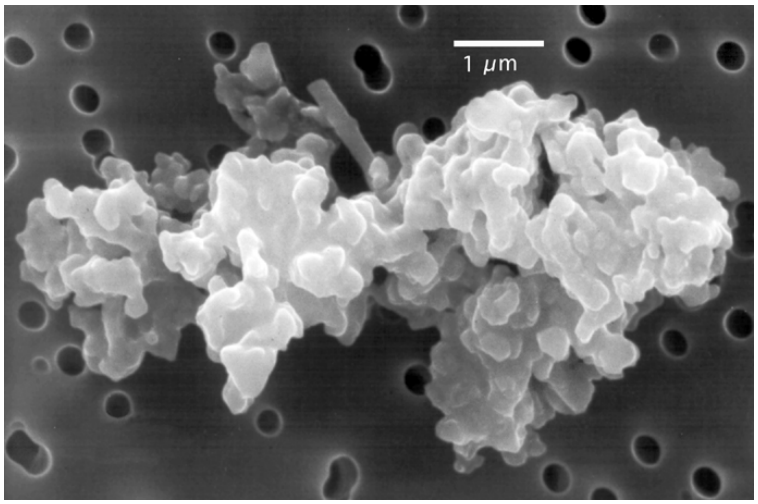

Figure 1.2: Interplanetary dust particle about 10 μm with irregular shape and porous.

1.4 The properties of dust

1.4.1 The nature of the dust particles

Cometary dust should contain some of the least altered material surviving from the solar nebula. Thus, the mineralogy and structure of these particles give us important clues about the early ages of the solar system. The dust composition must reflect the radial gradients in the chemical composition and temperature of the solar nebula, and the mixing of material from cold outer regions and warm inner regions. These dust particles scatter the solar light, leading to the cometary tails and comae. The Stardust mission has given the first direct evidence of the irregularity and porosity of these particles, which range from compact units to fluffy structures (Hörz et al. 2006) (see Fig. 1.2). Some of those particles have been regularly collected in the stratosphere by aircraft instrumentation (Brownlee 1981). However, it has been common practice to assume those particles to be spherically-shaped. This is because the simplicity of the Lorentz-Mie theory for calculation of the scattering matrix as compared with current numerical light scattering codes for non-spherical particles, which in practice are limited to particles with size on the order of wavelength or smaller, because of the huge CPU/memory resources needed. Comet dust is composed of an heterogeneous mixture of mineral condensates at both low and high temperature, likely from different regions. Thus, the silicate component in comets is a mixture of amorphous grains formed at low temperatures and crystalline grains formed at the much hotter temperatures (T$\sim$1000 K) typical of the innermost regions of the solar system. Hence, the ratio of amorphous to crystalline components is giving information about the pre-planetary disc, when they were incorporated into comets. Therefore, the study of the dust grains of comets, attending to their chemical composition, structure and properties, is an important topic in the puzzle of the comet formation and evolution.

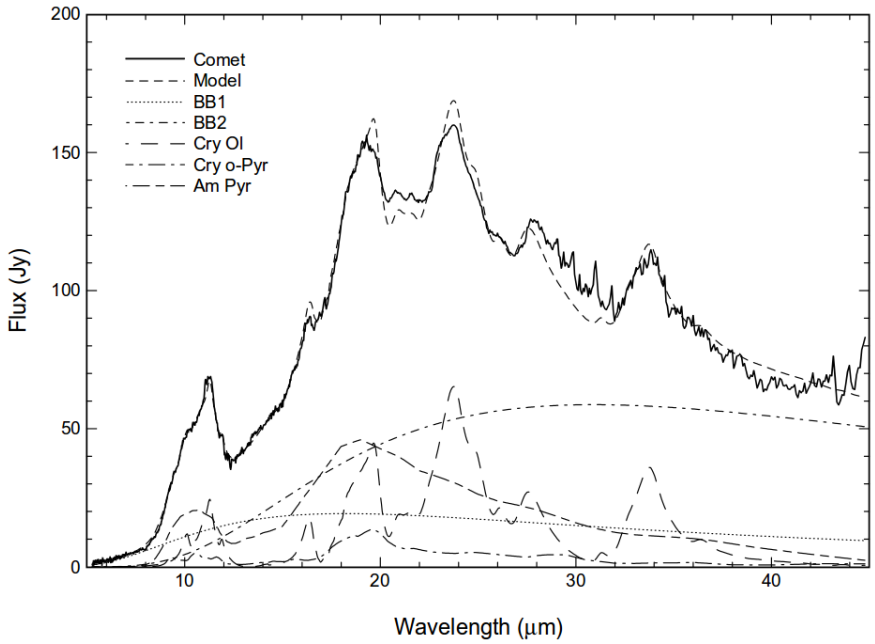

Figure 1.3: ISO SWS spectrum of comet Hale-Bopp (Crovisier et al. 2000). Some silicates emission features are shown superimposed on a black body spectrum.

Composition

Information about the chemical composition of the cometary dust grains can be obtained by spectral observations. These spectral studies, show strong emission features in the infrared wavelength range. There is a broad Si-O stretch emission feature at about 10 μm, which can be observed using ground-based instruments thanks to the atmospheric window at those wavelengths. This strong silicate emission feature has been observed in several comets, such as comet Hale-Bopp, where the silicate emission was by far the strongest observed in any comet (see Fig. 1.3). These observations have been compared to models and laboratory spectra of silicates in order to identify the mineralogical composition. The best fits found consist of a mixture of amorphous and crystalline grains, mainly olivine and pyroxene (e.g. Min et al. 2005; Moreno et al. 2003; Crovisier et al. 2000). Therefore, cometary grains are a combination of condensed material at low temperatures (amorphous) and processed material at high temperatures (crystalline), and it is likely that, this composition is the result of mixing processes in the proto-planetary disc. Apart from LPCs, this silicate emission feature has also been seen in SPCs, where it shows up as a much weaker feature (Hanner et al. 1996). This could be due either to a compositional difference between Kuiper belt and Oort cloud comets or to a lower abundance of sub-micrometer particles in SPCs, owing to the many orbits in the inner solar system expelling material.

The most important source of information about the chemical composition of cometary grains comes from *in situ* missions, such as Giotto and Vega, which used a mass spectrometer (Langevin et al. 1987). So far, the most complete chemical analysis of dust grains has come from Stardust mission, which returned grains from comet 81P/Wild-2 back to Earth embedded in an aerogel

panel. From these studies, the chemical composition shows, in general, three types of grains, with about equal relative abundance:

- Particles consisting of light atoms ($\sim$ 30%): C, H, O, and N.
- Particles consisting of silicates ($\sim$ 35%): Mg, Si, Na, Ca, and Fe.
- Particles consisting of a mixture of light atoms and silicates, similar to the CO chondrites ($\sim$ 35%).

However, large variations in the composition of individual particles, which present a range from compact to fluffy nature, have been found.

Size distribution

The size distribution of particles is an essential parameter in describing the dust environment of comets. It, however, can not be determined observationally from the ground by direct methods. Thus, the *in situ* measurements, are the best way to derive the size distribution of particles in cometary comae. Unfortunately, just a few comets have been visited by spacecrafts. The results derived from *in situ* missions show that, assuming a mean density of 1 g cm^{-3}, most particles have small radii and the dust mass is concentrated in a few large particles. Then, it is customary to describe the size distribution as a power-law of the form:

$$dn \sim r^{\,\delta}\, dr, \tag{1.18}$$

where dn is the number of particles in the size interval $(r, r + dr)$, and δ is the power index of the distribution.

From *in situ* measurements comet Halley dust by Giotto, Mazets et al. (1986) gave $-1.5 > \delta > -2.5$ for masses lower than 10^{-12} g, i.e., for $r < 0.6$ μm. In the interval $0.6 < r < 6$ μm, then $-2.5 > \delta > -3.0$ and for $r > 0.6$ μm, $\delta \approx 3.4$. In addition, McDonnell et al. (1987) provide a mean cumulative mass index $\xi = 0.69$, which can be related to δ through $\delta = -3\xi - 1 = -3.07$ (Green et al. 1987). For large dust masses, when sizes are >100 μm, they gave $\delta = -2.5$ or even larger. To reduce the number of free parameters, it is often assumed a single power exponent δ for the whole distribution, which is a realistic assumption.

Very small (Rayleigh) particles have a low contribution to the brightness of scattered light (scattered intensity $\sim r^6$). For particles much larger than the wavelength, the intensity of scattered light is proportional to their surface area. Thus, in the limit of very small particles or very large particles, the intensity of light scattered by grains having a power law distribution is given by (Jockers 1997):

$$Scattered\ light\ \sim \left\{ \begin{array}{ll} r^{2+\delta} & \text{for } r >> \lambda : \sim area \\ r^{6+\delta} & \text{for } r << \lambda : \sim Rayleight\ limit \end{array} \right\} \tag{1.19}$$

For $-2 > \delta > -6$, the contribution to the total brightness of a certain size will asymptotically decrease with increasing as well as with decreasing size. If $-3 > \delta > -6$. then the total brightness

will be finite, so, it will not depend on a lower or upper cutoff for the grain size. In both cases, the Rayleigh limit ($r << \lambda$), and macroscopic bodies ($r >> \lambda$), the scattering efficiency does not depend on particle shape (Jockers 1997).

To get an idea about of contribution of particles of different sizes to the mass budget and to the scattered light, we can establish the following rules (Fulle 2004):

- If $\delta < -4$, the brightness and the mass depend on the micrometer size particles.
- If $\delta > -3$, both the mass and brightness depend on the largest ejected grains.
- If $-4 < \delta < -3$, the brightness and the mass are decoupled, the micrometer grains control the brightness, while the the mass mostly depends on the largest particles.

1.4.2 Scattered light by dust grains

The most straight forward method to obtain comet dust physical properties by remote sensing techniques is to study the light scattered by those particles. The intensity and the degree of linear polarization are the magnitudes that give information on the properties of the dust (size, shape, refractive index). These magnitudes depend on the phase angle, α, of the comet at the observation date, which is the angle between the Earth and the Sun as seen from the comet. The relation between the phase angle and the scattering angle, θ, is $\alpha = \pi - \theta$. Other parameters that should be taken into account for observations of the intensity are the geocentric and heliocentric distances of the comet, Δ, and r_h. For very distant objects, α is nearly zero, and values of α larger than $\pi/2$ are only possible when $r_h < 1$ AU.

Angular scattering function

The angular scattering function, or phase function, $\Phi(\alpha)$ indicates how the intensity of the scattered light varies with the phase angle α. This function is difficult to determine since the observed brightness depends on the physical properties of the dust, and the amount of particles within the field of view, which depends on the comet activity, which generally depends inversely on the square of the heliocentric distance. Thus, to normalize the observed intensity, two methods have been used: (1) to assume that the ratio of the dust to gas production rates remain constant over time, and use this ratio to normalize the intensity of the scattered light. This has been done by some authors such as Millis et al. (1982) who derived that the scattering function was a factor of 2 higher at 3°-4° than at 30°, corresponding to a linear phase coefficient, κ, of ~ 0.02 mag deg^{-1}, while Meech & Jewitt (1987), from a sample of four comets observed, at $\alpha = 0° - 25°$, determined κ=0.02-0.04 mag deg^{-1}. (2) The second method consists of comparing the measured scattered light to the thermal emission from the same volume in the coma, assuming that the emission properties of the dust remain constant. This method has been applied to several comets and provides three zones: first, a relatively flat scattering function from phase angles 35°-80° (Tokunaga et al. 1986; Hanner & Newburn 1989; Gehrz & Ney 1992); second, a strong forward scattering for large phase angles $120° < \alpha < 150°$ (Ney & Merrill 1976; Ney 1982; Gehrz & Ney 1992); and third, a gentle backscattering peak at low phase angles $\alpha < 30°$ (see Fig 1.4).

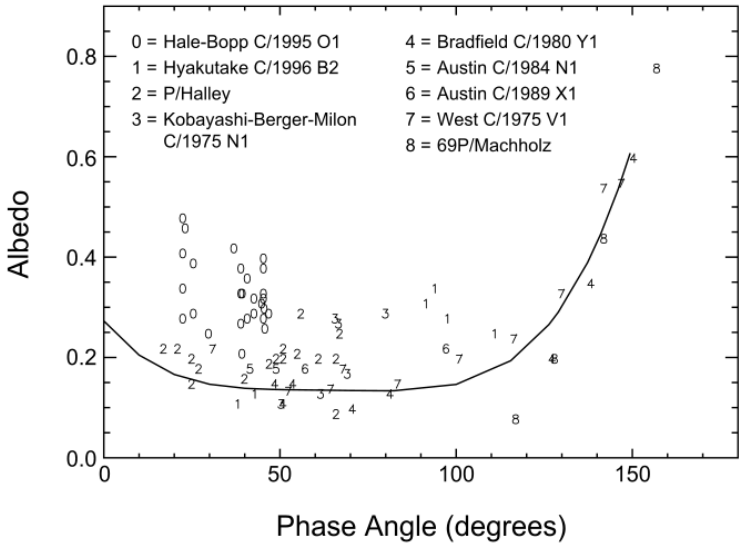

Figure 1.4: Dependence of albedo on the phase angle, extracted from Kolokolova et al. (2004). The numbers correspond to the comet measured and the solid line is the lest-squares fit to the data.

The albedo

In general, the single-scattering albedo A is defined as the ratio of the energy scattered in all directions to the energy removed from the incident beam through reflection, absorption, diffraction, and refraction, by an isolated particle (van de Hulst 1957; Hanner et al. 1981). The albedo is a function of the physical properties of the particle, i.e., its size, its shape, and its refractive index. The geometric albedo A_p, is defined as the ratio of the energy scattered at $\alpha = 0°$ to that scattered by a white Lambert disk of the same geometric cross section (Hanner et al. 1981). Since, usually, comets are not observed at $\alpha = 0°$, it is convenient to redefine A_p as a function of α via the angular scattering function, i.e., $A_p\Phi(\alpha) = A_p(\alpha)$. It is formulated as:

$$A_p(\alpha) = \frac{i_{coma}}{i_\odot}\left(\frac{r_h}{R_{odot}}\right)^2 \frac{1}{f_{coma}} \ , \tag{1.20}$$

where f_{coma} is the geometric filling factor, which is the fraction of the projected area of the sky covered by cometary dust particles, i_{coma} is the intensity averaged over the aperture, which is the observed flux divided by the solid angle of the diaphragm projected on the sky, $i_\odot$ is the mean intensity of the solar disk, r_h is the heliocentric distance, and $R_\odot$ is the solar radius.

1.4.3 Formation and dynamics of the dust tails

Comets develop an extended tail when they approach to the Sun, reaching lengths of up to 10^8 km. These tails are usually curved in shape, and their visible spectrum correspond roughly to that of the Sun, corresponding to solar light scattered by the dust grains. The dust particles are accelerated by gas drag from sublimating ices on the nucleus surface, up to a height of approximately 20 times

the nuclear radius above the surface, when drag vanishes. The particles are then exposed to the solar gravity and radiation pressure forces, which can be written as:

$$F^d_{grav} = \frac{GM_\odot}{r_h^2}\left(\frac{4}{3}\pi r^3 \rho\right) \tag{1.21}$$

$$F^d_{rad} = \frac{Q_{pr}}{c}\left(\frac{L_\odot}{4\pi r_h^2}\right)\pi r^2 \tag{1.22}$$

In these equations, r is the particle radius, c the speed of light, $L_\odot$ the Solar luminosity, ρ the dust particle density, and Q_{pr} the efficiency factor for radiation pressure, i.e., the ratio of particle's cross section for radiation pressure to its geometric cross section πr^2. The efficiency factor can be computed using Mie theory for homogeneous, isotropic spherical grains of known refractive index, and it is given by $Q_{pr} \sim 1$ for large absorbing grains (Burns et al. 1979). The forces F_{grav} and F_{rad} act in the same direction, but in the opposite sense, so that the net force is a central force that varies as $1/r_h^2$, implying that the trajectory will be a Keplerian orbit around the Sun with an effective gravitation reduced by the factor $(1 - \beta)$:

$$F^{eff}_{grav} = F^{grav}_d(1 - \beta), \tag{1.23}$$

where the β parameter is the ratio between the radiation force and the gravitational force:

$$\beta = \frac{F^d_{rad}}{F^d_{grav}} = \frac{3L_\odot}{16\pi cGM_\odot}\frac{Q_{pr}}{\rho r} \tag{1.24}$$

The dynamics of the dust particles is then determined, among other parameters, by the β coefficient (Fulle 1989). The first comprehensive dust tail model was developed by Finson & Probstein (1968a,b), who introduced the concepts of syndynes and synchrones. A syndyne, or syndyname, is the geometric locus, in the plane of sky, of particles of a given size that have been ejected from the comet with zero velocity at different times. A synchrone is the geometric locus of particles of any size ejected at a given time, with zero velocity. This syndyne-synchrone formalism constitutes a zero-order description of a dust tail, but does not provide information on dust loss rates, ejection velocities, or size distribution of the grains.

1.4.4 The $Af\rho$ parameter

The $Af\rho$ parameter, introduced by A'Hearn et al. (1984) is commonly used in cometary science to describe the intrinsic brightness of cometary dust comae. In the $Af\rho$ parameter, A is dust geometric albedo, f is the filling factor in the aperture field of view (proportional to the dust optical thickness), and ρ is the linear radius of aperture centered on the comet, on the plane of the sky. This parameter can be directly derived from photometric observations. It is formulated as follows:

$$Af\rho = \frac{4r_h^2\Delta^2}{\rho}\frac{F_c}{F_s}\ , \tag{1.25}$$

where r_h is the heliocentric distance and Δ is the geocentric distance. The parameter, F_c, is the measured cometary flux integrated within an aperture of radius ρ, and F_s is the total solar flux. It must be noted that since $Af\rho$ depends on the phase angle of the observation α through F_c. This parameter has linear dimensions. Notwithstanding that, it is commonly used as a proxy of the dust production rate. However, it can be shown that $Af\rho$ and dust loss rates only correlate if the expansion velocity of the particles and their size distribution is constant with time, and these conditions are very unlikely to occur in real comets Fulle (2000). The value of this parameter is that it is highly independent of the observing equipment, so that it can be used to characterize cometary activity on long time scales by a number of observers, providing a database for modeling purposes. In fact, in our modeling procedure, we regularly used the $Af\rho$ data kindly provided by the amateur astronomical association *Cometas-Obs*. These data refer to an aperture of $\rho = 10^4$ km, and normally span the orbital arc of the comets while they are available for observing. We also compute the $Af\rho$ parameter from our images, collected generally at the 1.52m telescope of Sierra Nevada Observatory (OSN), so we can compare both amateur and professional data sets. As anticipated, some of these $Af\rho$ measurements correspond to values of the phase angle α close to zero degree. Then, data affected by the backscattering effect (e.g. Kolokolova et al. 2004), producing a brightness enhancement (see Fig. 1.5), independently of the outbursts that can occur anytime during the comet orbital path. This effect can not be modeled in our code, since we assume absorbing spherical particles, for which the phase angle function is nearly constant except for the forward spike for particles with radius $\geq \lambda$. In order to remove this effect from the $Af\rho$ data at small phase angles, we suggest a correction based on previous determinations of the linear phase coefficient, such as those provided by Meech & Jewitt (1987), who gave coefficients κ in the range 0.02-0.04 mag deg^{-1} for various comets when $\alpha \leq 30°$. Thus, the corrected $Af\rho'$ values are computed as a function of the original uncorrected $Af\rho$ values at phase angle α as:

$$Af\rho' = 10^{\frac{-\kappa(30-\alpha)}{2.5}} Af\rho \, . \tag{1.26}$$

An example of the correction performed to the original dataset for comet 78P/Gehrels, when $\alpha \leq 30°$, for various values of κ, is given in Fig. 1.6.

1.5 Outbursts

Cometary outbursts, unexpected brightness enhancements owing to a sudden increase of activity, have been detected in almost every comet. These outbursts were first observed back in the 40's by Richter (1941) and Bobrovnikoff (1954), who studied a sample of comets which had suffered outbursts and proposed the first ideas about what drives those events. During those years some explanations were proposed, such as the change in the energy absorbed by comets (enhancement of solar activity or changes in the albedo of the bodies) or the sudden vaporization of large quantities of methane or CO_2 (Whitney 1955). Later, Klinger (1980) and Smoluchowski (1981) introduced the idea of the transition from amorphous to crystalline ices trapped in the nucleus as a mechanism to explain such changes of activity. Hughes (1990) studied these events, and concluded that at heliocentric distances shorter than 7.5 AU they are apparently random, but tend to occur in pairs and after perihelion passage.

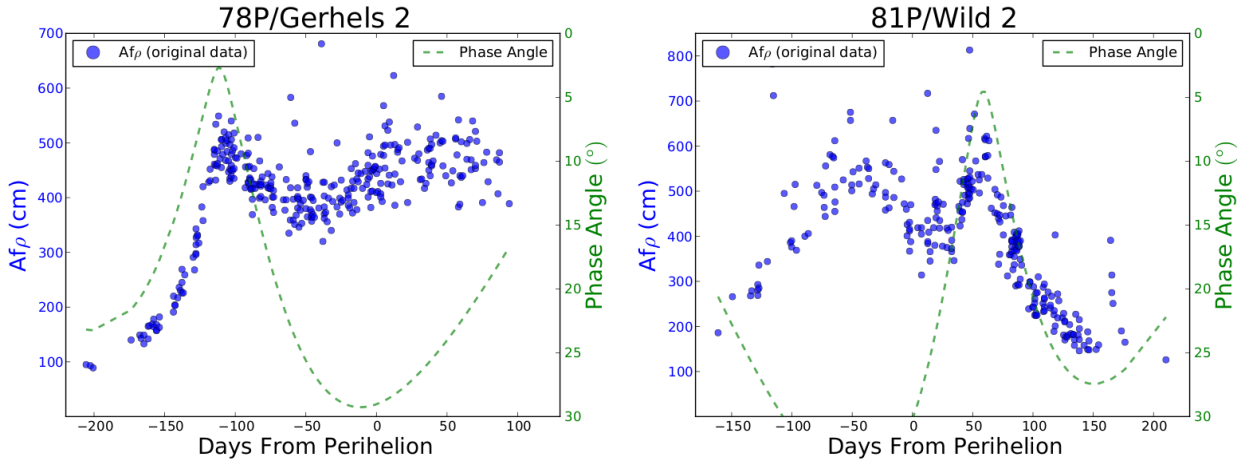

Figure 1.5: $Af\rho$ measurements and phase angle α versus time from perihelion for two comets, 78P/Gehrels 2 (right panel), and 81P/Wild 2 (left panel). In both cases, it can be noticed the clear correlation between $Af\rho$ and α. These values of $Af\rho$ are provided by *Cometas-Obs* (see text).

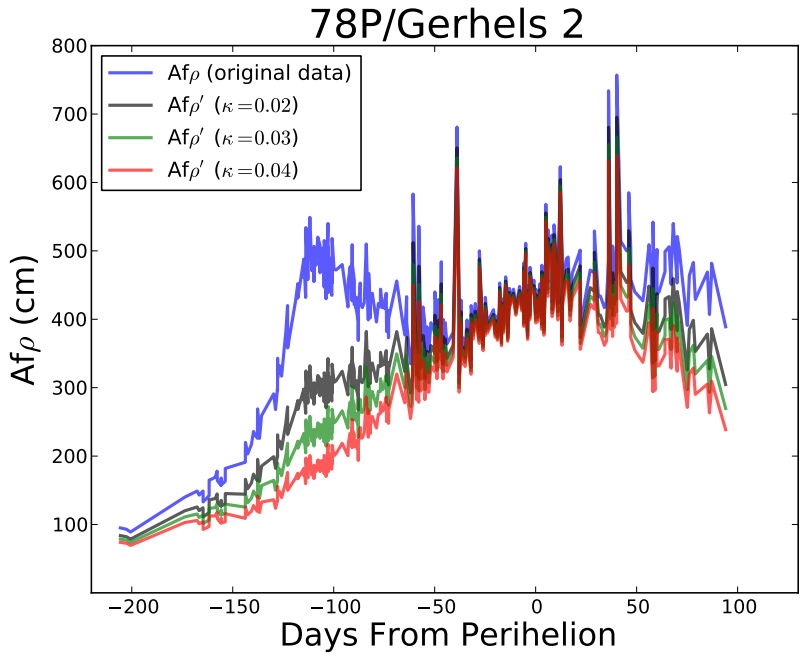

Figure 1.6: Original $Af\rho$ measurements (blue line), and the corrected $Af\rho'$ applying equation 1.26 when $\alpha \leq 30°$ for different values of κ: 0.02 (black line), 0.03 (green line), 0.04 (red line).

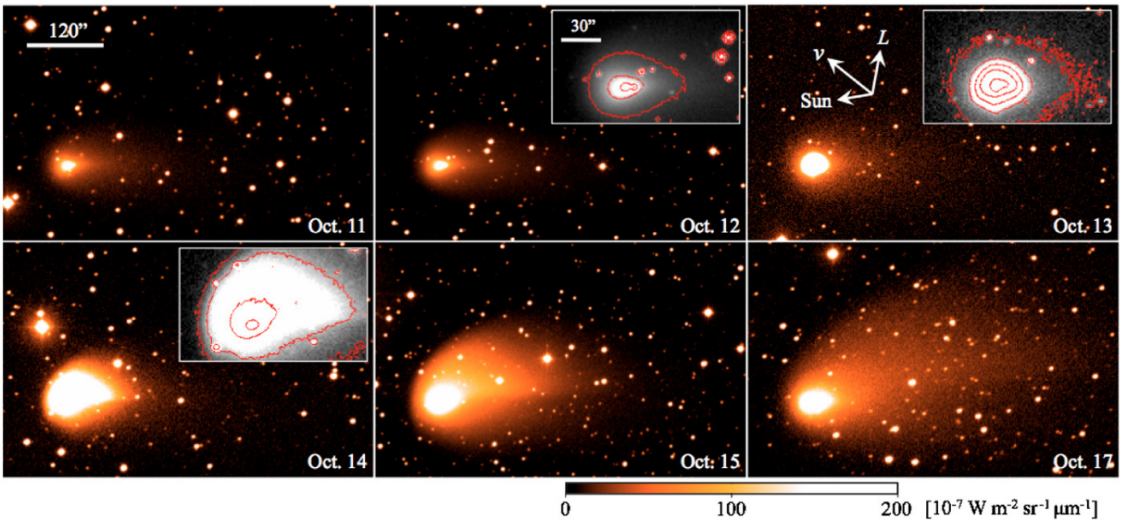

Figure 1.7: Outburst of the comet 217P/Linear, extracted from Sarugaku et al. (2010). The images were taken with the Kiso 105 cm Schmidt Telescope (Japan), from 11 to 17 October 2010. The images revealed a significant day-to-day expansion of the dust tail, indicating the occurrence of an outburst event.

Despite efforts in the study of those events, the driving mechanism involved in these sudden activity enhancements is not clear. Prialnik et al. (2008), in their studies about outbursts of comet 9P/Temple 1, proposed the immediate evaporation at local sunrise of recondensed ices at noon, producing a short-lived surge of activity. Miles (2007) tried to explain the famous 17P/Holmes outburst by the oxidation of water in the porous surface of the comet to form hydrogen peroxide due to the exposure to UV radiation, to energetic solar wind particles, and to cosmic radiation. Fernández (1990) studied the frequency and physical effects of the collision of interplanetary boulders with comets, resulting in two orders of magnitude greater than in the case of planets. In Gronkowski (2007), four probable sources of outbursts' mechanisms were studied: (1) Polymerization of hydrogen cyanide HCN; (2) Impacts with meteoroids; (3) Destruction of cometary grains in the field of strong solar wind; (4) Transformation of amorphous water-ice into crystalline. For each mechanism, the author gave the values of the released energy and jumps of cometary brightness, and concluded that the cometary outburst can have different causes, the most probable being the amorphous to crystalline water-ice transformation. Actually, this mechanism was proposed to be the one that produced the brightness enhancement at 14 AU in comet 1P/Halley by (e.g. Espinasse et al. 1991; Klinger 1991), who assumed that a source of CO was activated below the surface by exothermic water-ice transformation from its amorphous phase to the cubic configuration. In addition, it has been proposed as the responsible driver in the 17P/Holmes intense outburst by Hillman & Prialnik (2012), in the quasi-periodic mini-outbursts suffered by 9P/Temple 1 (González et al. 2008), and the multi-outbursts suffered by 29P/S-W (González 2012).

Fig. 1.7 shows the time evolution of the dust tail after an outburst event suffered by comet 217P/Linear (Sarugaku et al. 2010). In that case, the authors established a brightness increase of 1.7-2.3 mag, where the dust shell expanded at a velocity of 120-140 m s^{-1} and the total dust ejected

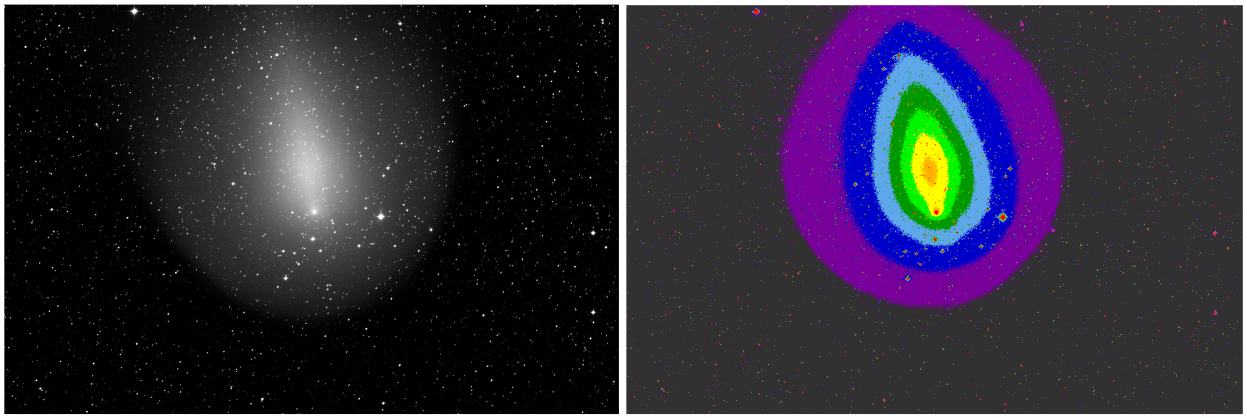

Figure 1.8: 17P/Holmes on December 8, 2007, taken at La Sagra Observatory (Spain), five weeks after the outburst event. The right panel corresponds to the original image and the left one is in false color to identify easily the different intensity levels in the dust shell. The dust shell had dimensions larger than 3.8×10^6 km, more than twice the Sun's diameter. North is up and east to the right.

was in the range of 10^6-10^9 kg. One of the most spectacular outbursts recorded is the one suffered by 17P/Holmes on October 2007, when the comet increased it brightness by 13-14 magnitudes, and the cloud of gas and dust released from the nucleus became larger than the Sun, being the largest object in the solar system for a number of days (see Fig.1.8). The dust ejected during that outburst has been estimated in the range of 10^{10}-10^{12} kg by several authors (see e.g. Moreno et al. 2008; Li et al. 2011; Boissier et al. 2012).

One interesting case of outbursts, is the Centaur 29P/S-W. Trigo-Rodríguez et al. (2010) monitored its nuclear activity from 2008 to 2010 and found that this object suffers periodically 7.4 outbursts per year. Another case of "multi-outbursts" is the comet 9P/Temple 1, the target of the Deep Impact Mission. During its extended observation period carried out by Farnham et al. (2007) and Belton et al. (2008), 10 mini-outbursts were detected, with brightness enhancement between 0.2-0.6 magnitudes, and a later study developed by Filonenko & Churyumov (2009) concluded that this comet suffered at least 6 outbursts of the order of ∼1 magnitude during its last 4 orbits. Belton et al. (2013) studied the geological features in the surface of 9P, as the pits, which are quasi-circular depressions, and concluded that they can have different origins, but the vast majority of them are probably due to outburst activity. The authors also related outbursts to the structures found in the surface of comet 81P/Wild 2 during the Stardust mission.

1.6 Rosetta mission

The international Rosetta mission is a robotic spacecraft designed by the European Space Agency (ESA), whose target is comet 67P/Churyumov-Gerasimenko (hereafter 67P/C-G). Rosetta was launched in March 2004, and will perform a rendezvous with the comet and follow it from ∼4 AU pre-perihelion (May-July 2014) to ∼2 AU post-perihelion (December 2015). In January 2014,

the spacecraft woke up after 31 months of deep-space hibernation and, at the time of writing, is approaching the comet. The expected arrival is in July-August 2014. It will be the first time that such a long-term evolution of the physical, chemical, and dynamical parameters of comet dust will be studied *in situ*. The spacecraft consists of two different modules: a space probe orbiter, which has 11 scientific instruments, and a robotic lander, called *Philae*, with 9 more instruments. The orbiter will build a map and a characterization of the nucleus, in order to locate the best place for *Philae* landing. Out of the 11 instruments of the orbiter, there are two instruments in which the Instituto de Astrofísica de Andalucía is involved in terms of both technical and scientific participation: OSIRIS (Optical, Spectroscopic and Infrared Remote Imaging System), and GIADA (Grain Impact Analyser and Dust Accumulator).

OSIRIS has two CCD cameras of 2048×2048 pixels with a resolution of 20μrad px^{-1} and 100μrad px^{-1}, which means a resolution of 2-10 cm at 1 km of distance. This resolution is optimized to study the nucleus surface with high resolution and to view large fractions of the inner coma to investigate the gas and dust emission from the surface (Thomas et al. 1998). Keller et al. (2007) gave an overview of the scientific objectives of this instrument. Here, we just summarize the most relevant ones in connection with this work.

In reference to the cometary nucleus:

- *Position and size of the nucleus*. For planning purposes, the first aim is to localize the cometary nucleus and estimate its size and shape as quickly as possible. This task will be performed near the end of the approaching phase, at 10^3 to 10^4 km from the target.

- *Rotational state*. Another important goal is to determinate the rotational state, the total angular momentum vector $\vec{L}$, the changing total spin vector, and the processional behavior. With this information, the range of possible inhomogeneities of the nucleus will be derived, as well as the influence of the non-gravitational forces due to the onset of jet activity, estimating the torque caused by the outgassing.

- *Shape, volume and density*. A highly irregular nucleus on all scales as a consequence of cratering, outgassing, and non-uniform sublimation it is expected (Keller et al. 1988). Once the model shape is available, it can be used to determine moments of inertia and surface gravity, as well as to build surface maps.

- *Nucleus formation and surface topography*. OSIRIS will perform a detailed investigation of the entire surface of 67P/C-G on the smallest scale, to identify the hierarchy of cometary building blocks. It is supposed that in these scales, the cometary nucleus may be a heterogeneous mixture of interplanetary and interstellar dust and ices, where the structure and composition will show the chemistry and the physical conditions of the protoplanetary disc. In addition, the surface topography will determine the heat flow in the uppermost layers (Gutiérrez et al. 2000).

- *Color, mineralogy, and inhomogeneity*. The inhomogeneities of mineral composition and color, will provide information about the size of the building blocks which form the comet. The study of mineralogy will be performed through the acquisition of images covering the

entire wavelength range from 250 to 1000 nm. Thus, specific absorption bands associated with possible mineral constituents will be searched for. In addition, the water of hydration feature at 700 nm will be studied.

- *Active and inactive regions*. The processes of how cometary activity starts, evolves and ceases, leaving an inert comet, will be studied. This will give information on how affects to those regions the presence of inactive spots spread on them. The correlation between near-nucleus jets and active spots with the topography will also be studied.

- *Physics of the sublimation process*. The outgassing due to the sublimation process depends on the physical structure of the surface and the distribution of volatile and refractory material in the nucleus. The relationship between the dust particles and the ices, where they can be intimately mixed or separated in different regions, will be analyzed.

- *Outbursts*. This will shed light on their influence on the topography and the spectral features of the comet surface.

- *Mass loss rate*. Some active regions will be monitored to determine the mass loss rate during the perihelion passage, trying to establish the contribution of the large particles.

- *Characterization of the landing site*. The nucleus surface will be mapped at ~2 cm px^{-1}, revealing inhomogeneities of the surface at scale lengths comparable to *Philae* size. In principle, heterogeneous sites will be scientifically more interesting. To this end, OSIRIS needs to be able to characterize the landing place and identify the terrain type.

In reference to the near-nucleus dust:

- *Detection of emission at rendezvous*. Determination of the activity at large distances to plan the approach manoeuvre.

- *Temporal evolution*. Previous *in situ* mission observations, such as Giotto flyby, reveal that the dust production rate is remarkably stable on the order of hours. However, from ground based observations, large and rapid changes in the dust production are inferred. Thus, one of the aims will be to monitor the variation in the production rate as a function of the heliocentric distance, and compare it to the rotational state of the nucleus, with special emphasis on the switch-on after sunrise, and switch-off after sunset.

  The high porosity of the surface and the resulting low thermal conductivity suggest that the activity should decrease rapidly and stop when the energy source is removed.

- *Night side activity and thermal inertia*. The low thermal conductivity owing to the high porosity of the surface implys that the activity should decrease rapidly and stop when the source of energy is removed. To confirm this hypothesis, the dust emission from an active region while crossing the evening terminator, will be monitored.

- *Short-term variability*. The short-term variation of the dust emission (order of minutes) has not yet been observed, but due to the nature of the active regions, this might happen. These variations would provide strong constraints on the hydrodynamics of the flow and improve the understanding of the gas-to-dust interaction near the active regions.

- *Large particles in bound orbits*. From EPOXI mission and radar observations of 103P/Hartley 2 (see e.g. A'Hearn et al. 2011; Harmon et al. 2011), it is known that large clouds of centimeter-size objects can be in orbit around cometary nuclei. This has also been found from theoretical studies (Fulle, 1997; Molina et al. Earth, Moon, and Planets, 102, 521, 2008). Using OSIRIS cameras near the nucleus, it will be possible to determine the density of objects with a radius of $a > 5$ mm. This study will be crucial in the determination of the gas-to-dust ratio.

- *Optical properties of the dust*. This can be retrieved from observations of light scattered by dust at many phase angles (0°-135°) over a wide wavelength range, and will give information on the single scattering albedo, the phase function and the characteristic particle size.

- *Eclipses*. The best information on size distribution and nature of the dust particles is provided by the forward scattering peak of the phase function, and this can be determined by performing eclipse measurements.

The GIADA instrument has been designed to monitor and characterize the comet dust. It consists of three different subsystems: (1) The Grain Detection System (GDS), which is an optical device to measure the optical cross section of individual dust grains; (2) The Impact Sensor (IS), which is an aluminum plate with 5 piezoelectric sensors to detect the momentum of the particles; and (3) The Micro Balance System (MBS), constituted by 5 QCM (Quartz Micro Balances), to measure the cumulative dust deposition with time. The characteristics of the instrument and the scientific objectives are can be found in detail in Colangeli et al. (2007). Here, we just summarize the scientific goals:

- *Dust flux of direct and reflected grains*. Two grain populations can be identified: "direct grains", which come from the nucleus direction, and "reflected grains", which experience the action of the Solar radiation pressure and come from the Sun direction. The dynamical evolution of these two populations is totally different. The instrument will monitor grain fluxes coming from different directions, allowing the determination of the contributions to the coma of each type of grain population. This study is fundamental in determining the *in situ* dust size distribution, which is necessary to establish the dust mass loss rate.

- *Dust velocity distribution*. By pointing the instrument towards the nucleus direction and measuring the "direct grains" , it will be possible to deduce the grain mass, the dependence of the dust ejection velocity on size and mass, the relationship between the most probable velocity and the particle mass, the velocity distribution according to the grain mass, and the velocity dispersion as a function of dust mass.

- *Dust evolution in the coma*. The grain size distribution can evolve with space and time due to several processes which affect the properties of the particles, e.g. fragmentation Crifo (1995). These changes in the size distribution at different locations in the coma will be useful to ascertain the efficiency of the mechanisms in the coma in modifying dust properties.

- *Dust changes Vs. nucleus evolution and emission anisotropy*. The dust environment of the nucleus will evolve with heliocentric distance. This evolution will be characterized by the continuous monitoring of GIADA of the dust flux and the dynamic properties of the ejected grains.

- *Determination of the dust-to-gas ratio*. This key parameter will be measured by GIADA in combination with other experiments, such as ROSINA gas mass spectrometer.

The *Philae* lander is due to be detached from the comet in November 2014, when it will approach the comet surface at a relative velocity of $\sim$1 m s^{-1}, and will use harpoons to anchor itself to the surface, preventing the lander from bouncing off. A full description of the scientific objectives and the 10 scientific instruments on board *Philae*, can be found in Bibring et al. (2007), and references therein.

Despite the expected inactivity of the comet at such distances from the Sun, a sequence of OSIRIS images from March 24 to May 4, 2014, reveals that the comet is already active at distances >4 AU, displaying a coma of more than 1300 km in diameter.

In addition to its main objective, comet 67P, Rosetta spacecraft has already performed two fly-by submissions. The targets of these submissions were asteroids (2867) Steins (Keller et al. 2010), in September 2008, and (21) Lutetia, in July 2010 (see e.g. Stern et al. 2011; de León et al. 2011).

Figure 1.9: Rosetta and Philae at the comet. Artist's impression of the Rosetta orbiter and the *Philae* lander to 67P/C-G. The image is not to scale; Rosetta spacecraft measures $\sim$ 32 m, while the comet nucleus is estimated to be about 4 km wide. The image has been extracted from the Rosetta-ESA web page `http://www.esa.int/Our_Activities/Space_Science/Rosetta`. Under the copyright of: ESA-C. Carreau/ATG medialа.

Chapter 2

Motivation and objectives of this thesis

2.1 Motivation

In chapter 1 we made some introductory remarks on the evolution of cometary science since ancient times. Although many scientific questions have already been solved, many unsolved problems still remain. Basic physical parameters, like size, shape, and albedo, are only known for some specific targets, mainly from *in situ* space-borne instrumentation. Other basic parameter are model-dependent. Thus, the density is estimated in the range $0.5 - 0.6$ g cm^{-3}, but there are no direct measurements. There are approximately 80 chemical species identified in comets, and although our understanding of the chemical process in the coma is reasonably mature, our interpretation of the abundance of those species in the nucleus is still primitive, and still requires a lot of work. In general terms, our understanding of the dynamical evolution of comets is high, but some details are unclear. For example, the injection of comets from the Oort cloud into the inner regions of the solar system, or the relative proportion of comets formed at different distances from the Sun, are explained using models of planetary evolution, which are sensitive to models for the formation and evolution of the solar system as a whole, and these are not well constrained. The influence of comets on the terrestrial planets in the early solar system is also unclear: did the comets bring water and organics to Earth?. The D/H ratio found in comets is not the same as in the Earth's oceans, at least for Oort cloud comets. For 103P, this ratio matches that of the terrestrial oceans, but it is unknown for the all the other JFCs. Other ideas on the water content of Earth are related to the impact of asteroids containing hydrated minerals, or to a new class of objects known as MBCs, where water ice sublimation seems to be the driver of their activity.

The characterization of the dust environment of comets is necessary for the understanding of the physical processes behind it, from the hydrodynamical processes in the near circumnuclear coma (the particle acceleration region) to the short-and long scale effects of solar radiation on their motion, and even in their changes of state (e.g. vaporization processes for grazing comets like the recent C/2012 S1 (ISON). Since 1986, M. Fulle and colleagues (e.g. Fulle 2004) have provided the dust environments of many comets, both SPCs and LPCs, using an inverse Monte Carlo dust tail model. These authors demonstrated the power of such models in determining the best possible solution to the dust environment of comets. Unfortunately, many of those results were derived from

a reduced collection of observations, generally during a tiny orbital arc. We have found that since the problem is multiparametric, and surely allows for more than one solution, the only possible way to reduce the uncertainties is to solve the problem for a larger data set covering the largest possible orbital path, or various orbits, if there are available data. This has been done just once by Fulle et al. (2010), in the characterization of the dust environment of the Rosetta target, 67P/Churyumov-Gerasimenko. On the other hand, although *in situ* measurements have been capable of providing us with a deep understanding of comet dust, it has only been the case for a few targets, and for a specific time frame during the short fly-by's. It is then the aim of this work to provide the dust environments of a large sample of both SPCs and LPCs during a significant portion of their orbits, and to try to link this with their dynamical history in an attempt to relate their activity to their time spent in different reservoirs in the solar system.

2.2 Objectives

Following the arguments posed in the previous section, the objective is to determine the dust environment of a sample of JFCs comets, some LPCs and MBCs, and the dynamical properties of the sample of SPCs. Specifically, the primary objectives are:

- Characterization of a sample of JFCs. To this end, we try to determine the dust properties, i.e., the dust production rate, the ejection velocities, the size distributions and the emission pattern, of all of these parameters as a function of the heliocentric distance.
- Determination of the dynamical evolution of those targets during the last 15 Myr, establishing the solar system regions where those targets have been residing, and studying the relationship between dust environment and dynamical history.
- Analysis of the dust environment of the MBCs activated during the last four years, in an attempt to establish their trigger mechanism (water-ice driven, collision-induced, or rotational break-up).
- Characterization of a sample of LPCs, to compare their activity and dust properties with those of SPCs.

Chapter 3

Monte Carlo dust tail code

Outline of the method and input parameters

During the past several years, our group has developed a Monte Carlo dust tail code, in order to derive the dust environment from dust tail/coma/trail images, generally acquired using ground-based instruments, although in some cases it has also been applied to space-borne instruments (e.g. Hubble Scape Telescope, or Solar and Heliospheric Observatory imagers). The code is designed to generate synthetic cometary images in the spectral regions where light scattered by dust becomes the dominant process, e.g. the red region of the spectrum. In this spectral region, the molecular emissions, although present, become much less intense than the continuum scattered light. However, in some cases, such as when the active LPCs pass near perihelion, the comet tail is dominated by ion emissions in the red region, among other species, by the intense H_2O^+ lines, and the dust tail analysis becomes difficult.

The computer code, developed by Fernando Moreno and written in FORTRAN, will only be briefly outlined here. A more comprehensive description can be found in the literature (see e.g. Moreno et al. 2012, and references therein). The code has two main parts, one is the dynamical part, where the trajectory of a large amount of particles ejected from the comet nucleus at different heliocentric positions is computed, and the other is a light scattering part, where the tail brightness at each image pixel is calculated. The trajectory of the particles can be calculated analytically, starting from the assumption that the only forces acting on those particles are the solar gravity, F_{grav}, and the radiation pressure, F_{rad}, and neglecting the cometary nucleus gravity, which is a reasonable assumption for most comets ($R_N \lesssim 1$ km). Then, since these two forces have same direction but opposite sense, the particle moves in a central gravity field with a reduced gravity given by the so-called β parameter:

$$\beta = \frac{F^d_{rad}}{F^d_{grav}}, \tag{3.1}$$

(see eq. 1.24) and the resulting trajectory will be Keplerian. The type of orbit of the dust particle (elliptical, hyperbolic, or parabolic) is a function of its ejection velocity and the β parameter, which, for spherical particles, is related to the grain radius r and density ρ_d by:

$$\beta = eq.\ 1.24\ = \frac{C_{pr} Q_{pr}}{2\rho_d r} \tag{3.2}$$

where it can be shown that $C_{pr} = 1.19 \times 10^{-3}$ kg m^{-2}, and Q_{pr} is the scattering efficiency for radiation pressure, which is $Q_{pr} \sim 1$ for large absorbing grains (Burns et al. 1979). The exact values of Q_{pr} for any size and refractive index can be obtained from Mie theory.

The terminal velocity of grains, after being accelerated by gas drag from sublimating ices, is usually parametrized by a function which depends on size and time (or heliocentric distance) such as:

$$v_{eject} = v_1(t) \cdot \sqrt{\beta} \tag{3.3}$$

where $v_1(t)$ is the time dependent function, and the size dependence comes from hydrodynamical models of the inner coma (e.g. Fulle 1989). The terminal velocity of the grains is reached at $\sim 20 R_N$. One condition that the ejected particles must verify is that the ejection velocity should always be larger than the escape velocity. The escape velocity is a function of the nucleus mass M_c through the equation:

$$v_{esc} = \sqrt{2GM_c/R} \tag{3.4}$$

where G is the universal gravitational constant, and R is the distance to the nucleus center of mass ($R \sim 20 R_N$). If the nucleus is assumed spherical and its density is known, v_{esc} can be related to the nucleus size.

Once the particle is ejected from the nucleus at a given time before the observation, its position relative to the nucleus at the observation time is computed, and then projected on the photographic or sky plane, using the so-called (N, M) coordinate system, where M is the prolonged Sun-to-comet radius vector and N is perpendicular to M in the opposite half-plane with respect to the nucleus velocity vector (Finson & Probstein 1968a; Fulle 1987). The equations to obtain the orbital elements of the particle and its position on the (N, M) plane can be found, e.g. in Finson & Probstein (1968a), and Fulle (1989).

The second part of the code is the computation of the contribution to the brightness of each emitted particle to the dust tail image. This is a function of the geometric albedo p_v, that can be computed from Mie theory for spheres, as a function of size, incident wavelength, refractive index, and phase (or scattering) angle. *In situ* measurements of comet Halley suggested very dark particles of visible albedo p_v=0.04 at 0° phase angle. For carbonaceous particles of $r > 1$ μm, and refractive index of $1.88 + 0.71i$ (Edoh 1983), we get p_v=0.036, in agreement with Halley's results. However, the assumption of particle sphericity has some serious drawbacks. It is well-known that the behavior of the scattering function for natural, irregularly-shaped, particles is very different from those of spherical particles. In particular, the backscattering enhancement, an increase of the scattered light near 0° phase, that occurs in comets (e.g. Meech & Jewitt 1987), cannot be properly modeled using spherical particles. And yet, simulations of the scattering pattern for non-spherical particles of sizes larger than the wavelength of the incident light, is so costly nowadays in terms of CPU and memory requirements that even with the fastest computer arrays existing in the world this task has not been completed. Therefore, we need to resort to the spherical dust assumption until

some better approach becomes available. Another parameter related to light scattering, and very much dependent on the shape of the particles, is the degree of linear polarization, which is also retrievable from the code, although it is not used at present because the spherical dust assumption makes the resulting synthetic polarimetric images completely unrealistic.

Naturally, the brightness of each pixel defining the synthetic dust tail image to be computed, is a function of the total dust mass production rate, dM/dt, and the size distribution, $n(r)$, both of which are functions of the heliocentric distance. The size distribution is generally assumed as a power-law function of the form:

$$dn(r) \propto r^{\delta} dr \tag{3.5}$$

where $dn(r)$ is the number of particles in the interval $[r,\ r + dr]$, and δ is the index of the distribution. The limiting particle sizes, r_{min}, and r_{max}, which might also depend on heliocentric distance, constitute another set of free parameters of the model.

Finally, the last set of parameters pertain to the definition of the outgassing behavior, i.e., whether an isotropic ejection pattern or an anisotropic ejection pattern holds. In the latter case, we assume a spherically shaped rotating nucleus with a certain rotation period, and two angles determining its rotational state: the obliquity, I, and the argument of the subsolar meridian at perihelion, Φ. As a result, a set of active areas spanning certain ranges in latitude/longitude on the nucleus can be defined. Thus, assuming radial ejection, the velocity vector of the particles can be determined from the expressions given by e.g. Sekanina (1981).

The general procedure

In order to make a simulation of a dust tail, all the parameters described above must be introduced as inputs of the code. Due to the large number of parameters, the solution is generally not unique. Thus, assuming another set of input parameters we could find approximately the same tail brightness. However, the range of possible solutions is considerably reduced when the available observations span a large fraction of the orbital arc of the comets. The general procedure to fit the observations and obtain the dust parameter consists of a trial-and-error procedure, starting from the most simple scenario, where we consider an isotropic ejection outgassing model, having minimum and maximum particle radius of $r_{min} = 1\ \mu$m, $r_{max} = 1$ cm, $\delta = -3.5$, and $v_1(t)$ and dM/dt having a monotonically symmetric evolution with respect to perihelion (see Fig 3.1). From this point, we start to vary the parameters, assuming a certain different dependence with the heliocentric distance, until an acceptable agreement with the observational data is reached. When the observations can not be reproduced by isotropic emission, we set active areas on the surfaces, i.e., an anisotropic emission pattern, and repeat different combinations of the dust parameters until acceptable results are obtained in terms of a χ^2 fit.

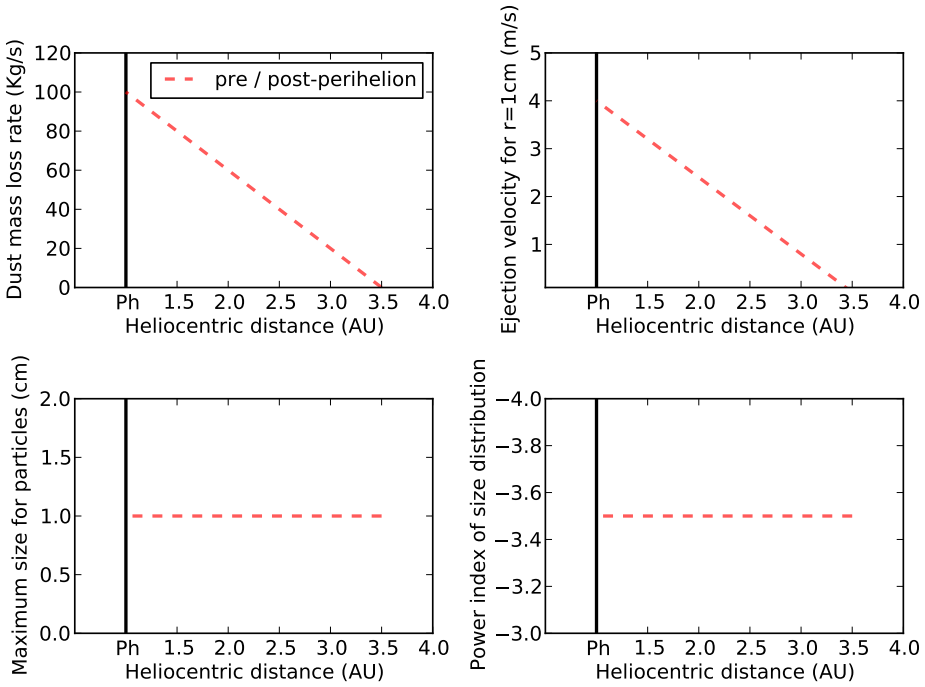

Figure 3.1: Initial dust parameters in the modeling procedure. All parameters are given as a function of the heliocentric distance. From up to down and left to right the panels are: (a) Dust mass loss rate [kg s^{-1}]; (b) Ejection velocities for particles of r=1 cm glassy carbon spheres [m/s]; (c) Maximum size of the particles [cm]; (d) Power index of the size distribution δ. The evolution of the dust parameters are symmetric with respect to perihelion (Ph). The dashed red line corresponds with both pre- and post-perihelion. The vertical solid black line refers to a hypothetical perihelion distance of 1 AU. In the first instance the emission pattern is assumed to be isotropic.

Chapter 4

Results

4.1 Appended papers

Short-Period Comets

- **Paper I.**
  Comet 22P/Kopff: dust environment and grain ejection anisotropy from visible and infrared observations.
  Moreno, F; Pozuelos, F; Aceituno, F; Casanova, V; Sota, A; Castellano, J; Reina, E.
  The Astrophysical Journal, Volume 752, Issue 2, article id. 136, 12 pp. (2012).

- **Paper II.**
  Dust environment and dynamical history of a sample of short-period comets.
  Pozuelos, F. J.; Moreno, F.; Aceituno, F.; Casanova, V.; Sota, A.; López-Moreno, J. J.; Castellano, J.; Reina, E.; Diepvens, A.; Betoret, A.; Häusler, B.; González, C.; Rodríguez, D.; Bryssinck, E.; Cortés, E.; García, F.; García, F.; Limón, F.; Grau, F.; Fratev, F.; Baldrís, F.; Rodriguez, F. A.; Montalbán, F.; Soldán, F.; Muler, G.; Almendros, I.; Temprano, J.; Bel, J.; Sánchez, J.; Lopesino, J.; Báez, J.; Hernández, J. F.; Martín, J. L.; Ruiz, J. M.; Vidal, J. R.; Gaitán, J.; Salto, J. L.; Aymamí, J. M.; Bosch, J. M.; Henríquez, J. A.; Martín, J. J.; Lacruz, J.; Tremosa, L.; Lahuerta, L.; Reszelsky, M.; Rodríguez, M.; Camarasa, M.; Campas, M.; Canales, O.; Dekelver, P. J.; Moreno, Q.; Benavides, R.; Naves, R.; Dymoc, R.; García, R.; Lahuerta, S.; Climent, T. .
  Astronomy and Astrophysics, Volume 568, article id. A3, 13 pp. (2014).

- **Paper III.**
  Dust environment and dynamical history of a sample of short-period comets II: 81P/Wild 2 and 103P/Hartley 2.
  Pozuelos, F. J.; Moreno, F.; Aceituno, F.; Casanova, V.; Sota, A.; López-Moreno, J. J.; Castellano, J.; Reina, E.; Climent, A.; Fernández, A.; San Segundo, A.; Häusler, B.; González, C.; Rodriguez, D.; Bryssinck, E.; Cortés, E.; Rodriguez, F.A.; Baldris, F.; García, F.; Gómez, F.; Limón, F.; Tifner, F.; Muler, G.; Almendros, I.; De los Reyes, J.A.; Henríquez, J.A.; Moreno, J.A.; Báez, J.; Bel, J.; Camarasa, J.; Curto, J.; Hernández, J.F.; González J.J.; Martín, J.J.; Salto, J.L.; Lopesino, J.; Bosch, J.M.; Ruiz, J.M.; Vidal, J.R.; Ruiz, J.; Sánchez, J.; Temprano, J.; Aymamí, J.M.; Lahuerta, L.; Montoro, L. Campas, M.; García, M.A.; Canales, O.; Benavides, R.; Dymock, R.; García, R.; Ligustri, R.; Naves, R.; Lahuerta, S.; Pastor, S.
  Astronomy and Astrophysics, Volume 571, article id. A64, 12 pp. (2014).

The Astrophysical Journal, 752:136 (12pp), 2012 June 20 doi:10.1088/0004-637X/752/2/136

COMET 22P/KOPFF: DUST ENVIRONMENT AND GRAIN EJECTION ANISOTROPY FROM VISIBLE AND INFRARED OBSERVATIONS

Fernando Moreno[1], Francisco Pozuelos[1], Francisco Aceituno[1], Víctor Casanova[1], Alfredo Sota[1], Julio Castellano[2], and Esteban Reina[2]
[1] Instituto de Astrofísica de Andalucía, CSIC, Glorieta de la Astronomía s/n, 18008 Granada, Spain; fernando@iaa.es
[2] Amateur Association Cometas-Obs, Spain
Received 2012 March 13; accepted 2012 April 17; published 2012 June 5

ABSTRACT

We present optical observations and Monte Carlo models of the dust coma, tail, and trail structures of the comet 22P/Kopff during the 2002 and 2009 apparitions. Dust loss rates, ejection velocities, and power-law size distribution functions are derived as functions of the heliocentric distance using pre- and post-perihelion imaging observations during both apparitions. The 2009 post-perihelion images can be accurately fitted by an isotropic ejection model. On the other hand, strong dust ejection anisotropies are required to fit the near-coma regions at large heliocentric distances (both inbound at $r_h = 2.5$ AU and outbound at $r_h = 2.6$ AU) for the 2002 apparition. These asymmetries are compatible with a scenario where dust ejection is mostly seasonally driven, coming mainly from regions near subsolar latitudes at far heliocentric distances inbound and outbound. At intermediate to near-perihelion heliocentric distances, the outgassing would affect much more extended latitude regions, the emission becoming almost isotropic near perihelion. We derived a maximum dust production rate of 260 kg s^{-1} at perihelion, and an averaged production rate over one orbit of 40 kg s^{-1}. An enhanced emission rate, also accompanied by a large ejection velocity, is predicted at $r_h > 2.5$ pre-perihelion. The model has also been extended to the thermal infrared in order to be applied to available trail observations of this comet taken with *IRAS* and *Infrared Space Observatory* spacecrafts. The modeled trail intensities are in good agreement with those observations, which is remarkable taking into account that those data are sensitive to dust ejection patterns corresponding to several orbits before the 2002 and 2009 apparitions.

Key words: comets: general – comets: individual (22P/Kopff) – methods: numerical

Online-only material: color figures

1. INTRODUCTION

Comet 22P/Kopff is a Jupiter-family comet with a current orbital period of 6.43 years and perihelion distance of $q = 1.577$ AU. In 1954 March, it approached Jupiter at a distance of only 0.17 AU, which induced a shortening in perihelion distance and orbital period. Yeomans (1974) found significant non-gravitational effects for this object, with secular changes of quasi-regular nature in the parameter A_2. These changes have been attributed to nucleus precession (Yeomans 1974; Sekanina 1984; Rickman et al. 1987). Nucleus size determinations converge to a value near $R_N = 1.8$ km (Lamy et al. 2002; Tancredi et al. 2000; Lowry & Fitzsimmons 2001; Groussin et al. 2009), while the geometric albedo is estimated at $p_v = 0.042 \pm 0.006$ (Lamy et al. 2002).

Estimates of the dust production rate for comet 22P are based on a limited amount of data. Lamy et al. (2002) reported 130 kg s^{-1} near perihelion at $r_h = 1.59$ AU, an estimation based on the value of the measured Afρ parameter (A'Hearn et al. 1984). Ishiguro et al. (2007) gave (710 ± 70) $(r_h/\mathrm{AU})^{-4}$ kg s^{-1} based on optical trail images obtained during the 2002 apparition, roughly in accordance with the Lamy et al. (2002) value at $r_h = 1.59$ AU and an averaged production rate over one orbital period of 17 ± 3 kg s^{-1}. However, Sykes & Walker (1992) using trail images from *IRAS* satellite data reported $dM/dt = 3.16 \times 10^{13}$ g century^{-1} or 10 kg s^{-1} averaged over one revolution.

In order to report an accurate characterization of the comet dust environment, an extended set of observations covering a large fraction of the comet's orbit is needed. In this paper, we combine post-perihelion image observations of 22P/Kopff obtained during the last 2009 apparition with pre- and post-perihelion archived images from the previous revolution around the Sun, the 2002 apparition. In addition, CCD light curves and Afρ data from amateur observers (the astronomical association *Cometas-Obs*), also corresponding to the 2002 and 2009 apparition, have been taken into account. We used our Monte Carlo dust tail modeling procedure in an attempt to fit the complete image set, which allows us to derive the dust parameters: size distribution, ejection velocities, mass loss rate, and ejection morphology.

Once a best-fit model was found, we also considered the available trail data in the infrared, as reported by Sykes & Walker (1992) and Davies et al. (1997), from observations by *IRAS* and *Infrared Space Observatory* (*ISO*) spacecrafts. To that end, we developed a version of our Monte Carlo code to retrieve both optical and infrared fluxes.

2. OBSERVATIONS

We acquired images of the comet through a Johnson's R bandpass using a 1024×1024 CCD camera at the Sierra Nevada Observatory (OSN) in Granada, Spain, at several epochs after the 2009 perihelion (2009 May 25.218). The pixel size on the sky was $0\farcs46$ and the field of view $7\farcm8 \times 7\farcm8$. Table 1 shows the log of the observations. The individual images at each night were bias subtracted and flat-fielded. At each night, the comet was repeatedly imaged and we combined the individual frames using a median stacking method. Whenever possible, calibration stars were also imaged. For all the other nights, the calibration was

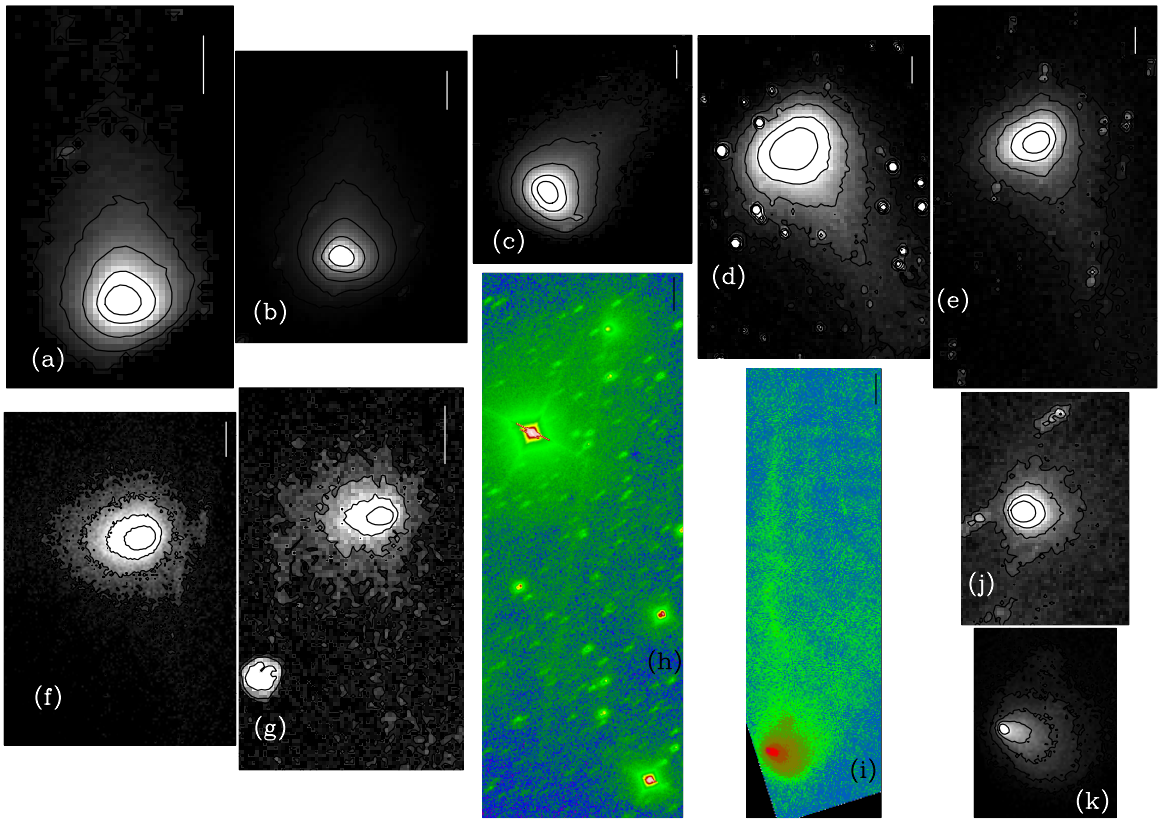

Figure 1. Observations of comet 22P/Kopff through red filter bandpasses. Images (a) to (g) correspond to the 2009 apparition and were obtained using a CCD camera at the 1.52 m telescope of the Observatorio de Sierra Nevada in Granada, Spain. The observation date of each image is as follows: (a) 2009 July 31; (b) 2009 August 15; (c) 2009 August 28; (d) 2009 September 21; (e) 2009 October 12; (f) 2009 November 09; (g) 2009 November 24. Panel (h) corresponds to Kiso observatory, acquired on 2002-05-12, and panel (i) corresponds to the CFHT observation on 2003-07-31 (Ishiguro et al. 2007). Panels (j) and (k) are zoomed regions of images (h) and (i) near the coma regions. In all panels, vertical bars correspond to 20,000 km on the sky, except for panel (h), where the bar represents 80,000 km. See Table 1 for the associated physical parameters of each image.

(A color version of this figure is available in the online journal.)

Table 1
Log of the Observations

Date (UT)	Days From Perihelion	r_h (AU)	Δ (AU)	Resolution (km pixel^{-1})	Phase Angle (°)	Afρ ($\rho = 10^4$ km) (cm)
2009 Jul 27 03:40	67.0	1.712	0.775	2068.5	19.6	189
2009 Aug 15 01:29	81.9	1.773	0.784	2098.9	10.7	222
2009 Aug 28 03:40	94.9	1.832	0.826	2204.6	3.9	320
2009 Sep 21 23:17	119.8	1.959	1.002	2669.0	12.4	241
2009 Oct 12 20:10	140.6	2.075	1.242	3314.9	19.7	114
2009 Nov 9 19:06	168.6	2.237	1.662	1109.0	24.1	74
2009 Nov 24 20:05	183.6	2.327	1.920	1281.1	24.6	59
2002 May 12 13:30	−213.5	2.508	1.866	2029.6	20.8	74
2003 Jul 31 14:17	231.5	2.615	2.508	673.0	22.7	78

performed using field stars with the USNO-B1.0 star catalog (Monet et al. 2003), which provides a 0.3 mag accuracy. The resulting images at each night were calibrated to mag arcsec^{-2} and then converted to solar disk intensity units. In order to compare with the modeled images, and to improve the signal-to-noise ratio, we needed to rebin some of the images. Their final resolution at each date is indicated in Table 1.

For our modeling purposes, we also considered images from the previous comet orbit, i.e., images from the 2002 apparition. Specifically, we considered coma/trail images obtained at large heliocentric distances by Masateru Ishiguro at the Kiso 1.05 m Schmidt telescope in Nagano, Japan, and the Canada–France–Hawaii 3.6 m telescope (CFHT), previously described by Ishiguro et al. (2007). M. Ishiguro kindly made available to us the Kiso data, while the CFHT data were downloaded from the CFHT archive server. In both cases, we followed a similar reduction procedure as that described for the OSN data. We used field stars as calibration sources. Table 1 also lists the relevant information corresponding to those data sets.

Figure 1 displays all the final product images described above. As stated, some of them were rebinned in order to make them tractable with the Monte Carlo models and to improve the signal-to-noise ratio. All the images have been rotated to the (N, M) photographic plane (Finson & Probstein 1968), so that the Sun is toward the bottom. No contours have been displayed for the 2002/2003 images (Ishiguro et al. 2007), so that the

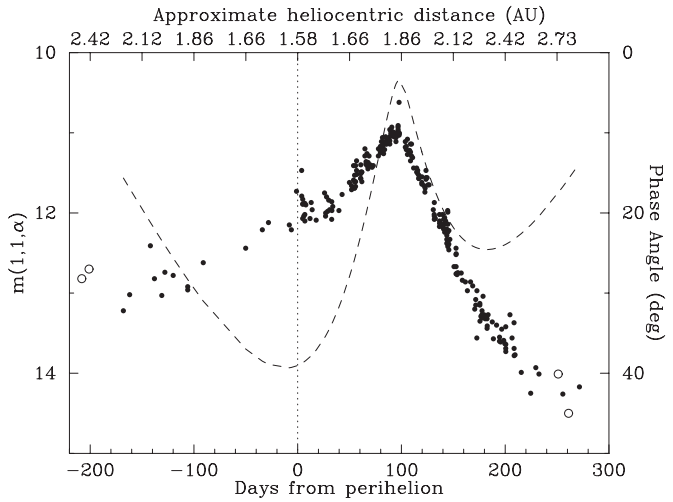

Figure 2. Cometary magnitude $m(1, 1, \alpha)$ as a function of time and heliocentric distance by *Cometas-Obs*. Filled circles correspond to the 2009 apparition and open circles to the 2002 apparition. The dashed line indicates the phase angle as a function of time.

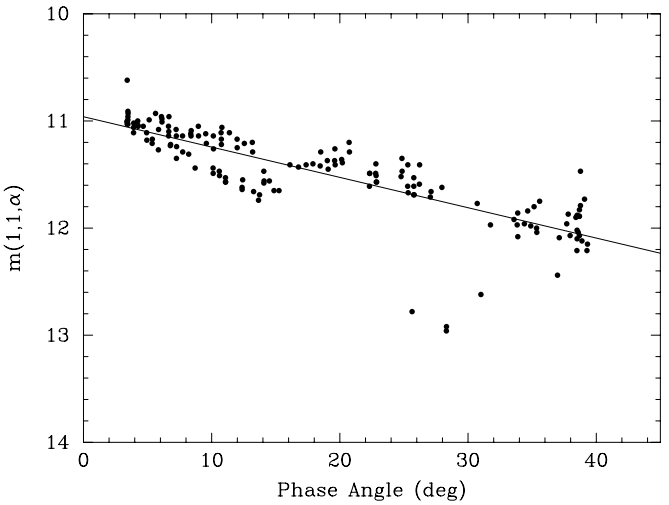

Figure 3. Cometary magnitude $m(1, 1, \alpha)$ as a function of phase angle for data points of $r_h < 2$ AU, for the 2009 apparition. Filled circles are data from *Cometas-Obs*. The solid line represents a linear fit to the data, whose slope corresponds to the linear phase coefficient, 0.028 ± 0.002 mag deg^{-1}.

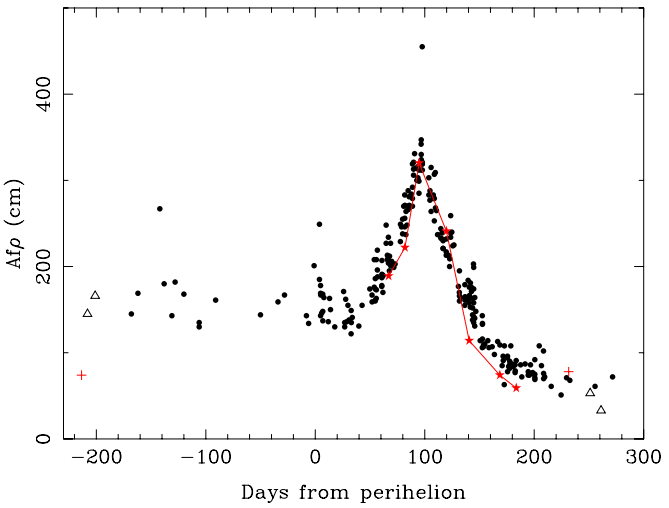

Figure 4. Afρ vs. days from perihelion. The filled circles correspond to the 2009 apparition data from *Cometas-Obs*, while the open triangles correspond to the 2002 apparition from the same group. The crosses (in red) correspond to the 2002 apparition data from Kiso (pre-perihelion) and CFHT (pos-perihelion) data. The star symbols joined by a solid line (in red) correspond to the 2009 apparition OSN data.

(A color version of this figure is available in the online journal.)

neck-line/trail structures are visible. The neck line, first described by Kimura & Liu (1977), corresponds to large particles ejected at a true anomaly of 180° before the observation date and appears to ground-based observers as a bright linear feature when the cometocentric latitude of the Earth is small (the Earth is near the comet orbital plane). A trail is formed by large particles that are ejected at low velocities from the nucleus so that they remain along the cometary orbit for many orbital periods. Neck-line structures are formed in the current orbital revolution, while trails correspond to particles ejected during the previous several orbits. In Figure 1, neck-line structures are clearly seen in, e.g., panels (d) and (e), while the linear feature seen in panel (h) is clearly a trail, as this image was taken at large heliocentric distance ($r_h = 2.5$ AU) pre-perihelion (Ishiguro et al. 2007).

In addition to the image data described above, we have also benefited from amateur observations carried out by the astronomical association *Cometas-Obs* (see http://www.astrosurf.com/Cometas-Obs), from both the 2002 and 2009 apparitions, providing a CCD light curve and Afρ measurements as a function of heliocentric distance. Both the magnitude and Afρ measurements are referred to an aperture of radius 10^4 km projected on the sky at each observation date. This choice is made to permit a direct comparison with the OSN Afρ data at the same ρ value. The data reduction was accomplished by using field stars and the CMC-14/USNO A2.0 star catalogs. Figure 2 presents the CCD light curve where the magnitudes m have been reduced to heliocentric and geocentric distances of 1 AU by the equation:

$$m(1, 1, \alpha) = m - 2.5 \log\left(\Delta r_h^2\right), \quad (1)$$

where Δ and r_h are the geocentric and heliocentric distances of the comet in AU, respectively. Most of the data points correspond to the 2009 apparition, where the light curve shows a conspicuous maximum approximately 100 days from perihelion. In Figure 2, the dependence of comet phase angle with time is also displayed. It is interesting to note that the maximum brightness corresponds to the minimum value of phase angle reached ($\alpha \sim 3\overset{\circ}{.}4$). This means that the spike can in principle be attributed to the brightness opposition effect, although, overimposed to that, an enhancement of cometary activity during those dates post-perihelion cannot be ruled out. In order to show the brightness opposition effect, Figure 3 displays $m(1, 1, \alpha)$ versus the phase angle for those points having $r_h < 2$ AU. As can be seen, these data can be well fitted by a linear phase coefficient of 0.028 ± 0.002 mag deg^{-1}. This estimate is in the range of values obtained for other comets (e.g., Meech & Jewitt 1987).

The maximum at 100 days post-perihelion also appears in the Afρ data, as could be expected. Figure 4 shows the Afρ data for a projected distance of $\rho = 10^4$ km together with the Afρ data derived from the 2009 OSN images. The agreement between the *Cometas-Obs* group data and the OSN data for the 2009 apparition is excellent. This emphasizes the importance of amateur astronomy groups in deriving information that is very useful for professional astronomers. Also displayed are the Kiso/CFHT data and those from *Cometas-Obs* from the 2002 apparition.

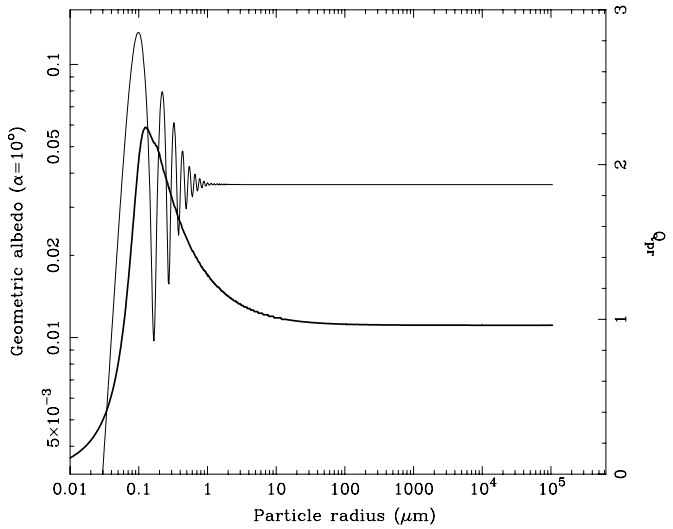

Figure 5. Generalized geometric albedo (at 10° phase angle) vs. particle radius for glassy carbon spheres (thin solid line, left axis). The thick line is the value of the radiation pressure coefficient, $Q_{\rm pr}$, as a function of particle radius (right scale).

3. THE MODEL

In order to model the images, we used a direct Monte Carlo dust tail code, which is based on previous works of cometary dust tail analysis (e.g., Moreno 2009; Moreno et al. 2011), and in the characterization of the dust environment of comet 67P/Churyumov-Gerasimenko before *Rosetta*'s arrival in 2014 (the so-called Granada model; see Fulle et al. 2010). Briefly, the code computes the trajectories of a large number of particles ejected from a cometary nucleus surface, submitted to the solar gravity and radiation pressure fields. The gravity of the comet itself is neglected, which is a good approximation for 22P owing to its small size (see Section 1). The particles are accelerated to their terminal velocities by the gas molecules coming from the sublimating ices. These terminal velocities correspond to the input ejection velocities considered in the model. The particles describe a Keplerian trajectory around the Sun, whose orbital elements are computed from the terminal velocity and the β parameter, which is the ratio of the force exerted by the solar radiation pressure and the solar gravity (Fulle 1989). This parameter can be expressed as $\beta = C_{\rm pr}Q_{\rm pr}/(2\rho_d r)$, where $C_{\rm pr} = 1.19 \times 10^{-3}$ kg m^{-2}, and ρ_d is the particle density, assumed to be $\rho_d = 1000$ kg m^{-3} throughout. We used the Mie theory for spherical particles to compute both the radiation pressure coefficient, $Q_{\rm pr}$, and the geometric albedo, p_v. $Q_{\rm pr}$ is a function of the particle radius, and p_v is a function of the phase angle α and the particle radius. p_v is obtained as $S_{11}(\alpha)\pi/k^2G$, where S_{11} is the (1,1) element of the scattering matrix, $k = 2\pi/\lambda$ (the wavenumber), and G is the geometrical cross section of the particle, i.e., $G = \pi r^2$. We assumed the particles as glassy carbon spheres of refractive index $m = 1.88 + 0.71i$, which is the value reported by Edoh (1983) for an incident wavelength of $\lambda = 0.6$ μm. Highly absorbing particles have often been invoked to represent cometary material (e.g., Kimura et al. 2003). Figure 5 gives the dependence of $Q_{\rm pr}$ and p_v on particle radius. The values graphed for p_v correspond to a phase angle of $\alpha = 10°$, but the results are identical for phase angles $\alpha < 40°$ for particle radii $r > 1$ μm. The asymptotic value of p_v at $r > 1$ μm becomes $p_v = 0.036$, which is within the error bar of the value of $p_v = 0.042 \pm 0.006$ estimated by Lamy et al. (2002). Regarding $Q_{\rm pr}$, we obtain $Q_{\rm pr} \sim 1$ for particle radii $r \gtrsim 1$ μm. The main difficulty when dealing with absorbing spherical particles is that the brightness opposition effect cannot be modeled, as the phase function keeps constant for phase angles $\alpha < 40°$. In principle, the scattering properties of non-spherical particles can be computed with dedicated light scattering codes such as the Discrete Dipole Approximation or the T-matrix method (e.g., Draine 2000; Mishchenko et al. 2000). However, the amount of CPU time and memory needed to make such calculations for realistic particle sizes becomes prohibitive, so that computations are only available for particle sizes of the order of the wavelength of the incident light or slightly larger (e.g., Kimura et al. 2003; Kolokolova et al. 2004; Moreno et al. 2007; Zubko 2011).

For each observation date, the trajectories of a large number of dust particles are computed, and their positions on the (N, M) plane are calculated. Then, their contribution to the tail brightness is computed. The synthetic tail brightness obtained at each date depends on the ejection velocity law assumed, the particle size distribution, the dust mass loss rate, and the geometric albedo of the particles, apart from the ejection pattern (anisotropy).

As stated in the previous section, the image taken in 2002 May 12 (Ishiguro et al. 2007) shows a trail, which corresponds to dust ejected during many previous apparitions. The encounter of the comet with Jupiter in 1954 March modified its orbital elements (Kępiński 1958, 1963) in such a way that the particles ejected prior to 1954 probably followed very distinct orbits to those ejected since then. In consequence, for the interpretation of trails, we considered that their age is the difference between the observation date and 1954 March. We also assumed that the dust ejection pattern did not change with time: we do not have any information on dust ejection parameters back to 1954, so there is no reason to assume any temporal change.

4. RESULTS AND DISCUSSION

In addition to the assumptions described in the previous section on some of the parameters involved in the model, and owing to their large number, we needed to make more additional hypotheses. Thus, the particle velocity is parameterized as $v(t, \beta) = v_1(t)\beta^{1/2}$, where $v_1(t)$ is a time-dependent function to be determined in the modeling. In principle, we assumed that $v_1(t)$ was a symmetric function of the heliocentric distance. Regarding the dust mass loss rate, we assumed a time-dependent asymmetric function with respect to perihelion based on the light curve described in Section 2. Excluding the brightness opposition effect, for heliocentric distances $r_h > 2$ AU, the light curve is clearly asymmetric, indicating higher production rates pre- than post-perihelion.

The particle size distribution is assumed to be described by a power law with a constant power index, independent of the heliocentric distance. The minimum and maximum values for the particle radii must also be determined. In principle, there are no constraints for the minimum particle size. However, the maximum size ejected is constrained by the escape velocity, $v_{\rm esc} = (2GM_c/R_{cm})^{1/2}$, where G is the universal gravitational constant, M_c is the comet mass, and $R_{\rm cm}$ is the distance to the nucleus center of mass. For comet 22P, the mass has been determined from non-gravitational forces by Sosa & Fernández (2009), who reported $M_c = 5.3 \times 10^{12}$ kg. We assume that for a distance of ~20 nuclear radii, the effect of outgassing has vanished so that for $R_N = 1.8$ km as given above, we get $v_{\rm esc} = 18.8$ cm s^{-1}.

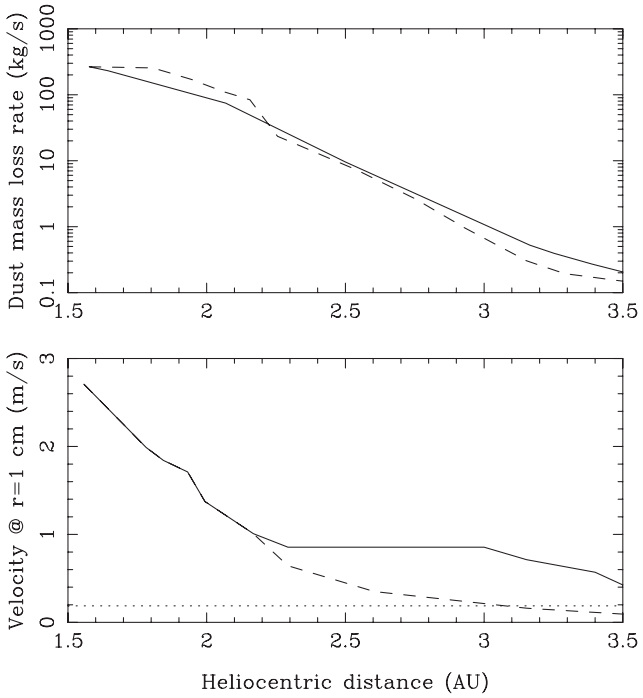

Figure 6. Upper panel: dust mass loss rate as a function of the heliocentric distance. Lower panel: ejection velocity of $r = 1$ cm glassy carbon spheres as a function of heliocentric distance. In both panels, the solid line corresponds to pre-perihelion, and the dashed line to post-perihelion.

4.1. Isotropic Ejection Models

We first assumed the most simple model to fit the observations, i.e., an isotropic ejection model. With the set of assumptions described above, we attempted first to fit all the observations together, i.e., those OSN images corresponding to the 2009 and those of the 2002 apparitions (Ishiguro et al. 2007), assuming the same model inputs. Since it is not practical to show the modeling results for each parameter combination, we will just give a summary of how we proceeded to find the final model parameters. Our first modeling attempts to adopt the maximum particle sizes as constrained by the escape velocity, which implies ejection of particles in excess of $r = 14$ cm near perihelion, resulted in very bright neck-line structures in each image, much brighter than observed. In addition, the trail intensities for the modeled 20020512 image were also too high. In consequence, we had to decrease that upper limit by an order of magnitude to 1.4 cm. With this upper limit, we started to find models which produced a closer approximation to the full data set. Also, we realized that both symmetric dust mass loss rates and ejection velocities did not give acceptable fits. Much better fits were found for asymmetric curves, with a steeper decay of activity post-perihelion than pre-perihelion. This is expected, based on the asymmetry observed in both the magnitude and the Afρ parameter. The best fits are obtained for a size distribution function having a power index of $\alpha = -3.1$ and a minimum particle size of 1 μm, both parameters being independent of the heliocentric distance. Figure 6 gives the dependence of dust mass loss rates and velocities on heliocentric distance. The comparison of the isophote fields for all the images is given in Figure 7.

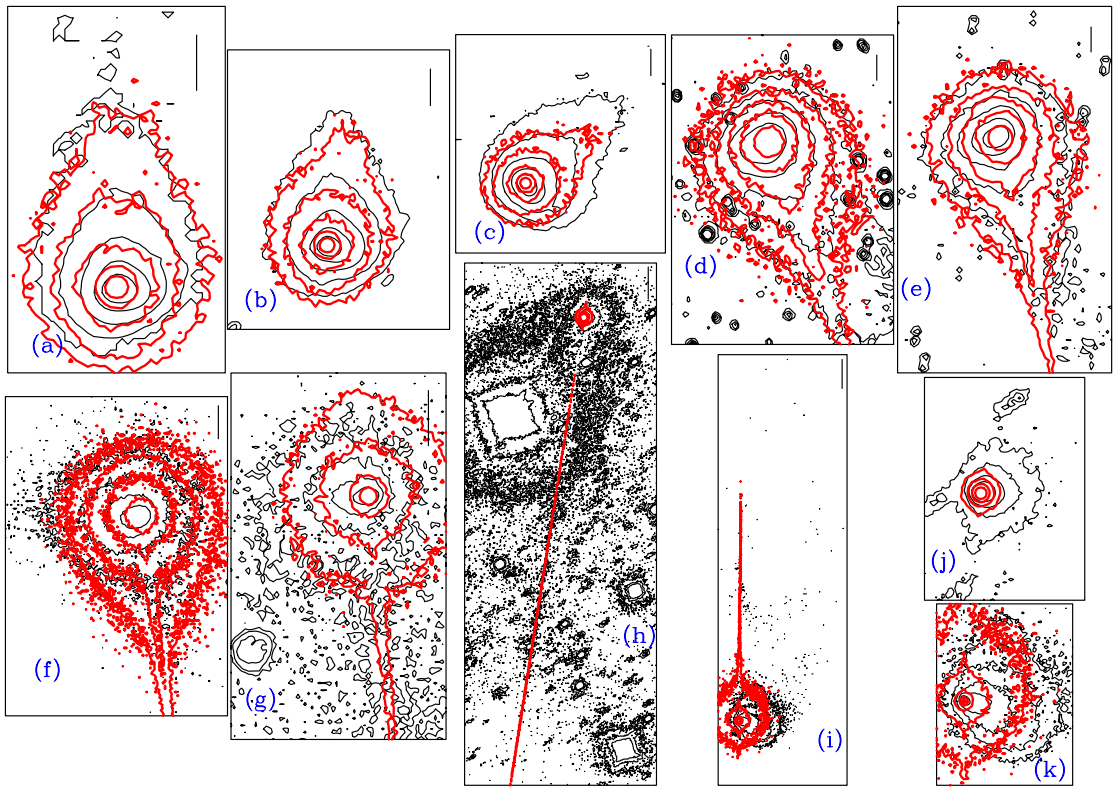

Figure 7. Isotropic ejection model compared to the observations. The observation dates and layout corresponds to that shown in Figure 1. In panels (a)–(c), the innermost isophotes are 3.2×10^{-13} solar disk intensity units; in panels (d) and (e) 8×10^{-14}; in panel (f) 6×10^{-14}; in panels (g) and (h) 1.2×10^{-13}; in panel (i) 1.2×10^{-13}; in panel (j) 4.8×10^{-14}; and in panel (k) 2.4×10^{-13}. Isophotes vary in factors of two between consecutive levels. In all panels, thin (black) contours correspond to the observations, and thick (red) contours correspond to the model. Vertical bars represent 20,000 km in the images, except in (h), where it indicates 80,000 km.

(A color version of this figure is available in the online journal.)

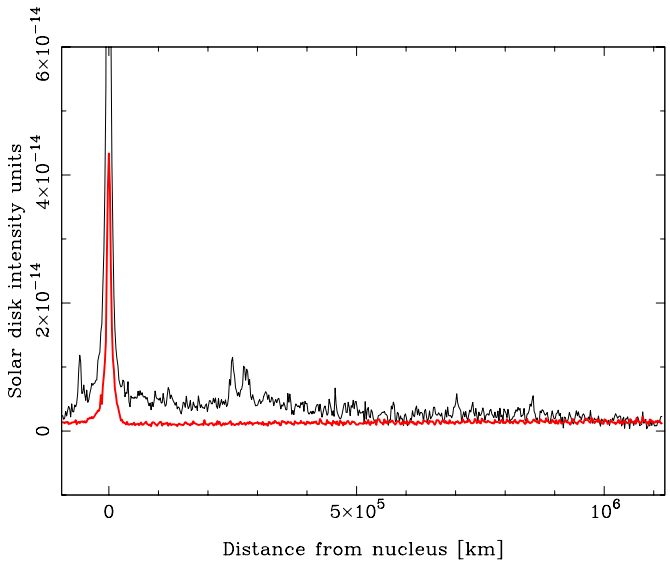

Figure 8. Intensity scans along the trail in Figure 7(h). The thin (black) line corresponds to the observation, while the thick (red) line is the model.

(A color version of this figure is available in the online journal.)

As can be seen, the agreement between the observed and modeled images for the 2009 apparition is quite good (see Figures 7(a)– (g)), except for the 20090828 image (Figure 7(c)) where the phase angle is minimum ($\alpha = 3.^{\circ}9$), and the brightness opposition effect is maximum. As stated above, this effect cannot be modeled by using absorbing spherical particles, as the phase function does not experience any increase toward backscattering, so that the synthetic image remains darker than observed. The maximum dust loss rate corresponds to perihelion, with a value of 260 kg s^{-1}. This is twice the value reported by Lamy et al. (2002), who gave 130 kg s^{-1} near perihelion, although their estimation corresponds to the earlier 1996 apparition.

When the same isotropic model is applied to the images of the previous orbital revolution, several fitting problems were encountered (see Figures 7(h)–(k)). Regarding the 20030731 image, while the overall observed and modeled intensity levels agree, the experimental isophotes depart significantly from the modeled ones, which are very asymmetric, as already noted by Ishiguro et al. (2007). In the case of the 20020512 image, there is a mismatch not only in the overall intensities, but also in the shape of the isophotes, that disagree strongly, as well in the trail intensities, which are much lower than observed (Figure 8). The coma/tail region of the 20020512 synthetic image is far weaker than observed, implying a higher dust mass loss rate prior to the observations. In fact, the Afρ measurements by *Cometas-Obs* group (Figure 4) confirm a high activity of 22P at those heliocentric distances pre-perihelion ($r_h > 2.5$ AU), with Afρ values comparable to those found near-perihelion. In an attempt to fit the intensity levels of the 20020512 image, we increased both the mass loss rate and the particle ejection velocities at distances of $r_h > 2.5$ pre-perihelion. We found that the mass loss rate of Figure 6 should be multiplied by a factor of the order of 10 at least, and the ejection velocity by a factor of 5 at $r_h > 2.5$. The effect of doing these modifications is shown in Figure 9. In this

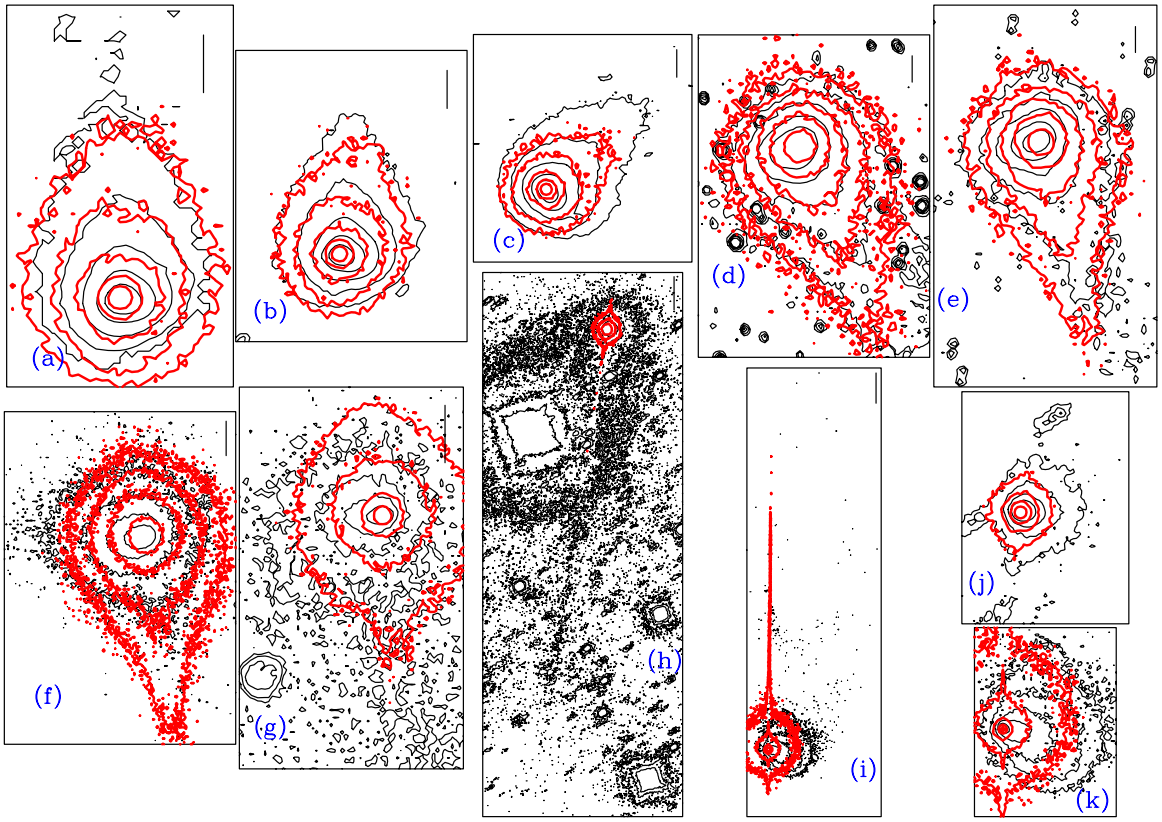

Figure 9. Same as Figure 7, but for the mass loss rate being multiplied by a factor of 15, and the ejection velocity by a factor of 5, for $r_h > 2.5$ AU pre-perihelion, with respect to the values shown in Figure 6. These factors have been imposed in order to obtain a better fit for the coma region in the 2002-05-12 image (compare panels (k) and (j) with Figures 7(k) and (j)). Also, the neck lines appear broader and closer to the observations than in Figure 7 (compare panel (d) to (g) in both graphs), an effect produced by the substantially higher velocities at $r_h > 2.5$ AU.

(A color version of this figure is available in the online journal.)

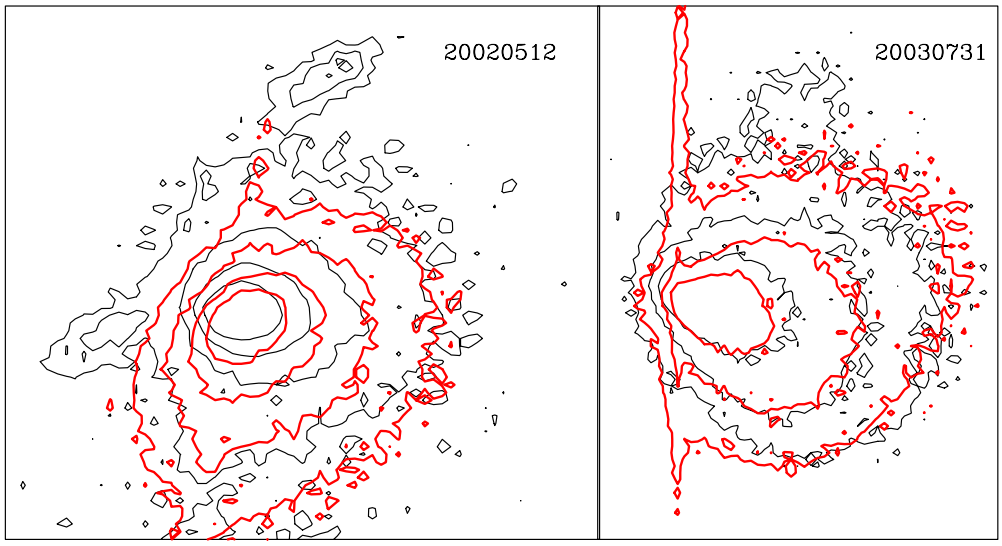

Figure 10. Anisotropic ejection model applied to the 2002-05-12 and 2003-07-31 images (see Table 1 for the observational parameters and Table 2 for the model parameters). As in Figure 9, the mass loss rate and the velocity have been increased at $r_h > 2.5$ pre-perihelion. In this case, a factor of 30 has been applied to the mass loss rate, and the same factor of 5 in velocity.

(A color version of this figure is available in the online journal.)

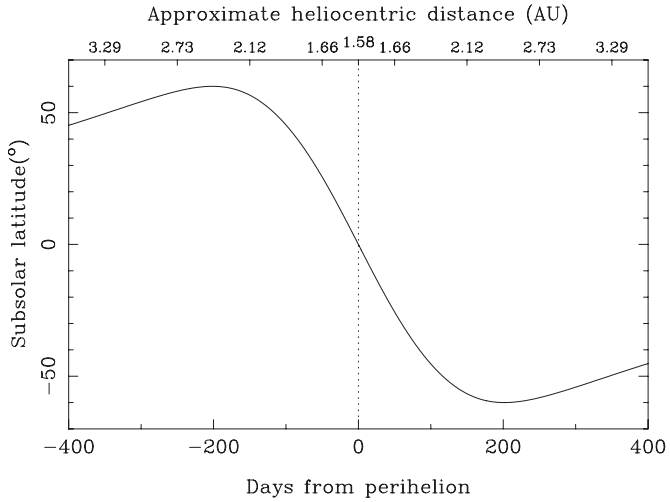

Figure 11. Latitude of the subsolar point of 22P/Kopff nucleus as a function of time to perihelion, and heliocentric distance, for the rotational parameters $\Phi = 180°$, $I = 60°$ (see the text).

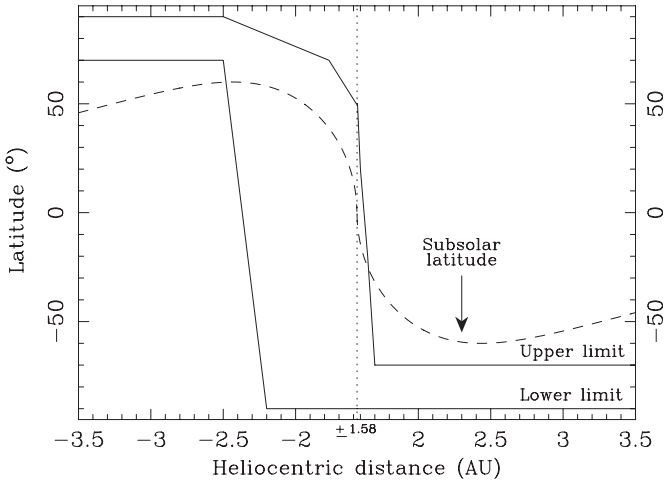

Figure 12. Upper and lower latitude boundaries of the active area in the anisotropic dust ejection model as a function of the heliocentric distance. Also displayed is the latitude of the subsolar point, which shows a similar behavior with time.

figure, the mass loss rates are increased by a factor of 15, and the velocity by a factor of 5, at $r_h > 2.5$ AU. As can be seen, there is now a better match between isophotes for the 20020512 image, although a higher factor would give a still better agreement (see the next subsection). On the other hand, these changes improve the fits on all the 2009 images, as the neck-line structures appear broader and closer to the observations than those with the reduced mass loss rate (compare, e.g., Figures 7 and 9, panels (d) to (g)), which is a consequence of the larger velocities imposed at $r_h > 2.5$ AU pre-perihelion.

We then focused on the asymmetries found in the isophote field in the near-nucleus region in the two images of the 2002 apparition. We will show in the next subsection that the analysis of those images provides clues on the dust ejection anisotropy.

4.2. Anisotropic Ejection Models

As explained in the previous subsection, while the 2009 apparition post-perihelion images can be adequately matched with isotropic ejection models, the 20020512 and 20030731 images from the previous orbit show clear departures from an isotropic dust ejection scenario. In order to fit these images, we then tried anisotropic ejection models. In principle, we experimented with a rotating spherical nucleus with an active area on it, with a rotation period of 12.3 hr (Lowry & Weissman 2003). The spin axis orientation is specified by two angles, the argument of the subsolar meridian at perihelion, Φ, and the obliquity, I (Sekanina 1981). The active area is specified by setting a latitude–longitude box where the particles are assumed to be ejected from. Since the age of the tails is much longer than a rotational period, the choice of a particular longitude range turns out to be irrelevant for the resulting synthetic images.

The approach consisted of considering as inputs the best-fit parameters found for the isotropic ejection models, and then searching for the best-fit I and Φ and latitude box $[\lambda_{min}, \lambda_{max}]$ for each of the two images, 20020512 and 20030731. The minimization procedure was accomplished by using the downhill simplex method of Nelder & Mead (1965) with the FORTRAN implementation by Press et al. (1992). The function to minimize

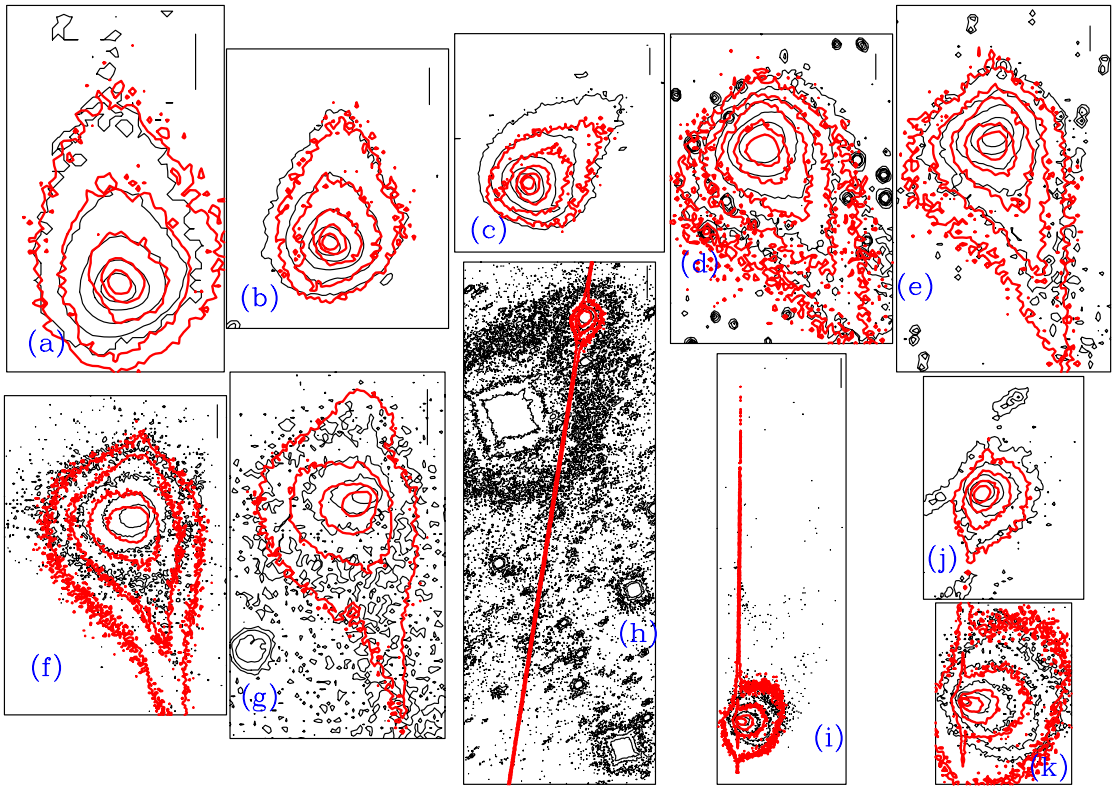

Figure 13. Final version of the anisotropic model applied to all the available observations. For information on contours' levels see Figure 7. Thin (black) contours are the observations, and thick (red) contours, the model. The mass loss rates and ejection velocities are those of Figure 6, but increased in factors of 20 and 5, respectively, at $r_h > 2.5$ AU pre-perihelion. The vertical bars correspond to projected distances of 20,000 km, except for panel (k), where it corresponds to 80,000 km.

(A color version of this figure is available in the online journal.)

was the standard deviation of the synthetic image from the observation. We are aware that this procedure only gives a local minimum: the code was run repeatedly with a varied starting simplex so that a more generic solution could be found. The input mass loss rates and velocities were those assumed in the previous subsection, but with a higher factor for the mass loss rate of 30 at $r_h > 2.5$ AU pre-perihelion, which produces a better fit to the 20020512 image. With this modified input mass, the total dust mass ejected per orbit becomes 8×10^9 kg, with an averaged production rate per orbital revolution of 40 kg s^{-1} or 1.3×10^9 kg yr^{-1}, which represents a modest contribution to the interplanetary dust cloud as compared to the (1.6–6.3) $\times$ 10^{10} kg yr^{-1} of comet 29P/Schwassmann–Wachmann (Moreno 2009). In comparison, Ishiguro et al. (2007) obtained an orbital averaged contribution of only 17 ± 3 kg s^{-1} for 22P/Kopff, although these authors stated that since their data only cover a small portion of the comet orbit, they probably underestimated the production rate near perihelion. On the other hand, as already indicated in the introduction, Sykes & Walker (1992) obtained 10 kg s^{-1}, averaged over an orbital period, from *IRAS* satellite images. The origin of this discrepancy is probably related to the fact that the trail data refer only to the large particle component of the dust ejection.

The best solutions for both the 20020512 and 20030731 images corresponded to Φ between 170° and 210°, while I was between 50° and 70°, with latitude boxes of [−90°, −70°] for the 20020512 image and [70°, 90°] for the 20030731 image. The values for the overall best fits for the two images were $\Phi = 180°$ and $I = 60°$, so that the rotational axis points to either R.A. = 3°, decl. = 25° (prograde), or the opposite direction for retrograde rotation, R.A. = 183°, decl. = −25°, since the sense of rotation is unconstrained. This procedure served to find the location of the active areas. However, the resulting synthetic images had too sharp borders, with a very fast decrease of brightness outward in some directions. In order to smooth out the resulting images, we implemented two procedures. One was to impose some fraction of particles being ejected isotropically. The other was to consider that every point source on the surface in the Monte Carlo procedure was actually an emission cone with a certain width $\Delta\phi$, so that each particle ejected from a given latitude, instead of being ejected normal to the spherical nucleus surface, is ejected with a random azimuthal angle around that direction and a random angle (smaller than or equal to the cone width) with respect to that normal direction. In this way, the sharp borders disappear and the synthetic images become closer to the observations. Two additional parameters then have to be defined, the fraction of particles ejected isotropically, and the cone angle width, which can be, in principle, different for the two images under analysis (20020512 and 20030731). After many simulations, we concluded that for the 20020512 image, the best-fit parameters were $\Delta\phi = 60°$, with no need for an isotropic ejection fraction. In contrast, for the 20030731 image, the best-fit parameters were $\Delta\phi = 20°$, with 30% of particles being ejected isotropically. Figure 10 shows the fits to the near-coma regions of these two images. While we recognize the complexity of these models, with such a large number of parameters, we also remark that they are actually needed in order to reproduce the details seen in the images with a certain degree of accuracy. As can be is seen in Figure 10, these synthetic images reproduce the observations very closely.

The location of the inferred active areas for the 20020512 and 20030731 images differ drastically: while the southernmost

latitude region is active prior to the 20050512 observation, it is the northernmost latitude area which is most active prior ($r_h > 1.7$ AU) to the 20030731 observation. In order to see whether or not there is some relation to solar insolation, Figure 11 shows the location of the subsolar point as a function of the heliocentric distance. As can be seen, the northern high latitudes ($\lambda \sim 50^\circ$) are indeed those exposed to the highest solar radiation at heliocentric distances of $r_h > 2.5$ AU pre-perihelion, and, conversely, the southern high latitudes ($\lambda \sim -50^\circ$) are those exposed to highest radiation after perihelion. Therefore, although the active areas we have inferred are somewhat displaced toward the north pole for the 20020512 simulation, and toward the south pole for the 20030731 simulation, they are close to the subsolar point. Therefore, these 2002/2003 data are consistent with the picture in which the region near the subsolar point is the first to experience significant outgassing inbound, while it is the latest to be active outbound.

The final step was to consider a model that is able to fit all the available observations. We have attempted to fit such an asymmetric ejection model to the whole image set, including both the 2003 and 2009 apparition images. In order to fit the 20020512 and 20030731 images, we have just shown that the active area at heliocentric distances of $r_h > 2.5$ pre-perihelion should be located near the north pole, and near the south pole at heliocentric distances of $r_h > 1.7$ post-perihelion, in such a way that the subsolar point is close to those areas. On the other hand, we have shown previously that all the 2009 post-perihelion images can be fitted by assuming isotropic ejection. Therefore, the logical approach would be to assume that the active area limits converge toward the narrow latitude regions found for the two images 20020512 and 20030731 when the comet is at large heliocentric distance inbound and outbound, respectively. Those borders would define a broader latitude region at intermediate heliocentric distances. Figure 12 shows the upper and lower latitude limits of the active area as a function of the heliocentric distance, in which we have also drawn the location of the subsolar point. As we can see, the location on the active area correlates with the location of the subsolar point. Also, as the derived cone widths were different for the 20020512 and 20030731 images, we also set this parameter as time dependent. Since the best fits were $\Delta\phi = 60^\circ$ at $r_h > 2.5$ AU pre-perihelion, and $\Delta\phi = 20^\circ$ at $r_h \gtrsim 1.7$ post-perihelion, we just considered an interpolated solution in between, as shown in Figure 12 and also in Table 2, which summarizes all the parameters that apply to the final version of the model. In addition, a fraction of 30% of particles were assumed to undergo isotropic ejection for all heliocentric distances. Figure 13 shows the results of the synthetic isophotes compared with the observations. It is clear that the asymmetric model reproduces with great detail most features observed at each epoch for both 2002 and 2009 apparitions.

Finally, the 20020512 synthetic trail intensity is compared with the observation in Figure 14. The agreement is also remarkable. This asymmetric ejection model has then proved to be valid for all the observations covering a large fraction of the comet orbit and two consecutive apparitions.

5. APPLICATION OF THE DUST MODEL TO OBSERVATIONS OF TRAILS IN THE INFRARED

In order to take into account all available observations of dust from comet 22P/Kopff, we also considered the application of the final version of the anisotropic dust model to trail observations in the infrared, such as the *IRAS* data reported by Sykes & Walker (1992) and the *ISO*/*IRAS* data by Davies et al. (1997). To do

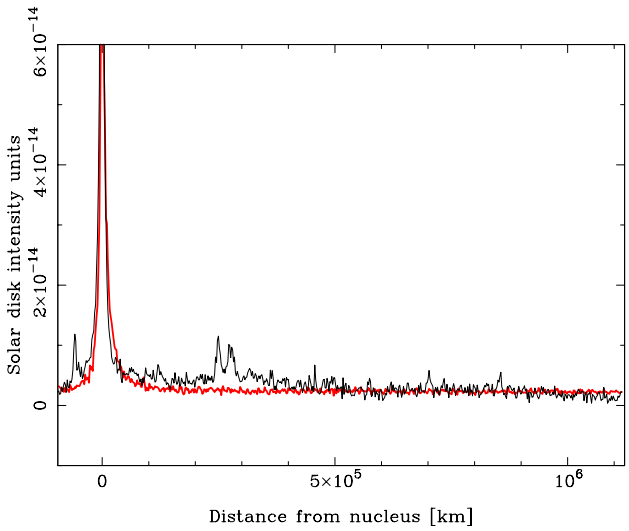

Figure 14. Intensity scans along the trail in Figure 13(h). The thin (black) line corresponds to the observation, while the thick (red) line is the model.
(A color version of this figure is available in the online journal.)

that, we developed a modified version of our Monte Carlo code to retrieve thermal fluxes. The thermal radiation from a single grain is given by

$$F_\lambda = \frac{r^2}{\Delta^2}\epsilon(\lambda, r)\pi B_\lambda[T(r)], \tag{2}$$

where $\epsilon(\lambda, r)$ is the grain emissivity at wavelength λ and $B(\lambda, T)$ is the Planck function for grain temperature T (Hanner et al. 1997). The emissivities are computed by applying Kirchoff's law, so that $\epsilon(\lambda, r) = Q_{\rm abs}(\lambda, r)$, where $Q_{\rm abs}(\lambda, r)$ is the absorption efficiency of the grain. This quantity is computed by the Mie theory for glassy carbon spheres, the same composition assumed to compute the scattering parameters at red wavelengths, using the variation of refractive index with wavelength reported by Edoh (1983).

The temperature from a single grain at a given heliocentric distance is computed from the balance between the energy absorbed in the visual and the energy emitted in the infrared as (Hanner et al. 1997)

$$\frac{\pi r^2}{r_h^2}\int_0^\infty S(\lambda)Q_{\rm abs}(\lambda, r)d\lambda = 4\pi r^2\int_0^\infty Q_{\rm abs}(\lambda, r)\pi B_\lambda[T(r)]d\lambda, \tag{3}$$

where $S(\lambda)$ is the solar flux at 1 AU, which we consider as a blackbody at $T = 5900$ K. This equation is solved for $T(r)$ by Brent's algorithm. In this way, we generate a table from which we derive the equilibrium temperature as a function of particle radius and heliocentric distance by a two-dimensional interpolation. Then, using Equation (2), we compute the infrared flux of a given particle as a function of the position in the (N, M) plane. The rest of the Monte Carlo procedure is analogous to the one developed for the analysis at red wavelengths shown in previous sections.

Davies et al. (1997) obtained IR fluxes from the 22P/Kopff trail images on 1992 March 26 using ISOCAM, the infrared camera on the *ISO* satellite. They reported IR fluxes at 12 μm and trail widths at two positions of the trail behind the comet, one at $+0.^\circ5$ in mean anomaly and another at $+1^\circ$ in mean anomaly.

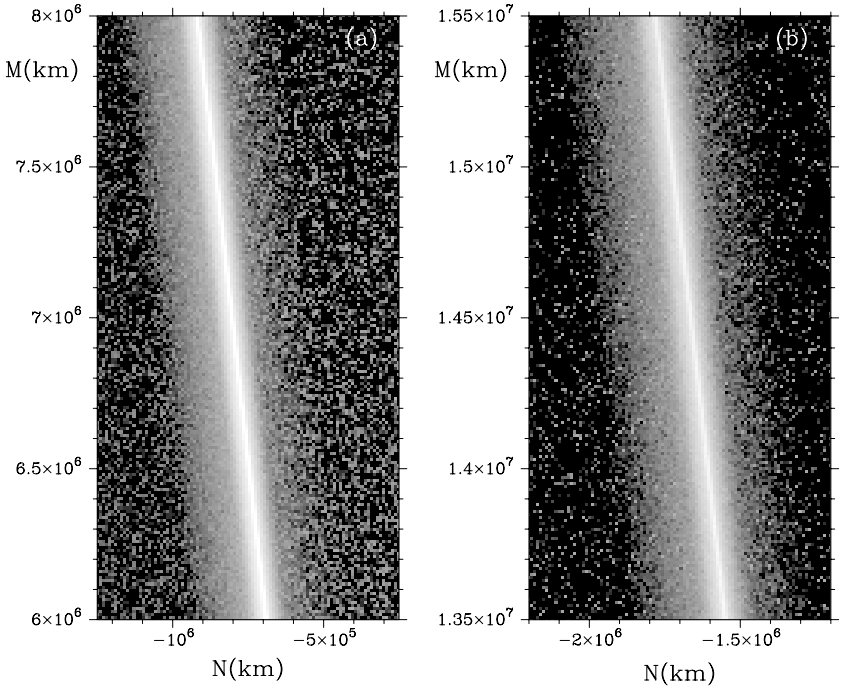

Figure 15. Simulated trails at 12 μm wavelength on 1992 March 26, centered on regions of δMA = +0.°5 (a) and δMA = +1.°0 (b) as in the ISOCAM observations by Davies et al. (1997). The maximum intensity level in the images corresponds to 0.40 MJy sr^{-1}. Peak intensities are 0.40 MJy sr^{-1} and 0.25 MJy sr^{-1}, at δMA = +0.°5 and δMA = +1.°0, respectively.

Table 2
Model Physical Parameters for Anisotropic Ejection Models

Parameter	Value Adopted/Retrieved
Grain density	1000 kg m^{-3}
Grain refractive index	$m = 1.88 + 0.71i$
Grain geometric albedo	$p_v = 0.036$
Ejection velocity	$v(t, \beta) = v_1(t)\beta^{1/2}$, see Figure 6
Peak ejection velocity of 1-cm grains	2.7 m s^{-1}
Size distribution: $r_{\rm min}$, $r_{\rm max}$	10^{-4} cm, 1.4 cm
Size distribution: power index	−3.1
Peak dust mass loss rate (perihelion)	260 kg s^{-1}
Averaged dust mass loss rate per orbit	40 kg s^{-1}
Total dust mass ejected per orbit	8×10^9 kg
Pre-perihelion switch-on activity	$r_h \gtrsim 3.5$ AU
Nucleus rotation period	12.3 hr (Lowry & Weissman 2003)
Argument of subsolar meridian at perihelion	$\Phi = 180^\circ$
Obliquity	$I = 60^\circ$
Active area location	Time dependent, see Figure 12
Cone angle width	$\Delta\phi = 60^\circ$ for $r_h > 2.5$ AU pre-perihelion $\Delta\phi = 20^\circ$ for $r_h > 1.95$ AU post-perihelion $\Delta\phi = 40^\circ$ otherwise
Isotropic emission percentage	30%

Table 3
Comparison of *ISO* and *IRAS* Data with Model Results at 12 μm Wavelength

δMA$^\circ$	Measured Brightness (MJy sr^{-1})	Modeled Brightness (MJy sr^{-1})	Measured FWHM (km)	Modeled FWHM (km)
+0.5	0.33 ± 0.07 (*ISO*)	0.40	48000 ± 3000	26000
+0.5	0.66 ± 0.07 (*IRAS*)	0.63	32000 ± 16000	21000
+1.0	0.26 ± 0.07 (*ISO*)	0.25	61000 ± 3000	29000
+1.0	1.35 ± 0.11 (*IRAS*)	0.32	32000 ± 11000	31000

We have performed a simulation of the trail brightness at that wavelength, and at that date, as shown in Figure 15. In that simulation, we used a trail age of 38 years, which is the time spanned between the 1954 close encounter of the comet with Jupiter and the observation. Davies et al. (1997) also reported updated *IRAS* fluxes and widths of the dust trail of the comet at

the same wavelength and same positions in mean anomaly, but with the comet at different heliocentric and geocentric distances. Since the *IRAS* images are built from scans taken over a period of several weeks, the observation date selected in our code should be representative of the mean date of that period. For the *IRAS* observations, in Table 2 of Davies et al. (1997), there appear to be heliocentric distances of 1.69 and 1.66 AU, and geocentric distances of 1.48 and 1.45 AU, for the observations at mean anomalies of +0.°5 and +1.°0, respectively. These distances are approximately those that apply on 1983 October 15 (r_h = 1.7 AU, Δ = 1.47 AU), which is the date we selected to compare with those *IRAS* observations. Therefore, the trail age is 29.8 years. Table 3 shows the model results compared to *IRAS* and ISOCAM observations. As can be seen, there is a good agreement with the ISOCAM intensities and with the *IRAS* intensity at δMA = +0.°5, but not with the intensity at δMA = +1.°0, where the modeled intensity is more than four times smaller than measured. Observations of the 22P/Kopff trail were also performed with instrumentation on board the *Midcourse Space Experiment* mission (Kraemer et al. 2005). The comet was observed about two months post-perihelion, on 1996 September 11, and the resulting trail maximum brightness at 12.1 μm wavelength and δMA = +0.°16 was 0.74 MJy sr^{-1}, which is also significantly smaller than the *IRAS* result.

On the other hand, the modeled trail widths are within the estimated errors of the *IRAS* measurements, but narrower than the ISOCAM widths in a factor of two to three. Since those trails contain information on the dust ejected several orbits before the observations, these width discrepancies could very well be attributed to differences in ejection velocities over many orbits back to the 2009 apparition, to which the model actually applies. Nevertheless, the excellent agreement of the modeled intensities with the observations (with the exception of the *IRAS* intensity at δMA = +1.°0) is remarkable.

6. CONCLUSIONS

The analysis of a large image data set of comet 22P/Kopff during two consecutive apparitions has permitted us to develop a model by which the most relevant cometary dust parameters have been retrieved accurately. The observations have been compared to amateur astronomical observations by the *Cometas-Obs* group, showing a remarkable agreement in the behavior of the Afρ parameter as a function of the heliocentric distance. Both the CCD light curve and Afρ observations indicate a brightness excess at 100 days from perihelion which is clearly correlated with the phase angle, and therefore indicative of a brightness opposition effect. The linear phase coefficient is 0.028 $\pm$ 0.002 mag deg^{-1}.

Assuming spherical particles of a density of ρ_d = 1000 kg m^{-3} and glassy carbon composition (refractive index at red wavelengths of $m = 1.88 + 0.71i$), which gives a geometric albedo of $p_v = 0.036$, the mass loss rate peaks near perihelion with a value of 260 kg s^{-1}. The comet onset of activity occurs at heliocentric distances of $r_h \gtrsim 3.5$ AU, showing a clear time-dependent asymmetric behavior, with an enhanced activity at heliocentric distances beyond 2.5 AU pre-perihelion, also accompanied by an enhanced particle ejection velocity. The total mass ejected per orbit is 8×10^9 kg, with an averaged dust mass loss rate per orbital period of 40 kg s^{-1}. The images can all be modeled assuming a time-constant differential size distribution function characterized by a power law of index -3.1.

The analysis of archive images corresponding to the 2002 apparition, acquired at large heliocentric distances pre- and post-perihelion, provides clues on the dust ejection anisotropy. Such a model suggests an ejection scenario where the outgassing comes from regions near subsolar latitudes at far heliocentric distances pre- and post-perihelion, but becoming nearly isotropic at intermediate heliocentric distances pre- and near-perihelion. The anisotropic model is characterized by a latitude-dependent active area on a rotating nucleus with rotational parameters of $\Phi = 180^\circ$ and $I = 60^\circ$. The dust ejection is produced from emission cones randomly distributed on the active area surface with time-dependent cone angle widths varying between 20° (at far distances pre-perihelion) and 60° (at far distances post-perihelion).

We have demonstrated that such a model is compatible with all the available observations. Besides, the trail intensities that characterize the time-averaged behavior of the large particle component of the dust are reproduced accurately, providing additional strength on the results obtained.

In order to compare with infrared trail intensities obtained by *IRAS* and *ISO* satellites, a modified version of the Monte Carlo code has been developed to produce synthetic thermal images. The modeled intensities are in agreement with ISOCAM observations at δMA = +0.°5 and at δMA = +1.°0, while the trail widths are significantly narrower than reported by Davies et al. (1997). However, they are similar to the *IRAS* data (Sykes & Walker 1992) when re-analyzed by Davies et al. (1997). Since those observations correspond to several orbits before the 2002 and 2009 apparitions to which the model actually applies, the discrepancies could just reflect real variations in dust ejection velocities and/or dust loss masses among different cometary orbits.

We thank an anonymous referee for comments and suggestions for improving the paper.

We are grateful to M. Ishiguro, who granted access to Kiso Observatory 105 cm Schmidt telescope images.

We are indebted to the amateur astronomers of the association *Cometas-Obs* for providing us with 22P/Kopff observations, in particular to I. Almendros, R. Naves, M. Campas, J. R. Vidal, F. Baldris, J. L. Salto, E. Cortés, F. García, J. Camarasa, J. Lopesino, J. M. Bosch, C. González, C. Colazo, F. Tifner, D. Cardeñosa, M. Rodríguez de Viguri, J. F. Hernández, J. C. Millán, F. García, J. M. Ruiz, F. A. Rodríguez, C. Piret, G. Muler, J. A. Henríquez, O. Canales, R. Benavides, and J. Temprano.

This research was based on data obtained at the Observatorio de Sierra Nevada, which is operated by the Instituto de Astrofísica de Andalucía, CSIC.

Part of the data used in this paper were downloaded from the CFHT Science Data Archive. This research used the facilities of the Canadian Astronomy Data Centre operated by the National Research Council of Canada with the support of the Canadian Space Agency.

This work was supported by contracts AYA2009-08011 and P09-FQM-4555 (Proyecto de Excelencia, Junta de Andalucía).

Facility: CFHT

REFERENCES

A'Hearn, M. F., Schleicher, D. G., Millis, R. L., Feldman, P. D., & Thompson, D. T. 1984, AJ, 89, 579

Davies, J. K., Sykes, M. V., Reach, W. T., et al. 1997, Icarus, 127, 251

Draine, B. T. 2000, in Light Scattering by Nonspherical Particles, ed. M. I. Mishchenko, J. W. Hovenier, & L. D. Travis (San Diego: Academic Press), 131

Edoh, O. 1983, PhD thesis, Univ. Arizona

Finson, M., & Probstein, R. 1968, ApJ, 154, 327

Fulle, M. 1989, A&A, 217, 283
Fulle, M., Colangeli, L., Agarwal, J., et al. 2010, A&A, 522, 63
Groussin, O., Lamy, P., Toth, I., et al. 2009, Icarus, 199, 568
Hanner, M. S., Gehrz, R. D., Harker, D. E., et al. 1997, Earth Moon Planets, 79, 247
Ishiguro, M., Sarugaku, Y., Ueno, M., et al. 2007, Icarus, 189, 169
Kępiński, F. 1958, Acta Astron., 8, 193
Kępiński, F. 1963, Acta Astron., 13, 87
Kimura, H., Kolokolova, L., & Mann, I. 2003, A&A, 407, L5
Kimura, H., & Liu, C. 1977, Chin. Astron., 1, 235
Kolokolova, L., Hanner, M. S., Levasseur-Regourd, A.-Ch., & Gustafson, B. A. S. 2004, in Comets II, ed. M. C. Festou, H. U. Keller, & H. A. Weaver (Tucson, AZ: Univ. Arizona Press), 577
Kraemer, K. E., Lisse, C. M., Price, S. D., et al. 2005, AJ, 130, 2363
Lamy, P. L., Toth, I., Jorda, L., et al. 2002, Icarus, 156, 442
Lowry, S. C., & Fitzsimmons, A. 2001, A&A, 365, 204
Lowry, S. C., & Weissman, P. R. 2003, Icarus, 164, 492
Meech, K., & Jewitt, D. 1987, A&A, 187, 585
Mishchenko, M. I., Travis, L. D., & Macke, A. 2000, in Light Scattering by Nonspherical Particles, ed. M. I. Mishchenko, J. W. Hovenier, & L. D. Travis (San Diego: Academic Press), 131
Monet, D. G., Levine, S. E., Canzian, B., et al. 2003, AJ, 125, 984
Moreno, F. 2009, ApJS, 183, 33
Moreno, F., Lara, L. M., Licandro, J., et al. 2011, ApJ, 738, L16
Moreno, F., Muñoz, O., Guirado, D., & Vilaplana, R. 2007, J. Quant. Spectrosc. Radiat. Transfer, 106, 348
Nelder, J. A., & Mead, R. 1965, Comput. J., 7, 308
Press, W. H., Teukolsky, S. A., Vetterling, W. T., & Flannery, B. P. 1992, in Numerical Recipes in FORTRAN (Cambridge: Cambridge Univ. Press), 402
Rickman, H., Sitarski, G., & Todorovic-Juchniewicz, B. 1987, A&A, 188, 206
Sekanina, Z. 1981, Ann. Rev. Earth Planet. Sci., 9, 113
Sekanina, Z. 1984, AJ, 89, 1573
Sosa, A., & Fernández, J. A. 2009, MNRAS, 393, 192
Sykes, M. V., & Walker, R. G. 1992, Icarus, 95, 180
Tancredi, G., Fernández, J. A., Rickman, H., & Licandro, J. 2000, A&A, 146, 73
Yeomans, D. K. 1974, PASP, 86, 125
Zubko, E. 2011, in Light Scattering by Irregularly Shaped Particles with Sizes Comparable to the Wavelength, in Light Scattering Reviews, Vol. 6, Light Scattering and Remote Sensing of Atmosphere and Surface, ed. A. A. Kokhanovsky (Berlin: Springer), 39

A&A 568, A3 (2014)
DOI: 10.1051/0004-6361/201423762

Astronomy & Astrophysics

Dust environment and dynamical history of a sample of short-period comets⋆

F. J. Pozuelos[1,3], F. Moreno[1], F. Aceituno[1], V. Casanova[1], A. Sota[1], J. J. López-Moreno[1], J. Castellano[2], E. Reina[2], A. Diepvens[2], A. Betoret[2], B. Häusler[2], C. Gonález[2], D. Rodríguez[2], E. Bryssinck[2], E. Cortés[2], F. García[2], F. García[2], F. Limón[2], F. Grau[2], F. Fratev[2], F. Baldrís[2], F. A. Rodriguez[2], F. Montalbán[2], F. Soldán[2], G. Muler[2], I. Almendros[2], J. Temprano[2], J. Bel[2], J. Sánchez[2], J. Lopesino[2], J. Báez[2], J. F. Hernández[2], J. L. Martín[2], J. M. Ruiz[2], J. R. Vidal[2], J. Gaitán[2], J. L. Salto[2], J. M. Aymamí[2], J. M. Bosch[2], J. A. Henríquez[2], J. J. Martín[2], J. Lacruz[2], L. Tremosa[2], L. Lahuerta[2], M. Reszelsky[2], M. Rodríguez[2], M. Camarasa[2], M. Campas[2], O. Canales[2], P.J. Dekelver[2], Q. Moreno[2], R. Benavides[2], R. Naves[2], R. Dymoc[2], R. García[2], S. Lahuerta[2], and T. Climent[2]

[1] Instituto de Astrofísica de Andalucía (CSIC), Glorieta de la Astronomía s/n, 18008 Granada, Spain
e-mail: pozuelos@iaa.es
[2] Amateur Association Cometas-Obs, Spain
[3] Universidad de Granada-PhD Program in Physics and Mathematics (FisyMat), Spain

Received 5 March 2014 / Accepted 1 May 2014

ABSTRACT

Aims. In this work, we present an extended study of the dust environment of a sample of short-period comets and their dynamical history. With this aim, we characterize the dust tails when the comets are active, and we make a statistical study to determine their dynamical evolution. The targets selected were 22P/Kopff, 30P/Reinmuth 1, 78P/Gehrels 2, 115P/Maury, 118P/Shoemaker-Levy 4, 123P/West-Hartley, 157P/Tritton, 185/Petriew, and P/2011 W2 (Rinner).
Methods. We use two different observational data sets: a set of images taken at the Observatorio de Sierra Nevada and, the $Af\rho$ curves provided by the amateur astronomical association Cometas-Obs. To model these observations, we use our Monte Carlo dust tail code. From this analysis, we derive the dust parameters, which best describe the dust environment: dust loss rates, ejection velocities, and size distribution of particles. On the other hand, we use a numerical integrator to study the dynamical history of the comets, which allows us to determine with a 90% confidence level the time spent by these objects in the region of Jupiter family comets.
Results. From the Monte Carlo dust tail code, we derived three categories according to the amount of dust emitted: weakly active (115P, 157P, and Rinner), moderately active (30P, 123P, and 185P), and highly active (22P, 78P, and 118P). The dynamical studies showed that the comets of this sample are young in the Jupiter family region, where the youngest ones are 22P (∼100 yr), 78P (∼500 yr), and 118P (∼600 yr). The study points to a certain correlation between comet activity and time spent in the Jupiter family region, although this trend is not always fulfilled. The largest particle sizes are not tightly constrained, so that the total dust mass derived should be regarded as a lower limit.

Key words. comets: general – methods: numerical – methods: observational

1. Introduction

According to the current theories, comets are the most volatile and least processed materials in our solar system, which was formed from the primitive nebula 4.6 Gyr ago. They are considered as fundamental building blocks of giant planets and might be an important source of water on Earth (e.g. Hartogh et al. 2011). For these reasons, comet research is a hot topic in science today, and quite a few spacecraft missions were devoted to their study: *Giotto* to 1P/Halley (Keller et al. 1986), Deep Space 1 to 19P/Borrelly (Soderblom et al. 2002), Stardust to 81P/Wild 2 (Brownlee et al. 2004), Deep Impact to 9P/Temple 1 (A'Hearn et al. 2005), and the current Rosetta mission on its way to 67P/Churyumov-Gerasimenko (Schwehm & Schulz 1998) are some examples. It is well known that the importance of the study of short-period comets, which are also called Jupiter family comets (JFCs), because they offer the possibility to be studied during several passages near perihelion when the activity increases, which allows us to determine the dust environment and its evolution along the orbital path. This information is necessary to constraint the models describing evolution of different comet families and their contribution to the interplanetary dust (Sykes et al. 2004). In this work, we focus on nine JFCs 22P/Kopff, 30P/Reinmuth 1, 78P/Gehrels 2, 115P/Maury, 118P/Shoemaker-Levy 4, 123P/West-Hartley, 157P/Tritton, 185P/Petriew, and P/2011 W2 (Rinner) (hereafter 22P, 30P, 78P, 115P, 118P, 123P, 157P, 185P, and Rinner, respectively). The perihelion distance, aphelion distance, orbital period, and latest perihelion date are displayed in Table 1. The analysis we have done consists of two different parts: the first one is a dust characterization using our Monte Carlo dust tail code, which was developed by Moreno (2009) and was used successfully on previous studies (e.g. Moreno et al. 2012, from which we adopt the results for comet 22P, see below). This procedure allows us to derive the dust parameters: mass loss rates, ejection velocities, and size

⋆ Appendices are available in electronic form at http://www.aanda.org

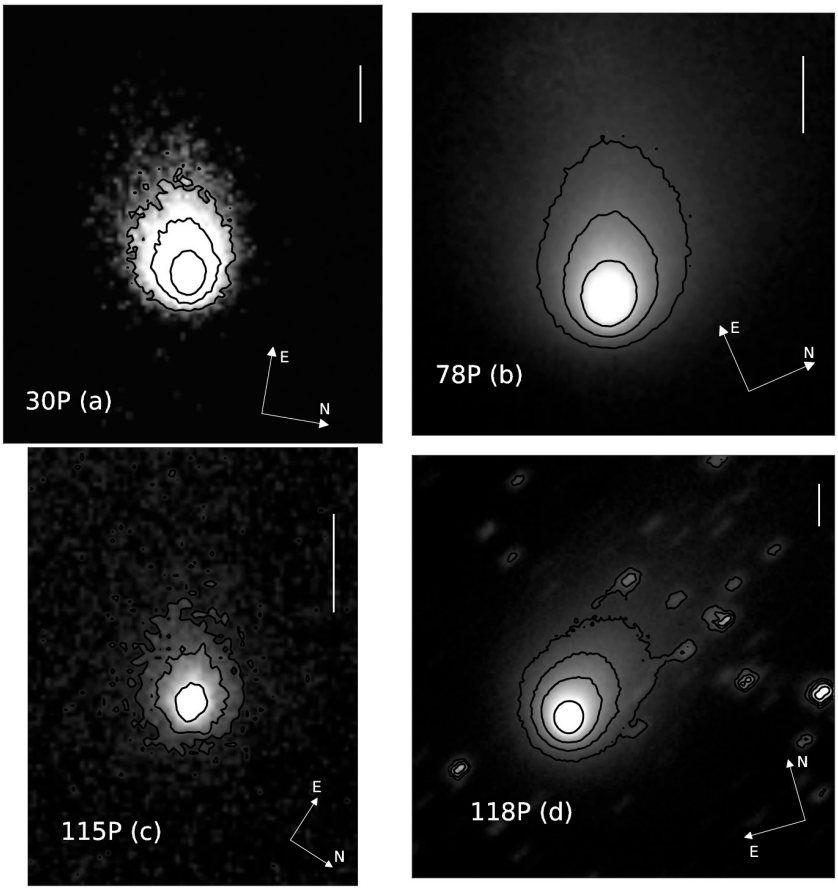

Fig. 1. Observations obtained using a CCD camera at the 1.52 m telescope of the Observatorio de Sierra Nevada in Granada, Spain. **a)** 30P/Reinmuth 1 on May 15, 2010. Isophote levels in solar disk units (SDU) are 2.00×10^{-13}, 0.75×10^{-13}, and 0.25×10^{-13}. **b)** 78P/Gehrels 2 on December 19, 2011. Isophote levels are 0.55×10^{-12}, 2.65×10^{-13}, and 1.35×10^{-13}. **c)** 115P/Maury on July 15, 2011. Isophote levels are 1.00×10^{-13}, 3.00×10^{-14}, and 1.30×10^{-14}. **d)** 118P/Shoemaker-Levy 4 on December 12, 2009. Isophote levels are 1.50×10^{-13}, 6.00×10^{-14}, 3.50×10^{-14}, and 2.00×10^{-14}. In all cases, the directions of celestial North and East are given. The vertical bars correspond to 10^4km in the sky.

Table 1. Targets list.

Comet	q (AU)	Q (AU)	Period (yr)	Last perihelion date
22P	1.57	5.33	6.43	May 25, 2009
30P	1.88	5.66	7.34	April 19, 2010
78P	2.00	5.46	7.22	January 12, 2012
115P	2.03	6.46	8.76	October 6, 2011
118P	1.98	4.94	6.45	January 2, 2010
123P	2.12	5.59	7.59	July 4, 2011
157P	1.35	5.46	6.31	February 20, 2010
185P	0.93	5.26	5.46	August 13, 2012
Rinner	2.30	5.29	7.40	November 6, 2011

distribution of particles (i.e. maximum size, minimum size, and the power index of the distribution δ). We can also obtain information on the emission pattern, specifically on the emission anisotropy. For the cases where we determine that the emission is anisotropic, we can establish the location of the active areas on the surface and the rotational parameters, as introduced by Sekanina (1981), which are the obliquity of the orbit plane to the cometary equator, I, and the argument of the subsolar meridian at perihelion, ϕ. The second part in our study is the analysis of the recent (15 Myr) dynamical history for each target. To perform this task, we use the numerical integrator developed by Chambers (1999) as did by other authors before (e.g., Hsieh et al. 2012a,b; Lacerda 2013).This will serve to derive the time spent by each comet in each region and, specifically, in the Jupiter family region, where it is supposed that the comets become active periodically. For some of these comets, this is the first available study to our knowledge.

2. Observations and data reduction

The first block of our observation data were taken at the 1.52 m telescope of Sierra Nevada Observatory (OSN) in Granada, Spain. We used a 1024×1024 pixel CCD camera with a Johnson red filter to minimize gaseous emissions. The pixel size in the sky was $0\farcs46$, so the field of view was $7\farcm8 \times 7\farcm8$. To improve the signal-to-noise ratio, the comets were imaged several times using integration times in the range 60–300 s. The individual images at each night were bias subtracted and flat-fielded using standard techniques. The flux calibration was made using the USNO-B1.0 star catalog (Monet et al. 2003).The individual images of the comets were calibrated to mag arcsec^{-2} and then converted to solar disk intensity units (hereafter SDU). After calibration, the images corresponding to each single night were shifted to a reference image by taking their apparent sky motion into account, and then a median of those images was taken. For the modeling purposes, the final images are rotated to the photographic plane (N, M) (Finson & Probstein 1968), where the Sun is toward $-M$. Table 2 shows the log of the observations. Negative values in time to perihelion correspond to pre-perihelion observations. Representative images are displayed in Figs. 1 and 2.

The second block of observational data correspond to the $Af\rho$ curves around perihelion date (~300 days). These observations were carried out by the amateur astronomical association Cometas-Obs. The $Af\rho$ measurements are presented as a

Table 2. Log of the OSN observations.

Comet	Observation date (UT)	r_h[1] (AU)	Δ (AU)	Resolution (km pixel^{-1})	Phase Angle (°)	Position Angle (°)	$Af\rho$ ($\rho = 10^4$ km)[2] (cm)
30P/Reinmuth 1	2010 Mar. 10 21:45	–1.916	1.579	526.8	31.1	87.1	52
	2010 May 15 21:10	1.898	2.147	716.3	28.0	99.6	61
78P/Gehrels 2	2011 Dec. 19 20:00	–2.018	1.647	549.5	28.9	66.5	380
	2012 Jan. 4 20:15	–2.009	1.805	602.2	29.2	67.0	470
115P/Maury	2011 Jul. 2 22:00	–2.146	1.343	448.0	18.5	122.7	17
118P/Shoemaker-Levy 4	2009 Dec. 12 01:45	–1.991	1.032	1377.2	8.9	324.9	103
123P/West-Hartley	2011 Feb. 26 23:00	–2.346	1.970	657.3	24.5	86.4	40
	2011 Mar. 31 21:00	2.253	2.252	751.3	25.6	85.4	50
157P/Tritton	2010 Mar. 10 21:30	1.376	1.343	448.0	42.8	77.0	20
185P/Petriew	2012 Jul. 15 03:15	–1.027	1.097	366.0	57.0	260.2	17
P/2011 W2 (Rinner)	2011 Dec. 22 03:00	2.326	1.451	484.1	14.0	309.9	18
	2012 Jan. 4 02:00	2.340	1.412	471.2	10.2	332.2	22

Notes. [(1)] Negative values correspond to pre-perihelion, positive values to post-perihelion. [(2)] The $Af\rho$ values for phase angle ≤30° have been corrected according to Eq. (2) (see text).

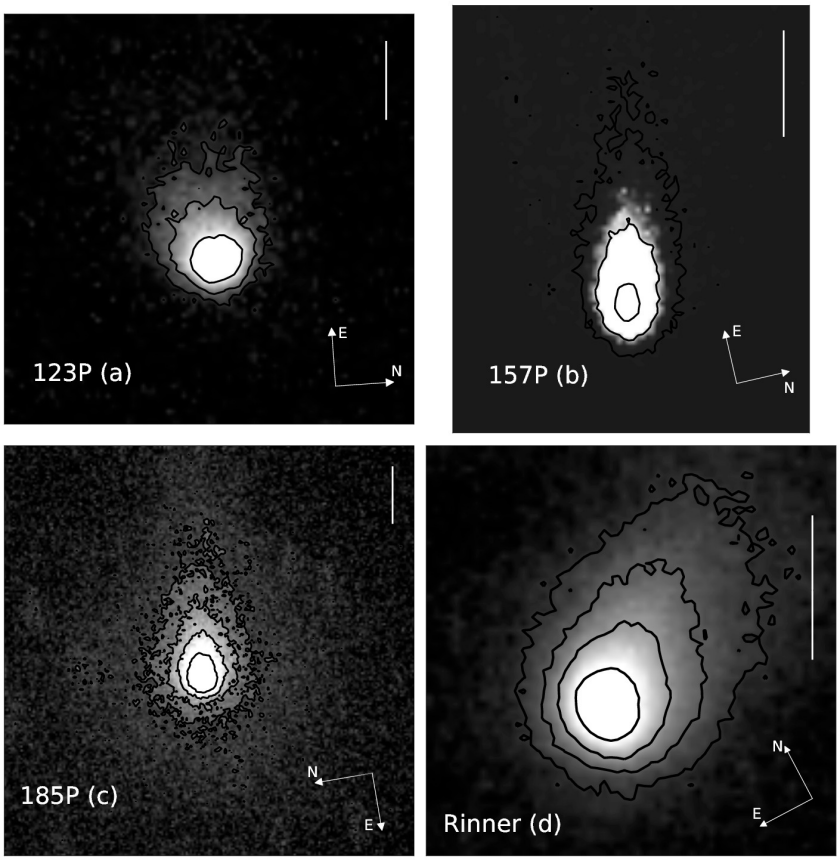

Fig. 2. Observations obtained using a CCD camera at the 1.52 m telescope of the Observatorio de Sierra Nevada in Granada, Spain. **a)** 123P/West-Hartley on February 26, 2011. Isophote levels in solar disk units (SDU) are 1.00×10^{-13}, 0.35×10^{-13}, and 0.15×10^{-13}. **b)** 157P/Tritton on March 10, 2010. Isophote levels are 6.00×10^{-13}, 0.75×10^{-13}, and 2.65×10^{-14}. **c)** 185P/Petriew on July 15, 2012. Isophote levels are 1.80×10^{-13}, 1.00×10^{-13}, 0.60×10^{-13}, and 0.35×10^{-13}. **d)** P/2011 W2 (Rinner) on January 4, 2012. Isophote levels are 6.00×10^{-14}, 2.70×10^{-14}, 1.50×10^{-14}, and 0.80×10^{-14}. In all cases, the directions of celestial North and East are given. The vertical bars correspond to 10^4 km in the sky.

function of the heliocentric distance and are always referred to an aperture of radius $\rho = 10^4$ km projected on the sky at each observation date. The calibration of the Cometas-Obs observations was performed with the star catalogs CMC-14 and USNO A2.0.

3. Monte Carlo dust tail model

The dust tail analysis was performed by the Monte Carlo dust tail code, which allows us to fit the OSN images and the observational $Af\rho$ curves provided by Cometas-Obs. This code has been successfully used on previous works on characterization of dust environments of comets and Main-belt comets, such as 29P/Schwassmann-Wachmann 1 and P/2010 R2 (La Sagra) (Moreno 2009; Moreno et al. 2011). This code is also called the Granada model (see Fulle et al. 2010) in the dust studies for the Rosetta mission target, 67P/Churyumov-Gerasimenko. The model describes the motion of the particles when they leave the nucleus and are submitted to the gravity force of the Sun and the radiation pressure, so that the trajectory of the particles around the Sun is Keplerian. The β parameter is defined

as the ratio of the radiation pressure force to the gravity force and is given for spherical particles as $\beta = C_{\rm pr}Q_{\rm pr}/(\rho_{\rm d}d)$, where $C_{\rm pr} = 1.19 \times 10^{-3}$ km m^{-2}; $Q_{\rm pr}$ is the scattering efficiency for radiation pressure, which is $Q_{\rm pr} \sim 1$ for large absorbing grains (Burns et al. 1979); $\rho_{\rm d}$ is the mass density, assumed at $\rho_{\rm d} = 10^3$ kg m^{-3}; and d is the particle diameter. We use Mie theory for the interaction of the electromagnetic field with the spherical particles to compute the geometric albedo, p_v, and $Q_{\rm pr}$. The parameter, p_v, is a function of the phase angle α and the particle radius. We assume the particles as glassy carbon spheres of refractive index $m = 1.88 + 0.71i$ (Edoh 1983) at $\lambda = 0.6$ μm. We compute a large number of dust particle trayectories and calculate their positions on the (N, M) plane and their contribution to the tail brightness. The free parameters of the model are dust mass loss rate, the ejection velocities of the particles, the size distribution, and the dust ejection pattern.

3.1. Afρ

The $Af\rho$ quantity [cm] (A'Hearn et al. 1984) is related to the dust coma brightness, where A is the dust geometric albedo, f the filling factor in the aperture field of view (proportional to the dust optical thickness), and ρ is the linear radius of aperture at the comet, which is the sky-plane radius. When the cometary coma is in steady-state, $Af\rho$ is independent of the observation coma radius ρ if the surface brightness of the dust coma is proportional to ρ^{-1}. It is formulated as follows:

$$Af\rho = \frac{4r_{\rm h}^2\Delta^2}{\rho}\frac{F_{\rm c}}{F_{\rm s}}, \quad (1)$$

where $r_{\rm h}$ is the heliocentric distance and Δ the geocentric distance. The parameter, $F_{\rm c}$, is the measured cometary flux integrated within a radius of aperture ρ, and $F_{\rm s}$ is the total solar flux. For each comet, we have the $Af\rho$ curve as heliocentric distance function provided by Cometas-Obs for an aperture of radius $\rho = 10^4$ km, ~300 days around perihelion, and the $Af\rho$ measurements derived from the OSN observations with the same aperture. Some of the $Af\rho$ data correspond to times, where the phase angle was close to zero degree, so that the backscattering enhancement became apparent (Kolokolova et al. 2004). We could not model this enhancement: for the assumed absorbing spherical particles, the phase function is approximately constant except for the forward spike for particles whose radius is $r \geq \lambda$. Then, we corrected these enlarged $Af\rho$ at small phase angles by assuming a certain linear phase coefficient, which we apply to the data at phase angles $\alpha \leq 30°$. We adopted a linear phase coefficient of 0.03 mag deg^{-1}, which is in the range 0.02–0.04 mag deg^{-1} estimated by Meech & Jewitt (1987) from various comets. In this way, the corrected $Af\rho'$ values are computed as a function of the original $Af\rho$ values at phase angle α as:

$$Af\rho' = 10^{\frac{-\beta(30-\alpha)}{2.5}} Af\rho. \quad (2)$$

To illustrate this correction, we show in its application to comet 78P/Gehrels 2 in Fig. 3. In the upper panel, the correlation of the original $Af\rho$ data with the phase angle and the lower panel the final $Af\rho$ curve after correcting those values by Eq. (2) is seen. The same equation is applied to the OSN images when the phase angle is $\alpha \leq 30°$ (see Table 2).

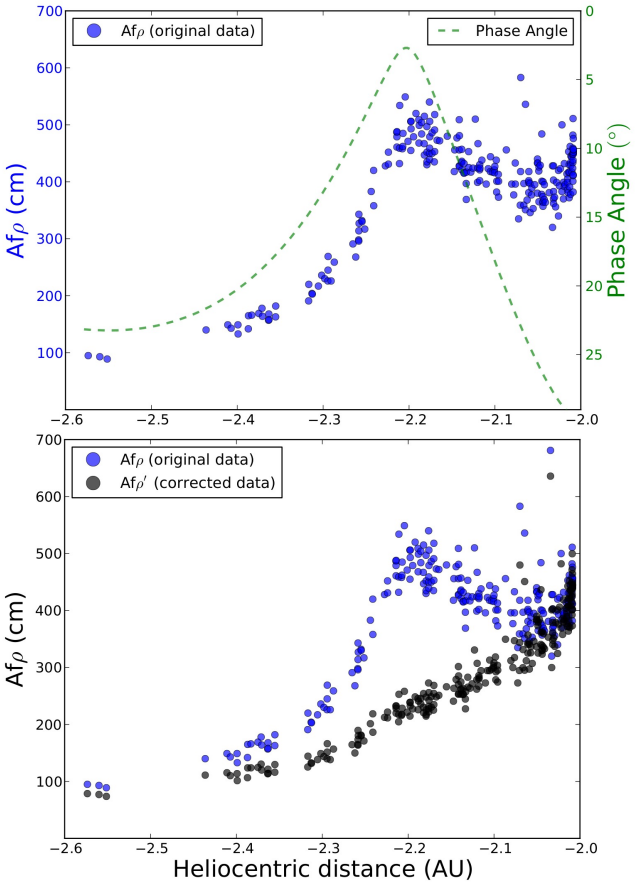

Fig. 3. $Af\rho$ pre-perihelion measurements of comet 78P/Gehrels 2 provided by Cometas-Obs. *Upper panel*: original $Af\rho$ measurements and phase angle as a function of heliocentric distance. *Lower panel*: $Af\rho$ and $Af\rho'$ after the backscattering effect correction using Eq. (2) as a function of the heliocentric distance.

4. Dust analysis

As described in the previous section, we use our Monte Carlo dust tail code to retrieve the dust properties of each comet in our sample. The code has many important parameters, so that a number of simplifying assumptions should be made to make the problem tractable. The dust particles are assumed spherical with a density of 1000 kg m^{-3} and a refractive index of $m = 1.88 + 0.71i$, which is typical of carbonaceous spheres at red wavelengths (Edoh 1983). This gives a geometric albedo of $p_v = 0.04$ for particle sizes of $r \gtrsim 1$ μm at a wide range of phase angles. The particle ejection velocity is parametrized as $v(t,\beta) = v_1(t) \times \beta^{1/2}$, where $v_1(t)$ is a time dependent function to be determined in the modeling procedure. In addition, the emission pattern, which are possible spatial asymmetries in the particle ejection, might appear. The asymmetric ejection pattern is parametrized by considering a rotating nucleus with active areas on it, whose rotating axis is defined by the obliquity, I, and the argument of the subsolar meridian at perihelion, as defined in Sekanina (1981). The rotation period, P, is not generally constrained if the ejecta age is much longer than P, which is normally the case. The particles are assumed distributed broadly in size, so that the minimum size is always set in principle in the sub-micrometer range, while the maximum size is set in the centimetre range. The size distribution is assumed to be given by a power law, $n(r) \propto r^{-\delta}$, where δ is set to vary in the −4.2 to −3 domain, which is the range that has been determined for other comets (e.g., Jockers 1997). All of those parameters, $v_1(t)$, $r_{\rm min}$, $r_{\rm max}$, and δ, and the mass loss rate are a

function of the heliocentric distance, so that some kind of dependence on r_h must be established. In addition, the activity onset time should also be specified. On the other hand, current knowledge of physical properties of cometary nuclei established the bulk density below $\rho = 1000$ kg m^{-3} (Carry 2012). Values of $\rho = 600$ kg m^{-3} have been reported for comets 81P/Wild 2 (Davidsson & Gutierrez 2004) and Temple 1 (A'Hearn et al. 2005), so we adopted that value. The ejection velocity at a distance $R \sim 20R_N$, where R_N is the nucleus radii and R is the distance where the gas drag vanishes, should overcome the escape velocity, which is given by $v_{esc} = \sqrt{2GM/R}$. Assuming a spherically shaped nucleus, we get $v_{esc} = R_N\sqrt{(2/15)\pi\rho G}$, where $\rho = 600$ kg m^{-3}. In cases where R_N has been estimated by other authors, the minimum ejection velocity should verify the condition $v_{min} \gtrsim v_{esc}$. Considering that the minimum particle velocity determined in the model is $v_{min} \sim v_{esc}$, we can give an upper limit estimate of the nucleus radius in all the other cases.

The Monte Carlo dust tail code, is a forward code whose output is a dust tail image corresponding to a given set of input parameters. Given the large amount of parameters, the solution is likely not unique: approximately the same tail brightness can be likely achieved by assuming another set of input parameters. However, if the number of available images and/or $Af\rho$ measurements cover a significant orbital arc, it is clear that the indetermination is reduced. Our general procedure first consists in assuming the most simple case: isotropic particle ejection, $r_{min} = 1$ μm, $r_{max} = 1$ cm, $v_1(t)$ monotonically increasing toward perihelion, $\delta = -3.5$, and dM/dt set to a value, which reproduce the measured tail intensity in the optocenter, assuming a monotonic decrease with heliocentric distance. From this starting point, we then start to vary the parameters, assuming a certain different dependence with heliocentric distance, until an acceptable agreement with both the dust tail images and the $Af\rho$ measurements is reached. Then, if we find no way to fit the data using an isotropic ejection model after many trial-and-error procedures, we switch to the anisotropic model where the active area location and rotational parameters must be set.

Using the procedure described above for each comet in the sample, we present the results on the dust parameters organized in the following way: in tabular form, where the main properties derived of the dust environment of each comet is given (Tables 3 and 4), and a series of plots on the dependence on the heliocentric distance of the dust mass loss rate, the ejection velocities for $r = 1$ cm particles, the maximum particle size, and the power index of the size distribution. Representative plot is shown in the case of the comet 30P in Fig. 4 and in Appendix B, the results for each comet are individually displayed (see Figs. B.1 to B.7). In addition, the representative plot of the comparison between observations and model in the case of the comet 30P is shown in Fig. 5, and the comparison between observations and models for each comet individually are displayed in the Appendix C (Figs. C.1 to C.7).

4.1. Discussion

The dust environment of the 22P was already reported by Moreno et al. (2012), where the authors concluded that this comet shows a clear time dependent asymmetric ejection behavior with an enhanced activity at heliocentric distances beyond 2.5 AU pre-perihelion. This is also accompanied by enhanced particle ejection velocity. The maximum size for the particles were estimated as 1.4 cm with a constant power index of −3.1. The peak of dust mass loss rate and the peak

Table 3. Dust properties summary of the targets under study I.

Comet	Emission pattern[1]	Active areas location (°)	Size distribution r_{min}, r_{max} (cm)	Size distribution $\delta_{min}, \delta_{max}$	Maximum nucleus radius (km)	Obliquity (°)	Argument of subsolar meridan at perihelion (°)
30P/Reinmuth 1	Ani (50%)	−30 to +30	10^{-4}, 3.5	−3.35, −3.18	3.9[2]	107[3]	133[3]
78P/Gehrels 2	Iso (100%)	–	10^{-4}, 3.0	−3.40, −3.05	3.6	–	–
115P/Maury	Ani (70%)	−20 to +60	10^{-4}, 4.0	−3.13, −3.05	4.0	25	280
118P/Shoemaker-Levy 4	Iso (100%)	–	10^{-4}, 3.0	−3.20, −3.05	2.4[4]	–	–
123P/West-Hartley	Iso (100%)	–	10^{-4}, 2.5	−3.32, −3.15	2.0[5]	–	–
157P/Tritton	Ani (70%)	−30 to +30	10^{-4}, 3.0	−3.35, −3.15	1.6	10	150
185P/Petriew	Iso (100%)	–	10^{-4}, 6.0	−3.60, −3.00	5.7	–	–
P/2011 W2 (Rinner)	Iso (100%)	–	10^{-4}, 2.5	−3.20, −3.15	2.2	–	–

Notes. [(1)] Iso = Isotropic ejection; Ani=Anisotropic ejection; [(2)] Scotti (1994); [(3)] Krolikowska et al. (1998); [(4)] Lamy et al. (2004); [(5)] Tancredi et al. (2006).

Table 4. Dust properties summary of the targets under study II.

Comet	Peak dust-loss rate (kg/s)	Peak ejection velocity of 1-cm grains (m/s)	Total dust mass ejected (kg)	Total dust mass ejected per year (kg/yr)	Averaged dust mass-loss rate (kg/s)	Contribution to the interplanetary dust (%)[1]
30P/Reinmuth 1	73.0	1.4	8.2×10^8	2.1×10^8	6.8	0.07
78P/Gehrels 2	530.0	2.1	5.8×10^9	1.5×10^9	47.5	0.52
115P/Maury	45.0	1.4	2.9×10^8	6.9×10^7	2.1	0.02
118P/Shoemaker-Levy 4	180.0	2.3	2.3×10^9	6.5×10^8	20.8	0.22
123P/West-Hartley	65.0	1.8	5.4×10^8	1.4×10^8	4.5	0.05
157P/Tritton	50.0	2.1	2.9×10^8	8.7×10^7	2.7	0.03
185P/Petriew	143.0	7.2	9.0×10^8	3.0×10^8	9.6	0.10
P/2011 W2 (Rinner)	15.0	1.7	2.6×10^8	6.4×10^7	2.0	0.02

Notes. [(1)] Annual contribution to the interplanetary dust replacement (Grun et al. 1985).

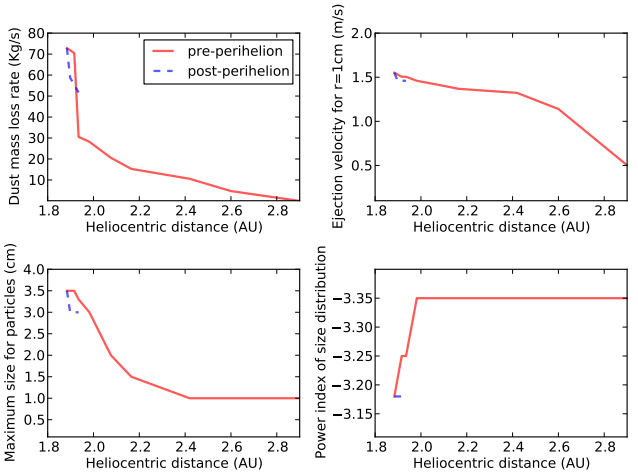

Fig. 4. Representative figure of the evolution of the dust parameter evolution obtained in the model versus the heliocentric distance for comet 30P/Reinmuth 1. The panels are as follows: **a)** dust mass-loss rate [kg/s]; **b)** ejection velocities for particles of $r = 1$ cm glassy carbon spheres [m/s]; **c)** maximum size of the particles [cm]; and **d)** power index of the size distribution. In all cases, the solid red lines correspond to pre-perihelion and the dashed blue lines to post-perihelion. In Appendix B, the results for each comet individually are displayed (see Figs. B.1 to B.7).

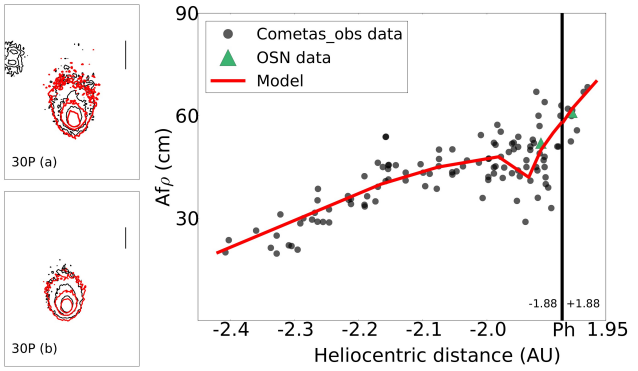

Fig. 5. Representative figure of the comparison between observations and model of comet 30P/Reinmuth 1. *Left panels*: isophote fields **a)** March 10, 2010; and **b)** May 15, 2010. In both cases, isophote levels are 2.00×10^{-13}, 0.75×10^{-13}, and 0.25×10^{-13} SDU. The black contours correspond to the OSN observations and the red contours to the model. Vertical bars correspond to 10^4 km on the sky. *Right panel*: parameter $Af\rho$ versus heliocentric distance. The black dots correspond to Cometas-Obs data, and the green triangles are the OSN data, which correspond to March 10 and May 15, 2010. The red line is the model. The observations and the model refer to $\rho = 10^4$ km. In Appendix C, the comparison between observations and models for each comet individually are displayed (see Figs. C.1 to C.7).

of ejection velocities were reached at perihelion with values $Q_d = 260$ kg s^{-1} and $v = 2.7$ m s^{-1} for 1 cm grains. The total dust lost per orbit was 8×10^9 kg. The annual dust loss rate is $T_d = 1.24 \times 10^9$ kg yr^{-1}, and the averaged dust mass loss rate per orbit is 40 kg/s. The contribution to the interplanetary dust of this comet corresponds to about 0.4% of the $\sim 2.9 \times 10^{11}$ kg yr^{-1} that must be replenished if the cloud of interplanetary dust is in steady state (Grun et al. 1985).

For 30P, 115P, and 157P, we derived an anisotropic ejection pattern with active areas on the nucleus surface (see Table 3). In the case of 30P, the rotational parameters, I and ϕ, have been taken from Krolikowska et al. (1998) as $I = 107°$ and $\phi = 321°$. However, for 115P and 157P, these parameters have been derived from the model. The 78P is the most active comet in our sample with a peak dust loss rate at perihelion with a value of $Q_d = 530$ kg s^{-1} and a total dust mass ejected of 5.8×10^9 kg. This comet was study by Mazzotta Epifani & Palumbo (2011) in its previous perihelion passage in October 2004. The authors estimated that the dust production rate at perihelion with values within $Q_d = 14-345$ kg s^{-1} using a method derived from the one used by Jewitt (2009) to compute the dust production rate of active Centarus. They also obtained $Af\rho = 846 \pm 55$ cm in an aperture of radius $\rho = 7.3 \times 10^3$ km, and they concluded that this comet is more active than the average at a given heliocentric distance. In addition, Lowry & Weissman (2003) reported a stellar appearance of 78P at $r_h = 5.46$ AU pre-perihelion, and any possible coma contribution to the observed flux was likely to be small or non existent, which is consistent with our model where the comet is not active at such large pre-perihelion distances. From our studies, we can classify our targets in three different categories: weakly active comets (115P, 157P, and Rinner) with an average annual dust production rate of $T_d < 1 \times 10^8$ kg yr^{-1}; moderately active comets (30P, 123P, and 185P) with $T_d = 1-3\times10^8$ kg yr^{-1}; and highly active comets (22P, 78P, and 118P) with $T_d > 8 \times 10^8$ kg yr^{-1}. It is necessary to consider that we do not have observations after perihelion for the comet 115P and 123P. That is, our observational information covers less than half of the orbit, losing the part of the branch which is supposed to be the most active. For this reason, our results for these comets are lower limits in the T_d measurements.

5. Dynamical history analysis

Levison & Duncan (1994) were the first to make a comprehensive set of long-term integrations (up to 10^7 yr) to study the dynamical evolution of short period comets. The authors argue that it is necessary to make a statistical study using several orbits for each comet with slightly different initial orbital elements due to the chaotic nature of each individual orbit. For this reason, the authors made a 10 Myr backward (and forward) integration for the 160 short period comets know at that time and 3 clones for each comet with offsets in the positions along the x, y, and z directions of +0.01 AU. That is, they used 640 test particles for their integrations. They conclude that the long-term integrations into the the past or future are statistically equivalent, and they obtained that ~92% of the total particles were ejected from the solar system, and ~6% were destroyed by becoming Sun-grazers. The median lifetime of JFCs was derived as 3.25×10^5 yr. In a later study of the same authors (Levison & Duncan 1997), they estimated that the physical lifetime of JFCs is between (3–25) $\times$ 10^3 yr, where the most likely value is 12×10^3 yr. In our case, we use the Mercury package version 6.2, a numerical integrator developed by Chambers (1999), to determine the dynamical evolution of our targets, that has been used by other authors with the same purpose (e.g., Hsieh et al. 2012a,b; Lacerda 2013). Due to the chaotic nature of the targets, which was mentioned in the Levison & Duncan (1994) study, we generate a total of 99 clones having 2σ dispersion in three of the orbital elements: semi-major axis, eccentricity, and inclination (hereafter a, e, and i), where σ is the uncertainty in the corresponding parameter as given in the JPL Horizons online solar system data[1]. In Table A.1, we show the orbital parameters and the 1σ uncertainty of our targets extracted from that web page. These 99 clones plus the real object make a total of 100 massless test particles to perform a statistical study for each comet, which supposes 900 massless test particles. The Sun and the eight planets are considered as massive bodies. We used the hybrid algorithm, which combines a second-order mixed-variable symplectic algorithm with a Burlisch-Stoer integrator to control close encounters. The initial time step is 8 days, and the clones are removed any time during the integration when they are beyond 1000 AU from the Sun. The total integration time was 15 Myr, which is time enough to determine the most visited regions for each comet and derive the time spent in the region of JFCs, region that is supposed to be the location where the comets reach a temperature high enough to be active periodically. We divide the possible locations of the comets in four regions attending to their dynamical properties at each moment in the study: JFC-type with $a < a_S/(1 + e)$; Centaur-type, confined by $a_S/(1 + e) < a < a_N$ and $e < 0.8$; Halley-type, which is similar to Centaur-type but with $e > 0.8$; and Transneptunian-type with $a > a_N$, where a_S and a_N are the semi-major axes of Saturn and Neptune, respectively.

In this study, we neglect the non-gravitational forces using the same arguments as Lacerda (2013). Thus, assuming that the non-gravitational acceleration, T, is due to a single sublimation jet tangential to the comet orbit, the change rate of the semi-major axis is described by

$$da/dt = 2Va^2T/GM_\odot, \quad (3)$$

where T is the acceleration due to the single jet and is given by

$$T = (dM_d/dt)(v_d/m_{nuc}). \quad (4)$$

In these equations, V is the orbital velocity, a is the semi-major axis, G is the gravitational constant, $M_\odot$ is the Sun mass, v_d is the dust velocity, and m_{nuc} is the mass of the nucleus. To show a general justification to neglect the gravitational forces that are valid to our complete list of targets, we compute the maximum rate of change of the semi-major axis that corresponds to the comet using the maximum a, maximum dM/dt, maximum v_d, and minimum m_{nuc}. From our comet sample, these values are $a_{max} = 4.25$ AU (115P), $(dM/dt)_{max} = 47.5$ kg s^{-1} (78P), $(v_d)_{max} = 708$ m s^{-1} (185P). The minimum comet nucleus was inferred for 157P as $R_N \leq 1.6$ km, so we adopt $(R_N)_{min} = 1.6$ km, which is a minimum nucleus of $(m_{nuc})_{min} = 1.03\times10^{13}$ kg. Taken all those values together, we get $T = 2.2 \times 10^{-5}$ AU yr^{-2} and $da/dt = 4.8 \times 10^{-5}$ AU yr^{-1}. On the other hand, the lifetime of sublimation from a single jet would be $t_{sub} = 6871$ yr, which is based on the nucleus size and $(dM/dt)_{max}$. Then, the total deviation in semi-major axis would be $(da/dt)_{max} \times t_{sub} = 0.33$ AU. This deviation, which should be considered as an upper limit, is completely negligible in the scale of variations we are dealing with in the dynamical analysis of the orbital evolution. This result is close to the one derived for Lacerda (2013), where the author gives the maximum semi-major deviation for P/2010 T020 LINEAR-Grauer as 0.42 AU.

As a result of our 15 Myr backward integration for all targets, we find that the ~98% of the particles are ejected before the end of the integration, and in almost all cases, the surviving clones are in the transneptunian region. Thus, we focused on the first 1 Myr of backward in the orbital evolution, where the ~20% of the test particles still remain in the solar system. This time is

[1] See ssd.pjl.nasa.gov/?horizons

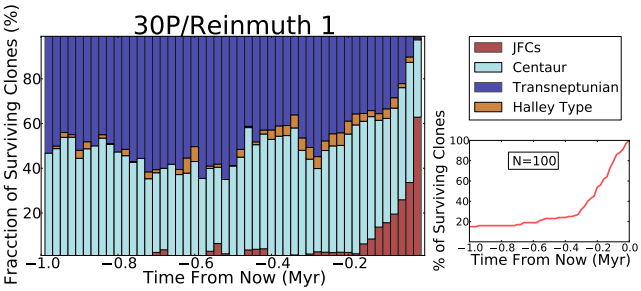

Fig. 6. 30P/Reinmuth 1 backward in time orbital evolution during 1 Myr. *Left panel*: fraction of surviving clones (%) versus time from now (Myr). The colors represent the regions visited by the test particles (red: Jupiter family region; cyan: Centaur; blue: Transneptunian; yellow: Halley Type). The resolution is 2×10^4 yr. *Bottom right panel*: the % of surviving clones versus time from now (Myr), where $N = 100$ is the number of the initial test massless particles.

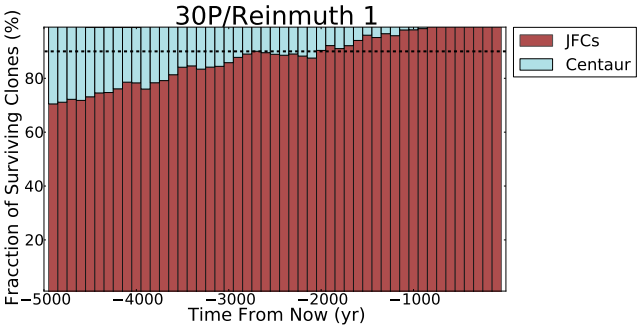

Fig. 7. 30P/Reinmuth 1 during the last 5×10^3 yr. Fraction of surviving clones (%) versus time from now (Myr). The colors represent the regions visited by the test particles (red: Jupiter family region; cyan: Centaur). The dashed line marks the bars with a confidence level equal to or larger than 90% of the clones in the Jupiter family region. The resolution is 100 yr, and the number of the initial test particles is $N = 100$.

enough to obtain a general view of the visited regions by each comet. After that, we display the last 5000 yr with a 100 yr temporal resolution to obtain the time spent by these comets in the JFCs region with a confidence level of 90%.

As an example of this procedure, we show the results for 30P (see Fig. 6) in detail. For this comet, we determined that 85% of the particles were ejected from the solar system after 1 Myr of backward integration. We can see that most of the particles stay in the JFCs region during the first $\sim 2 \times 10^4$ yr , but they moved on into further regions as centaurs and transneptunian objects at $\sim 2 \times 10^5$ yr. To determine the time spent by 30P in the JFCs region, we show the last 5×10^3 yr with a resolution of 100 yr in Fig. 7. We derive with 90% of confidence level that 30P comet spent $\sim 2 \times 10^3$ yr in this location.

A special case within the sample is comet 22P, which turned to be the youngest one in our study. Its dynamical analysis shows that the 88% of the test particles are ejected from the solar system before 1 Myr. The probability to be at the JFCs region in this period remains always under 20% (Fig. 8). If we focused on the last 5×10^3 yr (see Fig. 9), we determine the time spent in JFCs region as ~100 yr. This agrees with its discovery in 1906. It seems that this comet came from the Centaur region, which is the most likely region occupied by the object along this period.

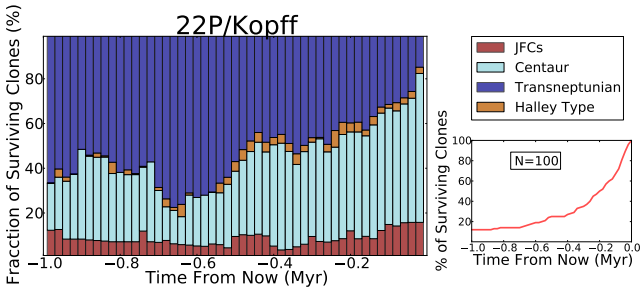

Fig. 8. As in Fig. 6, but for comet 22P/Kopff.

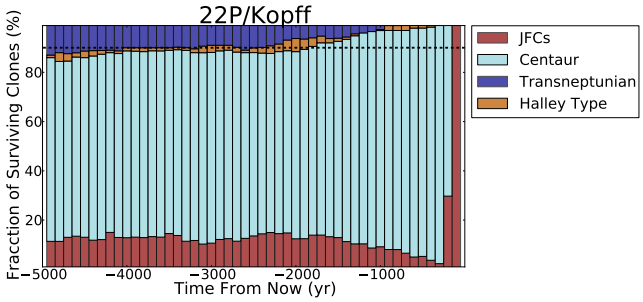

Fig. 9. As in Fig. 7, but for comet 22P/Kopff.

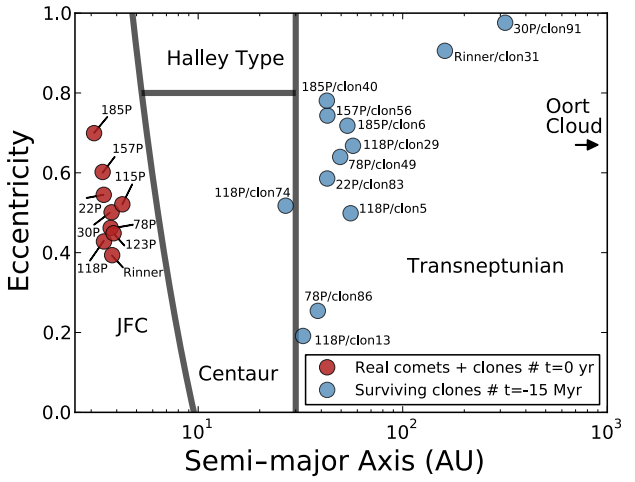

Fig. 10. Time evolution of the 900 initial particles in the 15 Myr backward integration. Red circles are the real comets and their clones (in the same location for $t = 0$ yr, which is current position, just 2σ dispersion in the orbital parameters), and the blue circles are the surving particles after 15 Myr.

5.1. Discussion

From the dynamical analysis, we determine that, just 12 of the initial 900 particles (9 real comets + 99 clones per each one) survived after a 15 Myr backward integration, which means 1.3%. This result agrees with Levison & Duncan (1994), who concluded that just 11 ± 4 particles, or 1.5 ± 0.6%, remained in the solar system after integration from their dynamical study. In Fig. 10, we show the surviving clones in the a–e plane, where just one of the clones is in the Centaur region (118P/clon74) and the rest of them are in the transneptunian region. Two of the

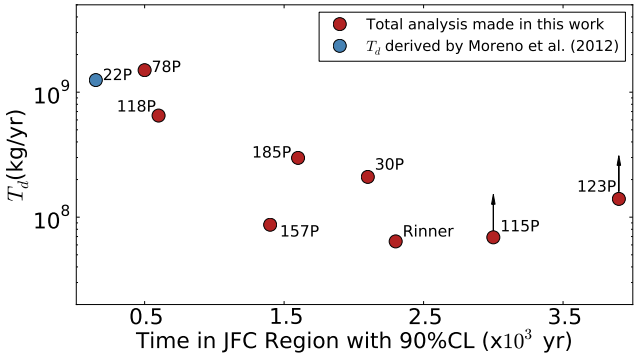

Fig. 11. Annual dust production rate of our targets obtained in the dust analysis (see Sect. 4) versus the time in the JFCs region with a 90% confidence level derived in dynamical studies (see Sect. 5). The comets with arrows mean the T_d given for them are lower limits.

clones have $a > 100$ AU with a very high eccentricity ($e > 0.9$), 30P/clon91 and Rinner/clon31. On the other hand, there are two comets with low eccentricity, 78P/clon86 and 118P/clon13, with $e < 0.25$. The rest of the surviving clones have intermediate values of eccentricity, $0.45 < e < 0.8$, and it seems that these comets are in a transition state between Kuiper Belt and the Scattered Disk objects (Levison & Duncan 1997).

In addition, we derived the time spent by all the comets under study in the JFCs region with a 90% of confidence level. We can see that the youngest is 22P, followed by 78P, and 118P (~100, ~500, and ~600 yr respectively). On the other hand, the oldest comet in our sample is 123P with ~3.9×10^3 yr. This result is shown in Fig. 11, where we relate the annual dust production rate (T_d, see Sect. 4) within the time spent in the JFCs region for each comet. It seems that the most active comets in our sample are at the same time the youngest ones, which are, 22P, 78P and 118P.

6. Summary and conclusions

We presented optical observations, which were carried out at Sierra Nevada Observatory on the 1.52 m telescope, of eight JFCs comets during their last perihelion passage: 30P/Reinmuth 1, 78P/Gehrels 2, 115P/Maury, 118P/Shoemaker-Levy 4, 123P/ West-Hartley, 157P/Tritton, 185/Petriew, and P/2011 W2 (Rinner). We also benefited from $Af\rho$ curves of these targets along ~300 days around perihelion, which is provided by Cometas-Obs. We used our Monte Carlo dust tail code (e.g. Moreno 2009) to derive the dust properties of our targets. These properties were dust loss rate, ejection velocities of particles, and size distribution of particles, where we gave the minimum and maximum size of particles and the power index of the size distribution δ. We also obtained the overall emission pattern for each comet, which could be either isotropic or anisotropic. When the ejection was derived as anisotropic, we could estimate the location of the active areas on the surface and the rotational parameters given by ϕ and I. From this analysis, we have determined three categories according to the amount of dust emitted:

1. Weakly active: 115P, 157P, and Rinner with an annual production rate $T_d < 1 \times 10^8$ kg yr^{-1}.
2. Moderately active: 30P, 123P, and 185P with an annual production rate of $T_d = 1 - 3 \times 10^8$ kg yr^{-1}.
3. Highly active: 78P and 118P with values $T_d > 8 \times 10^8$ kg yr^{-1}. In addition to these targets, we also considered for our purposes the results of the dust characterization given in a previous work by Moreno et al. (2012) for the comet 22P/Kopff. For this object, the annual production rate was derived as $T_d = 1.24 \times 10^9$ kg yr^{-1}, which allowed us introduced it in this category.

These results should be regarded as lower limits because largest size particles are not tightly constrained.

The second part of our study was the determination of the dynamical evolution followed by the comets of the sample in the last 1 Myr. With this purpose, we used the numerical integrator developed by Chambers (1999). In that case, we neglected the non-gravitational forces due to the little contribution of a single jet in the motion of our targets. We derived its maximum influence over a as 0.33 AU during the lifetime of the sublimation jet. To make a statistical study of the dynamical evolution, we used 99 clones with 2σ dispersion in the orbital parameters (a, e, and i) and the real one. Thus, we had 100 test particles to determine, which were the most visited regions by each comet and when. That analysis allowed us to determine how long these comets spent as members of JFCs, region of special interest because it is supposed that this is the place where the comets became active by sublimating the ices trapped in the nucleus, which belong to the primitive chemical components of the solar system when was formed. From the dynamical study, we inferred that our targets were relatively young in the JFC region with ages between $100 < t < 4000$ years, and all of them have a Centaur and Transneptunian past, as expected.

The last point in our conclusions led us to relate the results in the previous points. In Fig. 11, we plotted each comet by attending to the averaged dust production rate [kg/yr] derived in the dust characterizations (see Table 4 in Sect. 4) and the time spent in the JFCs region that are obtained in the dynamical analysis (see Sect. 5). Attending to that figure, we concluded that the most active comets in our target list are at the same time the youngest ones (22P, 78P, and 118P). Although the other targets showed a similar trend in general, there were some exceptions (e.g., 157P and 123P) that prevent us from reaching a firm conclusion. A more extended study of this kind would then be desirable.

Acknowledgements. We thank to F. Aceituno, V. Casanova, and A. Sota for their support as staff members in the Sierra Nevada Observatory; and the amateur astronomical association Cometas-Obs and the full grid of observers who spend the nights looking for comets. We also want to thank Dr. Chambers for his help using his numerical integrator, and the anonymous referee for comments and suggestion that improved the paper. This work was supported by contracts AYA2012-3961-CO2-01 and FQM-4555 (Proyecto de Excelencia, Junta de Andalucia).

References

A'Hearn, M. F., Schleicher, D. G., Millis, R. L., Feldman, P. D., & Thompson, D. T. 1984, AJ, 89, 579
A'Hearn, M. F., Belton, M. J. S., Delamere, W. A., et al. 2005, Science, 310, 258
Brownlee, D. E., Horz, F., Newburn, R. L., et al. 2004, Science, 304, 1764
Burns, J. A., Lamy, P. L., & Soter, S. 1979, Icarus, 40, 1
Carry, B. 2012, Planet. Space Sci., 73, 98
Chambers, J. E. 1999, MNRAS, 304, 793
Davidsson, B. J. R., & Gutierrez, P. J. 2004, in AAS/Division for Planetary Sciences Meeting Abstracts #36, BAAS, 36, 1118
Edoh, O. 1983, PhD Thesis, Univ. Arizona, Dissertation Abstracts International, Vol. 44-03, Sect. B, p. 0839
Finson, M. J., & Probstein, R. F. 1968, ApJ, 154, 327
Fulle, M., Colangeli, L., Agarwal, J., et al. 2010, A&A, 522, A63

Grun, E., Zook, H. A., Fechtig, H., & Giese, R. H. 1985, Icarus, 62, 244
Hartogh, P., Lis, D. C., Bockelée-Morvan, D., et al. 2011, Nature, 478, 218
Hsieh, H. H., Yang, B., & Haghighipour, N. 2012a, ApJ, 744, 9
Hsieh, H. H., Yang, B., Haghighipour, N., et al. 2012b, AJ, 143, 104
Jewitt, D. 2009, AJ, 137, 4296
Jockers, K. 1997, Earth Moon and Planets, 79, 221
Keller, H. U., Arpigny, C., Barbieri, C., et al. 1986, Nature, 321, 320
Kolokolova, L., Hanner, M. S., Levasseur-Regourd, A.-C., & Gustafson, B. Å. S. 2004, in Comets II, eds. M. C. Festou, H. U. Keller, & H. A. Weaver (University of Arizona Press), 577
Krolikowska, M., Sitarski, G., & Szutowicz, S. 1998, Acta Astron., 48, 91
Lacerda, P. 2013, MNRAS, 428, 1818
Lamy, P. L., Toth, I., Fernandez, Y. R., & Weaver, H. A. 2004, in Comets II, eds. M. C. Festou, H. U. Keller, & H. A. Weaver (University of Arizona Press), 223
Levison, H. F., & Duncan, M. J. 1994, Icarus, 108, 18
Levison, H. F., & Duncan, M. J. 1997, Icarus, 127, 13
Lowry, S. C., & Weissman, P. R. 2003, Icarus, 164, 492
Mazzotta Epifani, E. & Palumbo, P. 2011, A&A, 525, A62
Meech, K. J., & Jewitt, D. C. 1987, A&A, 187, 585
Monet, D. G., Levine, S. E., Canzian, B., et al. 2003, AJ, 125, 984
Moreno, F. 2009, ApJS, 183, 33
Moreno, F., Lara, L. M., Licandro, J., et al. 2011, ApJ, 738, L16
Moreno, F., Pozuelos, F., Aceituno, F., et al. 2012, ApJ, 752, 136
Schwehm, G., & Schulz, R. 1998, in Laboratory astrophysics and space research, eds. P. Ehrenfreund, C. Krafft, H. Kochan, & V. Pirronello, Astrophys. Space Sci. Lib., 236, 537
Scotti, J. V. 1994, in American Astronomical Society Meeting Abstracts, BAAS 26, 1375
Sekanina, Z. 1981, Ann. Rev. Earth Planet. Sci., 9, 113
Soderblom, L. A., Becker, T. L., Bennett, G., et al. 2002, Science, 296, 1087
Sykes, M. V., Grün, E., Reach, W. T., & Jenniskens, P. 2004, in Comets II, eds. M. C. Festou, H. U. Keller, & H. A. Weaver (University of Arizona Press), 677
Tancredi, G., Fernández, J. A., Rickman, H., & Licandro, J. 2006, Icarus, 182, 527

Pages 11 to 13 are available in the electronic edition of the journal at http://www.aanda.org

Appendix A: Orbital parameters of the comets

In Table A.1, we show the orbital elements of the comets used during the dynamical studies in Sect. 5. They are extracted from JPL Horizons online solar system data.

Table A.1. Orbital parameters of the short-period comets under study.

Comet	$e \pm \sigma$	$a \pm \sigma$ (AU)	$i \pm \sigma$ (°)	node (°)	peri (°)	M (°)
22P JPL K154/2	0.54493307 ±9e-8	3.4557183 ±4e-7	4.727895 ±5e-6	120.86178	162.64134	206.26869
30P JPL K103/1	0.5011951 ±2e-7	3.7754076 ±2e-7	8.12265 ±1e-5	119.74115	13.17407	61.00371
78P JPL K114/7	0.46219966 ±9e-8	3.73541262 ±9e-8	6.25491 ±1e-5	210.55664	192.74376	76.36107
115P JPL 16	0.5211645 ±1e-7	4.2597076 ±5e-7	11.687384 ±8e-6	176.50309	120.41045	58.59101
118P JPL 49	0.42817557 ±8e-8	3.4654879 ±2e-7	8.508415 ±5e-6	151.77018	302.17416	143.78902
123P JPL 63	0.4486260 ±1e-7	3.8607445 ±4e-7	15.35692 ±1e-5	46.59827	102.82020	43.33196
157P JPL 28	0.60217 ±1e-5	3.4134 ±1e-4	7.28480 ±7e-5	300.01451	148.84243	174.36079
185P JPL 43	0.6993216 ±1e-7	3.0996991 ±1e-7	14.00701 ±1e-5	214.09101	181.94033	62.38997
Rinner JPL 19	0.39372 ±1e-5	3.79871 ±5e-5	13.77393 ±8e-5	232.01759	221.06138	8.62661

Appendix B: Dust environment of the comets in the sample

In this Appendix, we present the evolution of the dust parameters versus heliocentric distance for each comet in the sample (Figs. B.1 to B.7). These parameters are dust production rate [kg/s], ejection velocities for particles of r = 1 cm glassy carbon spheres [m/s], the maximum size of the particles [cm], and the power index of the size distribution (δ). Solid red lines correspond to pre-perihelion, and dashed blue lines to post-perihelion.

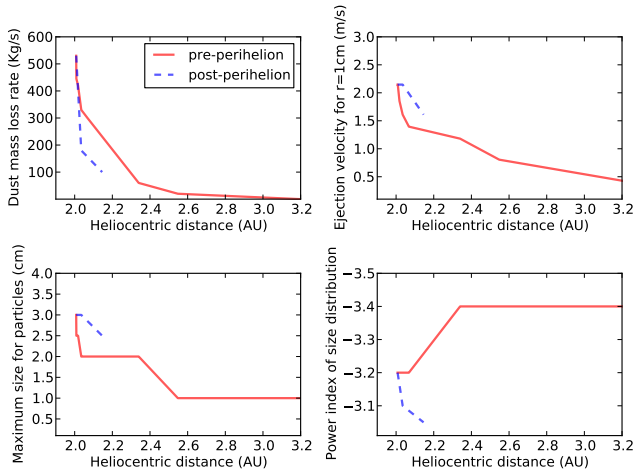

Fig. B.1. As in Fig. 4, but for comet 78P/Gehrels 2.

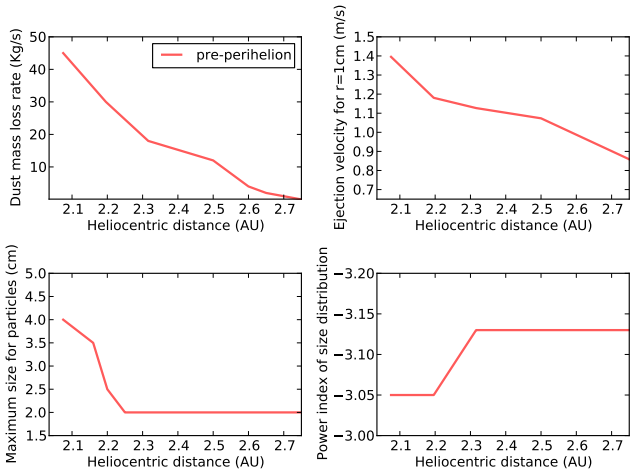

Fig. B.2. As in Fig. 4, but for comet 115P/Maury.

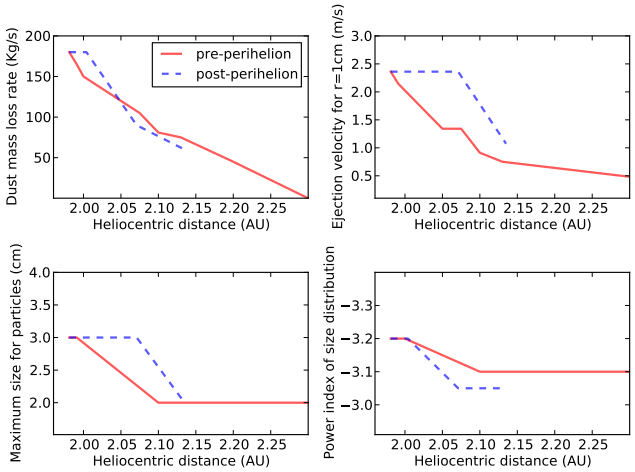

Fig. B.3. As in Fig. 4, but for comet 118P/Shoemaker-Levy 4.

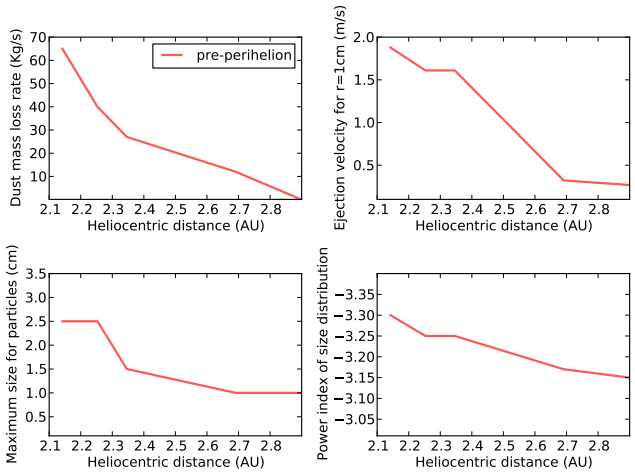

Fig. B.4. As in Fig. 4, but for comet 123P/West-Hartley.

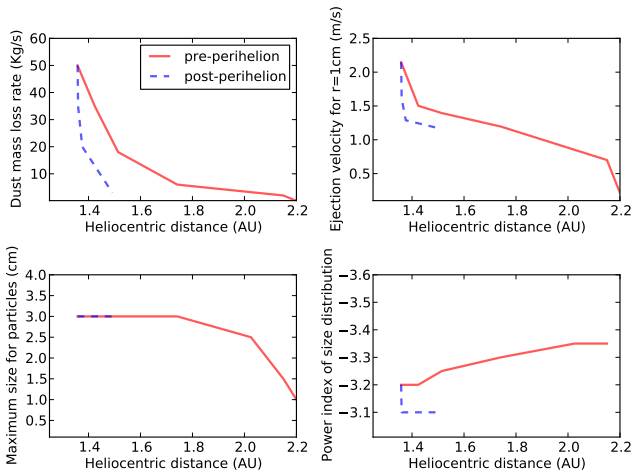

Fig. B.5. As in Fig. 4, but for comet 157P/Tritton.

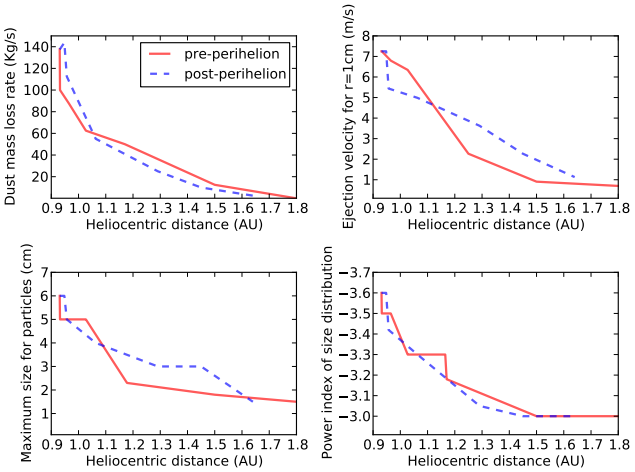

Fig. B.6. As in Fig. 4, but for comet 185P/Petriew.

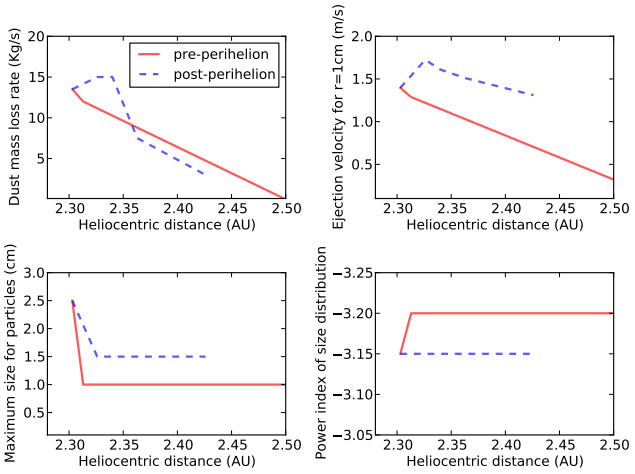

Fig. B.7. As in Fig. 4, but for comet P/2011 W2 (Rinner).

Appendix C: Comparison between observational data and models

In this Appendix (Figs. C.1 to C.7), we show the comparison between the observational data and the models proposed in Sect. 4, which describe the dust environments of the comets of the sample, as in Fig. 5.

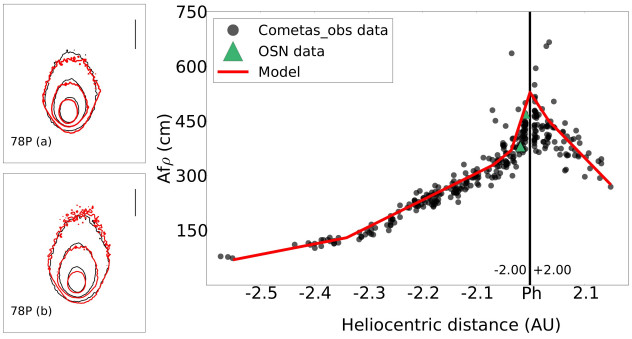

Fig. C.1. As in Fig. 5, but for comet 78P/Gehrels 2. Isophote fields: **a)** December 19, 2011. **b)** January 4, 2012. In both cases the isophote levels are 0.55×10^{-12}, 2.65×10^{-13}, and 1.35×10^{-13} SDU.

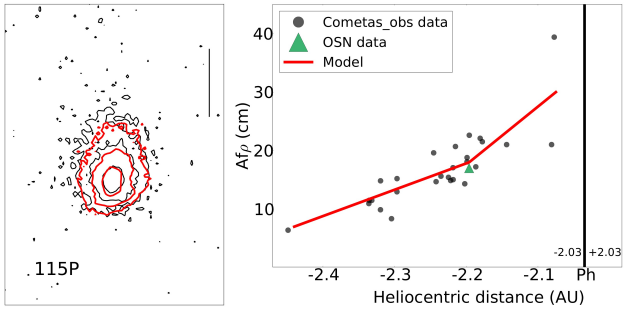

Fig. C.2. As in Fig. 5, but for comet 115P/Maury. Isophote fields: July 15, 2011. Isophote levels are 1.00×10^{-13}, 3.00×10^{-14}, and 1.30×10^{-14} SDU.

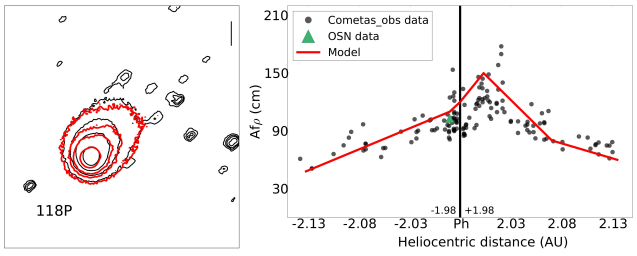

Fig. C.3. As in Fig. 5, but for comet 118P/Shoemaker-Levy 4. Isophote fields: December 12, 2009. Isophote levels are 1.50×10^{-13}, 6.00×10^{-14} 3.50×10^{-14}, and 2.00×10^{-14} SDU.

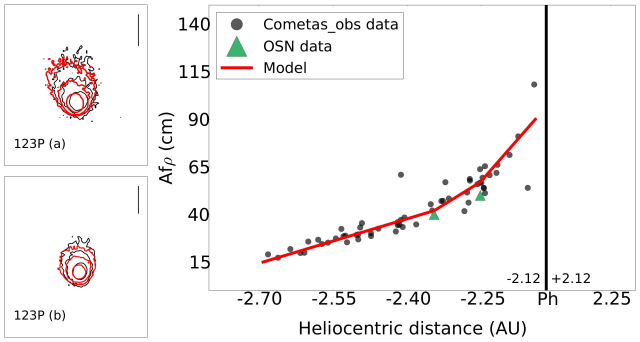

Fig. C.4. As in Fig. 5, but for comet 123P/West-Hartley. Isophote fields: **a)** February 26, 2011. **b)** March 31, 2011. Isophote levels are 1.00×10^{-13}, 0.35×10^{-13}, and 0.15×10^{-13} SDU in **a)** and 1.50×10^{-13}, 0.50×10^{-13}, and 0.25×10^{-13} SDU in **b)**.

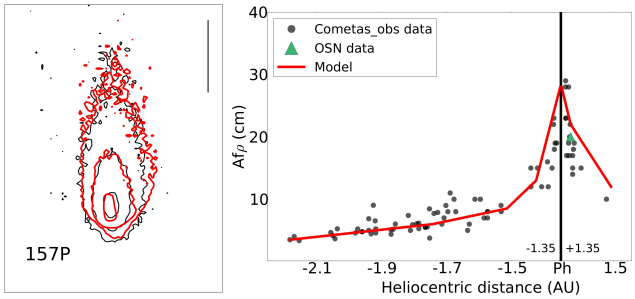

Fig. C.5. As in Fig. 5, but for comet 157P/Tritton. Isophote fields: March 10, 2010. Isophote levels are 6.00×10^{-13}, 0.75×10^{-13}, and 2.65×10^{-14} SDU.

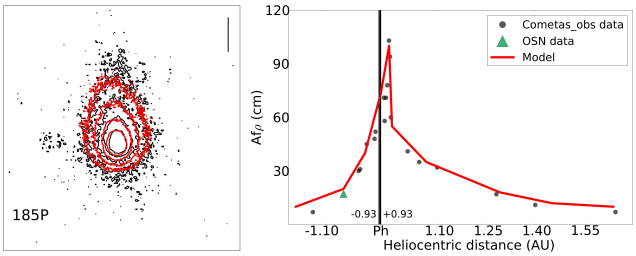

Fig. C.6. As in Fig. 5, but for comet 185P/Petriew. Isophote fields: July 15, 2012. Isophote levels are 1.80×10^{-13}, 1.00×10^{-13} 0.60×10^{-13}, and 0.35×10^{-13} SDU.

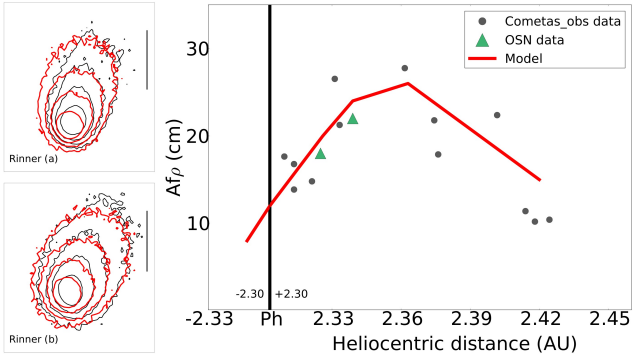

Fig. C.7. As in Fig. 5, but for comet P/2011 W2 (Rinner). Isophote fields: **a)** December 22, 2011. **b)** January 4. In both cases the isophote are 6.00×10^{-14}, 2.70×10^{-14}, 1.50×10^{-14}, and 0.80×10^{-14} SDU.

A&A 571, A64 (2014)
DOI: 10.1051/0004-6361/201424331

Astronomy & Astrophysics

Dust environment and dynamical history of a sample of short-period comets

II. 81P/Wild 2 and 103P/Hartley 2

F. J. Pozuelos[1,3], F. Moreno[1], F. Aceituno[1], V. Casanova[1], A. Sota[1], J. J. López-Moreno[1], J. Castellano[2], E. Reina[2], A. Climent[2], A. Fernández[2], A. San Segundo[2], B. Häusler[2], C. González[2], D. Rodriguez[2], E. Bryssinck[2], E. Cortés[2], F. A. Rodriguez[2], F. Baldris[2], F. García[2], F. Gómez[2], F. Limón[2], F. Tifner[2], G. Muler[2], I. Almendros[2], J. A. de los Reyes[2], J. A. Henríquez[2], J. A. Moreno[2], J. Báez[2], J. Bel[2], J. Camarasa[2], J. Curto[2], J. F. Hernández[2], J. J. González[2], J. J. Martín[2], J. L. Salto[2], J. Lopesino[2], J. M. Bosch[2], J. M. Ruiz[2], J. R. Vidal[2], J. Ruiz[2], J. Sánchez[2], J. Temprano[2], J. M. Aymamí[2], L. Lahuerta[2], L. Montoro[2], M. Campas[2], M. A. García[2], O. Canales[2], R. Benavides[2], R. Dymock[2], R. García[2], R. Ligustri[2], R. Naves[2], S. Lahuerta[2], and S. Pastor[2]

[1] Instituto de Astrofísica de Andalucía (CSIC), Glorieta de la Astronomía s/n, 18008 Granada, Spain
e-mail: pozuelos@iaa.es
[2] Amateur Association Cometas-Obs, Spain
[3] Universidad de Granada-Phd Program in Physics and Mathematics (FisyMat), 18071 Granada, Spain

Received 3 June 2014 / Accepted 5 August 2014

ABSTRACT

Aims. This paper is a continuation of the first paper in this series, where we presented an extended study of the dust environment of a sample of short-period comets and their dynamical history. On this occasion, we focus on comets 81P/Wild 2 and 103P/Hartley 2, which are of special interest as targets of the spacecraft missions Stardust and EPOXI.
Methods. As in the previous study, we used two sets of observational data: a set of images, acquired at Sierra Nevada and Lulin observatories, and the $Af\rho$ data as a function of the heliocentric distance provided by the amateur astronomical association *Cometas-Obs*. The dust environment of comets (dust loss rate, ejection velocities, and size distribution of the particles) was derived from our Monte Carlo dust tail code. To determine their dynamical history we used the numerical integrator Mercury 6.2 to ascertain the time spent by these objects in the Jupiter family Comet region.
Results. From the dust analysis, we conclude that both 81P/Wild 2 and 103P/Hartley 2 are dusty comets, with an annual dust production rate of 2.8×10^9 kg yr^{-1} and $(0.4–1.5) \times 10^9$ kg yr^{-1}, respectively. From the dynamical analysis, we determined their time spent in the Jupiter family Comet region as ∼40 yr in the case of 81P/Wild 2 and ∼1000 yr for comet 103P/Hartley 2. These results imply that 81P/Wild 2 is the youngest and the most active comet of the eleven short-period comets studied so far, which tends to favor the correlation between the time spent in JFCs region and the comet activity previously discussed.

Key words. methods: observational – methods: numerical – comets: individual: 81P/Wild 2 – comets: individual: 103P/Hartley 2 – comets: general

1. Introduction

Cometary science has been revolutionized by in situ missions over the last several decades. It will continue to develop and transform with the arrival of Rosetta Spacecraft at Comet 67P/Churyumov-Gerasimenko. Unfortunately, only a few comets have been studied by spacecraft missions. In this paper we focus on comets 81P/Wild 2 and 103P/Hartley 2. Both comets have been the subject of extensive studies in past years and were the targets of the Stardust and EPOXI missions.

Comet nucleus 81P/Wild 2 (hereafter 81P) has been determined as a triaxial ellipsoid having radii of $(1.65 \times 2.00 \times 2.75) \pm 0.05$ km by Duxbury et al. (2004). The surface shows an ancient terrain composed of cohesive porous materials, probably as a consequence of a mixture of fine dust and volatiles when the comet was formed. It also shows the presence of large-impact craters, implying that the cohesive nature of the surface is old, since it was present before the comet entered the inner part of the solar system (Brownlee et al. 2004). Sekanina (2003) established its current orbit as a consequence of a close encounter with Jupiter in 1974, when its perihelion and aphelion distances decreased from 5.0 to 1.5 AU and from 24.7 to 5.2 AU respectively. Comet 103P/Hartley 2 (hereafter 103P), has a small nucleus with a bilobed shape and a diameter in the range of 0.69 to 2.33 km (A'Hearn et al. 2011). It is considered to be a hyperactive comet, with large-grain production with velocities of several to tens of meters per second (Harmon et al. 2011; Kelley et al. 2013; Boissier et al. 2014). Its orbit period is 6.47 yr, with current perihelion and aphelion distances of $q = 1.05$ AU and $Q = 5.88$ AU.

In this paper we study these comets in the same way as in Pozuelos et al. (2014, hereafter Paper I). Thus, we use our Monte Carlo dust tail code (e.g., Moreno 2009), which allows us to obtain the dust parameters: i.e., dust loss rate, ejection velocities and the size distribution of particles, and the emission pattern. For anisotropic emission, we introduce active area regions, along with the rotational parameters of the nucleus: rotation period and orientation of the spin axis defined by the angles

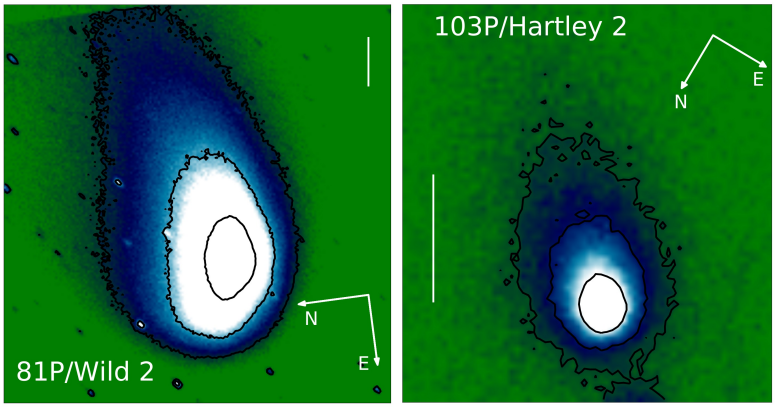

Fig. 1. Representative images of the observations obtained using a CCD camera at 1.52 m telescope at the Observatorio de Sierra Nevada in Granada, Spain. *Right panel* corresponds to 81P/Wild 2 on April 9, 2010. Isophote levels in solar disk units (SDU) are: 0.25×10^{-13}, 0.77×10^{-13}, 2.20×10^{-13}. *Left panel* corresponds with comet 103P/Hartley 2 on August 4, 2010. Isophote levels are: 0.20×10^{-13}, 0.40×10^{-13}, 1.10×10^{-13}. In both cases the directions of celestial north and east are given. The vertical bars correspond to 2×10^4 km in the sky.

I (obliquity) and ϕ (argument of the subsolar meridian at perihelion) (e.g., Sekanina 1981). In the second part of our study we analyze the dynamical history of these comets. To perform this task we use the numerical integrator developed by Chambers (1999), which has been used before by other authors, such as Hsieh et al. (2012a,b) and Lacerda (2013). From this analysis we studied the last 15 Myr of these comets, and we obtained the time spent by them in the region of the Jupiter family Comets (JFCs). Both dust environment and dynamical studies allowed us to determine how active these comets are as a function of the time spent as JFCs. We based our studies on two different kinds of observational data: direct imaging in Johnson R filter from ground-based telescopes, most of them obtained at the 1.52-m Sierra Nevada Observatory (Spain), and some of them at the 1-m telescope of Lulin Observatory (Taiwan) (Lin et al. 2012). The second block of observational data corresponds to $Af\rho$ measurements provided by the amateur astronomical association *Cometas-Obs*. These observations almost completely cover the orbital path when the comets are active.

The observations and the data reduction are explained in Sect. 2; the model is described in Sect. 3 ; the dust analysis, and comparison with others currently available are given in Sect. 4; the dynamical study appears in Sect. 5; and finally the summary and conclusions are given in Sect. 6.

2. Observations and data reduction

Most of the images of 81P and 103P were taken at the 1.52 m telescope at the Sierra Nevada Observatory (OSN) in Granada, Spain. We used a 1024 × 1024 pixel CCD camera with a R Johnson filter. For comet 81P, we also used observations acquired at the 1 m telescope at Lulin Observatory in Taiwan, using a 1340×1300 pixel CCD with an Ashi R broadband filter. Table 1 shows the log of the observations. Additional details for the observations at Lulin Observatory are given in Lin et al. (2012) and the references therein. Several images of the comets were taken in order to improve the signal-to-noise ratio. A median stack was obtained from available images. The individual images from each night were bias-subtracted and flat-fielded using standard techniques. To perform the flux calibration, we used the USNO-B1.0 star catalog (Monet et al. 2003), so that each image we acquired was calibrated to mag arcsec^{-2} and then converted to solar disk units (SDU). We rotated each image to the (N, M) system (Finson & Probstein 1968), where M is the projected Sun-comet radius vector, and N is perpendicular to M in the opposite half plane with respect to the nucleus velocity vector. The images were finally rebinned so that the physical dimensions were small enough to be analyzed with our Monte Carlo dust tail code. Representative reduced images of 81P and 103P are displayed in Fig. 1.

The second block of our observational data are the $Af\rho$ (A'Hearn et al. 1984) measurements carried out by the amateur astronomical association *Cometas-Obs*[1]. These observations cover most of the orbital arc where the comets are active. They are given as a function of the heliocentric distance and are always referred to as an aperture of $\rho = 10^4$ km projected on the sky at each observation date. The calibration was made using the star catalogs CMC-14 and USNO A2.0. To make a direct comparison, we computed the $Af\rho$ with $\rho = 10^4$ km from the OSN and Lulin image observations (see Table 1).

It is important to note that some of the observational data correspond to times where the phase angle is close to zero degree. We corrected for the backscattering enhancement (Kolokolova et al. 2004) by the expression:

$$Af\rho\prime = 10^{\frac{-\beta(30-\alpha)}{2.5}} \times Af\rho, \quad (1)$$

where β is the linear phase coefficient, for which we assumed $\beta = 0.03$ mag deg^{-1}, based on the studies by Meech & Jewitt (1987) for several comets. The correction is applied when $\alpha \leq 30°$. More details are given in Sect. 3 of Paper I. This backscattering effect becomes especially important for comet 81P. In Fig. 2 we observe a clear increase in $Af\rho$ for small phase angles and see how these data are corrected after application of Eq. (1). Despite this clear correlation between $Af\rho$ and α, there are authors who attributed this enhancement to an outburst experienced by the comet after perihelion passage. We discuss this in Sect. 4.

3. Monte Carlo dust tail model

As in Paper I, to fit the observational data described in the previous section, we used our Monte Carlo dust tail code (see e.g., Moreno 2009). This code allowed us to generate synthetic images that can be directly compared with the observations, from which we can derive the synthetic $Af\rho$ curves.

[1] See http://www.astrosurf.com/cometas-obs/

Table 1. Log of the observations.

Comet	Observation date	r_h [1] (AU)	Δ (AU)	Resolution (km pixel^{-1})	Phase angle (°)	Position angle (°)	$Af\rho$ ($\rho = 10^4$ km) [2] (cm)	Telescope
81P/Wild 2	(a) 2010 Jan. 16.81	−1.639	1.080	808.4	35.4	292.6	566 ± 113	Lulin
	(b) 2010 Apr. 9.06	1.660	0.674	899.5	10.1	262.3	351 ± 70	OSN
	(c) 2010 Apr. 21.06	1.695	0.694	926.2	4.7	208.7	272 ± 54	OSN
	(d) 2010 May 15.96	1.789	0.822	1097.2	14.0	125.2	236 ± 47	OSN
	(e) 2010 Jun. 3.93	1.875	0.992	1323.9	21.0	116.7	258 ± 51	OSN
	(f) 2010 Jul. 6.89	2.046	1.404	1873.7	26.8	110.3	139 ± 27	OSN
	(g) 2010 Aug. 21.85	2.302	2.119	2827.9	25.9	103.7	148 ± 29	OSN
103P/Hartley 2	(a) 2010 Jul. 12.14	−1.744	0.916	641.2	29.0	228.5	9 ± 1	OSN
	(b) 2010 Aug. 4.11	−1.541	0.666	444.4	29.4	210.7	16 ± 3	OSN
	(c) 2010 Sept. 6.04	−1.274	0.352	469.7	35.4	179.6	24 ± 4	OSN
	(d) 2010 Nov. 3.16	1.061	0.150	400.3	58.7	282.4	65 ± 13	OSN

Notes. [1] Negative values correspond to pre-perihelion, positive values to post-perihelion dates. [2] The $Af\rho$ values for phase angle ≤30° have been corrected according to the Eq. (2) (see text).

This code was successfully used in previous works to determine the dust properties of some short-period comets such as 29P/Schwassmann-Wachmann 1 and 22P/Kopff (Moreno 2009; Moreno et al. 2012), as well as some Main-belt comets: P/2010 R2 (La Sagra), P/2012 T1 (PANSTARRS), and P/2013 P5 (PANSTARRS; Moreno et al. 2011, 2013, 2014). This code is also called the Granada model in Fulle et al. (2010) where the authors describe the dust environment of the Rosetta target 67P/Churyumov-Gerasimenko. The model computes the trajectory of a large number of particles when they are ejected from the nucleus surface and are submitted to the solar gravity and radiation pressure force, describing a Keplerian orbit around the Sun. Considered to be spherically shaped, the particles are characterized by the β parameter, which is the ratio of the radiation pressure force to the gravity force. For those particles $\beta = C_{\rm pr}Q_{\rm pr}/(\rho_{\rm d}d)$, where $C_{\rm pr} = 1.19 \times 10^{-3}$ kg m^{-2}, $Q_{\rm pr}$ is the radiation pressure coefficient, ρ the particle density, assumed as $\rho = 1000$ kg m^{-3}, and d the particle diameter.

To compute the geometric albedo p_v and $Q_{\rm pr}$, we used the Mie theory to describe the interaction of the electromagnetic field with spherical particles, assuming a refractive index of $m = 1.88 + 0.71i$ that is typical of carbonaceous spheres at red wavelengths (Edoh 1983). This gives $p_v = 0.04$ for $r \geq 1$ μm at most of the phase angles, and $Q_{\rm pr} \sim 1$ (Burns et al. 1979).

In the model, the trajectories and positions of the particles in the N, M plane and their contribution to the tail brightness are computed. The free parameters dust loss rate, ejection velocities, size distribution of the particles, and the dust ejection pattern, which can be either isotropic or anisotropic. In cases where an anisotropic outgassing is obtained, the emission is parametrized by a rotating nucleus with active areas on the surface. The rotation state is parametrized by two angles: the obliquity I of the orbit plane to the equator and the argument ϕ of the subsolar meridian at perihelion (Sekanina 1981). The size distribution of the particles is defined by the maximum and minimum sizes $r_{\rm max}$, $r_{\rm min}$, and the index δ of the power law function $n(r) \propto r^{\delta}$, which describes the size distribution. For simplicity $r_{\rm min}$ has been set to 1 μm in all calculations. For large sets of comets, δ has been concluded to be in the range of −4.2 and −3.0 (e.g., Jockers 1997). The terminal velocity is parametrized as $v(t,\beta) = v_1(t) \times \beta^{\gamma}$ where $v_1(t)$ is determined during the modeling process, and the index γ is a constant assumed as $\gamma = 1/2$, which is the value commonly accepted for hydrodynamical drag from sublimating ices (e.g., Moreno et al. 2011; Licandro et al. 2013). Owing to the large number of parameters that are used in the model, the solution is not unique and it is possible to find an alternative set of parameters to fit the observational data. However, the range of possible solutions is considerably reduced when the available observations cover most of the orbital arc of the comets. For this reason, we combined direct imaging observations and a large number of $Af\rho$ measurements given by different observers in different locations, such as those provided by the association *Cometas-Obs*.

4. Dust analysis

In Paper I, we determined three categories according to the amount of dust emitted: (i) weakly active: 115P, 157P and Rinner with an annual production rate of $T_{\rm d} \leq 1 \times 10^8$ kg yr^{-1}; (ii) moderately active: 30P, 123P, and 185P where the annual production rate is $T_{\rm d} = 1 - 3 \times 10^8$ kg yr^{-1}; and (iii) highly active: 78P, 22P, and 118P with an annual production rate of $T_{\rm d} \geq 8 \times 10^8$ kg yr^{-1}. For three of those targets, an anisotropic ejection pattern was obtained: 30P, 115P, and 157P. The general method used to fit the observations and obtain the dust parameters is a trial-and-error procedure, starting with the simplest scenario, where we consider an isotropic ejection outgassing model, with $r_{\rm min} = 1$ μm, $r_{\rm max} = 1$ cm, $\delta = -3.5$, and both $v_1(t)$ and dM/dt monotonically symmetric evolution with respect to perihelion. Once we reproduced the tail intensity in the optocenter, we started to vary the parameters and their dependence on the heliocentric distance to obtain the best possible fit. When the observations cannot be reproduced by isotropic emission, we set active areas on the surfaces, i.e., an anisotropic emission pattern, and repeat different combinations of the dust parameters until an acceptable result is obtained.

4.1. 81P/Wild 2

The comet 81P has an effective nucleus of $R_{\rm N} = 2.00$ km (Sekanina et al. 2004) and a bulk density of $\rho = 600$ kg m^{-3} reported by Davidsson & Gutierrez (2004). Our observational data for comet 81P are six direct images post-perihelion passage at OSN 1.52 m telescope and ∼300 $Af\rho$ measurements by *Cometas-Obs*, which cover from ∼−2.15 to ∼2.45 AU. In addition, we benefited from observations carried out in the 1 m Lulin telescope by Z.-Y. Lin. From these observations we selected one pre-perihelion image (January 16.81, 2010) and

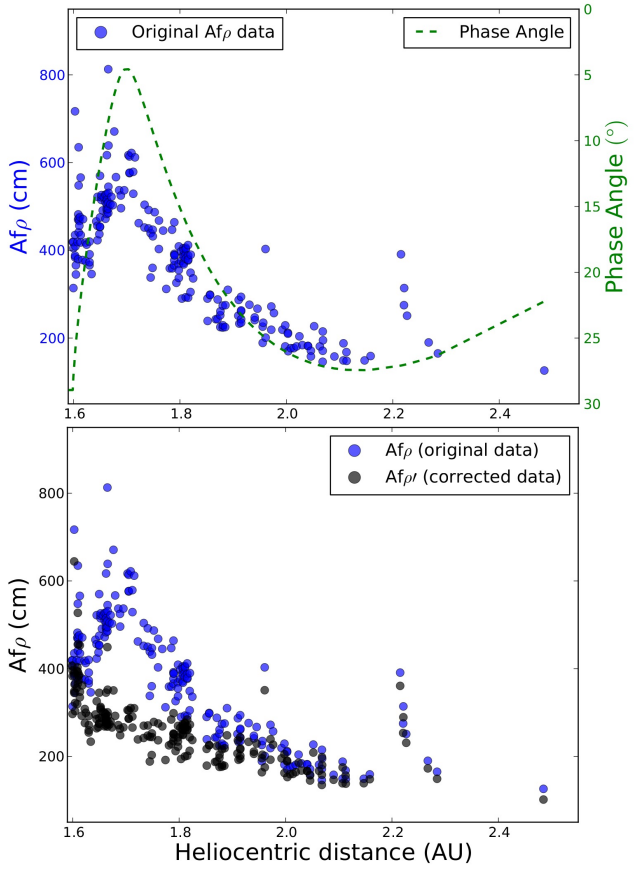

Fig. 2. 81P/Wild 2 $Af\rho$ measurements by *Cometas-Obs*. *Upper panel*: original data and phase angle as a function of heliocentric distance. *Lower panel*: original $Af\rho$ data and corrected $Af\rho$ data by Eq. (1) (see text).

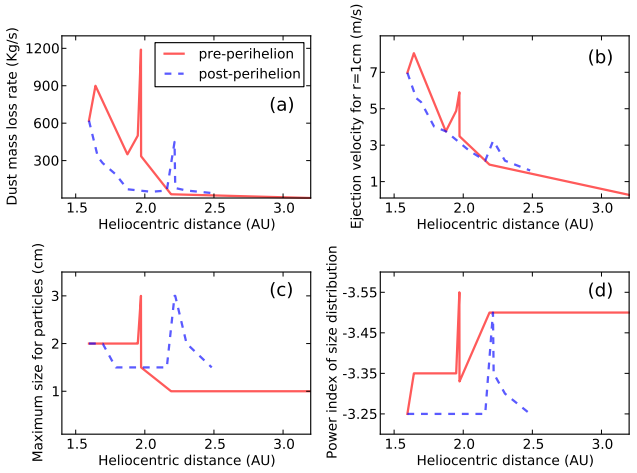

Fig. 3. Best-fit modeled parameters to the dust environment of 81P/Wild 2 $Af\rho$ data and images (Figs. 4 and 5). All parameters are given as a function of the heliocentric distance. From *top to bottom* and *left to right* the panels are **a)** dust production rate [kg s^{-1}]; **b)** ejection velocities of 1-cm particles [m s^{-1}]; **c)** maximum size of particles [cm]; **d)** power index of the size distribution, δ. The solid red line corresponds to pre-perihelion and the dashed blue line to post-perihelion.

5 $Af\rho$ measurements pre- and post-perihelion (see Table 1). The complete set of $Af\rho$ data as a function of the heliocentric distance is shown in Fig. 4, where all the data have been corrected from backscattering enhancement using Eq. (1).

We observed two enhancements in the measurements that were not related to low α values. We considered them as small outbursts suffered by the comet. The first one occurred on October 29 (2009), when the comet was at $r_h \sim 1.949$ AU inbound, where the maximum value of $Af\rho$ was ~782 cm. To our knowledge, this outburst has not been reported previously. In our dust characterization we concluded that the event duration was ~40 h, and the comet emitted $m_{ob.I} \sim 9.2 \times 10^8$ kg of dust, reaching a peak dust production rate of 1190 kg s^{-1}, returning to normal activity on November 13. However we only have a limited number of sample observations for this period, so this result must be read with caution. The second outburst was first identified by Bertini et al. (2012). This second event took place post-perihelion, August 5 (2010), at ~2.215 AU outbound, with a maximum value of $Af\rho \sim 380$ cm. Our dust analysis estimated this event as three times less intense than the first one, $m_{ob.II} \sim 3.0 \times 10^8$ kg with a duration of ~55 h and a peak dust production rate of 450 kg s^{-1}. During both outbursts, I and II, the maximum particle size was 3 cm.

Overall, without taking the outburst events into account, we concluded that the comet reached its maximum level of activity at $r_h \sim 1.64$ AU inbound, that is ~40 days before perihelion, with a dust production rate of 900 kg s^{-1}. The comet emission pattern is found to be anisotropic at 35%, with active areas located on the surface between +45° to −30°. From the anisotropic model we derived the rotational angles as $I = (50 \pm 5)°$ and $\phi = (300 \pm 20)°$. Figure 3 we display the evolution of the dust parameters as a function of heliocentric distance, and in Figs. 4 and 5 we present the comparison of the model with the observational data, which are remarkably similar. From the dust analysis, we determined that the total dust production rate of 81P was 1.1×10^{10} kg during the 3.8 yr covered by the study, that is, an annual dust production rate of $T_d = 2.8 \times 10^9$ kg yr^{-1} and an average dust mass lost rate of 87.5 kg s^{-1}. The contribution to the annual interplanetary dust replacement, established by Grun et al. (1985) as 2.9×10^{11} kg yr^{-1}, is ~0.96%.

4.2. 103P/Hartley 2

The observational data of comet 103P consist of four direct images obtained at the 1.52 m OSN telescope, three pre-perihelion and one post-perihelion (see Table 1), and ~430 $Af\rho$ measurements carried out by *Cometas-Obs*, covering pre- and post-perihelion branches in the orbit, from ~−2.00 to ~2.60 AU. The observations have been corrected by Eq. (1) for the data having $\alpha \leq 30°$ as in the case of 81P, but in this case there is not a strong dependence between α and any enhancements in the measurements. This comet has been subjected to an extensive study as a consequence of its encounter with the Deep Impact spacecraft in the framework of the EPOXI mission (see e.g., A'Hearn et al. 2011; Meech et al. 2011). For most of those studies it was considered as a hyperactive comet with an emission of large particles (see e.g., Harmon et al. 2011; Kelley et al. 2013; Boissier et al. 2014).The mean radius (radius of a sphere of equivalent volume) is calculated by Thomas et al. (2013b) as 0.580 ± 0.018 km, but the bulk density is not determined well, since it is in the range of $\rho = 140$–520 kg m^{-3} (A'Hearn et al. 2011; Richardson & Bowling 2014; Thomas et al. 2013b). Consequently, the escape velocity of particles is in the range of $v_{esc} = 3.6$–6.9 cm s^{-1}.

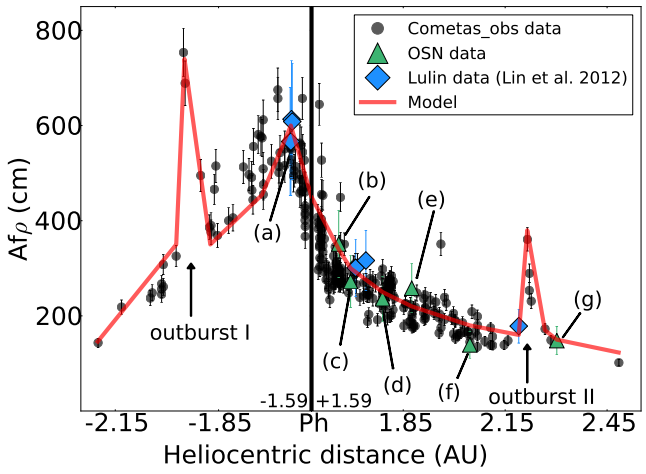

Fig. 4. Comparison of observed and modeled $Af\rho$ data as a function of heliocentric distance. Parameter $Af\rho$ versus heliocentric distance. The $Af\rho$ measurements have been corrected using Eq. (1). Black dots: $Af\rho$ data from *Cometas-Obs*. Green triangles: $Af\rho$ data derived from OSN images. Blue diamonds: $Af\rho$ data from Lulin observatory images. The observations labeled (a) to (g) correspond to the $Af\rho$ derived from images (a) to (g) in Fig. 5. The outbursts I (inbound) and II (outbound) described in the text are marked with arrows. All the $Af\rho$ values refer to $\rho = 10^4$ km.

Thus, for our purposes, we assume the maximum value of the bulk density as $\rho = 520$ kg m^{-3}, which corresponds to the upper limit of escape velocity. To perform the dust characterization we introduce two models, which agree with the observations. The first one is based on previous knowledge, i.e., large particle emission and high dust production rate (hyperactivity).The second one tries to reproduce the observations without the emission of large particles and with moderate dust production rate.

Model I or *hyperactive model*. In this case we consider the results derived from the EPOXI mission and other authors, such as Harmon et al. (2011), where a large size of particles were obtained, with sizes in the range of ∼20 cm and larger. To try to reproduce these results, we fixed the maximum size of particles to $r = 20$ cm around perihelion, where the comet reaches its maximum dust production rate. This model has a gentle increase in the dust parameters toward perihelion, where a strong increase occurs, peaking at ∼1.20 AU post-perihelion. This behavior is also seen in the $Af\rho$ measurements (Fig. 8). The maximum dust production rate is found to be 600 kg s^{-1}, and the ejection velocity of 1-cm size particles reaches ∼14 m s^{-1}. The total dust mass ejected during the 3.79 yr span in this study is 5.9×10^9 kg, so the annual dust production rate is $T_d = 1.5 \times 10^9$ kg yr^{-1}. This model represents an annual contribution of 0.51% to interplanetary dust. Figure 6 we show the evolution of the dust parameters as a function of the heliocentric distance, and in Figs. 8 and 9 we show the comparison between the available observations and the model.

Model II or *standard model*. In this case, the maximum particle size was not forced to 20 cm, but is a free parameter that can have any possible value. It reaches 3 cm at perihelion. As in *Model I* the peak of the dust parameter occurs after perihelion at ∼1.20 AU, where the dust production rate is 160 kg s^{-1}, and the ejection velocity for 1 cm particles is ∼7 m s^{-1}. In this case the total dust emitted by the comet was 1.7×10^9 kg, and the annual dust production rate was $T_d = 4.5 \times 10^8$ kg yr^{-1}. The contribution to the interplanetary dust per year represents 0.15% of the total. The evolution along the heliocentric distance of the dust parameters is displayed in Fig. 7, and the comparison of the observations to the model are shown in Figs. 8 and 10.

In both cases, *Models I* and *II*, the emissions have been found to be isotropic.

4.3. Discussion

The dust characterization of 81P shows the peak of activity around ∼40 days pre-perihelion. In previous studies of this comet during the perihelion passages in 1990, 1997, and 2004, the comet showed the peak of activity a few weeks pre-perihelion due to a seasonal effect. Sekanina (2003) studied this behavior when the comet activity reached its maximum value three weeks before perihelion with a post-perihelion fading. To explain this behavior, the author proposed that the spin axis is not quite normal to the orbital plane. In addition, Farnham & Schleicher (2005) attribute this conduct to a strong seasonal effect with at least one source region moving from summer to winter speedily. Analogous results of this behavior have also been obtained in independent studies by other authors (e.g., Hanner & Hayward 2003; Hadamcik & Levasseur-Regourd 2009).

In the analysis carried out by Bertini et al. (2012), the authors identified an enhancement of $Af\rho$ measurements ∼60 days post-perihelion. The authors also noticed that during that period there was a minimum phase angle, and they corrected the effect by reducing all $A(\alpha)f\rho$ values to $\alpha = 0°$, and using $A(0)f\rho$ as reference. After the authors applied the correction, the enhancement on $Af\rho$ measurements was still evident, which led them to consider it as an outburst event. In our case, *Cometas-Obs* also reported this enhancement in the $Af\rho$ measurements, but in contrast to Bertini et al. (2012), the enhancement completely disappeared after correction (using Eq. (1), see Fig. 2), so we concluded that the comet started to fade after the pre-perihelion peak.

During the Stardust flyby on 2 January 2004 (at $r_h = 1.855$ AU post-perihelion), Green et al. (2004) used the Dust Flux Monitor Instrument (DFMI) to obtain a cumulative mass distribution index ξ (where the number of particles of mass m or larger is given by the power law $N(m) \propto m^{-\xi}$) in the coma ranges from 0.3 to 1.1, where $\xi = 0.75 \pm 0.05$ was found to be the best fit for the data. From this cumulative mass distribution index we can conclude that the power index of the differential size distribution is $\delta = -3\xi - 1$. Thus, δ is in the range of −1.9 to −4.3, with the best match to the data being $\delta = -3.25 \pm 1.25$. This value perfectly agrees with the one derived from our model at the same heliocentric distance.

The rotational parameters derived from the model agree with the ones proposed by Sekanina et al. (2004), who concluded that $I = 55°$ and $\phi = 150°$. The equivalent solution for ϕ is $180° + \phi = 330$, Sekanina (1981), which is close of our value. Belton et al. (2013a) established a relationship between mini-outbursts suffered by the comet 9P/Temple 1 and pits (large population of quasi-circular depression) on the surface of the comet, reported by the encounter of Stardust-NExT spacecraft and Deep Impact mission (see e.g., Veverka et al. 2013; A'Hearn et al. 2005; Thomas et al. 2013a). The authors argue that ∼96% of these features were due to mini-outbursts, while ∼4% had their origin in other processes, such as collisions with asteroidal material and cryo-volcanism. From this relationship, the authors propose that the pits observed on the surface of 81P are also due to outburst events. In our model, we have identified two outbursts, one inbound and the other outbound, both more intense than the mini-outbursts studied by Belton et al. (2013a), which were in the range of $6-30 \times 10^4$ kg. However, Brownlee et al. (2004),

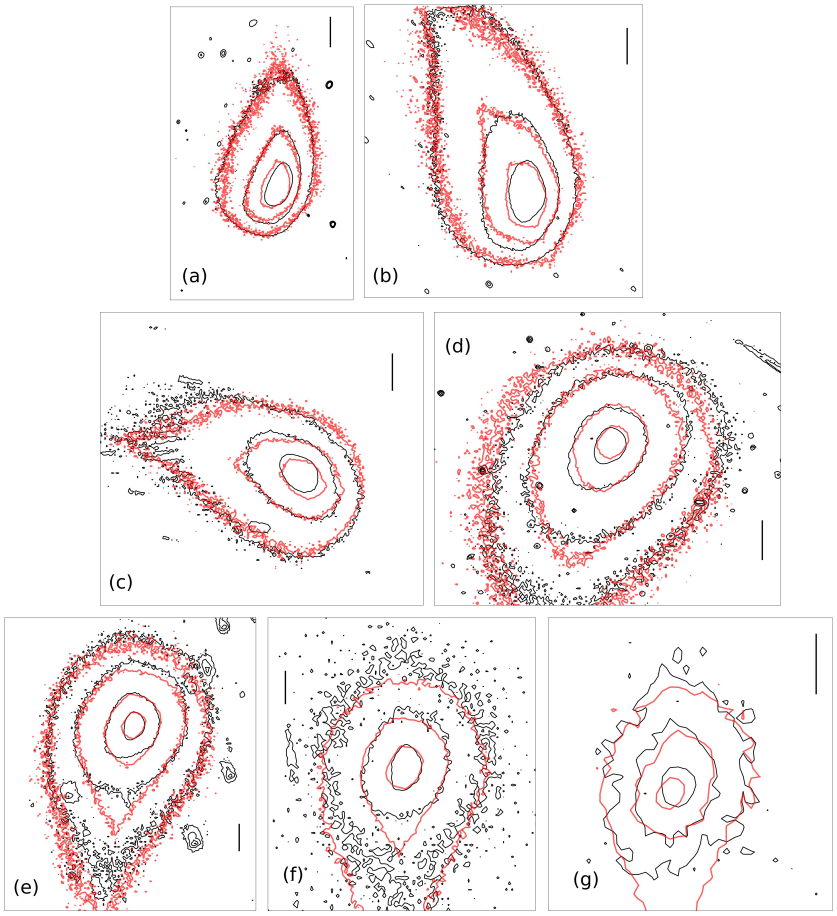

Fig. 5. Isophote field comparison between observations and model. The black contours correspond to the observations and the red ones to the model. The dates and the SDU levels are **a)** Jan. 16.81, 2010. Levels are 0.80×10^{-13}, 2.00×10^{-13}, and 5.00×10^{-13} SDU; **b)** Apr. 9.06, 2010. Levels are 0.25×10^{-13}, 0.77×10^{-13}, and 2.20×10^{-13} SDU; **c)** Apr. 21.06, 2010. Levels are 0.25×10^{-13}, 0.77×10^{-13}, and 2.20×10^{-13} SDU; **d)** May 15.96, 2010. Levels are 0.10×10^{-13}, 0.25×10^{-13}, 0.77×10^{-13}, and 2.20×10^{-13} SDU; **e)** Jun. 3.93, 2010. Levels are 0.10×10^{-13}, 0.25×10^{-13}, 0.77×10^{-13}, and 2.20×10^{-13} SDU; **f)** Jul. 6.89, 2010. Levels are 0.08×10^{-13}, 0.25×10^{-13}, and 0.77×10^{-13} SDU; **g)** Aug. 21.85, 2010. Levels are 0.25×10^{-13}, 0.77×10^{-13}, and 2.20×10^{-13} SDU. See log of the observations in Table 1.

Kirk et al. (2005) and Basilevsky & Keller (2006, 2007) considered the origin of pits in the context of impact phenomena. Therefore, the relationship between outbursts and pits are not clear in the case of 81P, and more studies would be desirable to determine how often the outbursts occur in this comet, and if they are the cause of pits on the surface.

The comet 81P has been found to be the most active one in the whole sample of short-period comets studied in Paper I and in this paper, with an annual dust production rate of $T_d = 2.8 \times 10^9$ kg yr^{-1}.

Our study of the 103P offers two solutions to fitting the observation: *Model I*, where the comet is found to be hyperactive, and *Model II* where we proposed a standard dust behavior. In *Model I* we imposed large size particles (up to $r_{max} = 20$ cm) and we concluded that the annual dust production rate is $T_d = 1.5 \times 10^9$ kg yr^{-1}, with a dust production rate of 300−550 kg s^{-1} during perihelion and Deep Impact spacecraft closet approach. In contrast, in *Model II* our solution also agrees with the observations but with a maximum particle size of $r_{max} = 3$ cm, where the annual dust production rate is $T_d = 4.5 \times 10^8$ kg yr^{-1}. During the perihelion and Deep Impact encounter, the dust mass loss rate was in the range of 120−140 kg s^{-1}. Thus, the range of the dust production rate obtained by our study is 120−550 kg s^{-1} during perihelion passage and spacecraft encounter. Harmon et al. (2011) established a value of 300 kg s^{-1} roughly in the same period, while Boissier et al. (2014) inferred a much wider range of 830−2700 kg s^{-1} based on their two models under various assumptions, such as the dust composition, size distribution,

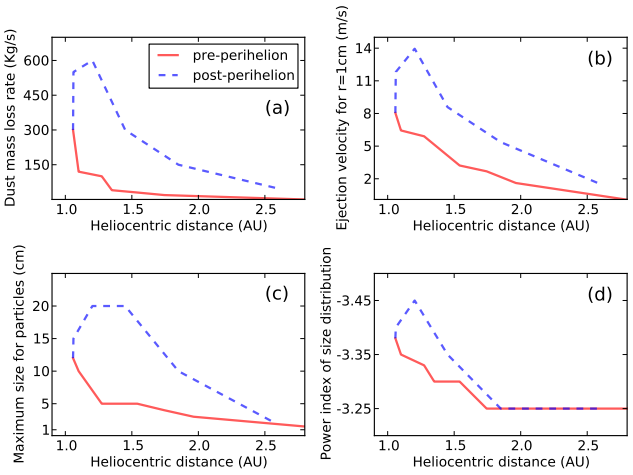

Fig. 6. As Fig. 3 but for comet 103P/Hartley 2. Corresponding to *Model I*. This model fits the observations displayed in Figs. 9 and 8, where it is represented by the red line.

and grain velocities. The authors attributed the uncertainty of their values to the uncertainties in the size distribution cut-off and kinematics. The total dust emitted by 103P for the whole orbit during 2010 perihelion passage, has been found to be in the range of 1−4 × 10^9 kg in previous studies (see e.g.,

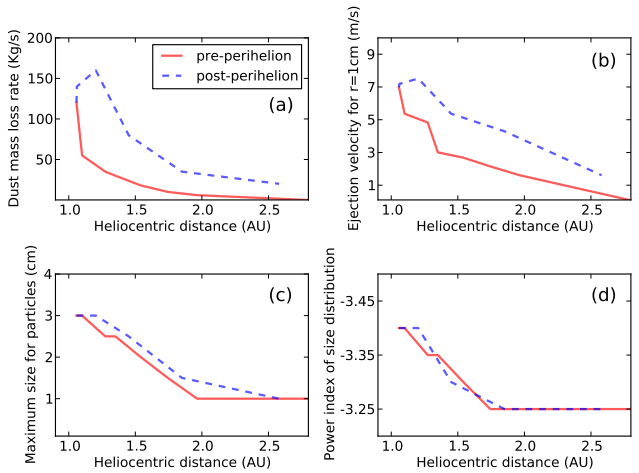

Fig. 7. As in Fig. 3 but for comet 103P/Hartley 2. Corresponding to *Model II*. This model fits the observations displayed in Figs. 10 and 8 where it is represented by the blue line.

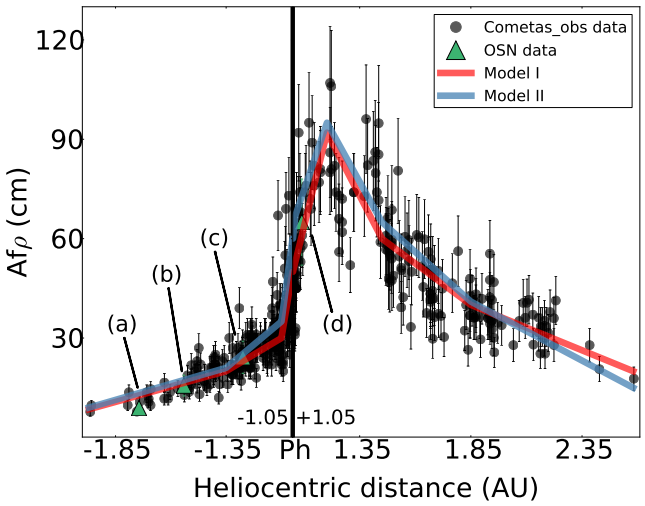

Fig. 8. Comparison between observational data and the models proposed for the comet 103P/Hartley 2. $Af\rho$ measurements have been corrected using Eq. (1). Black dots are the data from *Cometas-Obs*, and green triangles marked from (a) to (d) are the observations at OSN telescope. The red line corresponds to *Model I* or *Hyperactive model*, which fits the observations in Fig. 9. The blue line is the *Model II* or *Standard model*, and its fits with observations can be checked in Fig. 10. All the $Af\rho$ values are referred to $\rho = 10^4$ km.

Lisse et al. 2009; Bauer et al. 2011; Thomas et al. 2013b; Knight & Schleicher 2013). These values agree with the range of $1.7-5.9 \times 10^9$ kg derived from our models, which cover most of the time in which the comet is active.

The very complex rotational state of the nucleus was studied in detail in Belton et al. (2013b). In Belton (2013) the authors described the active areas migration over the lobes of the nucleus following the Sun; thus, the strong activity shown by this comet is correlated with the rotation of the nucleus. Two faint dust jets seem to have had their origin in those active areas (see e.g., Lara et al. 2011; Mueller et al. 2013; Tozzi et al. 2013). Thanks to this correlation between active areas and rotation of the nucleus, the comet has an isotropic pattern of time-averaged outgassing from its nuclear surface. This fact led Groussin et al. (2004), Lisse et al. (2009), and Knight & Schleicher (2013) to report the comet as a highly active nucleus with ∼100% of the surface area active. These results agree with the isotropic dust emission pattern derived from our *Models I* and *II*.

Another important point is the nature of the large chunks, observed during the EPOXI flyby and inferred from radar observations (see e.g., A'Hearn et al. 2011; Harmon et al. 2011), and the real size of them. Knight & Schleicher (2013) deduced that those chunks are large dust grains (up to 20 cm) because of the lack of interaction between the radiation pressure and the dust jets observed. However, Kelley et al. (2013) propose two models: (1) the icy case, where the particles have an albedo of 0.67, ρ = 0.1 g cm^{-3}, and the size of particles are in the range of 1−20 cm; (2) the dusty case, with an albedo of 0.049, ρ = 0.3 g cm^{-3}, and the particle sizes in the range of 10−210 cm. The authors concluded that the icy model is more likely. However, these models may not reflect the true nature of the particles, although they did produce useful information on the limits of particle size and the fact that a coma of both icy and dusty particles is possible.

To explain the relatively short life times of those large chunks, Tozzi et al. (2013) established that they need to have some impurities such as silicates embedded in them, and inferred the presence of grains which might have lot of organics. Finally, Boissier et al. (2014) present two models based on crystalline/amorphous (of ratio of 1) silicate particles with a grain density of ρ = 0.5 g cm^{-3}, where the maximum size of the particles was obtained depending on the escaping gas: (1) $a_{\max}$ = 1 m, to H_2O; (2) $a_{\max}$ = 2.4 m, to CO_2. Therefore, the true nature and the size of the large chunks observed are not completely accurate and are still under study. The presence of the large particles in the coma of this comet was already inferred in Epifani et al. (2001) during the observations of 1 January 1998 using the ISOCAM. The authors deduced that the dust production rate at perihelion ranged from 10 kg s^{-1} to 100 kg s^{-1}. The peak of the dust production rate and the ejection velocities of the particles occurred two weeks after perihelion, with a rapid decrease just before it. However, the authors attributed this behavior to the instability of the model outputs around perihelion, showing unrealistically large variations in the power index of the size distribution. The best fitting power law was found to be $\delta = -3.2 \pm 0.1$ by the authors. In the 2010 perihelion passage, the power index of the size distribution derived from our models take values from −3.45 to −3.25, which are bit higher than the values assumed/derived by other authors, such as Bauer et al. (2011) of −4.0, Kelley et al. (2013) in the range of −6.6 to −4.7, and Boissier et al. (2014) of −3.5.

It is important to note that in general, when the power index is $-3 < \delta < -4$, the dust mass depends on the largest particles, while the brightness in the tail depends on the smallest grains, so that it is always difficult to determine the large particle population in the tail (Fulle 2004). For this reason, the mass found in the models should be considered as lower limits of the total dust emitted (see Paper I). In the case of 103P, *Model I* is closer to a real solution than *Model II*, which represents a lower limit in the dust production.

As a result of the particle velocities obtained in Paper I, the characterization of 22P/Kopff in Moreno et al. (2012), the result presented by Fulle et al. (2010) to comet 67P/Churyumov-Gerasimenko, and this study, we found a definite relationship between the ejection velocities and the heliocentric distance. For example, for r = 1 cm particles, we found a power law given by $v = A \times r_h^{-B}$, where A and B parameters were given

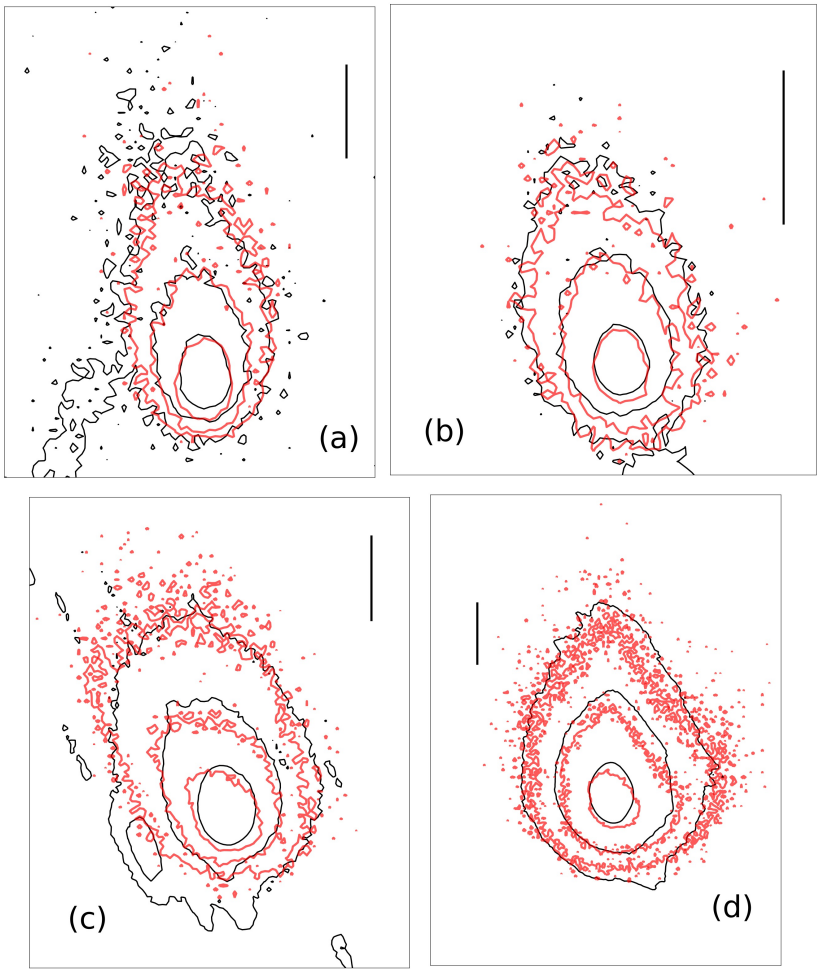

Fig. 9. Isophote field comparison between observations and *Model I* or *Hyperactive model*. The black contours correspond to the observations and the red ones to the model. The dates and the SDU levels are **a)** Jul. 12.14, 2010. Levels are 0.30×10^{-14}, 0.55×10^{-14}, and 1.20×10^{-14} SDU; **b)** Aug. 4.11, 2010. Levels are 0.20×10^{-13}, 0.40×10^{-13}, and 1.10×10^{-13} SDU; **c)** Sep. 6.04, 2010. Levels are 0.15×10^{-13}, 0.40×10^{-13}, and 1.10×10^{-13} SDU; **d)** Nov. 3.16, 2010. Levels are 0.55×10^{-13}, 1.25×10^{-13}, 4.00×10^{-13} SDU. See log of the observations in Table 1.

by $A = 7.067$ m^{B+1}/s and $B = 1.998$. Thus, the ejection velocity law is roughly inversely proportional to $\sim r_h^2$. This agrees with the results from hydrodynamical inner coma models by Crifo & Rodionov (1997) and disagrees with the r_h^{-1} dependence by Whipple (1951). The result of the fit is displayed in Fig. 11, where in addition to the 11 comets studied between Paper I and this study, we add the ejection velocity of 1 cm particles of the comet 67P/Churyumov-Gerasimenko, obtained by Fulle et al. (2010). In that figure, one can see that 81P at ~2.0 AU and 22P at $r_h > 2.5$ AU have deviated from this trend. In the case of 81P, this behavior it is due to the outburst I characterized in Sect. 4.1, and for 22P it comes from the strong dust ejection anisotropies at the large heliocentric distances identified by Moreno et al. (2012).

5. Dynamical history analysis

To obtain the dynamical evolution of the two comets studied in this paper, we followed the same procedure as described in Paper I, which is based on previous studies by Levison & Duncan (1994). We used version 6.2 of Mercury's numerical integrator developed by Chambers (1999). We generated 99 clones having 2σ dispersion in three of the orbital elements: semimajor axis, a, inclination, i, and eccentricity, e, where σ is the uncertainty in the corresponding parameter as given in the JPL Horizons online solar system data[2]. The orbital parameters and the σ values are given in Table A.1. The 99 clones plus the real object give a total of 100 massless particles to perform the statistical study. The Sun and the eight planets are considered to be massive bodies. To control the close encounters of the massless particles with the massive bodies, we used the hybrid algorithm that combines a symplectic algorithm with a Burlisch-Stoer integrator (see Chambers 1999). The initial time step was eight days, and the clones were removed when their heliocentric distance was >1000 AU.

We performed backward integrations of 15 Myr. The non-gravitational forces were neglected according to the same arguments posed by Lacerda (2013), where the change rate of the semimajor axis, da/dt, is produced by a non-gravitational acceleration, T, created by single sublimation jet tangential to the comet's orbit and affecting its motion during the life time of sublimation, t_{sub}:

$$\frac{da}{dt} = \frac{2Va^2T}{GM_\odot} \tag{2}$$

$$T = \frac{dM_d}{dt} \times \frac{v_d}{m_{nuc}} \tag{3}$$

$$t_{sub} = m_{nuc} \times \left(\frac{dM_d}{dt}\right)^{-1}. \tag{4}$$

Therefore, the total deviation of the semimajor axis D would be

$$D = \frac{da}{dt} \times t_{sub}. \tag{5}$$

[2] See ssd.pjl.nasa.gov/?horizons

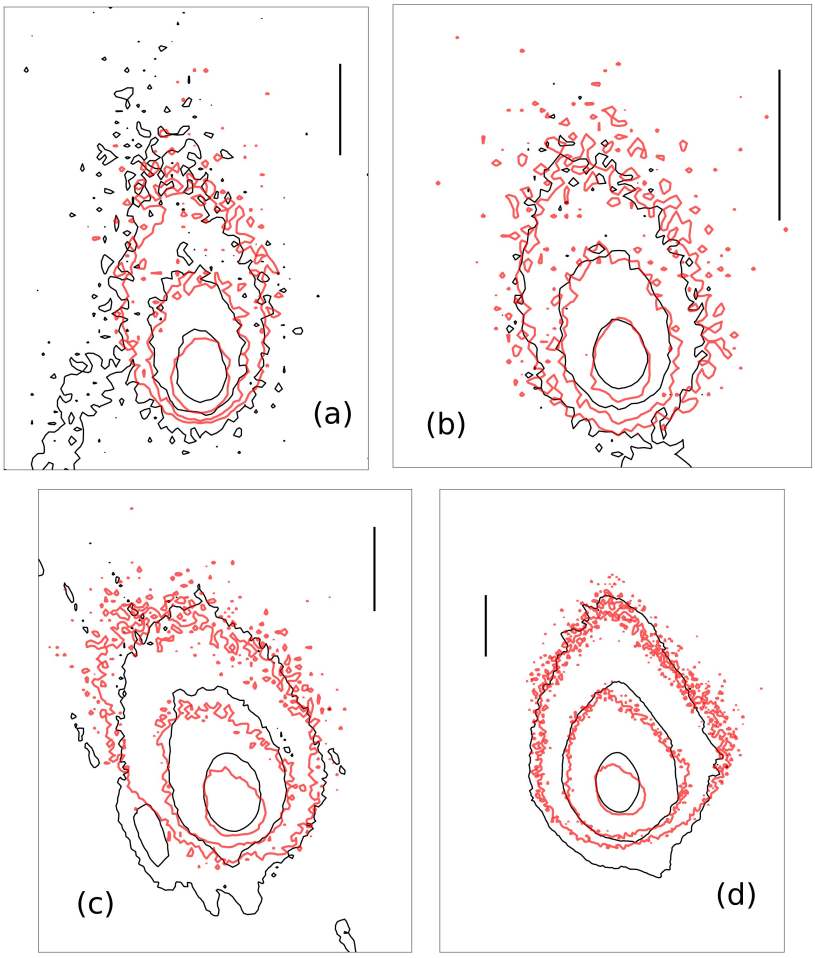

Fig. 10. As in Fig. 9 but for *Model II* or *standard model*.

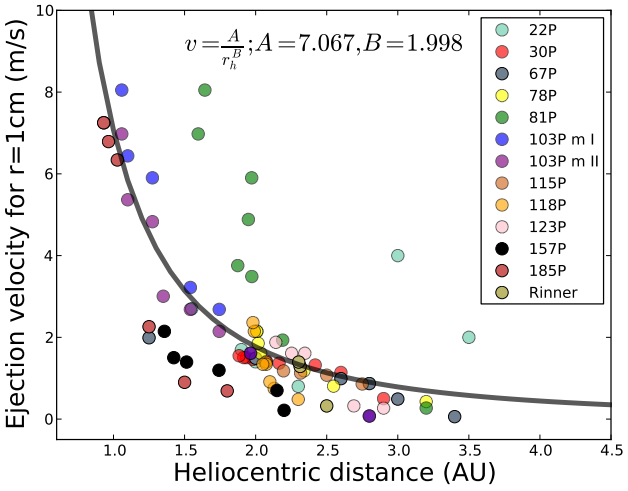

Fig. 11. Ejection velocities of 1 cm particles versus the heliocentric distance for all comets in the sample plus the result obtained by Fulle et al. (2010) in the study of comet 67P/Churyumov-Gerasimenko. The complete set of comets are: 22P/Kopff, 30P/Reinmuth 1, 67P/Churyumov-Gerasimenko, 78P/Gehrels 2, 81P/Wild 2, 103P/Hartley 2 (*Model I* and *Model II*), 115P/Maury, 118P/Shoemaker-Levy 4, 123P/West-Hartley, 157P/Tritton, 185P/Petriew, and P/2011 W2 (Rinner). The color code is given in the legend. The solid black line is the best fit found for that distribution: $v = A \times r_h^{-B}$, with A = 7.067 m^{B+1}/s and B = 1.998.

In these equations, dM_d/dt is the dust mass loss rate, V the orbital velocity, a the semimajor axis, G the gravitational constant, $M_\odot$ the Sun mass, v_d is the dust velocity, and m_{nuc} the mass of the nucleus. In Paper I, we estimated the highest deviation of the semimajor axis for the complete sample of comets as D = 0.32 AU. We found D_{81P} = 0.24 AU, $D_{103P\ Model\ I}$ = 0.24 AU, and $D_{103P\ Model\ II}$ = 0.21 AU. These values are in the same range as those found in Paper I and in Lacerda (2013). For further details we refer the readers to Sect. 5 of Paper I.

5.1. Discussion

In Paper I, we concluded that after the 15 Myr backward integration, just 12 of the initial 900 massless particles survived, which means ~98.7% were ejected form the solar system and ~1.3% remained in it. This result agrees with Levison & Duncan (1994), where the authors concluded that ~1.5% endured in the solar system after integration. Thus, in Paper I, eleven of the twelve remaining particles were in Transneptunian region, while one was in Centaur region (see Fig. 10 in Paper I). In this study, just 3 three clones of the initial 200 particles remained in the solar system after the 15 Myr integration, which is ~1.5%. These clones were 81P/clon34 and 81P/clon94, which are in Transneptunian region, and 103P/clon57 in Centaur region. Therefore, this result agrees with the one obtained in Paper I, and with Levison & Duncan (1994).

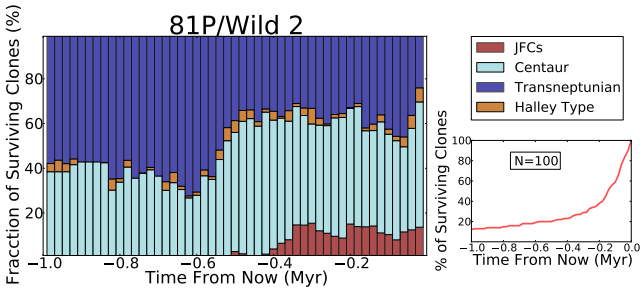

Fig. 12. 81P/Wild 2 backward in time orbital evolution during 1 Myr. *Left panel*: fraction of surviving clones (%) versus time from now (Myr). The colors represent the regions visited by the test particles (red: Jupiter family region; cyan: Centaur; blue: Transneptunian; yellow: Halley type). The resolution is 2×10^4 yr. *Right bottom panel*: the % of surviving clones versus time from now (Myr), where $N = 100$ is the number of the initial test massless particles.

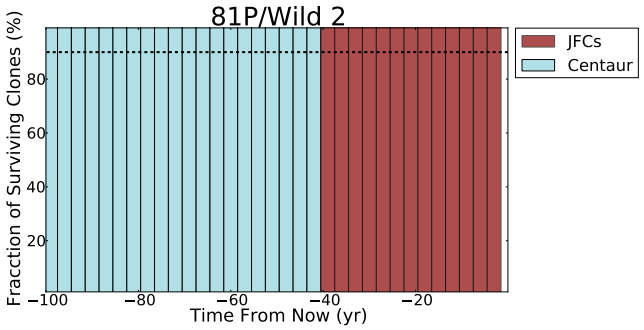

Fig. 13. 81P/wild 2 last 100 yr. fraction of surviving clones (%) versus time from now (yr). The colors represent the regions visited by the test particles (red: Jupiter family region; cyan: Centaur). The dashed line marks the bars with a confidence level equal or larger than 90% of the clones in the Jupiter family region. The resolution is 3 yr, and the number of the initial test particles is $N = 100$.

After the analysis of the 15 Myr integration in Paper I, to obtain a general view of the regions visited by comets, we focused on the first 1 Myr of backward integration in the orbital evolution, where ∼20% of the massless particles still remained in the solar system. We inferred that all of them have a Centaur and Transneptunian past, while the Halley Type region was the most unlikely source for those comets, as expected. This is consistent for the other comets, 81P and 103P, under study in this paper (see Figs. 12 and B.1).

After that, to obtain the time spent by each comet in the JFCs region, we displayed the last 5000 yr using a 100 yr temporal resolution. We found that all targets were relatively young in the JFCs region, with ages between $100 < t < 4000$ years. The youngest comets of the sample were 22P/Kopff (∼100 yr), 78P/Gehrels 2 (∼500 yr), and 118P/Shoemaker-Levy 4 (∼600 yr). On the other hand, the oldest comet was 123P with $\sim 3 \times 10^3$ yr. In this study, following the same steps, we have inferred that 81P is ∼40 yr, while 103P is ∼1000 yr (see Figs. 13 and B.2). The result for 81P agrees with the current knowledge about it: Sekanina & Yeomans (1985) described a very close encounter with Jupiter in 1974, and, as result of that approach, the comet was inserted in the inner regions of the solar system.

Finally, in Paper I we related the annual dust production rate for each comet (T_d) within the time spent in the JFCs region. We concluded that the most active comets in our sample were also

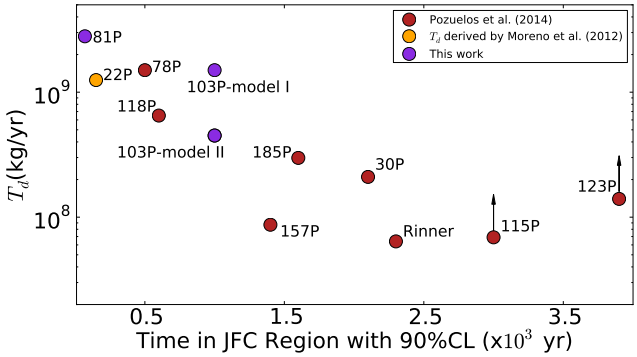

Fig. 14. Annual dust production rate of our targets obtained in the dust analysis (see Sect. 4) versus the time in the JFCs region with a 90% C.L. derived from dynamical studies (see Sect. 5). Red circles are the results derived from Pozuelos et al. (2014); yellow circle is the comet 22P/Koppf, where dust analysis was carried out in Moreno et al. (2012); violet circles are the results of the comets 81P/Wild 2 and 103P/Hartley 2, studied in this work. The comets with arrows mean the T_d given for them are lower limits (see text in Paper I).

the youngest ones, i.e., 22P, 78P, and 118P. Here we added the results obtained for 81P and 103P. We found that 81P is both the youngest and the most active comet in the whole sample. This result is displayed in Fig. 14, where the 11 comets under study are shown.

6. Summary and conclusions

To increase the number of comets analyzed in Paper I, in this work we extended the study to comets 81P/Wild 2 and 103P/Hartley 2, which are of special interest as targets of the spacecraft missions Stardust and EPOXI. We presented optical images of those comets and $Af\rho$ values as a function of the heliocentric distance provided by the amateur astronomical association *Cometas-Obs*. To fit the observational data, we used our Monte Carlo dust tail code (see e.g., Moreno 2009), from which we derived the dust parameters as a function of the heliocentric distance: dust loss rate, ejection velocities of particles, the size distribution, and the overall emission pattern.

The main results are as follows.

- Comet 81P/Wild 2 was found to be the most active in the whole sample of eleven comets, with an annual dust production rate of $T_d = 2.8 \times 10^9$ kg yr^{-1}. Its emission pattern was established as anisotropic with active areas located from 45° to −30° on the surface. The rotational parameters, I and ϕ, were found to be $I = (55 \pm 5)°$ and $\phi = (300 \pm 20)°$. In addition, we found two small outbursts suffered by the comet, one inbound and one outbound, where the total dust emitted was $m_{\mathrm{ob.I}} \sim 9.2 \times 10^8$ kg and $m_{\mathrm{ob.II}} \sim 3.0 \times 10^8$ kg, respectively.
- In the case of the comet 103P/Hartley 2, we proposed two models: *Model I* or the *hyperactive model*, where according to previous knowledge of this comet (see e.g., A'Hearn et al. 2011; Meech et al. 2011; Harmon et al. 2011), we forced the maximum size of particles to be in the range of $r_{\max} = 20$ cm. The dust production rate of this model was obtained as $T_d = 1.7 \times 10^9$ kg yr^{-1}. *Model II* or the *standard model* was carried out without the restriction in the maximum size of the particles. In that case, the result in the annual dust production rate was $T_d = 4.5 \times 10^8$ kg yr^{-1}. The ejection of comet 103P, in both models, was found to be isotropic.

- For both comets, the power index of the size distribution, δ, was found to be in the range $-4 < \delta - 3 <$. In this range, the brightness and mass are decoupled, so the mass depends on the largest ejected grains, while the brightness depends on the micrometer-size grains. For this reason, the dust production rate in our models should be regarded as lower limits. In the case of 103P, the presence of large chunks from the EPOXI mission and radar observations were found in the tail. While the true nature of these chunks is still under study, the size of them is estimated as ~20 cm. Thus, in our study, *Model I* seems to be more realistic than *Model II*, which should be considered as a lower limit for this comet.
- We concluded that the best match to the dust ejection velocity law is $v \propto r_h^{-1.998}$ which agrees with $v \propto r_h^{-2}$ obtained by Crifo & Rodionov (1997) from hydrodynamical models of the inner cometary comae, for intermediate-sized particles.

The second block of our study concerned determination of the dynamical evolution of the targets over the past 15 Myr. We used the numerical integrator developed by Chambers (1999). As in Paper I, the statistical study for each comet was implemented using 100 test massless particles: 1 real particle plus 99 clones with 2σ dispersion in the orbital parameters a, e, and i. In these integrations, the Sun and the eight planets were considered to be massive bodies, and close encounters between them and test particles were permitted. Therefore, from the initial 200 massless particles, we removed those that were beyond 1000 AU at any time during the integration. The main results were:

- The analysis showed that ~1.5% of the massless particles remained in the solar system after the 15 Myr integration, and the most likely sources of them were the Centaur and Transneptunian regions. This result agrees with Paper I and with the studies of Levison & Duncan (1994).
- We were able to deduce, with 90% confidence level, how long these targets spent as members of the JFCs: 81P ~40 yr and 103P ~1000 yr. Thus, 81P was found to be the youngest target in the whole sample of short-period comets studied between Paper I and this study.

In Fig. 14 we added the results from Paper I and the ones obtained from this work for the comets 81P and 103P. In that figure, we plotted the annual dust production rate [kg yr^{-1}] (see Table 3 in this work, and Table 4 in Paper I) versus the time spent by the comets in the JFCs region with a 90% confidence level obtained in the dynamical analysis. From this figure, we concluded that 81P is both the youngest and the most active comet. Therefore, the relationship between activity and the time spent in JFCs, still seems to be evident. Despite the general trend in our sample of comets, this result should be taken with caution, because two exceptions to this trend were found in Paper I, 157P/Tritton and 123P/West-Hartley. To establish firmer conclusions about the cometary activity and the dynamical evolution, it would be desirable to perform more studies on other short-period comets.

Acknowledgements. We would like to thank Dr. Z.-Y. Lin and Dr. L.M. Lara for sharing the observations of comet 81P/Wild 2 carried out in Lulin Observatory (Taiwan) with us. We would also like to thank the entire Amateur Astronomical Association *Cometas-Obs* for always looking for comets. We would also like to thank Dr. Chambers for his help using his numerical integrator. We are grateful to the anonymous referee for comments and suggestions to improve this paper. This work was supported by contracts *AYA2012-3961-CO2-01* and *FQM-4555* (Proyecto de Excelencia, Junta de Andalucía).

Table 2. Dust properties summary of the targets under study I.

Comet	Emission pattern [1]	Active areas location (°)	Size distribution r_{min}, r_{max} (cm)	Size distribution $\delta_{min}, \delta_{max}$	Obliquity (°)	Argument of subsolar meridian at perihelion (°)
81P/Wild 2	Ani (35%)	−30 to +45	10^{-4}, 3	−3.55, −3.25	50	300
103P/Hartley 2 (*Model I*)	Iso	–	10^{-4}, 20	−3.45, −3.25	–	–
103P/Hartley 2 (*Model II*)	Iso	–	10^{-4}, 3	−3.40, −3.25	–	–

Notes. [(1)] Iso = Isotropic ejection; Ani = Anisotropic ejection.

Table 3. Dust properties summary of the targets under study II.

Comet	Peak dust loss rate (kg s^{-1})	Peak ejection velocity of 1-cm grains (m s^{-1})	Total dust mass ejected (kg)	Total dust mass ejected per year (kg/yr)	Averaged dust mass loss rate (kg s^{-1})	Contribution to the interplanetary dust (%) [1]
81P/Wild 2	900	8.0	1.1×10^{10}	2.8×10^9	87.5	0.96
103P/Hartley 2 (*Model I*)	600	13.9	5.9×10^9	1.5×10^9	46.8	0.51
103P/Hartley 2 (*Model II*)	160	7.5	1.7×10^9	4.5×10^8	14.1	0.15

Notes. [(1)] Annual contribution to the interplanetary dust replacement (Grun et al. 1985).

Table A.1. Orbital parameters of the short-period comets under study.

Comet	$e \pm \sigma$	$a \pm \sigma$ (AU)	$i \pm \sigma$ (°)	node (°)	peri (°)	M (°)
81P JPL K103/7	0.53735432 ±5e-8	3.45011496 ±4e-8	3.238287 ±2e-6	136.10661	41.69284	171.41550
103P JPL 183	0.695145 ±1e-6	3.47276 ±1e-5	13.61716 ±2e-5	219.76266	118.19548	353.71670

Appendix A: Orbital parameters of comets 81P/Wild 2 and 103P/Hartley 2

In Table A.1 we show the orbital elements of the comets used during the dynamical studies in Sect. 5. They are extracted from JPL Horizons online solar system data[3].

Appendix B: Dynamical analysis of comet 103P/Hartley 2

In Figs. B.1 and B.2, we show the dynamical analysis of the comet 103P/Hartley 2 described in Sect. 5. We present the fraction of the surviving clones versus time from now on different time scales. In both cases, the colored bars correspond to different regions visited by test particles: red to Jupiter family; cyan to Centaur; yellow to Haley type; blue to Transneptunian. The number of the initial test particles is $N = 100$.

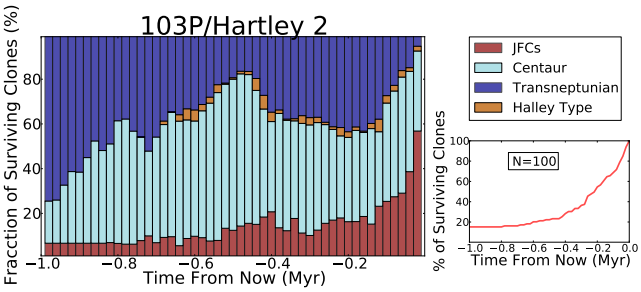

Fig. B.1. As in Fig. 12, but for comet 103P/Hartley 2.

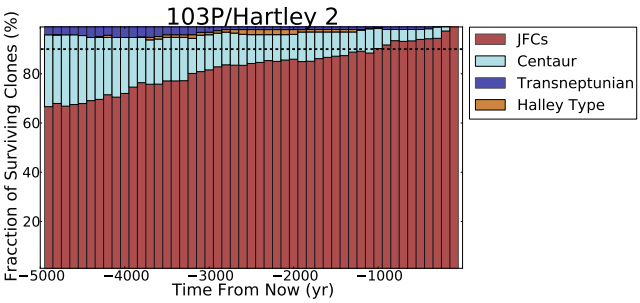

Fig. B.2. As in Fig. 13, but for the comet 103P/Hartley 2. The total plotted time is 5×10^3yr, with a resolution of 100 yr.

[3] See ssd.pjl.nasa.gov/?horizons

References

A'Hearn, M. F., Schleicher, D. G., Millis, R. L., Feldman, P. D., & Thompson, D. T. 1984, AJ, 89, 579
A'Hearn, M. F., Belton, M. J. S., Delamere, W. A., et al. 2005, Science, 310, 258
A'Hearn, M. F., Belton, M. J. S., Delamere, W. A., et al. 2011, Science, 332, 1396
Basilevsky, A. T., & Keller, H. U. 2006, Planet. Space Sci., 54, 808
Basilevsky, A. T., & Keller, H. U. 2007, Sol. Syst. Res., 41, 109
Bauer, J. M., Walker, R. G., Mainzer, A. K., et al. 2011, ApJ, 738, 171
Belton, M. J. S. 2013, Icarus, 222, 653
Belton, M. J. S., Thomas, P., Carcich, B., et al. 2013a, Icarus, 222, 477
Belton, M. J. S., Thomas, P., Li, J.-Y., et al. 2013b, Icarus, 222, 595
Bertini, I., Barbieri, C., Ho, T.-M., et al. 2012, A&A, 541, A159
Boissier, J., Bockelée-Morvan, D., Biver, N., et al. 2014, Icarus, 228, 197
Brownlee, D. E., Horz, F., Newburn, R. L., et al. 2004, Science, 304, 1764
Burns, J. A., Lamy, P. L., & Soter, S. 1979, Icarus, 40, 1
Chambers, J. E. 1999, MNRAS, 304, 793
Crifo, J. F., & Rodionov, A. V. 1997, Icarus, 127, 319
Davidsson, B. J. R., & Gutierrez, P. J. 2004, in BAAS, 36, 1118
Duxbury, T. C., Newburn, R. L., & Brownlee, D. E. 2004, J. Geophys. Res. (Planets), 109, 12
Edoh, O. 1983, Univ. Arizona, USA
Epifani, E., Colangeli, L., Fulle, M., et al. 2001, Icarus, 149, 339
Farnham, T. L., & Schleicher, D. G. 2005, Icarus, 173, 533
Finson, M. J., & Probstein, R. F. 1968, ApJ, 154, 327
Fulle, M. 2004, in Motion of cometary dust, eds. M. C. Festou, H. U. Keller, & H. A. Weaver (University of Arizona Press), 565
Fulle, M., Colangeli, L., Agarwal, J., et al. 2010, A&A, 522, A63
Green, S. F., McDonnell, J. A. M., McBride, N., et al. 2004, J. Geophys. Res. (Planets), 109, 12
Groussin, O., Lamy, P., Jorda, L., & Toth, I. 2004, A&A, 419, 375
Grun, E., Zook, H. A., Fechtig, H., & Giese, R. H. 1985, Icarus, 62, 244
Hadamcik, E., & Levasseur-Regourd, A. C. 2009, Planet. Space Sci., 57, 1118
Hanner, M. S., & Hayward, T. L. 2003, Icarus, 161, 164
Harmon, J. K., Nolan, M. C., Howell, E. S., Giorgini, J. D., & Taylor, P. A. 2011, ApJ, 734, L2
Hsieh, H. H., Yang, B., & Haghighipour, N. 2012a, ApJ, 744, 9
Hsieh, H. H., Yang, B., Haghighipour, N., et al. 2012b, AJ, 143, 104
Jockers, K. 1997, Earth Moon and Planets, 79, 221
Kelley, M. S., Lindler, D. J., Bodewits, D., et al. 2013, Icarus, 222, 634
Kirk, R. L., Duxbury, T. C., Hörz, F., et al. 2005, in 36th Annual Lunar and Planet. Sci. Conf., eds. S. Mackwell, & E. Stansbery, 2244
Knight, M. M., & Schleicher, D. G. 2013, Icarus, 222, 691
Kolokolova, L., Hanner, M. S., Levasseur-Regourd, A.-C., & Gustafson, B. Å. S. 2004, in Physical properties of cometary dust from light scattering and thermal emission, ed. G. W. Kronk, 577
Lacerda, P. 2013, MNRAS, 428, 1818
Lara, L. M., Lin, Z.-Y., & Meech, K. 2011, A&A, 532, A87
Levison, H. F., & Duncan, M. J. 1994, Icarus, 108, 18
Licandro, J., Moreno, F., de León, J., et al. 2013, A&A, 550, A17
Lin, Z.-Y., Lara, L. M., Vincent, J. B., & Ip, W.-H. 2012, A&A, 537, A101
Lisse, C. M., Fernandez, Y. R., Reach, W. T., et al. 2009, PASP, 121, 968
Meech, K. J., & Jewitt, D. C. 1987, A&A, 187, 585
Meech, K. J., A'Hearn, M. F., Adams, J. A., et al. 2011, ApJ, 734, L1
Monet, D. G., Levine, S. E., Canzian, B., et al. 2003, AJ, 125, 984
Moreno, F. 2009, ApJS, 183, 33
Moreno, F., Lara, L. M., Licandro, J., et al. 2011, ApJ, 738, L16
Moreno, F., Pozuelos, F., Aceituno, F., et al. 2012, ApJ, 752, 136
Moreno, F., Cabrera-Lavers, A., Vaduvescu, O., Licandro, J., & Pozuelos, F. 2013, ApJ, 770, L30
Moreno, F., Licandro, J., Álvarez-Iglesias, C., Cabrera-Lavers, A., & Pozuelos, F. 2014, ApJ, 781, 118
Mueller, B. E. A., Samarasinha, N. H., Farnham, T. L., & A'Hearn, M. F. 2013, Icarus, 222, 799
Pozuelos, F. J., Moreno, F., Aceituno, F., et al. 2014, A&A, 568, A3
Richardson, J. E., & Bowling, T. J. 2014, Icarus, 234, 53
Sekanina, Z. 1981, Ann. Rev. Earth Planetary Sci., 9, 113
Sekanina, Z. 2003, J. Geophys. Res. (Planets), 108, 8112
Sekanina, Z., & Yeomans, D. K. 1985, AJ, 90, 2335
Sekanina, Z., Brownlee, D. E., Economou, T. E., Tuzzolino, A. J., & Green, S. F. 2004, Science, 304, 1769
Thomas, P., A'Hearn, M., Belton, M. J. S., et al. 2013a, Icarus, 222, 453
Thomas, P. C., A'Hearn, M. F., Veverka, J., et al. 2013b, Icarus, 222, 550
Tozzi, G. P., Epifani, E. M., Hainaut, O. R., et al. 2013, Icarus, 222, 766
Veverka, J., Klaasen, K., A'Hearn, M., et al. 2013, Icarus, 222, 424
Whipple, F. L. 1951, ApJ, 113, 464

Main-Belt Comets

- **Paper IV.**
  The dust environment of Main-Belt Comet P/2012 T1 (PANSTARRS).
  Moreno, F.; Cabrera-Lavers, A.; Vaduvescu, O.; Licandro, J.; Pozuelos, F.
  The Astrophysical Journal Letters, Volume 770, Issue 2, article id. L30, 6 pp. (2013).

- **Paper V.**
  Intermittent dust mass loss from activated asteroid P/2013 P5 (PANSTARRS) .
  Moreno, F.; Licandro, J.; Álvarez-Iglesias, C.; Cabrera-Lavers, A.; Pozuelos, F..
  The Astrophysical Journal, Volume 781, Issue 2, article id. 118, 5 pp. (2014)

The Astrophysical Journal Letters, 770:L30 (6pp), 2013 June 20 doi:10.1088/2041-8205/770/2/L30

THE DUST ENVIRONMENT OF MAIN-BELT COMET P/2012 T1 (PANSTARRS)

F. Moreno[1], A. Cabrera-Lavers[2,3,4], O. Vaduvescu[2,5], J. Licandro[2,3], and F. Pozuelos[1]
[1] Instituto de Astrofísica de Andalucía, CSIC, Glorieta de la Astronomía s/n, E-18008 Granada, Spain; fernando@iaa.es
[2] Instituto de Astrofísica de Canarias, c/Vía Láctea s/n, E-38200 La Laguna, Tenerife, Spain
[3] Departamento de Astrofísica, Universidad de La Laguna (ULL), E-38205 La Laguna, Tenerife, Spain
[4] GTC Project, E-38205 La Laguna, Tenerife, Spain
[5] Isaac Newton Group of Telescopes, Apdo. de Correos 321, E-38700 Santa Cruz de la Palma, Canary Islands, Spain
Received 2013 April 16; accepted 2013 May 15; published 2013 June 3

ABSTRACT

The Main-Belt Comet P/2012 T1 (PANSTARRS) has been imaged using the 10.4 m Gran Telescopio Canarias and the 4.2 m William Herschel Telescope at six epochs in the period from 2012 November to 2013 February, with the aim of monitoring its dust environment. The dust tails' brightness and morphology are best interpreted in terms of a model of sustained dust emission spanning four to six months. The total dust mass ejected is estimated at ∼6–25 × 10^6 kg. We assume a time-independent power-law size distribution function, with particles in the micrometer to centimeter size range. Based on the quality of the fits to the isophote fields, an anisotropic emission pattern is favored against an isotropic one, in which the particle ejection is concentrated toward high latitudes (±45° to ±90°) in a high-obliquity object ($I = 80°$). This seasonally driven ejection behavior, along with the modeled particle ejection velocities, are in remarkable agreement to those we found for P/2010 R2 (La Sagra).

Key words: comets: individual (P/2012 T1 (PANSTARRS)) – methods: numerical – minor planets, asteroids: general

Online-only material: color figures

1. INTRODUCTION

The Main-Belt Comet P/2012 T1 (PANSTARRS) was discovered by the Pan-STARRS survey on UT 2012 October 6.53 (Wainscoat et al. 2012). The orbit was identified as that of a Main-Belt Comet (MBC), i.e., an active object in an orbit typical of a main belt asteroid. This object constitutes the 10th identified MBC. The general properties of those objects have been reviewed by, e.g., Jewitt (2012). *N*-body integrations of their orbits reveal that in general they are dynamically stable, with timescales of 100 Myr or longer (Hsieh et al. 2012), so they seem to be native members of the Main Asteroid Belt (Hsieh et al. 2009). This agrees with the fact that the spectra of some MBCs can be identified as those of well-known asteroidal families (Licandro et al. 2011), being markedly different to those of bona fide comets. Two objects have been found, however, with shorter lifetimes, namely 238P/Read and P/2008 R1, which were found to be dynamically stable for 20–30 Myr only (Jewitt et al. 2009; Haghighipour 2009), owing to their proximity to the 8:3 and 1:2 mean-motion resonances with Jupiter. Concerning their activity, some of those objects clearly show a sustained activity, of the order of several months, such as P/2010 R2 (La Sagra) (hereafter P/La Sagra) and 2006 VW139 (Moreno et al. 2011a; Licandro et al. 2013), while in some others the activity is restricted to a short time interval, as in the cases of (596) Scheila (e.g., Jewitt et al. 2011; Bing & Hsieh 2011; Moreno et al. 2011b; Ishiguro et al. 2011), and, recently, P/2012 F5 (Gibbs) (Stevenson et al. 2012; Moreno et al. 2012a). The object P/2010 A2 very likely belongs to this latter group (Jewitt et al. 2010; Snodgrass et al. 2010). These authors based their results on an extended data set covering various epochs and observation geometries, contradicting our results, which were based on a more limited data set, revealing sustained activity (Moreno et al. 2010). In addition, some MBCs have been detected to be recurrent in activity, such as 133P/Elst-Pizarro and 238P (Hsieh et al. 2010, 2011b). Given the small sample of MBCs, it is then very important to characterize the emission properties of any new member discovered.

2. OBSERVATIONS AND DATA REDUCTION

CCD images of P/2012 T1 were acquired on several nights from 2012 November until the end of 2013 February. Table 1 lists the log of the observations. The UT date referred to in the table is the mean time of the images acquired on the corresponding night. The labels (a)–(e) are used to facilitate the identification of the images in Figures 1–3 and in Table 2. On the William Herschel Telescope (WHT), we used the Prime Focus Imaging Platform (PFIP; Tulloch 1998), the Auxiliary CAMera-spectrograph (ACAM; Benn et al. 2008), both with a standard Johnson–Cousins *R* filter, and the Long-slit Intermediate Resolution Infrared Spectrograph (LIRIS; Manchado et al. 1998), with a K_s filter. On the Gran Telescopio Canarias (GTC), we used the Optical System for Image and Low Resolution Integrated Spectroscopy (OSIRIS) camera-spectrograph (Cepa 2010), with a Sloan r' filter. The images were bias and flat-field corrected, and calibrated in flux by standard procedures. Each night the object was imaged repeatedly, and a median stack image was obtained by adding the available images taking into account the sky motion of the object at the epoch. Figure 1 shows the final images at each night, except on 2013 February 27, in which the object was undetectable. The object appears to be active on all the other dates, displaying a comet-like tail. On 2013 February 17 the object was already very faint, with $m_{r'} = 22.9 \pm 0.3$ and a FWHM of 1.″8–2″. This is significantly larger than the average seeing on that night, ∼1″, indicating that some circumnuclear dust is still present. However, the noise is considerable, leading to irregularly shaped isophotes, so that only the measured magnitude will be considered for modeling purposes. We were unable to detect the object on February 27 with either the ACAM nor with LIRIS instruments. Strong

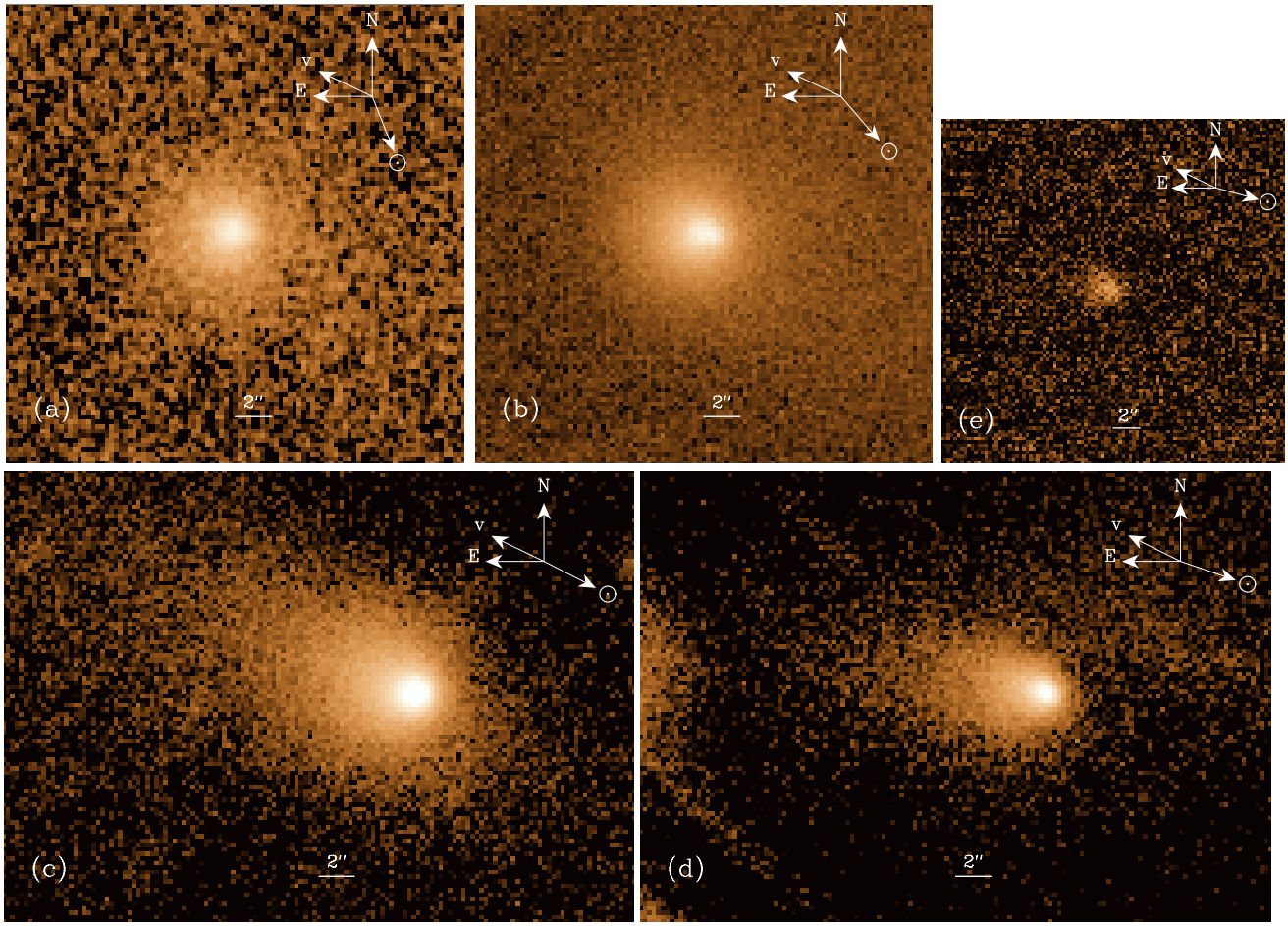

Figure 1. Median stack images of P/2012 T1 obtained with PFIP on the 4.2 m William Herschel Telescope (a) and OSIRIS on the 10.4 m Gran Telescopio Canarias (b)–(e). The corresponding dates are given in Table 1. The directions of the velocity vector, the Sun, and the astronomical north and east are indicated.

(A color version of this figure is available in the online journal.)

moonlight prevented us from detecting objects with $m_R > 18.5$ with ACAM. However, with LIRIS K_s band we could detect much fainter objects, allowing us to establish a limiting magnitude for P/2012 T1 of $m_{K_s} > 22.8 \pm 0.1$.

For consistency, we converted all the OSIRIS r' magnitudes to the common R standard Johnson–Cousins system by subtracting 0.33 mag, using the transformation equations by Fukugita et al. (1996), assuming for the object the same spectral dependence as the Sun within the bandpasses of these two red filters (Moreno et al. 2010). The last column in Table 1 lists the geometrically reduced magnitudes of the object calculated by using apertures between two and three times the FWHM. These magnitudes are given by $m(1, 1, 0) = m - 2.5\log(\Delta r_h^2) - \phi\alpha$, where m is the apparent magnitude, r_h and Δ are the heliocentric and geocentric distances in AU, ϕ is the phase coefficient, taken as 0.03 mag deg^{-1}, and α is the phase angle. In addition to the images just described, we will use for modeling an early observation by Buzzi (Wainscoat et al. 2012), giving $m_R = 19.8$, or $m_R(1, 1, 0) = 17.0$, on UT 2012 October 11.04.

After flux calibration, the images were rotated to the (N, M) system (Finson & Probstein 1968) through the position angle of the Sun to the target radius vector, and converted to solar disk

Table 1
Log of the Observations

Date (UT) (ID)	Instrument/Telescope	$T_{\rm exp}$ (s)$\times N_{\rm im}$[a]	r_h (AU)	Δ (AU)	α (°)	Resolution (km pixel^{-1})	$m(1, 1, 0)$[b]
2012 Nov 13.10 (a)	PFIP/WHT	20 × 14	2.43	1.47	6.2	265.8	16.9 ± 0.2
2012 Nov 19.98 (b)	OSIRIS/GTC	60 × 20	2.44	1.49	8.4	274.8	17.0 ± 0.2
2012 Dec 13.87 (c)	OSIRIS/GTC	60 × 15	2.46	1.67	16.5	307.1	17.3 ± 0.2
2013 Jan 17.94 (d)	OSIRIS/GTC	60 × 30	2.51	2.09	22.5	385.4	17.7 ± 0.2
2013 Feb 17.90 (e)	OSIRIS/GTC	20 × 61	2.55	2.53	22.4	466.4	18.9 ± 0.3
2013 Feb 27.90	LIRIS/WHT	44 × 60	2.57	2.67	21.7	485.0	>22.8 ± 0.1
2013 Feb 27.93	ACAM/WHT	31 × 60	2.57	2.68	21.6	485.0	...

Notes.

[a] Individual exposure time and number of images secured.

[b] Geometrically reduced magnitude in the R band except that of LIRIS/WHT which refers to the K_s band apparent magnitude.

intensity units (sdu), which are the output units of our Monte Carlo dust tail code.

3. THE MODEL

We applied our Monte Carlo code described previously (e.g., Moreno 2009; Fulle et al. 2010; Moreno et al. 2012b), which computes the trajectory of a large number of particles ejected from a small nucleus, assuming that the grains are affected by the solar gravitation and radiation pressure. The model has many input parameters, and a number of assumptions must be made, as described below. The particle orbital elements are computed from the terminal velocity and the β parameter (e.g., Fulle 1989), which is given by $\beta = C_{\rm pr} Q_{\rm pr}/(2\rho r)$, where $C_{\rm pr} = 1.19 \times 10^{-3}$ kg m^{-2}, $Q_{\rm pr}$ is the radiation pressure coefficient, and ρ is the particle density, assumed at $\rho = 1000$ kg m^{-3}. The pressure radiation coefficient for absorbing particles with radii $r \gtrsim 1\ \mu$m is $Q_{\rm pr} \sim 1$ (e.g., Moreno et al. 2012b). The particle geometric albedo is assumed at $p_v = 0.04$ (i.e., a Halley-like value).

The main inputs of the model are the ejection velocity law, the size distribution function, and the dust mass-loss rate. Of course, all these parameters can be time-dependent. Notwithstanding this, and in order to limit the amount of free parameters, we only allowed the dust mass-loss rate to be time-dependent. A power-law function was assumed for the size distribution of the particles, ejected with a terminal velocity of $v(\beta) = v_0 \beta^{\gamma}$, where v_0 and γ are constants. This expression is commonly accepted for the terminal velocities of grains dragged out from ice sublimation on the surface of cometary nuclei, and also for fragments ejected from collision experiments (e.g., Giblin 1998; Onose & Fujiwara 2004). Then, the onset time (t_0), the ejection velocity parameters, the power-law size distribution index, the limiting sizes of the particles ($r_{\rm min}$, $r_{\rm max}$), and the dust loss rate (dM/dt) are the free parameters of the model. We will work under the hypotheses of both isotropic and anisotropic particle ejection scenarios.

Based on the evolution of the dust tail brightness and morphology, we hypothesized a sustained activity pattern for P/2012 T1. The early observation by Buzzi on 2012 October 11.04 (Wainscoat et al. 2012) gives $m_R(1, 1, 0) = 17.0$, while on November 13.1 we estimate $m_R(1, 1, 0) = 16.9 \pm 0.2$ (Table 1). Thus, the observed magnitudes are essentially the same on these two dates. If an impulsive event had taken place, in principle we should have noted a significant magnitude increase in that month period, a logical consequence of having fewer dust particles inside the field of view as they travel away from the nucleus. The magnitude would only be constant in the very unlikely scenario where all particles ejected were slow-moving and large, being essentially unaffected by radiation pressure. But, even if that were the case, then the dust tails in the 2012 December and 2013 January images would be depleted of particles in the anti-sunward direction (upper part of the images in Figures 2(c) and (d)), and would have the wrong orientation. This has been confirmed by test models, and occurs because the synchrones older than those corresponding to the discovery date (~25 days post-perihelion) point to directions away from the anti-solar direction, which is populated mostly by dust particles ejected significantly later.

4. RESULTS AND DISCUSSION

In order to find the best-fit parameters, we start from our previous experience in the analysis of MBC dust tails, specifically on those for which sustained activity has been derived, as P/La Sagra and 2006 VW139 (Moreno et al. 2011a; Licandro et al. 2013). In those cases, the parameter γ of the ejection velocity was set to $\gamma = 1/2$, a value which is typical of hydrodynamical drag from sublimating ices and that will be adopted here as well. For the limiting particle sizes, we used a broad range between 5 μm and 1 cm, being distributed following a power-law index of -3.5, the same parameters derived for P/La Sagra. Then, we tried to fit the other parameters, namely t_0, v_0, and the dM/dt profile, in the assumption of isotropic ejection as a first approximation.

For a given date, the fitting quality to the observed images is measured by the quantity $\sigma = \sqrt{\sum (I_{\rm obs} - I_{\rm fit})^2/N}$, where $I_{\rm obs}$ and $I_{\rm fit}$ are the observed and fitted images, the sum being limited to all the observed image pixels N whose brightness is higher than a certain threshold. This threshold is given by the outermost contours of the observed images displayed in Figures 2 and 3. This eliminates from the evaluation of σ the regions of high noise, low brightness levels, that can contribute spuriously to that quantity. The σ parameters at each date are defined as σ_a to σ_d (see Table 2), corresponding to images (a)–(d) of Table 1, respectively.

Figure 2 displays the fits to the observed isophotes when the onset of activity is set at perihelion time, $v_0 = 25$ m s^{-1}, and the dust loss rate profile is that given at the lower rightmost panel of Figure 2 (solid line). We call this model ISO-1. The corresponding synthetic magnitudes on 2012 November 10 and 2013 February 17 are given in Table 2. The apertures used to obtain the synthetic magnitudes and their uncertainties on 2013 February 17 are the same as for the real image on that date. We used the same aperture sizes to estimate the magnitude of the synthetic image on 2012 November 10. Thus, as shown in Figure 2 and Table 2, this ISO-1 model provides a good agreement with all the available observations. The lower magnitude limit of $m_{K_s} > 22.8 \pm 0.1$ on 2013 February 27 essentially confirms the decrease in brightness predicted by the model: the dust loss rate decays to zero ~125 days after perihelion, so that the activity lasted about four months. The total ejected mass for this model is 5.8×10^6 kg.

Within the isotropic ejection scenario, we searched for other model parameters that can produce fits of approximately the same quality as those displayed in Figure 2. Thus, for example, the onset time can be displaced backward in time, provided a rearrangement is made in the dM/dt profile just derived for model ISO-1. Then, similar quality fits are obtained by setting the activation date back up to 50 days before perihelion (see also Table 2), if dM/dt is set as shown in Figure 3 by the dashed line (model ISO-2). In this case, the activity progresses more gently after onset time, instead of the impulsive character of the dM/dt profile of model ISO-1. In this case, $M_t = 7.8 \times 10^6$ kg, and the object is active for five and a half months. If the activation date is set even earlier than the mentioned 50 days before perihelion, then fitting problems mainly in the 2012 December 13 and 2013 January 17 images start to appear, specifically by an excess brightness in the sunward direction. We can then state that P/2012 T1 has been active for a maximum period of about six months.

Regarding the ejection velocities, we have no constraints on that parameter. We have no estimates on size and density of the body that could help at least to estimate the escape velocity. On the other hand, the combination $v_0 = 25$ m s^{-1} and $\gamma = 1/2$ agrees remarkably well with what we found for P/La Sagra, for which we obtained v_0 values ranging from

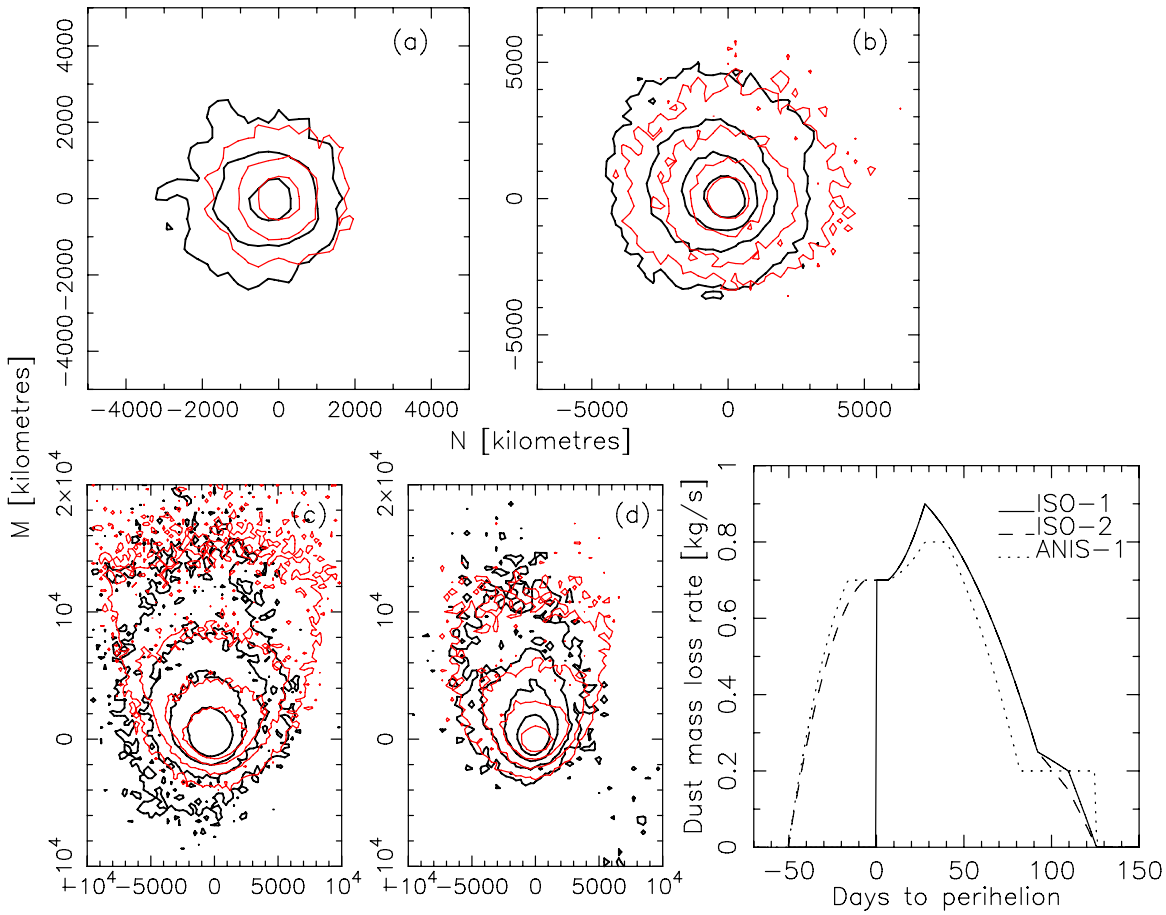

Figure 2. Isotropic model with MBC activation at perihelion time (ISO-1 model). Panels (a)–(d) correspond to the observations at the dates indicated in Table 1. The black thick solid lines in panels (a)–(d) indicate the observed isophotes, while the red thin lines correspond to the model. The innermost isophote level in each panel (all expressed in sdu) are (a) 8×10^{-14}, (b) 5.6×10^{-14}, (c) 1.2×10^{-14}, and (d) 1.2×10^{-14}. The isophotes vary by a factor of two between consecutive levels. The lower rightmost panel displays the dust mass-loss rate as a function of time to perihelion for three models: ISO-1, ISO-2, and ANIS-1 (see the text for a detailed description of the models).

(A color version of this figure is available in the online journal.)

Table 2
Parameters and Results of the Models

Parameter	Model ISO-1	Model ISO-2	Model ANIS-1	Measured
v_0 (m s^{-1}), γ	125, 1/2	125, 1/2	200, 1/2	
M_t (kg)	6–20 $\times$ 10^6	8–25 $\times$ 10^6	8–25 $\times$ 10^6	
t_0	Perihelion time	−50 days to perihelion	−50 days to perihelion	
Event duration	125 days	175 days	175 days	
$r_{\rm min}$	$\leqslant$5 μm	$\leqslant$5 μm	$\leqslant$5 μm	
$r_{\rm max}$	1–10 cm	1–10 cm	1–10 cm	
Power index	−3.5	−3.5	−3.5	
Rotational I, Φ	...	...	80°, 260°	
Active area	...	...	[±45°, ±90°]	
σ_a,σ_b (sdu)	3.8×10^{-14}, 1.7×10^{-14}	3.7×10^{-14}, 1.8×10^{-14}	3.1×10^{-14}, 1.3×10^{-14}	
σ_c,σ_d (sdu)	4.2×10^{-15}, 1.8×10^{-15}	4.4×10^{-15}, 1.9×10^{-15}	2.8×10^{-15}, 1.2×10^{-15}	
m_R (2012 Oct 11)	19.5 ± 0.2	19.4 ± 0.2	19.4 ± 0.3	19.8[a]
m_R (2013 Feb 17)	22.6 ± 0.4	22.5 ± 0.4	22.7 ± 0.4	22.6 ± 0.3

Note. [a] Reported R mag by Buzzi (Wainscoat et al. 2012).

15.8 to 31.7 m s^{-1} for $\gamma = 1/2$. Thus, although it is possible to find other solutions modifying both v_0 and γ, we have not attempted such combinations.

The particle size range affects significantly the model results only if $r_{\rm max}$ is varied. The minimum size has only a minor effect provided it decreases down to 0.5 μm. However, if the maximum size increases up to 10 cm, the dust mass-loss rate profile must be increased by an overall factor of ∼3, with respect to that shown in Figure 2, in order to maintain a similar quality fit to the data. In Table 2, the corresponding range of M_t for $r_{\rm max}$ = 1–10 cm is shown.

Even considering that the isotropic ejection scenario provides already a reasonable fit to the data, it is interesting to search for possible model solutions regarding anisotropic ejection patterns.

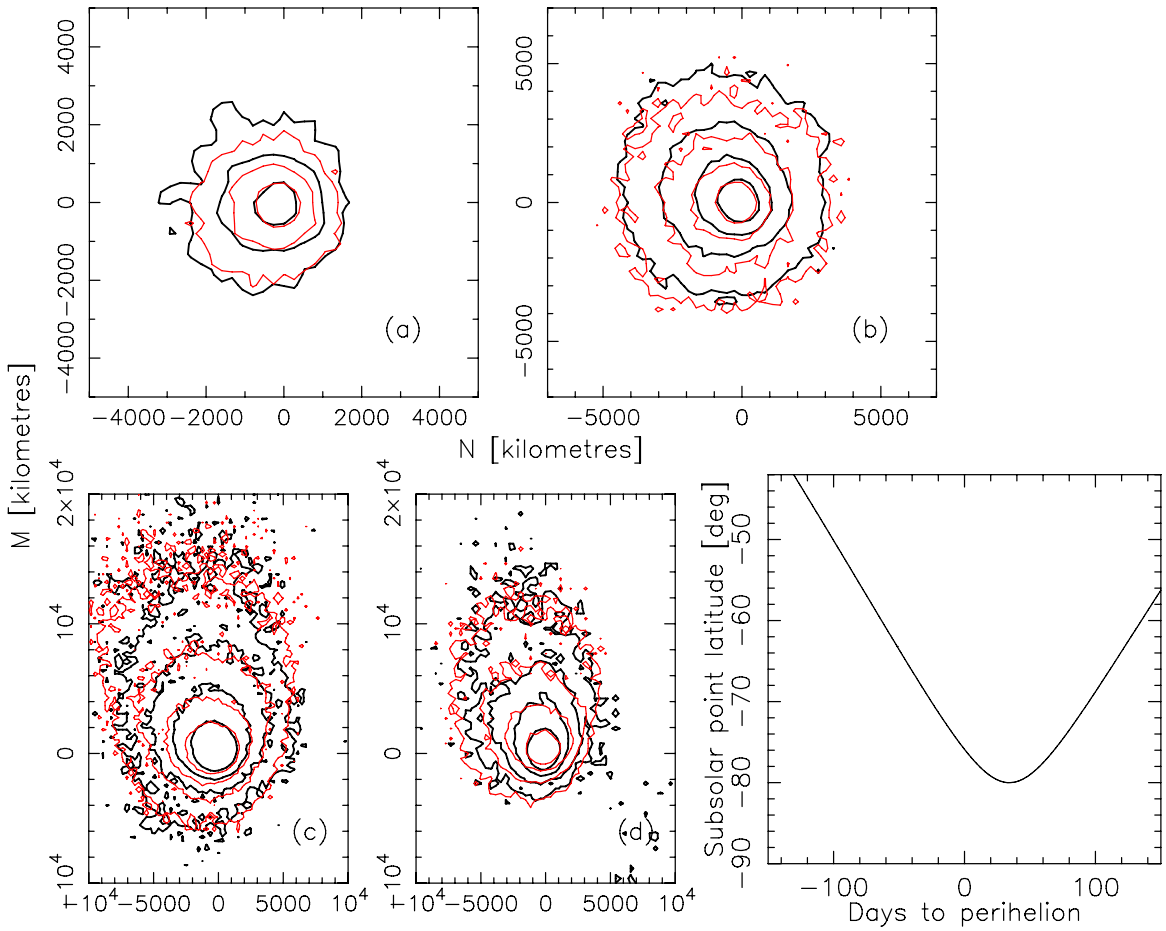

Figure 3. Anisotropic model with MBC activation at 50 days before perihelion time (ANIS-1 model). Panels (a)–(d) correspond to the observations at the dates indicated in Table 1. The black thick solid lines in panels (a)–(d) indicate the observed isophotes, while the red thin lines correspond to the model. The innermost isophote level in each panel (all expressed in sdu) are (a) 8×10^{-14}, (b) 5.6×10^{-14}, (c) 1.2×10^{-14}, and (d) 1.2×10^{-14}. The isophotes vary by a factor of two between consecutive levels. The lower rightmost panel displays the latitude of the subsolar point as a function of time to perihelion.

(A color version of this figure is available in the online journal.)

The reason is that for P/La Sagra we found a remarkable improvement of the fits for anisotropic ejection coming from a rotating spherical nucleus with high obliquity ($I = 90°$), i.e., the rotation axis located on the orbital plane, and oriented approximately toward the Sun at the time of maximum activity, mimicked the observed isophote field quite accurately. Also, interestingly, this kind of seasonal activity has also been clearly found for 176P for which an orbital obliquity of $\sim 60°$ was derived (Hsieh et al. 2011b), although it cannot be confirmed or rejected for the case of 133P (Hsieh et al. 2010).

Thus, we run the model starting from the parameters obtained for the ISO-2 model, but for a single active area located between two latitude circles on a spherical nucleus with rotational parameters I (obliquity) and Φ (argument of the subsolar meridian at perihelion). We limited the search to values of $I \sim 90°$, with an active area close to the south polar region. The choice of the south or north polar region is arbitrary, as the sense of rotation cannot be determined with this model, and the solution that is valid for a given pole orientation is automatically valid for the opposite pole orientation as well. We only set the south polar region to allow a direct comparison with P/La Sagra. The rotation period was set to 3 hr, which could be appropriate for a small asteroid, but it does not influence the results provided it is much shorter than the ejecta age. Our best fit to the data corresponds to rotational parameters set to $I = 80°$, $\Phi = 260°$, and the active are located southward of $-45°$ (see Figure 3). This anisotropic ejection model (called ANIS-1) also required changes with respect to the ISO-2 model in both the parameter v_0, which must increase to $v_0 = 40$ m s^{-1}, and in the dM/dt profile, which is very close to that of model ISO-2 (see Figure 2, lower rightmost panel). The total mass ejected for the anisotropic model is obviously near that of the ISO-2 model, with a value of 7.5×10^6 kg for $r_{\rm max} = 1$ cm. As can be seen from Figure 3 and the σ values of Table 2, the overall agreement with the observations for this model is better than for isotropic models. Considering the lower-rightmost panels of Figures 2 and 3, the maximum ejection rate occurs approximately 30 days post-perihelion, corresponding to a subsolar point latitude of $\sim -80°$. We have also tried to fit the observations with the ejection parameters of the ISO-1 model (i.e., starting activity suddenly at perihelion), but the results were poorer.

The significance of the results of the anisotropic model is that, in a remarkably similar way to MBCs P/La Sagra and 176P, the ejection pattern of P/2012 T1 is compatible with emission from a single high-latitude region of a nucleus whose rotation axis is near the orbital plane. Also the latitudes of the subsolar point at perihelion (where the outgassing is nearly maximum) are similar ($-60°$ for P/La Sagra and $-70°$ for P/2012 T1). This is important regarding the numerical calculations by Samarasinha (Samarasinha et al. 2004 and references therein)

which indicate that when a dominant active region is present on a comet the rotational angular momentum vector of the spin state evolves toward the orbital direction of the peak outgassing (or the opposite to it), owing to minimum torque reasons. It would then be interesting to see whether this ejection pattern appears again in subsequent perihelion passages and if other MBCs could be interpreted the same way.

5. CONCLUSIONS

The Monte Carlo dust tail model applied to images of P/2012 T1 acquired at La Palma WHT and GTC telescopes allowed us to infer the following conclusions.

1. Taking into account the time evolution of the brightness and morphology of the observed tails, we infer that the ejection of dust from P/2012 T1 has likely been sustained over time, and not produced by an impulsive event. As a result of the modeling we infer that the activity lasted for a period of ∼4–6 months, with a total ejected dust mass of the order of 6–25 $\times$ 10^6 kg, for maximum particle sizes of $r_{\max} = 1$–10 cm.
2. The activity pattern could be compatible with that produced by grains being dragged out from the asteroid surface by sublimating ices. However, the nature of the mechanism(s) triggering and maintaining the activity is unknown. The onset of the activity could have occurred either suddenly near perihelion time, or could have been triggered about a month earlier, and progressed more gradually. We favor this second scenario.
3. The best fits to the data occur for anisotropic ejection scenarios, where the activity takes place mostly from high-latitude locations on a nucleus whose rotating axis is nearly contained on the orbital plane and pointing close to the perihelion point. This scenario is remarkably consistent with that found for P/La Sagra, and agrees with the seasonally driven behavior also found for 176P (Hsieh et al. 2011a). If this behavior is confirmed at future perihelion passages or found on other MBCs, it would then have important consequences regarding their nature and evolutionary path. To date, however, the current MBCs' database is still small so as to establish any firm conclusion.

This Letter is based on observations made with the Gran Telescopio Canarias (GTC), installed on the Spanish Observatorio del Roque de los Muchachos of the Instituto de Astrofísica de Canarias, on the island of La Palma, and on observations made with the William Herschel Telescope (WHT) operated on the island of La Palma by the Isaac Newton Group in the Spanish Observatorio del Roque de los Muchachos of the Instituto de Astrofísica de Canarias.

We are indebted to Pedro J. Gutiérrez for fruitful discussions. This work was supported by contracts AYA2011-30613-C02-01, AYA2012-39691-C02-01, and FQM-4555 (Junta de Andalucía). J. Licandro gratefully acknowledges support from the Spanish "Ministerio de Ciencia e Innovación" projects AYA2011-29489-C03-02 and AYA2012-39115-C03-03.

REFERENCES

Benn, C., Dee, K., & Agócs, T. 2008, Proc. SPIE, 7014, 70146X
Bing, Y., & Hsieh, H. H. 2011, ApJL, 737, L39
Cepa, J. 2010, Highlights of Spanish Astrophysics V, Astrophysics and Space Science Proceedings (Berlin: Springer), 15
Finson, M., & Probstein, R. 1968, ApJ, 154, 327
Fukugita, M., Ichikawa, T., Gunn, J. E., et al. 1996, AJ, 111, 1748
Fulle, M. 1989, A&A, 217, 283
Fulle, M., Colangeli, L., Agarwal, J., et al. 2010, A&A, 522, 63
Giblin, I. 1998, P&SS, 46, 921
Haghighipour, N. 2009, M&PS, 44, 1863
Hsieh, H. H., Ishiguro, M., Lacerda, P., & Jewitt, D. 2011a, AJ, 142, 29
Hsieh, H. H., Jewitt, D., & Ishiguro, M. 2009, AJ, 137, 157
Hsieh, H. H., Jewitt, D., Lacerda, P., et al. 2010, MNRAS, 403, 363
Hsieh, H. H., Meech, K., & Pittichova, J. 2011b, ApJL, 736, L18
Hsieh, H. H., Yang, B., & Haghighipour, N. 2012, ApJ, 744, 9
Ishiguro, M., Hanayama, H., Hasegawa, S., et al. 2011, ApJL, 740, L11
Jewitt, D. 2012, AJ, 143, 21
Jewitt, D., Weaver, H., Agarwal, J., et al. 2010, Natur, 467, 817
Jewitt, D., Weaver, H., Mutchler, M., et al. 2011, ApJL, 733, L4
Jewitt, D., Yang, B., & Haghighipour, N. 2009, AJ, 137, 4313
Licandro, J., Campins, H., Tozzi, G. P., et al. 2011, A&A, 532, 65
Licandro, J., de León, J., Moreno, F., et al. 2013, A&A, 550, A17
Manchado, A., Fuentes, F. J., Prada, F., et al. 1998, Proc. SPIE, 3354, 448
Moreno, F. 2009, ApJS, 183, 33
Moreno, F., Lara, L. M., Licandro, J., et al. 2011a, ApJL, 738, L16
Moreno, F., Licandro, J., & Cabrera-Lavers, A. 2012a, ApJL, 761, L12
Moreno, F., Licandro, J., Ortiz, J. L., et al. 2011b, ApJ, 738, 130
Moreno, F., Licandro, J., Tozzi, G.-P., et al. 2010, ApJL, 718, L132
Moreno, F., Pozuelos, F., Aceituno, F., et al. 2012b, ApJ, 752, 136
Onose, N., & Fujiwara, A. 2004, M&PS, 39, 321
Samarasinha, N. H., Mueller, B. E. A., Belton, M. J. S., & Jorda, L. 2004, in Comets II, ed. M. C. Festou, H. U. Keller, & H. A. Weaver (Tucson, AZ: Univ. Arizona Press), 281
Snodgrass, C., Tubiana, C., Vincent, J.-B., et al. 2010, Natur, 467, 814
Stevenson, R., Kramer, E. A., Bauer, J. M., et al. 2012, ApJ, 759, 142
Tulloch, S. 1998, Isaac Newton Group of Telescopes, La Palma, Technical Note 119
Wainscoat, R., Hsieh, H., Denneau, L., et al. 2012, CBET, 3252, 1

The Astrophysical Journal, 781:118 (5pp), 2014 February 1 doi:10.1088/0004-637X/781/2/118

INTERMITTENT DUST MASS LOSS FROM ACTIVATED ASTEROID P/2013 P5 (PANSTARRS)

F. Moreno[1], J. Licandro[2,3], C. Álvarez-Iglesias[2,3,4], A. Cabrera-Lavers[2,3,4], and F. Pozuelos[1]
[1] Instituto de Astrofísica de Andalucía, CSIC, Glorieta de la Astronomía s/n, E-18008 Granada, Spain; fernando@iaa.es
[2] Instituto de Astrofísica de Canarias, c/Vía Láctea s/n, E-38200 La Laguna, Tenerife, Spain
[3] Departamento de Astrofísica, Universidad de La Laguna (ULL), E-38205 La Laguna, Tenerife, Spain
[4] GTC Project, E-38205 La Laguna, Tenerife, Spain
Received 2013 November 29; accepted 2013 December 16; published 2014 January 16

ABSTRACT

We present observations and models of the dust environment of activated asteroid P/2013 P5 (PANSTARRS). The object displayed a complex morphology during the observations, with the presence of multiple tails. We combined our own observations, all made with instrumentation attached to the 10.4 m Gran Telescopio Canarias on La Palma, with previously published *Hubble Space Telescope* images to build a model aimed at fitting all the observations. Altogether, the data cover a full three month period of observations which can be explained by intermittent dust loss. The most plausible scenario is that of an asteroid rotating with the spinning axis oriented perpendicular to the orbit plane and losing mass from the equatorial region, consistent with rotational break-up. Assuming that the ejection velocity of the particles ($v \sim 0.02$–0.05 m s^{-1}) corresponds to the escape velocity, the object diameter is constrained to ∼30–130 m for bulk densities 3000–1000 kg m^{-3}.

Key words: methods: numerical – minor planets, asteroids: individual (P/2013 P5 (PANSTARRS))

Online-only material: color figures

1. INTRODUCTION

Activated asteroid P/2013 P5 (PANSTARRS) was discovered by Pan-STARRS survey as a 21st magnitude comet on 2013 August 15.50 (Micheli et al. 2013). This object has a typical inner-belt asteroid orbit but displays a cometary-like tail, so it can be classified as a main-belt comet (MBC). The object shares similar orbital elements with previously discovered disrupted asteroid P/2010 A2 (LINEAR; Jewitt et al. 2010; Snodgrass et al. 2010; Moreno et al. 2013), both belonging to the Flora collisional family. The origin of the activity taking place in the MBCs is unknown for most of the those objects. While some have been associated with impulsive events, such as collisions with another body or rotational break-up, others are most likely linked to water–ice sublimation. For reviews on those objects and the likely mechanisms involved in their activity, see, e.g., Hsieh & Jewitt (2006), Bertini (2011), and Jewitt (2012).

A series of stunning images from the *Hubble Space Telescope* (*HST*; Jewitt et al. 2013) at two epochs reveal the asteroid as a multiple-tailed object. Using the Finson–Probstein formalism, these tails have been associated with a series of ejection events at different dates, and the likely cause of the activity has been linked to a rotational disruption. In this paper, we present our own data, which were acquired two months after the *HST* observations, and combine them with the *HST* data. Our aim is then to monitor the activity scenario during a longer time frame and, mostly, to characterize the dust activity in terms of the time variation of the mass loss, particle size distribution, and ejection velocities. Models mimicking an equatorial mass loss from the object have been incorporated in an attempt to investigate if a rotational disruption could be compatible with the ejection scenario.

2. OBSERVATIONS AND DATA REDUCTION

Images of P/2103 P5 through the Sloan r' and g' filters were recorded under photometric and excellent seeing conditions (0.″8–0.″9) on the nights of 2013 October 7 and 2013 November 8 (only r' images). We used the Optical System for Image and Low Resolution Integrated Spectroscopy (OSIRIS) camera-spectrograph (Cepa et al. 2000; Cepa 2010) at the Gran Telescopio Canarias (GTC). The OSIRIS instrument consists of two Marconi CCD detectors, each with 2048 × 4096 pixels and a total unvignetted field of view of 7.′8 × 7.′8. The plate scale was 0.″127 pixel^{-1}, but we used a 2 × 2 pixel binning in order to improve the signal-to-noise ratio, so that the spatial resolution of the images becomes 222 km pixel^{-1} and 270 km pixel^{-1} at the observation dates. The images were bias and flat-field corrected using standard techniques, and calibrated in flux using standard stars. A sequence of five images per filter were obtained. An average image was then obtained from the available images by shifting and stacking the frames with respect to a reference frame by taking into account the object's sky motion. We estimate that as a result of both the flux calibration and the stacking procedure, the total flux uncertainty in the combined images is ∼0.1 mag. The final combined images are shown in Figure 1. The log of the observations is shown in Table 1. In that table, the apparent (m) and absolute (H) magnitudes of a region of 10 pixel aperture radius (2.″5 diameter) centered on the asteroid optocenter of each image is given. The absolute magnitude is given as $H = m - 2.5\log(\Delta r_h) - \Phi(\alpha)$, where Δ and r_h are the geocentric and heliocentric distances of the asteroid, and $\Phi(\alpha)$ is the phase function, which is assumed to be that of an S-type asteroid, as most objects in the inner asteroid belt. The quantity $\Phi(\alpha)$ is computed using the Bowell et al. (1989) formalism, using a phase function parameter $g = 0.25$, which is typical of S-type asteroids, the most common objects in the inner belt. The phase terms become $\Phi(17.^\circ7) = -0.81$ on October 7, and $\Phi(27.^\circ0) = -1.07$ on November 8, and the absolute magnitude $H_{r'}$ converges to the value $H_{r'} = 18.0 \pm 0.1$ in both dates. To compare this value to the reported H_V by Jewitt et al. (2013; $H_V = 18.69$ on September 10 and $H_V = 18.54$ on September 23), we need a transformation from r' to V magnitudes. Using the transformation equations of Fukugita et al. (1996) and the magnitude of the Sun in the standard Johnson–Cousins filter ($V_\odot = -26.75$; Cox 2000), we derive $r'_\odot = -26.96$. If the object follows a spectral dependence on wavelength similar to that of the Sun within the

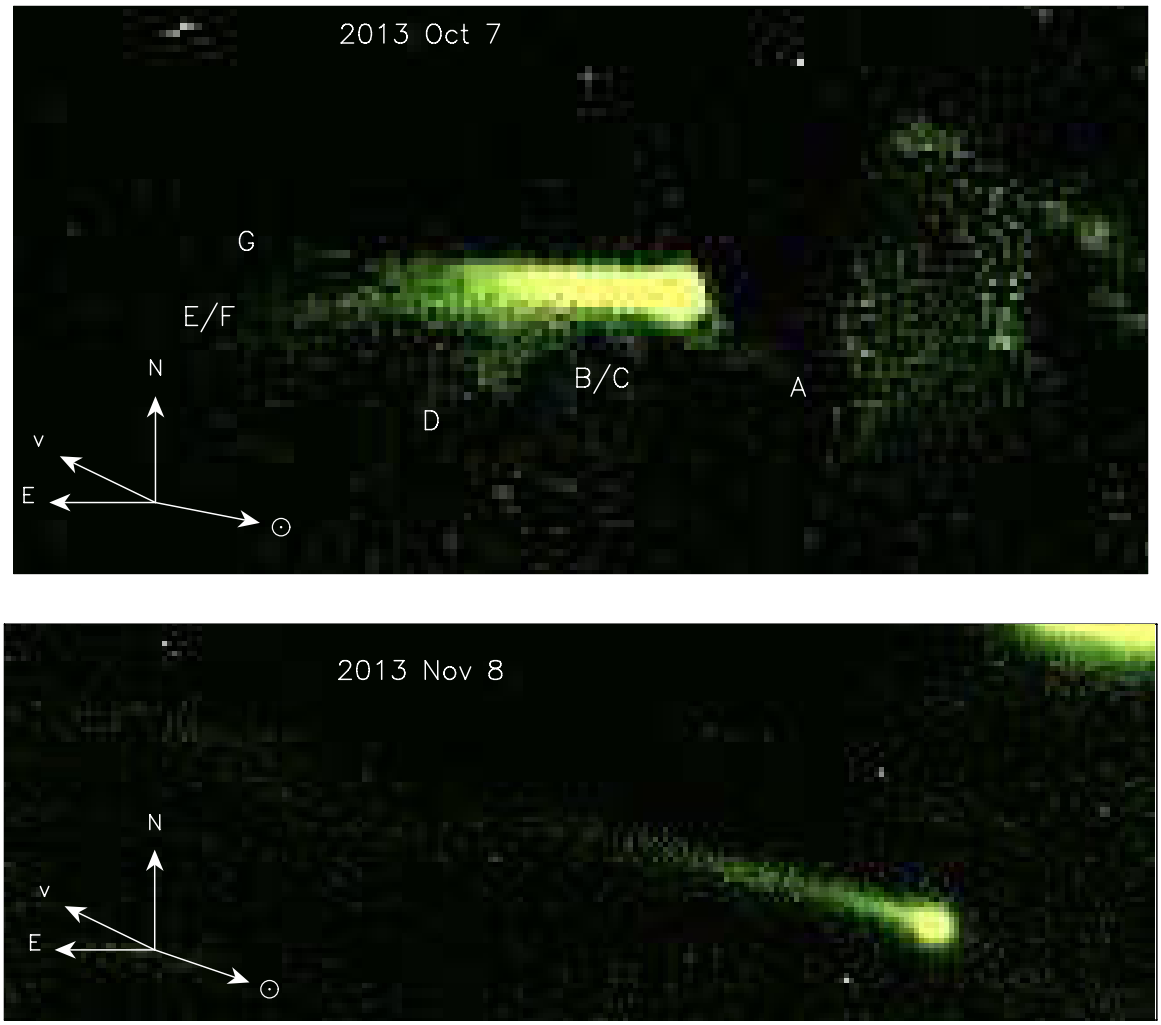

Figure 1. Stacked r' Sloan OSIRIS@GTC images of P/2013 P5 on the nights of UT 2013 October 7 (upper panel) and 2013 November 8 (lower panel). The dimensions of the upper and lower images are 35,488 × 17,744 km and 61,939 × 21,275 km, respectively. In the upper panel the different tails are marked. The nomenclature follows that of Jewitt et al. (2013). Tails marked as B/C and E/F are actually a blend of tails B and C, and E and F, respectively, as displayed in Figure 1 of Jewitt et al. (2013); see also Figure 2 in this paper. Note that tail G is the youngest tail and does not appear in the *HST* observations. The directions of celestial north and east are indicated, as well as the direction to the Sun and the asteroid velocity vector.

(A color version of this figure is available in the online journal.)

Table 1
Log of the Observations

Date (UT)	r_h (AU)	Δ (AU)	α (°)	δ (°)	m	H
2013 Oct 7 22:18	2.077	1.204	17.7	−4.10	$g' = 21.3 \pm 0.1$	18.5 ± 0.1
2013 Oct 7 22:26	2.077	1.204	17.7	−4.10	$r' = 20.8 \pm 0.1$	18.0 ± 0.1
2013 Nov 8 21:04	2.038	1.462	27.0	−2.68	$r' = 21.5 \pm 0.1$	18.0 ± 0.1

V and r' bandpasses (neutral color), the V magnitudes can be obtained from the r' magnitudes by adding 0.21 mag. Then, we would get $H_V = 18.2$. This would indicate a brightness increase since September 10 of ∼0.5 mag. This result immediately excludes a single event mechanism of dust ejection from the asteroid, as such event would have resulted in a brightness decrease as a function of time. Assuming that the brightness is entirely due to the asteroid and not to the surrounding dust, this would lead to an asteroid diameter of ∼590 m for a geometric albedo of $p_v = 0.29$, typical of Flora family asteroids (Masiero et al. 2013). We will, however, assume that such brightness is entirely associated with the presence of dust surrounding the asteroid, and not to the presence of a nucleus, its contribution to the brightness being negligible. A justification of this hypothesis is given in the Results section on the basis of the low ejection velocities of the dust particles that we found in the modeling procedure.

3. THE MODEL

To perform the analysis of the images, we used our direct Monte Carlo dust tail model, as described in previous works (e.g., Moreno et al. 2012b; Fulle et al. 2010). In that model, we compute the trajectory of a large number of particles after being ejected from an asteroidal or cometary surface. Those particles

move under the sole influence of solar gravity and radiation pressure forces, describing a Keplerian orbit around the Sun. The orbital elements of each ejected particle are functions of the ejection velocity and the β parameter (e.g., Fulle 1989). This parameter can be written as $\beta = C_{\rm pr} Q_{\rm pr}/(2\rho r)$, where $C_{\rm pr} = 1.19 \times 10^{-3}$ kg m^{-2}, $Q_{\rm pr}$ is the radiation pressure coefficient, and ρ is the particle density. The position of each particle in the plane of sky is then computed according to its orbital elements, and its contribution to the tail or coma brightness is evaluated, as a function of its size and geometric albedo. Owing to the many input models, we are forced to set some of them to a specific value. Then, the particles are considered spherical, their density is assumed at $\rho_p = 1000$ kg m^{-3}, and their refractive index is set at $1.88 + 0.71i$, which is typical of carbonaceous composition (Edoh 1983). Using Mie theory, we find that the geometric albedo is $p_v \sim 0.04$, and that the radiation pressure coefficient is $Q_{\rm pr} \sim 1$ for particles of radius $r \gtrsim 1\,\mu$m (Moreno et al. 2012b, their Figure 5). These choices of density and geometric albedo are highly arbitrary, since we do not know their real values, and were made actually to facilitate comparison with other MBCs analyzed, for which we assumed such values (e.g., Moreno et al. 2010, 2013).

We start by assuming an asteroid nucleus which is losing mass from its equator, where centrifugal acceleration is maximum, uniformly in longitude. This would correspond to a mass loss scenario driven by a rotational disruption, as suggested by Jewitt et al. (2013). This introduces three more model parameters to characterize the rotation properties: the orientation of the spinning axis with respect to the orbit plane, which is given by the obliquity, I, and the argument of the subsolar meridian at perihelion, Φ, and the rotational period, P (simple rotation is assumed). The nucleus is presumably very small, so that the rotation period should be very short, of the order of $P \lessapprox 3$ hr (Pravec et al. 2002). We assume $P = 3$ hr. The exact value of P does not influence the results if the tail age is much longer than that, as can be anticipated from the analysis by Jewitt et al. (2013). The rotation parameters I and Φ are set initially to $I = 0^\circ$ and $\Phi = 0^\circ$. To simplify, we also set all the possible time-variable parameters (except the dust mass loss rate) to a constant value. Thus, the size distribution power index is set to $\alpha = -3.5$, and the minimum and maximum particle sizes to 50 μm and 30 cm, respectively. These values were set after extensive experimentation with the code. Regarding velocities, we employed a function of the kind $v(\beta) = v_0 \beta^\gamma$, where we adopt $\gamma = 1/8$, i.e., a very weak dependence of $v(\beta)$ on β consistent with Moreno et al. (2012a) in their analysis of disrupted asteroid P/2012 F5 (Gibbs). The parameter v_0 and the dust mass loss rate as a function of the heliocentric distance are the fitting parameters.

4. RESULTS

The times of significant dust ejection are first estimated from the best fitting synchrones to the dust tails. This procedure was applied to the *HST* images first, owing to their superb spatial resolution, and then to the GTC images. In the GTC images, the tails named A to F in Jewitt et al. (2013, see Figure 2), the oldest being A, are sometimes blended because of poorer spatial resolution. Thus, in the GTC image of 2013 October 7, we have A, C/B, D, and E/F (see Figure 1). In addition, a younger tail not seen in the *HST* images (named G) appears. On the other hand, the last GTC image of 2013 November 8 does not show the complexity of the others, displaying a single and narrow tail extending to the northeast (see Figure 1). This is surely connected to the fact that the angle between Earth and the asteroid orbital plane (δ) is smaller than at the other dates (see Table 1).

The procedure was then to try different mass loss rates at those times, and set different ejection speeds (distinct v_0) until a good fit to the whole data set (*HST*+GTC) is found in terms of dust tail brightnesses. The synthetic images corresponding to the GTC data are convolved with a point spread Gaussian function in order to take into account the seeing conditions during the observations. During the fitting procedure, we realized that to fit the length of tail "G" in the GTC 2013 October 7 image, we needed to set $r_{\rm min} = 10\,\mu$m at the time of its peak emission, this being the only modification to the particle sizes in the time interval of ejection.

The results of the fits to the *HST* and GTC images are shown in Figures 2 (left panels) and 3. The model reproduces accurately all the features present in the *HST* and GTC images in terms of brightness, length, and width. The dust loss rate profile corresponding to those fits is displayed in Figure 4, resulting in a total dust mass loss of 10^7 kg. The best fitted ejection velocity is given by $v = 0.12\beta^{1/8}$ m s^{-1}. This corresponds to ejection velocities ranging from about 0.02 m s^{-1} to 0.07 m s^{-1}, for 30 cm to 50 μm particles. We have also attempted to fit the images using a constant value for the ejection velocity for all the particles. We found very similar results to those of Figures 2 (left panels) and 3 when a constant ejection velocity in the range 0.02–0.05 m s^{-1} is assumed. Regarding the maximum particle size ejected, we have verified that models having $r_{\rm max} \gtrapprox 1$ cm are compatible with the observations, provided the total mass ejected is modified accordingly. Thus, if $r_{\rm max}$ is set to its lowest acceptable limit, $r_{\rm max} = 1$ cm, the dust mass loss rate would be a factor of ~5 smaller than that shown in Figure 4, i.e., the total dust mass loss would become 2×10^6 kg. This constitutes the lower limit of ejected mass for the assumed particle density of 1000 kg m^{-3} and geometric albedo $p_v = 0.04$.

The range of possible ejection velocities is 0.02–0.05 m s^{-1}. If these values are associated with escape velocities, this translates to possible asteroid diameters (assumed spherical) in the range 30–134 m, and masses in the range 4.6×10^7–1.3×10^9 kg, for assumed bulk densities of 1000–3000 kg m^{-3}. This size estimate is well below the upper limit of 480 ± 80 m diameter derived by Jewitt et al. (2013) on the basis of magnitude measurements of the central condensation. As those authors recognize, this is an upper limit as the measurements could include dust near the nucleus. We believe that it is indeed the case, such that the magnitude of the central condensation is in fact attributable mainly to the dust around the nucleus and not to the nucleus itself, whose contribution must be minimal according to the small size imposed by the escape velocity.

Concerning the rotational parameters of the asteroid, we started, as mentioned, from a scenario in which the rotating axis is perpendicular to the orbit plane ($I = 0^\circ$). We have generated synthetic images by varying both I and Φ in the full ranges, 0°–180°, and 0°–360°, respectively. We found that the only possible fits correspond to obliquities of either $I \sim 0^\circ$ or $I \sim 180^\circ$, independently of Φ, i.e., with the rotating axis nearly perpendicular to the orbit plane, either pointing to the north or the south of the plane (prograde or retrograde motion). When the value of I departs significantly from either 0° or 180°, tails wider than observed are obtained.

Finally, we have also attempted to reproduce the observed brightness pattern using an isotropic ejection model, and the

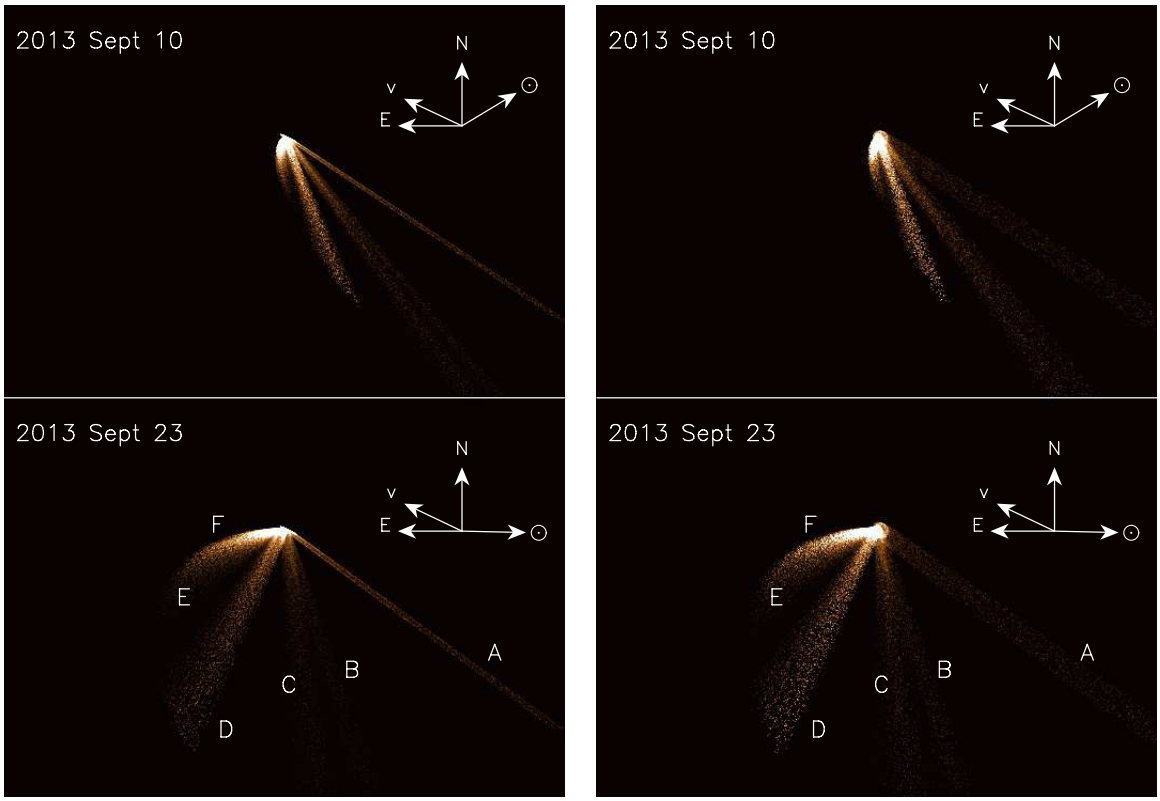

Figure 2. Model simulations of the *Hubble Space Telescope* images by Jewitt et al. (2013, see their Figure 1) at two epochs. The left panels correspond to an anisotropic ejection model, where the particles are ejected from the equator of a rotating nucleus with spin axis perpendicular to the orbit plane. The right panels correspond to an isotropic ejection model, with the same input parameters as the anisotropic model. In the lower panels, each tail is labeled according to the nomenclature by Jewitt et al. (2013). The panels are 23000 km in width, the same as in Figure 1 of Jewitt et al. (2013), to facilitate comparison. The directions of celestial north and east are indicated, as well as the direction to the Sun and the asteroid velocity vector.

(A color version of this figure is available in the online journal.)

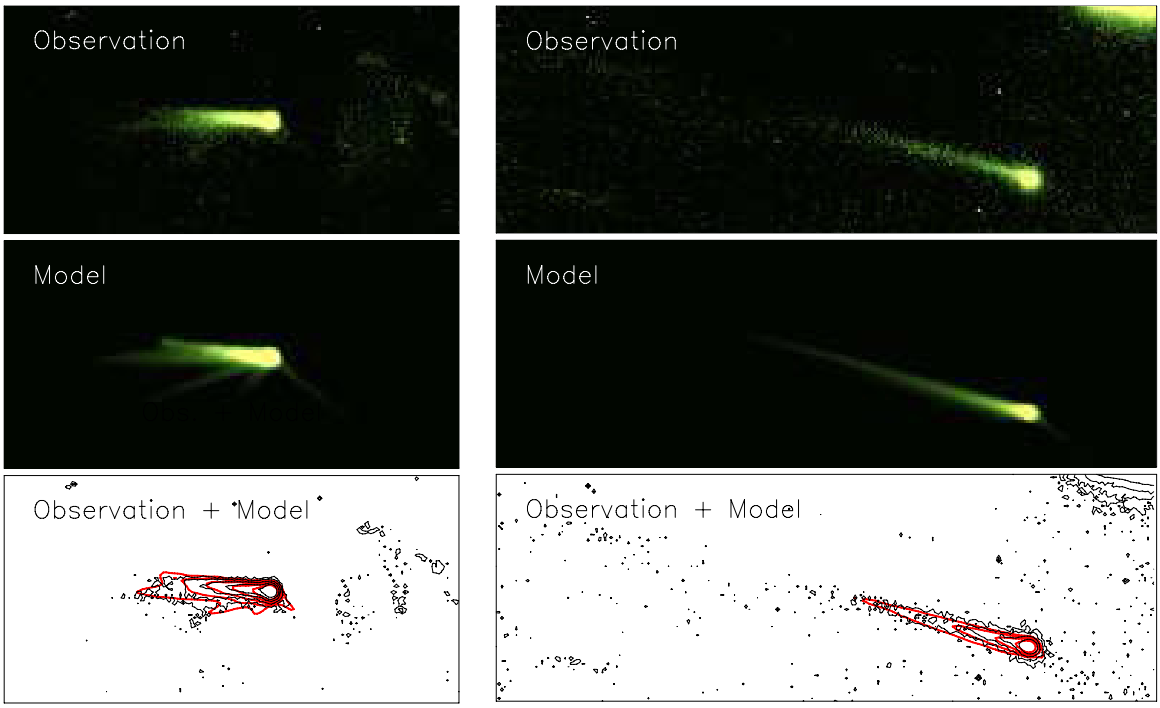

Figure 3. Left panels: observation and model simulation of the 2013 October 7 image. The bottom panel shows the comparison of the observed and modeled isophotes. The innermost isophote level is 3.8×10^{-14} solar disk intensity units, and the isophotes decrease by a factor of two between consecutive levels. Right panels: observation and model simulation of the 2013 November 8 image. The bottom panel shows the comparison of the observed and modeled isophotes. The innermost isophote level is 2×10^{-14} solar disk intensity units, and the isophotes decrease by a factor of two between adjacent levels. The dimensions of the images are the same as in Figure 1.

(A color version of this figure is available in the online journal.)

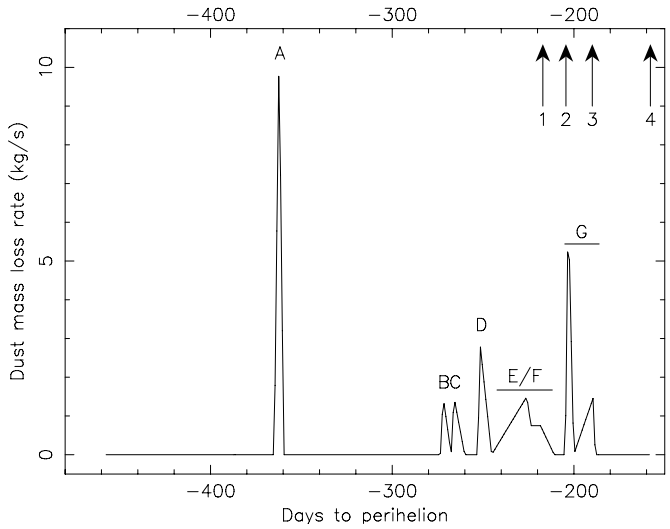

Figure 4. Modeled dust mass loss rate from P/2013 P5 as a function of time to perihelion. The sharp peaks of dust ejection are associated with the tails labeled "A" to "G" (see Figures 2 and 3). The arrows indicate the observation dates of the *HST* (1 and 2) and the GTC (3 and 4) data.

results we obtained for the GTC images are quite similar to those obtained with the above (anisotropic) model. However, the *HST* data are not well reproduced with this isotropic ejection model, as the oldest tails, especially "B," "C," and "A," become significantly broader than observed. This is clearly shown in Figure 2 (right panels).

5. CONCLUSIONS

From the Monte Carlo dust tail modeling of the observations of activated P/2013 P5 (PANSTARRS) we can extract the following conclusions.

1. The object has been subjected to an intermittent dust mass loss, most likely associated with a rotational disruption. This is confirmed from the analysis of both *HST* and GTC images. The total dust mass released was of the order of 10^7 kg, for particle density of 1000 kg m^{-3} and geometric albedo $p_v = 0.04$.
2. The model of rotational disruption, based on simulations of an object that loses mass from its equatorial region, and whose rotational axis is perpendicular to its orbit plane, reproduces to the last detail the observed complex brightness pattern at four different epochs of *HST* and GTC observations. For obliquities different from 0° or 180°, the fits get much worse. On the other hand, an isotropic ejection model does not fit the *HST* data because it produces much more diffuse tails than observed.
3. The ejection velocities are very low, of the order of 0.02–0.05 m s^{-1}. This places the limit on the size of the object to be in the range 30–134 m for assumed densities of 3000–1000 kg m^{-3}.

This article is based on observations made with the Gran Telescopio Canarias (GTC), installed in the Spanish Observatorio del Roque de los Muchachos of the Instituto de Astrofísica de Canarias, in the island of La Palma.

This work was supported by contracts AYA2011-30613-C02-01, AYA2012-39691-C02-01, and FQM-4555 (Proyecto de Excelencia, Junta de Andalucía). J. Licandro acknowledges financial support from the Spanish Ministry of Economy and Competitiveness (MINECO) under the 2011 Severo Ochoa Program MINECO SEV-2011-0187 and AYA2012-39115-C03-03.

REFERENCES

Bertini, I. 2011, P&SS, 59, 365
Bowell, E., Hapke, B., Domingue, D., et al. 1989, in Asteroids II, ed. R. P. Binzel, T. Gehrels, & M. S. Matthews (Tucson, AZ: Univ. Arizona Press), 524
Cepa, J. 2010, in Astrophysics and Space Science Proceedings, Highlights of Spanish Astrophysics V, ed. J. M. Diego, L. J. Goicoechea, & J. Ignacio Gonz (Berlin: Springer), 15
Cepa, J., Aguiar, M., Escalera, V., et al. 2000, Proc. SPIE, 4008, 623
Cox, A. 2000, Allen's Astrophysical Quantities (4th ed., New York: Springer)
Edoh, O. 1983, PhD thesis, Univ. Arizona
Fukugita, M., Ichikawa, T., Gunn, J. E., et al. 1996, AJ, 111, 1748
Fulle, M. 1989, A&A, 217, 283
Fulle, M., Colangeli, L., Agarwal, J., et al. 2010, A&A, 522, 63
Hsieh, H. H., & Jewitt, D. 2006, Sci, 312, 561
Jewitt, D. 2012, AJ, 143, 21
Jewitt, D., Agarwal, J., Weaver, H., et al. 2013, ApJL, 778, L21
Jewitt, D., Weaver, H., Agarwal, J., et al. 2010, Natur, 467, 817
Masiero, J. R., Mainzer, A. K., Bauer, J. M., et al. 2013, ApJ, 770, 7
Micheli, M., Tholen, D. J., Primak, N., et al. 2013, MPEC, 2013-Q37
Moreno, F., Licandro, J., & Cabrera-Lavers, A. 2012a, ApJL, 761, L12
Moreno, F., Licandro, J., & Ortiz, J. L. 2013, ApJ, submitted
Moreno, F., Licandro, J., Tozzi, G.-P., et al. 2010, ApJL, 718, L132
Moreno, F., Pozuelos, F., Aceituno, F., et al. 2012b, ApJ, 752, 136
Pravec, P., Harris, A. W., & Michalowski, T. 2002, in Asteroids III, ed. W. F. Bottke, A. Cellino, P. Paolicchi, & R. Binzel (Tucson, AZ: Univ. of Arizona Press), 113
Snodgrass, C., Tubiana, C., Vincent, J.-B., et al. 2010, Natur, 467, 814

Long-Period Comets

- **Paper VI.**
  On the dust environment of comet C/2012 S1 (ISON) from 12 AU pre-perihelion to the end of its activity around perihelion.
  Moreno, F.; Pozuelos, F.J.; Aceituno, F.; Casanova, V.; Duffard, R.; López-Moreno, J.J.; Molina, A.; Ortiz, J.L.; Santos-Sanz, P.; Sota, A.; Diepvens, A.; San Segundo, A.; Bell, C.; Labordena, C.; Bryssinck, E.; Cortés, E.; Reina, E.; García, F.; Gómez, F.; Limón, F.; Soldán, F.; Tifner, F.; Muler, G.; Almendros, I.; Aledo, J.; Bel, J.; Carrillo, J.; Castellano, J.; Curto, J.; Gaitan, J.; Salto, J.L.; Lopesino, J.; Lozano, J.; Hernández, J.F.; González, J.J.; Martín, J.L.; Aymamí, J.M.; Bosch, J.M.; Fernández, J.M.; Vidal, J.R.; Montoro, L.; Tremosa, L.; Campas, M.; Canales, O.; Dekelver, P.J.; Benavides, R.; Naves, R.; Castillo, R.; Climent, T.; Cupillari, T.; Yanamandra-Fisher, P.
  The Astrophysical Journal, Volume 791, Issue 2, article id. 118, 16 pp. (2014).

The Astrophysical Journal, 791:118 (16pp), 2014 August 20 doi:10.1088/0004-637X/791/2/118

ON THE DUST ENVIRONMENT OF COMET C/2012 S1 (ISON) FROM 12 AU PRE-PERIHELION TO THE END OF ITS ACTIVITY AROUND PERIHELION

F. Moreno[1], F. Pozuelos[1], F. Aceituno[1], V. Casanova[1], R. Duffard[1], J. J. López-Moreno[1], A. Molina[1,4], J. L. Ortiz[1], P. Santos-Sanz[1], A. Sota[1], A. Diepvens[2], A. S. Segundo[2], C. Bell[2], C. Labordena[2], E. Bryssinck[2], E. Cortés[2], E. Reina[2], F. García[2], F. Gómez[2], F. Limón[2], F. Soldán[2], F. Tifner[2], G. Muler[2], I. Almendros[2], J. Aledo[2], J. Bel[2], J. Carrillo[2], J. Castellano[2], J. Curto[2], J. Gaitan[2], J. L. Salto[2], J. Lopesino[2], J. Lozano[2], J. F. Hernández[2], J. J. González[2], J. L. Martín[2], J. M. Aymamí[2], J. M. Bosch[2], J. M. Fernández[2], J. R. Vidal[2], L. Montoro[2], L. Tremosa[2], M. Campas[2], O. Canales[2], P. J. Dekelver[2], R. Benavides[2], R. Naves[2], R. Castillo[2], T. Climent[2], T. Cupillari[2], and P. Yanamandra-Fisher[3]

[1] Instituto de Astrofísica de Andalucía, CSIC, Glorieta de la Astronomía s/n, E-18008 Granada, Spain
[2] Amateur Astronomical Association Cometas-Obs
[3] Space Science Institute, Boulder, CO 80301, USA
Received 2014 June 3; accepted 2014 July 2; published 2014 August 5

ABSTRACT

A Monte Carlo dust tail model has been applied to extract the dust environment parameters of the comet C/2012 S1 (ISON) from both Earth-based and *SOHO* LASCO C3 observations, performed from about six astronomical units (AU) inbound, to just after perihelion passage, when only a small portion of the original comet nucleus has survived in the form of a cloud of tiny particles. The early Afρ and image data are consistent with particle ejection from an extended active area located at latitudes 35°N to 90°N (for a prograde rotating nucleus), with the spin axis having a large obliquity ($I \sim 70°$). This configuration nicely fits the early images and Afρ data until 3.9 AU inbound, when the emission should become isotropic in order to fit the data. The analysis of LASCO images reveals that, assuming an original nucleus of $R_N = 500$ m with $\rho = 1000$ kg m^{-3}, at least half of its mass was vaporized when the comet was at about 17 $R_\odot$ inbound. We conclude that at that time the nucleus suffered a cataclysmic fragmentation releasing a huge amount of material of 2.3×10^{11} kg, equivalent to a sphere of 380 m in radius with density 1000 kg m^{-3}. The surviving material after perihelion passage consists of very small dust particles of 0.1–50 μm in radius with a total mass of just 6.7×10^8 kg.

Key words: comets: general – comets: individual (C/2012 S1 (ISON)) – methods: numerical – Oort Cloud

Online-only material: color figures

1. INTRODUCTION

The comet C/2012 S1 (ISON, comet ISON hereafter) was discovered by Nevski & Novichonok (2012) as a diffuse object of 8″ coma on September 21.06 UT with a 0.4 m reflector of the International Scientific Optical Network (ISON) near Kislovodsk, Russia. Just after its discovery, it soon attracted attention as an Oort cloud comet with a very short perihelion distance of just 2.7 $R_\odot$ ($R_\odot$ = solar radius, 6.955×10^8 m).

At the time of discovery, ISON was at 6.3 AU from the Sun, at a visual magnitude around 19. Given its level of activity at such a large distance and its predicted extreme proximity to the Sun at perihelion, it was expected to become a very bright target for Earth observers, becoming even brighter than the full moon. However, at around 4.2 AU inbound, the comet started to show an unexpected decrease in activity compared to its original tendency that led to a visual magnitude higher than the visual limit when it started to approach perihelion at 1–0.7 AU. After a quiescent period, the comet then experienced a strong outburst of activity at ∼0.65 AU, in which the HCN and OH production rates increased substantially, by more than an order of magnitude, over 48 hr (Biver at al. 2013; Opitom et al. 2013; Agúndez et al. 2014). On November 20, the comet was too close to the Sun for Earth-based observers, but it entered the field of view of the *Solar Terrestrial Relations Observatory* spacecraft at a heliocentric distance of 0.43 AU, apparently undisrupted, clearly displaying both dust and ion tails. Later on, on November 27, the comet entered the *Solar and Heliospheric Observatory* (*SOHO*) Large Angle and Spectrometric Coronagraph Experiment (LASCO) field of view, at a distance of 0.15 AU, showing two distinct tails, one northern component consisting of an intense narrow spike, and a much broader and diffuse southern branch. Late on November 27 and during the first half of November 28, the comet head displayed strong saturation effects in the *SOHO* LASCO C3 camera, possibly associated with either disruption of the nucleus (by tidal forces or thermal stress) and/or profuse vaporization of dust particles due to high temperatures. The *SOHO* LASCO C3 camera images for dates later than November 28 14:00 UT did not show an apparent nucleus. When the comet emerged from the C2 and C3 coronagraphs it displayed a bilobed tail, with some dust in between, which weakened very fast and almost disappeared when the comet finally left the C3 field of view on December 1.

In this paper, we analyze dust tail images of the comet taken from several observatories, and combine them with Afρ data obtained by the amateur association *Cometas-Obs*. We also analyze publicly available pre- and post-perihelion *SOHO* LASCO C3 images in order to have a complete view of the evolution of the dust until the comet was finally disrupted. To perform the analysis and to derive the dust parameters, we use our Monte Carlo dust tail code as in previous papers (e.g., Moreno et al. 2012, 2013).

[4] Also at Facultad de Ciencias, Universidad de Granada, Campus Universitario Fuentenueva, Calle Fuente Nueva, s/n, E-18001 Granada, Spain.

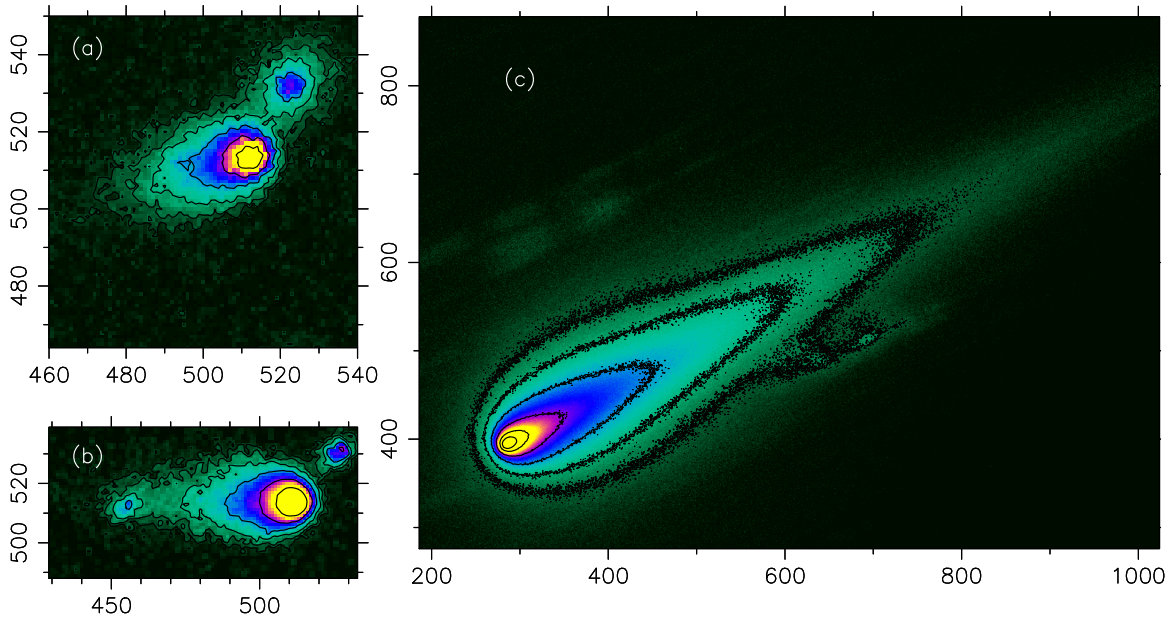

Figure 1. Panels (a) and (b): images of the comet ISON obtained at the 1.52 m telescope of the Observatorio de Sierra Nevada on 2013 February 14 and May 1, respectively. Panel (c): image obtained on 2013 October 10 with a CCD attached to the 1.23 m telescope at the Calar Alto Observatory. In all panels, north is up, and east is to the left. For more details, see Table 1.

(A color version of this figure is available in the online journal.)

Table 1
Log of the Image Observations

Date (UT)	r_h (AU)	Δ (AU)	PsAng (°)	Phase (°)	Obs/Telescope	Filter	Scale (arcsec pixel^{-1})
2013 Feb 14.04	4.784	4.008	106.433	8.01	OSN 1.52 m	Red	0.46
2013 May 01.86	3.887	4.326	90.206	12.70	OSN 1.52 m	Red	0.46
2013 Oct 06.21	1.551	1.996	291.832	29.47	OSN 1.52 m	Red	0.46
2013 Oct 10.22	1.472	1.876	292.131	31.89	CAHA 1.23 m	Red	0.50
2013 Nov 06.23	0.866	1.091	293.772	59.57	OSN 1.52 m	Red	0.46
2013 Nov 13.20	0.674	0.937	292.274	73.74	CAHA 2.2 m-CAFOS	Red	0.53
2013 Nov 15.24	0.613	0.904	291.202	78.84	OSN 0.90 m	Red	0.387
2013 Nov 28.02	0.081	0.960	251.896	106.71	*SOHO* LASCO C3	Clear	56.25
2013 Nov 28.07	0.077	0.962	250.817	106.11	*SOHO* LASCO C3	DeepRed	56.25
2013 Nov 28.62	0.026	0.991	221.337	80.19	*SOHO* LASCO C3	DeepRed	56.25
2013 Nov 28.63	0.025	0.991	219.657	78.52	*SOHO* LASCO C3	Clear	56.25
2013 Nov 29.26	0.057	0.956	11.574	120.65	*SOHO* LASCO C3	Clear	56.25
2013 Nov 29.28	0.059	0.955	10.705	121.12	*SOHO* LASCO C3	DeepRed	56.25
2013 Nov 30.21	0.128	0.902	351.353	127.80	*SOHO* LASCO C3	Clear	56.25

2. THE OBSERVATIONS

Our ground-based image data set was acquired at several telescopes from different observatories. Unless otherwise noted, all observations refer to CCD images taken through red Johnson–Cousins filters. We used the 1.52 m and 0.9 m telescopes at the Observatorio de Sierra Nevada, and the 1.23 m and 2.2 m telescopes at the Calar Alto Observatory Spain. In addition, we used several images from the *SOHO* LASCO C3 coronagraph when the comet was near perihelion. A summary of all the image observations is given in Table 1, where we provide information about the circumstances, as well as some technical aspects, of the observations. The ground-based data reduction was accomplished by standard procedures: bias subtraction and flat fielding was performed for each image, and then the frames were calibrated using the available stars on the field of view in combination with the USNO.B1.0 catalog. A median stack of the available images was then performed. The photometric calibration errors amount to ±0.3 mag. The spatial orientation of the images was also checked with the background star positions. A selection of those images are shown in Figures 1 and 2 for various epochs. Panels (a) and (b) of Figure 1 display the earliest images collected on 2013 February 14 and May 1, at 4.78 and 3.89 AU inbound, while Panel (c) displays the comet much closer to perihelion on 2013 October 10 at 1.55 AU. Figure 2 shows the comet at much shorter heliocentric distances, at 0.67 and 0.61 AU, just before and after an outburst of activity reported to occur during the earliest hours of November 14. These images display both dust and ion tails. The November 15 image is shown separately in Figure 3, after being enhanced by a Larson–Sekanina rotational filter, where wing-like features seem to emerge from the comet nucleus. This was interpreted by some authors as an indication of the fragmentation process (e.g., Boehnhardt et al. 2013).

As stated in the Introduction, we also analyzed *SOHO* LASCO C3 images in order to obtain complete coverage of the evolution of the dust around perihelion. *SOHO* continuously observes the Sun from Lagrangian point L1 (Domingo et al. 1995).

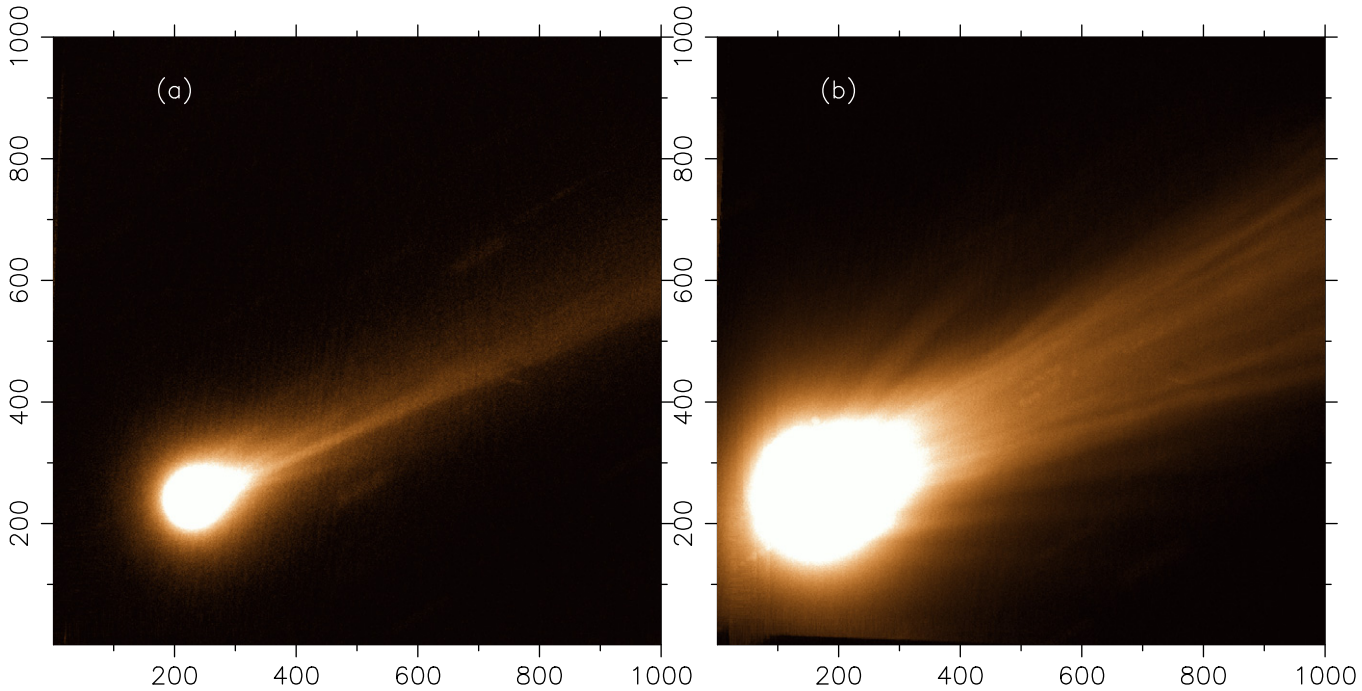

Figure 2. Panel (a): image of the comet ISON obtained on 2013 November 13 using CAFOS at the 2.2 m telescope of the Calar Alto Observatory. Panel (b): image obtained on 2013 November 15 at the 0.90 m telescope at the Sierra Nevada Observatory. In both panels, north is up, and east is to the left. More details on the images are given in Table 1.

(A color version of this figure is available in the online journal.)

For our purposes, we used pre- and post-perihelion "level-0.5" FITS images. We reduced both the DeepRed filter (at three epochs) and the Clear filter (at four epochs) images, as detailed in Table 1. The Clear filter images are mostly dominated by sodium emission (Knight et al. 2010; Knight & Battams 2014). Among the mechanisms proposed to explain the presence of alkali atom emission from comets is the evaporation of small grains (Wilson et al. 1998; Watanabe et al. 2003; Fulle et al. 2013). While other mechanisms might also play a role, this mechanism is likely operating on ISON near perihelion. Therefore, these Clear filter images are tracing cometary dust features. On the other hand, we assume that the DeepRed images are giving information on light scattered by cometary dust only. This filter bandpass (Morrill et al. 2006) is placed well outside the strong Na emission lines and the much weaker Li line at 6707.78 Å. The contamination by the weak K lines at 7664.90 and 7698.96 Å will be neglected. A quantitative estimate of the possible (small) contamination of these lines on the scattered dust flux is beyond the scope of this paper.

To perform the reduction of the *SOHO* LASCO C3 images, we built a background image by generating a median stack combining the Clear filter and DeepRed images taken at different times, so that all the background stars and the comet itself vanished, leaving a background image only. The spatial scale and rotation angle of the images with respect to the celestial north were found by fitting the stars' positions in the images to the stars in the *Hipparcos* catalog. An example of those fits for the two pre-perihelion Clear filter reduced images is given in Figure 4. This resulted in a spatial scale of $56\farcs25$ pixel^{-1}, in perfect agreement with the results of Morrill et al. (2006). Owing to the fact that the nucleus is at least partially vaporized during the observations, the position of the nucleus cannot be associated with the comet optocenter, as it is commonly done for cometary images. Instead, we located its theoretical position by using the JPL Ephemeris at the Horizons web page, taking into account that the images were taken from the location of the *SOHO* spacecraft. The position of the nucleus is displayed in the Clear images of Figure 4. Then, while the nucleus is inside the cloud of particles pre-perihelion, it is significantly away from the brightest pixel in the image in the two post-perihelion images. This fact implies that the activity (sublimation and/or refractory material vaporization) has ceased post-perihelion, which will be confirmed in the modeling procedure.

The absolute calibration was performed by using the final LASCO C3 calibration factors from Table IV of Morrill et al. (2006) for the DeepRed and Clear filters. The reduced Clear and DeepRed filter images are displayed in Figures 4 and 5. It is interesting to see the conspicuous spike along the northern part of the broader tail that is only seen in the two pre-perihelion Clear filter images. This spike is not seen at red wavelengths, possibly because it is under the detection threshold. Regarding the post-perihelion images, both the Clear and DeepRed images show two distinct tails with some material in between, one to the northeast, linked mostly to particle fragmentation near perihelion passage, as we will show in the modeling, and another to the southeast, associated with the remaining material ejected pre-perihelion.

In addition to the images, we also take into account the Afρ data provided by the amateur astronomical association *Cometas-Obs*. These data come from many observers, from several countries, mostly in Spain. These data are *R*-band Afρ data and all of them refer to a $\rho = 10^4$ km aperture radius. This data set is of great value, as they provide an almost continuous coverage of the comet dust evolution, which is very useful for retrieving dust properties from our the Monte Carlo modeling, as we will show below. Figure 6 shows the raw Afρ data as a

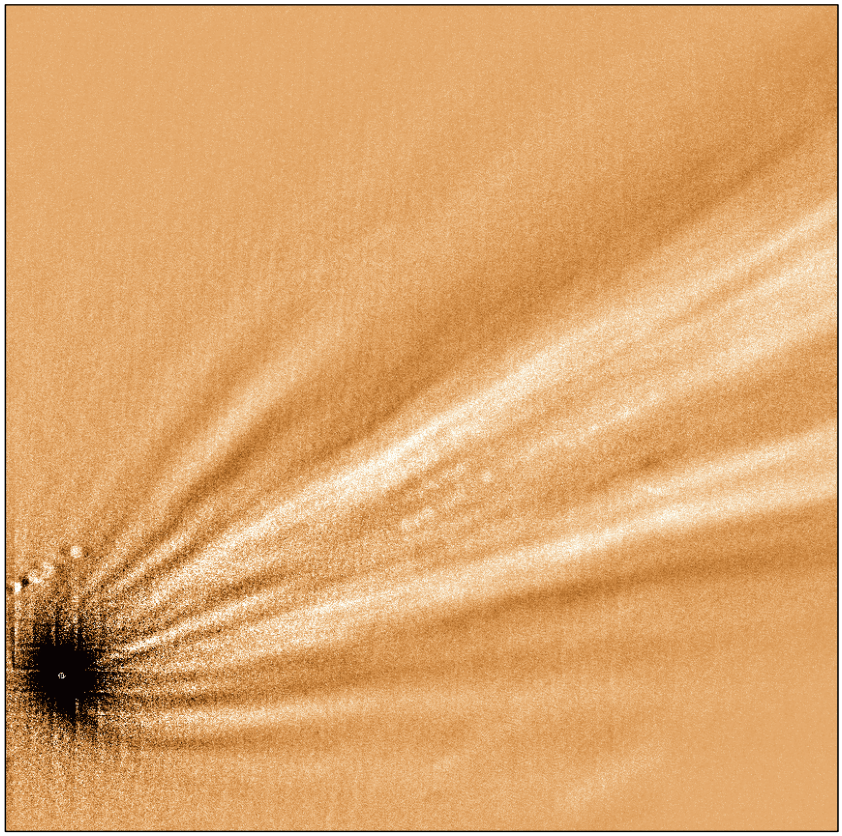

Figure 3. Larson–Sekanina filtered image of the comet ISON on 2013 November 15 (see Figure 2). North is up, and east is to the left.
(A color version of this figure is available in the online journal.)

function of time, in days related to perihelion passage (asterisks). The data begin just after discovery, shows a gap while the comet was behind the Sun in 2013 June, July, and part of August, and then span the remaining pre-perihelion branch until just 10 days before perihelion date, when the comet was again too close to the Sun. In this graph, the variation of the phase angle of the comet versus time is also shown. It is seen that the relative maximum around 320 days before perihelion is, at least partially, produced by a backscattering enhancement because of the excellent correlation of Afρ with the phase angle. In a first approximation, we corrected for this effect by assuming a linear phase coefficient of $\kappa = 0.03$ mag deg^{-1}, which is within the range of estimates of κ for other comets (e.g., Meech & Jewitt 1987). Then, for phase angles $\alpha \leqslant 30^{\circ}$, we corrected the Af$\rho$ values by the factor $10^{\kappa(30-\alpha)/2.5}$. This correcting factor was also applied to the images for which $\alpha \leqslant 30^{\circ}$. Although less pronounced, the maximum at -320 days still remains, but we did not make further corrections because we cannot be completely sure that an outburst of activity is also contributing.

3. THE MODEL

The interpretation of the images and the Afρ data is based on our Monte Carlo dust tail analysis code, which has been described previously in several papers (e.g., Moreno et al. 2012, 2013). The code is a forward model that produces synthetic dust tail images for a given observing date taking into account a set input parameters related to the dust parameters: differential size distribution, ejection velocities, and dust loss rates as a function of the heliocentric distance. In addition, the density ρ_p and the geometric albedo p_v of the dust grains must be specified. We adopt $\rho_p = 1000$ kg m^{-3}. The scattering properties of aspherical grains of a wide range of sizes, like those ejected from cometary nuclei, are very tedious to calculate using the available light scattering codes (e.g., the Discrete Dipole Approximation by Draine & Flatau 1994), mainly because of the long CPU time and huge memory needed for grains larger than the wavelength of the incident light, even for large computers. In consequence, we consider spherical dust grains, for which Mie theory gives an exact computation of the phase matrix at a given wavelength and refractive index. For a refractive index of $m = 1.88 + 0.71\,i$, which corresponds to glassy carbon, we obtain $p_v = 0.04$ at red wavelengths for grains having a radius $r \geqslant \lambda$. The main problem we face with this approximation is that the phase function is completely flat at backscattering, so that the backscattering enhancement cannot be modeled properly. This is why we resort to correct the data affected by the backscattering enhancement by the method described in the previous section.

From Mie theory, we can also obtain the radiation pressure coefficient $Q_{\rm pr}$, which turns out to be $Q_{\rm pr} \approx 1$ for $r \geqslant \lambda$. The ratio of solar radiation pressure to solar gravity force exerted on the grains can be computed as $\beta = C\,Q_{\rm pr}(2\rho_p r)^{-1}$, where $C = 1.19\ 10^{-3}$ kg m^{-2}. Neglecting cometary gravity, which is a reasonable assumption for nucleus sizes of the order of $R_N \sim 1$ km, like ISON, the grains move in Keplerian orbits around the Sun. The trajectory of the grains will be a function of the terminal velocities and the β parameter. The final position of the ejected grains on the photographic plane for a given observation date and their contribution to the tail brightness are computed by the Monte Carlo code.

The model can deal with the characteristics of the emission pattern. Adopting a spherical nucleus, it is possible to specify its rotation parameters (rotation period and orientation of the

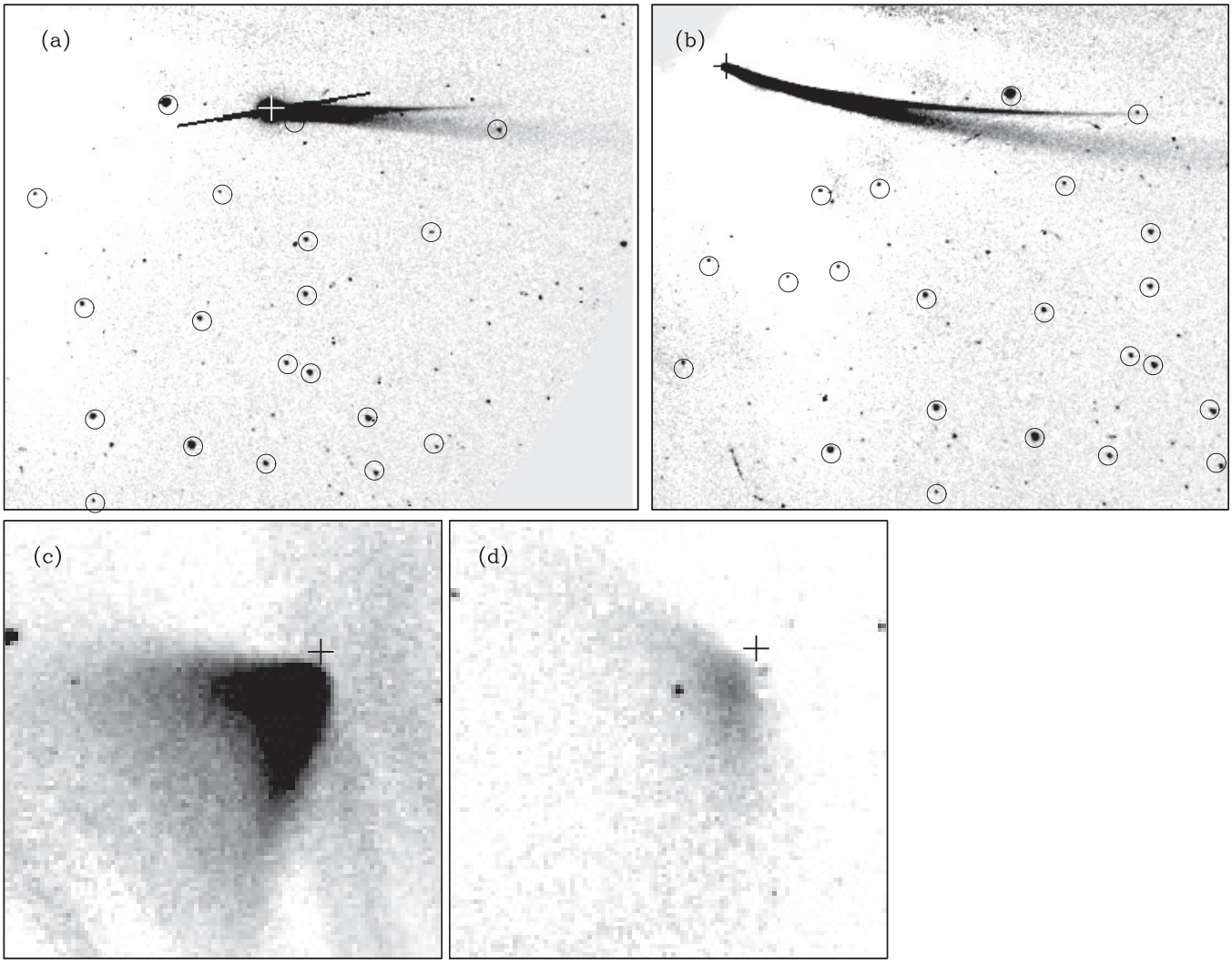

Figure 4. Reduced images of the comet ISON obtained through the Clear filter of the LASCO C3 coronagraph on the *SOHO* satellite. The dates are 2013 November 28.02 (a), 28.63 (b), 29.26 (c), and 30.21 (d). Panels (a) and (b) are pre-perihelion, and panels (c) and (d) are post-perihelion images. The crosses mark the nucleus position, according to the JPL-Horizons ephemeris. The encircled stars in panels (a) and (b) illustrate the fits to the *Hipparcos* catalog. In all panels, north is up, and east is to the left.

spin axis), and to set some active area(s) on its surface. The orientation of the spin axis is specified by the obliquity I, and the argument of the subsolar meridian at perihelion Φ (for a definition of those angles, see, e.g., Sekanina 1981). Owing to the large number of free parameters, we only resort to that anisotropic ejection model when we cannot find an acceptable fit for isotropic or hemispherical emission models.

The terminal velocity of the ejected grains is parameterized according to the expression $v(\beta, t) = v_1(t)\beta^{1/2}$. This formula has previously been used in other well-known models such as Fulle (1989), and separates the time and size dependencies of the velocity. The size dependence is appropriate to gas drag by the ice sublimation processes. The ejection velocities are parameterized as a three-dimensional vector whose components are directed outward in the direction of the comet radius vector (u_R), perpendicular to u_R, contained in the orbital plane, and in the opposite sense of the comet motion (u_θ), and normal to the orbital plane directed to the north pole of the orbit (u_z). These components must be calculated as a function of the active area coordinates and the angles I and Φ (Sekanina 1981).

To model the dust tail observations at different epochs, we start from a specific choice of input parameters as follows. The differential size distribution function is set in the interval 10^{-5} cm to an upper size limited by the escape velocity, given by $v_{\rm esc} = \sqrt{2GM/R}$, where R is the distance to the nucleus center of mass. We adopt $R = 20\ R_N$, the distance at which the gas drag becomes negligible. Then, for a spherical nucleus of $R_N = 500$ m, which would agree with the reported nucleus size by Combi et al. (2014), $0.3 < R_N < 1.3$ km, and a bulk nuclear density of $\rho_N = 1000$ kg m^{-3}, the nucleus mass is 5.2 10^{11} kg, and the escape velocity becomes 0.08 m s^{-1}. The differential size distribution function is initially assumed constant with the heliocentric distance and having a power index of -3.5, which is within the range estimated for many comets. The onset time of cometary activity was set at 12 AU. At the first pre-discovery observation by Pan-STARRS, on 2011 September 30 (see the available magnitude data for ISON in the Minor Planet Center database), the comet was at 9.4 AU, so that we placed a safe onset time earlier, as the comet might already be active at the time of the first observation. In any case, this date was tested in the modeling procedure. With these parameters, we attempted first to fit our earliest images on 2013 February 14 and May 2, in combination with the first part of Afρ data from -430 to -200 days to perihelion, and then the rest of images and Afρ

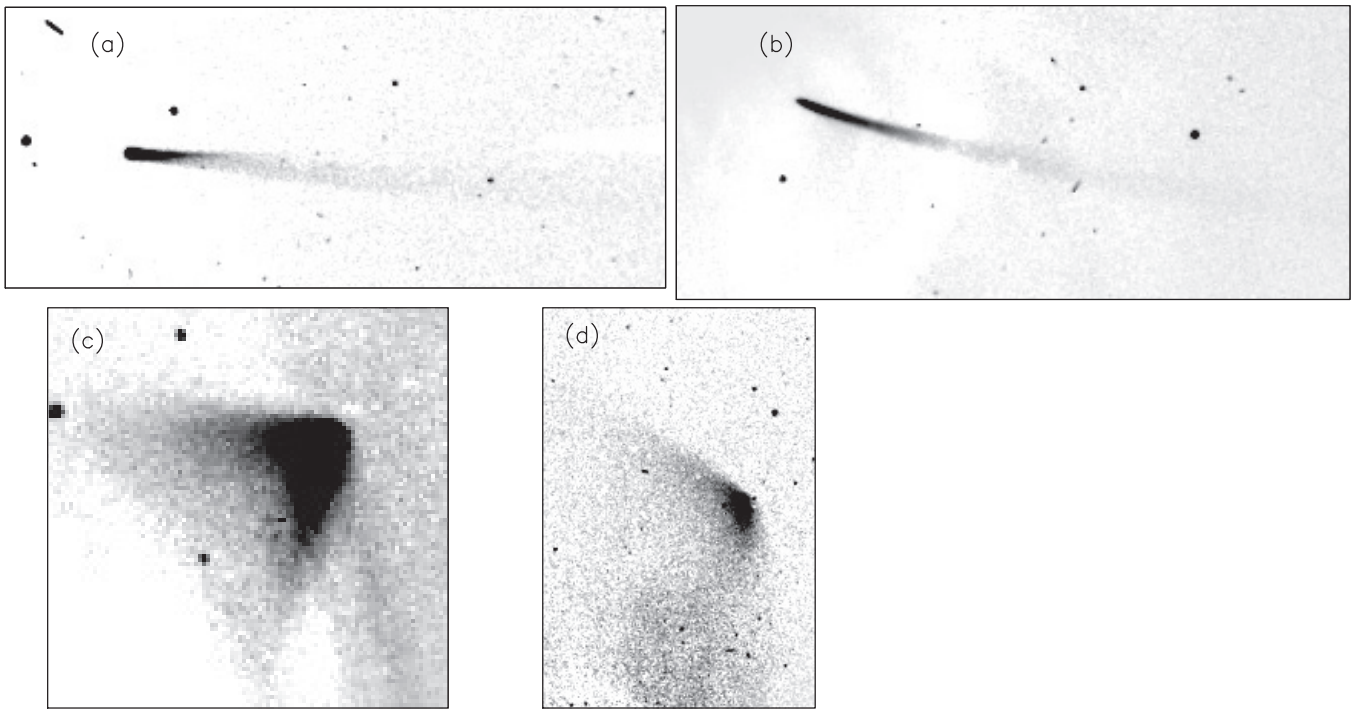

Figure 5. Panels (a), (b), and (c): reduced images of the comet ISON obtained through the DeepRed filter of the LASCO C3 coronagraph on the *SOHO* satellite. The dates are 2013 November 28.07 (a), 28.62 (b), and 29.28 (c). Panel (d) is the image obtained through a Clear filter on 2013 November 30.21, already displayed in Figure 4(d), but shown here again for clarity. These images are those used in the modeling procedure. In all panels, north is up, and east is to the left.

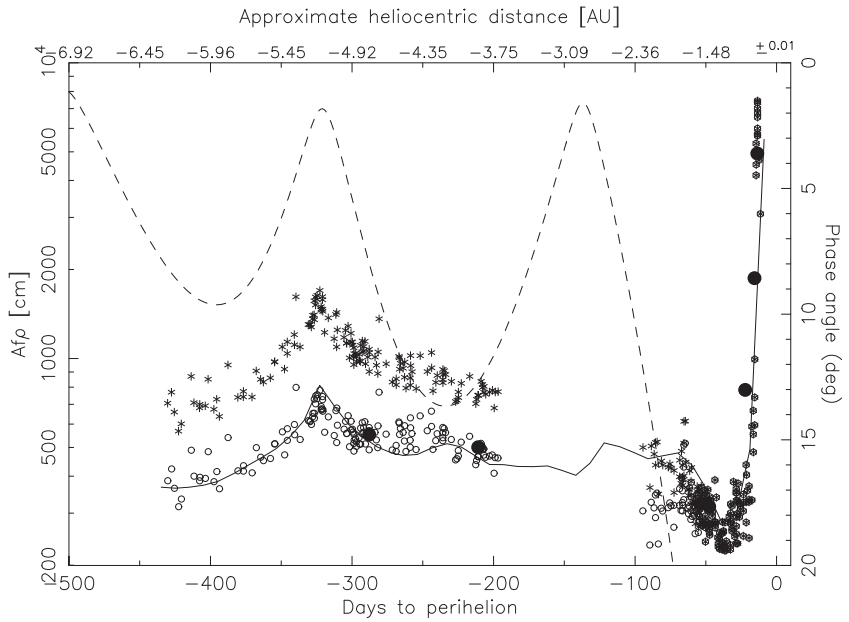

Figure 6. Original Afρ measurements by the amateur astronomical Association *Cometas-Obs* (asterisks), as a function of the heliocentric distance and time to perihelion. The open circles are the same data but corrected by the factor $10^{\kappa(30-\alpha)/2.5}$, with $\kappa = 0.03$ mag deg^{-1} for phase angles $\alpha \leqslant 30^{\circ}$ (see the text). The phase angle of the comet is displayed as a dashed line referring to the right ordinate axis. The large solid circles are the Afρ measurements obtained for the images shown in Table 1. The solid line is the modeled Afρ from synthetic images generated every 10 days for the best-fit model parameters.

data, except the *SOHO* images. These images were fitted in the last phase of the fitting procedure, since they required a special treatment, as other processes such as particle vaporization are taking place at those dates very close to perihelion.

The synthetic Afρ data were generated by computing synthetic images evenly spaced every ∼10 days with the model input parameters, and calculating Afρ at $\rho = 10^4$ km from those images. Not surprisingly, the first model results were very far from the real data set, needing corrections in several parameters of the model. Then a trial-and-error procedure is begun, in which we modified each of the input parameters at a time, then several at a time, until a reasonable fitting is found. Given the large amount of free parameters (many of them functions of the heliocentric distance), it is very difficult to follow a specific fitting strategy, other than first starting with the earlier data. After finding a reasonable order zero fit to the earliest data, we proceed to more recent data, by trying to modify only the time-dependent parameters between the last two epochs, so that

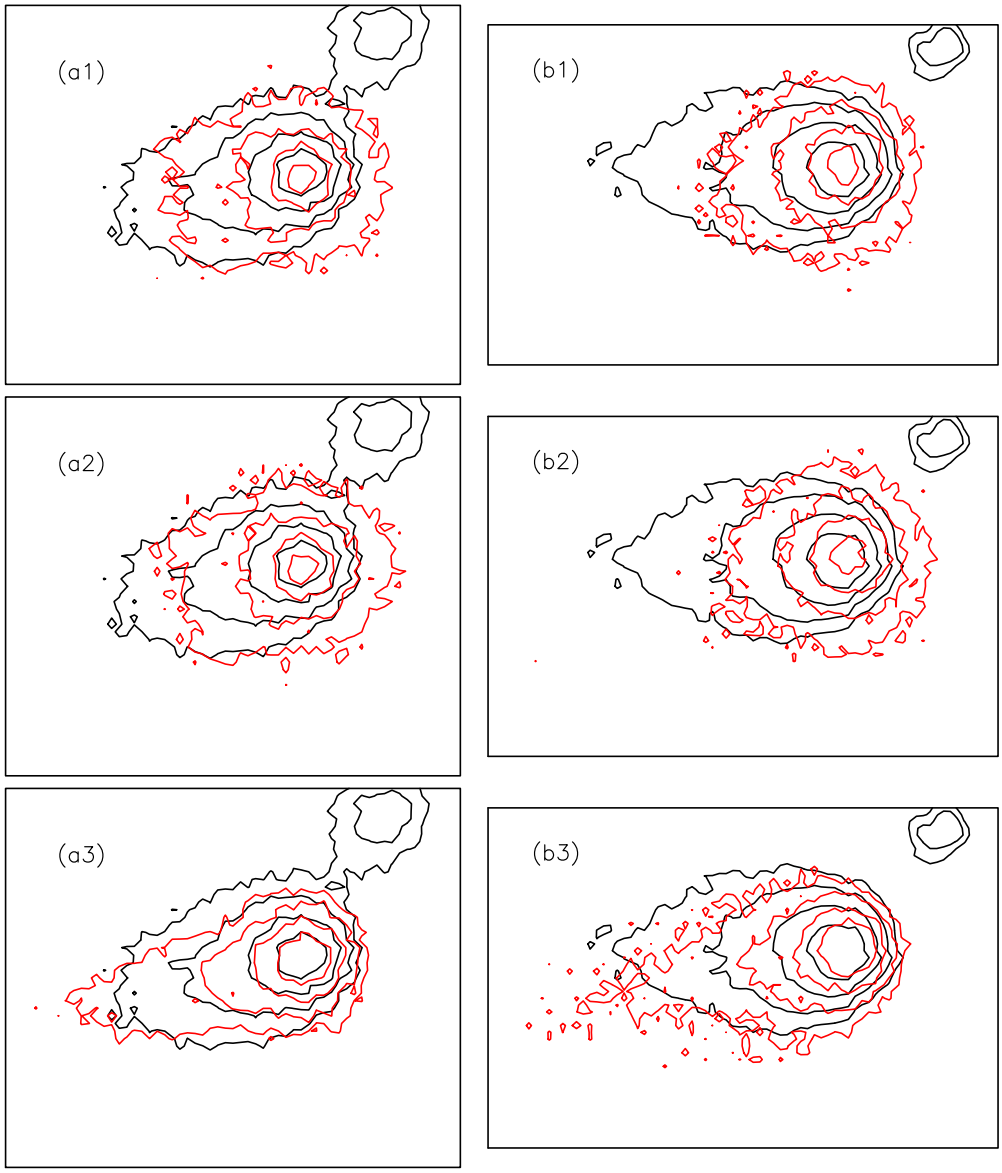

Figure 7. Observed brightness contours (black lines) and modeled contours (red lines) for the images obtained on 2013 February 14 (Panels (a1), (a2), and (a3)) and 2013 May 1 (Panels (b1), (b2), and (b3)). Panels (a1) and (b1) correspond to an isotropic ejection model. Panels (a2) and (b2) correspond to a hemispherical ejection model. Panels (a3) and (b3) correspond to a 45° emission cone toward the Sun.

(A color version of this figure is available in the online journal.)

the earlier input data are not modified. Much of the time it is impossible to find a fit to a given image without modifying earlier parameters affecting the images already fitted, so that we must go back and forth until reaching a reasonable global fit to all the data. We must recognize that the fit found is surely not unique, but taking into account the amount of data constraining the model, it is possibly the best that can be achieved with the available data.

4. RESULTS

We divided the analysis into three parts, as a function of time: the first part of data correspond to the early images and Afρ data, until approximately 200 days pre-perihelion, when the comet went behind the Sun from the Earth and could not be observed; the second part of data corresponds to those data between approximately 100 days and 13 days to perihelion, i.e., when the comet was available again to Earth's observers; and the third part corresponds to the *SOHO* data, in which the comet was $\approx\pm2$ days to perihelion. The first and second blocks of data constitute the ground-based observations and are described and analyzed in the next subsection, while the *SOHO* images and models are described in the last subsection.

The model analysis is made by first considering the simplest kind of particle ejection pattern, in which particle emission occurs within a cone of a given aperture around the vector from the comet to the Sun. This emission cone is assumed to have either a broad aperture of 90 deg (hemispherical emission), or a more focused emission of 45 deg aperture.

4.1. Ground-based Data

The first part of the data apply to the earliest images on 2013 February 14 and May 2. We first attempted to fit those images using isotropic ejection models, but those synthetic images did not accurately fit the observed images. A hemispherical ejection

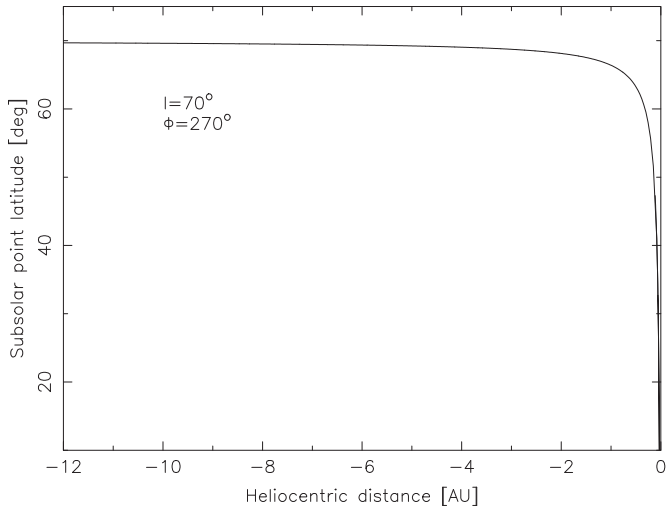

Figure 8. Variation of the latitude of the subsolar point of the comet ISON as a function of the heliocentric distance assuming a spherical nucleus with rotational axis parameters of $I = 70°$, and $\Phi = 270°$.

model (a 90 deg aperture emission cone toward the Sun) was also built up, but the results did not improve significantly. However, for narrower emission cones toward the Sun, the fits started to improve considerably. Figure 7 shows the improvement on the fits to the images from changing the emission pattern from isotropic to a 45 deg emission cone toward the Sun. In terms of a model of a rotating nucleus with an active area on it, which would be, at least conceptually, a more realistic scenario than the simple emission cone, we searched for models giving similar ejection patterns to that given by the 45 deg aperture ejection. Then, we searched in the space of parameters I, Φ, and latitude range for an active area yielding model fits of similar or better quality than those displayed in Figures 7(a3) and (b3). The best fits were found when I was near 70°, Φ close to 270°, and an active area latitude extending from 35° to 90° north. We note that the sense of rotation of the nucleus around the spin axis cannot be constrained with this model, so that this configuration would be equivalent to $I = 110°$, $\Phi = 45°$, (retrograde motion). For simplicity, we will adopt the prograde solution. The cometocentric latitude of the subsolar point, λ_{ss}, as a function of the true anomaly, θ, is given by $\sin\lambda_{ss} = \sin I \sin(\Phi + \theta)$. For $I = 70°$ and $\Phi = 270°$, λ_{ss} becomes ∼70° for a large portion of the inbound branch of the comet (see Figure 8), meaning that the comet is always approximately facing the same hemisphere to the Sun inbound except for small heliocentric distances $r_h \leqslant 1$ AU, where the subsolar point changes very fast with time toward southern latitudes. The model resulting fits to the isophote field of the two images on February 14 and May 2 can be seen in Figures 9(a) and (b). These fits constitute further improvement against the simple 45 deg ejection cone. Note that the model fits must also be consistent with the evolution of the model parameters back to the onset of activity, specifically with the heliocentric variation of the Afρ curve as well. We verified that the model in fact simultaneously fits the images and the Afρ parameter as a function of time (see Figures 6 and 9) for the first part of the data, from the onset of activity to 200 days to perihelion.

The second block of data corresponds to images and Afρ data from 100 to 13 days to comet's perihelion, or from $r_h = 1.55$ to $r_h = 0.61$ AU. The application of the previously described anisotropic ejection model to those images resulted in poor fits, showing a prominent brightness excess in the sunward direction. For those images, simple isotropic ejection models performed much better, however. To satisfy both the images and Afρ data

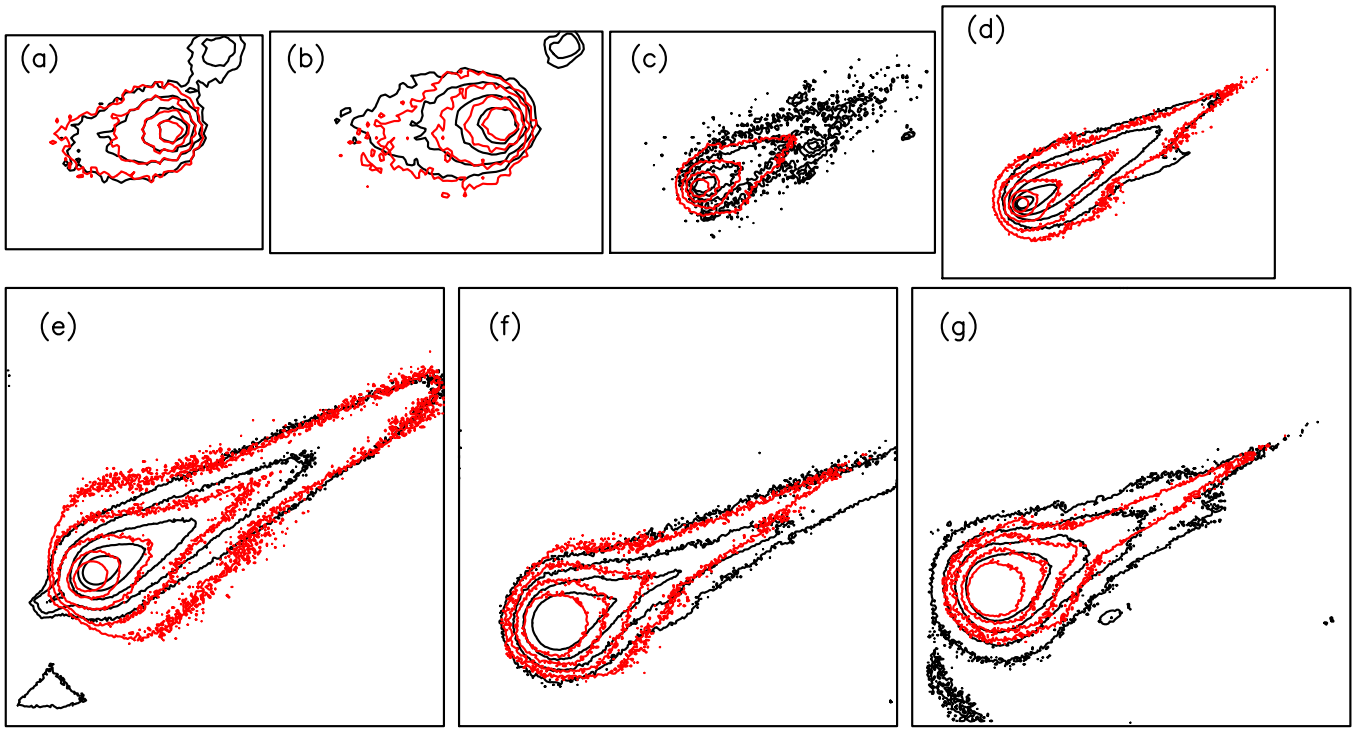

Figure 9. Observed brightness isophotes (black contours) and best-fit modeled isophotes (red contours) for the seven images labeled (a)–(g) (see Table 1 for a description of the image parameters). The best-fit model parameters are displayed in Figure 11. In all panels, north is up, and east is to the left.

(A color version of this figure is available in the online journal.)

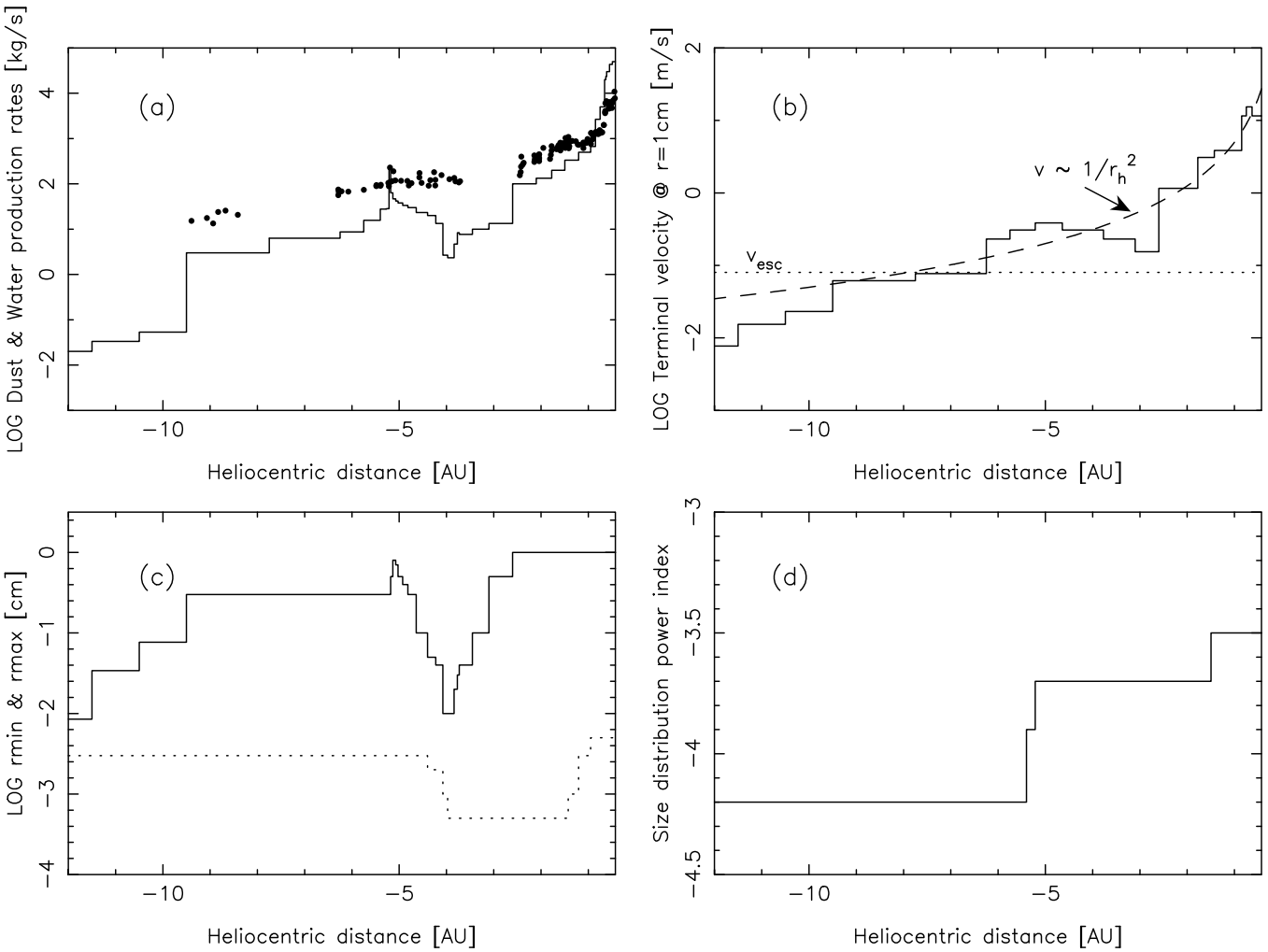

Figure 10. Best-fit parameters for the dust environment of the comet ISON. In panel (a), the dust-loss rate as a function of the heliocentric distance is shown by a solid line, while the filled circles are the water production rates calculated from the heliocentric magnitudes by the expression of Jorda et al. (2008). Panel (b) shows the variation of the ejection velocity referred to a grain of 1 cm in radius. The dashed line corresponds to a $1/r_h^2$ dependence of the velocity on r_h. The dotted line is the escape velocity assuming a spherical nucleus of radius $R_N = 500$ m and density $\rho = 1000$ kg m^{-3}. Panel (c) shows the variation of the maximum (solid line) and minimum (dotted line) grain radius as a function of the heliocentric distance. Panel (d) displays the variation of the power index of the size distribution function vs. the heliocentric distance.

for both blocks of data, we had to assume anisotropic ejection from the onset time until the May 1.86 image at $r_h = 3.89$ AU and then switch to an isotropic ejection model for heliocentric distances $r_h < 3.89$ AU. In this way, we could consistently fit all the images and the evolution of the Afρ parameter for the first and second blocks of data (Figures 6 and 9).

The large obliquity of the spin axis ($I = 70°$) agrees with the analysis of *Hubble Space Telescope* (*HST*) observations of the comet on 2013 April 10 by Li et al. (2013), who also suggests a high obliquity, in the range $I = 50°$–$80°$. Since the latitude of the subsolar point remains essentially constant until $r_h \sim 1$ AU, a potential problem of the model would be in how the emission could become isotropic for $r_h < 3.89$ AU, if only one hemisphere of the comet is continuously illuminated, and the dominating process is gas drag from sublimating ices. One possibility is the propagation of a thermal wave into the nucleus that activate subsurface sublimation in areas that previously had been inactive. Another possibility, but much more unlikely, is that the nucleus of the comet is highly elongated and has the rotating axis aligned with the long axis (i.e., in an unstable configuration because of its high energy for its angular momentum) so that very small variations in the subsolar point latitude would result in the illumination of fresh ices in the southern hemisphere, leading to sublimation.

The model parameters that best fit all available images and Afρ data are displayed in Figure 10. The dust mass-loss rate as a function of the comet heliocentric distance is displayed together with the water production rate obtained by converting the available heliocentric magnitude (m_h) data (Minor Planet Center database and N. Biver 2014, private communication) to $Q[H_2O]$ (in s^{-1}) by the expression $\log Q[H_2O] = 30.675$–$0.2453\, m_h$ (Jorda et al. 2008). In general, both quantities correlate, except for the local minimum near −4.8 AU. The dust-to-gas ratio tends to decrease with increasing heliocentric distance in general and keeps < 1 except at $|r_h| > 1$ AU. It is, however, important to note that the latest images on 2013 November 6.23, November 13.20, and, especially, November 15.24, at $r_h = 0.87$, 0.67, and 0.61 AU, respectively, are increasingly contaminated by the plasma tail, so that the dust-loss rates derived are actually an upper limit. Most of this contamination presumably comes from the H_2O^+ ion, which is the one that dominates the red region of the spectrum covered by the red bandpasses. The narrow local maximum of dust-loss rate at ∼–5.2 AU does not have a counterpart in the gas-loss rate (except for two

single magnitude estimates), and is associated to the brightness increase very likely produced by the brightness opposition effect or backscattering enhancement.

Regarding ejection velocities, as stated previously, we imposed a maximum grain size limit set by the escape velocity appropriate for an assumed 500 m radius body with a bulk density $\rho = 1000$ kg m^{-3} at a distance of 20 R_N (see the dotted line in Figure 10(b)). Then, at heliocentric distances of $|r_h| \lesssim 9$ AU, ~1 cm radius grains could in principle be ejected. However, the maximum size set at heliocentric distances $5 < |r_h| < 9$ was 0.3 cm. The reason is that the ejection of larger particles would result in the presence of a strong sunward brightness spike in the images for $|r_h| < 1$ AU, which is not observed. The grain velocities experience a strong decrease with increasing heliocentric distance, which might be approximated closely by a $1/r_h^2$ dependence (see Figure 10(b)). This agrees with the terminal subsolar velocity found by Crifo & Rodionov (1997) from advanced three-dimensional circumnuclear coma models at intermediate particle sizes, and departs from the approximate $1/r_h$ dependence stated by Whipple (1951).

The derived range of ejected grain sizes as a function of the heliocentric distance is generally constrained by the escape velocity in the upper bound. The lower size limit is constrained in combination with the power index, controlling both the absolute brightness levels of the outermost isophotes, and the variation of brightness across the tail images. The power index ranges between −4.2 at far pre-perihelion distances and −3.5 at perihelion. These are rather common values for the power index found in the literature. As an example, Fulle et al. (2010) found similar values in the post-perihelion branch in their model analysis of the dust environment of comet 67P/Churyumov-Gerasimenko.

4.2. Analysis of SOHO Images

The third block of data pertain to the previously described "level-0.5" *SOHO* fits images in both the Clear and DeepRed filters obtained with the LASCO C3 coronagraph spanning the dates around perihelion. With our Monte Carlo model we analyzed two pre-perihelion and one post-perihelion DeepRed images, and one post-perihelion Clear image. These images are described in Table 1 and are displayed in Figure 5. As stated previously, it is assumed that the DeepRed images are providing information on light scattered by dust only. The brightness observed in the pre-perihelion Clear filter images is mostly attributed to sodium emission (e.g., Knight & Battams 2014). As stated in Section 2, alkali atoms should be expected to be extracted from dust, where up to five possible mechanisms have been identified (Fulle et al. 2013), including thermal- and/or photon-stimulated desorption, solar wind sputtering, vaporization, and photodissociation of parent molecules. In consequence, the pre-perihelion Clear filter images can trace the dust grains, but their analysis should obviously take into account the emission mechanism(s) involved, and this is beyond the scope of the paper. We will only use those Clear filter pre-perihelion images to compare with the dust features observed in the DeepRed images pre-perihelion.

The choice of the LASCO C3 images analyzed was not arbitrary: we selected Clear and DeepRed images taken as close in time as possible in order to compare the observed dust features at each epoch. The first images selected correspond to 2013 November 28.02 (Clear) and 28.07 (DeepRed). At that time, the Clear filter image shows nearly the maximum level of saturation, with an apparent magnitude near −2.0, in contrast with the apparent magnitude in the DeepRed filter of ~+2.0 (Knight & Battams 2014). The next images were selected at 2013 November 28.62 (Clear) and 28.63 (DeepRed), just before the comet head was hidden by the coronagraph. Then, we selected images at 29.26 (Clear) and 29.28 (DeepRed), just after the comet emerged from the coronagraph, and yet another one when the comet was headed toward the edge of LASCO C3 field of view, but still retaining some significant signal on the Clear filter on November 30.21. At that time, no DeepRed images were available. However, and since the fluxes in the Clear and DeepRed images were similar since November 29.0 onward (Knight & Battams 2014), we assumed in principle that the flux in the Clear filter at that time (November 30.21) is given information on light scattered by dust, as in the DeepRed images, and that the alkali emission is negligible.

The analysis of the *SOHO* images is complicated by the fact that particle sublimation, among other processes, is surely playing a role. Our approach consist in fitting the tails as if they were generated in some interval of time where dust is being produced according to a set of model input parameters, but without taking into account that in the very same interval there is an unspecified fraction of particles that surely undergo variations in size, or even disappear because of sublimation. As a consequence, our estimates of the mass of particles contained in a dust tail for these *SOHO* images are always lower limits to the real dust mass ejected. For these fits, and for lack of better information, we assumed the same ejection velocity law as for the gas drag in the previous analysis. The dust ejection was assumed in principle to be isotropic.

We started the analysis with the DeepRed image on 2013 November 28.07. The close Clear filter image on November 28.02 is becoming saturated near the head of the comet, reaching approximately maximum brightness (Figure 4). The parameters of the best fit to the DeepRed image, as well as for the other *SOHO* images are shown in Figures 11 (pre-perihelion) and 12 (post-perihelion). The most remarkable feature of the fit is the large amount of dust mass needed to fit the tail, which is 2.3×10^{11} kg, equivalent to a sphere of 380 m in radius with density 1000 kg m^{-3}. This is a very significant dust mass, nearly half of that of a 500 m nucleus with $\rho = 1000$ kg m^{-3} (5.2×10^{11} kg). This is much larger than the total dust mass ejected from the onset time until the observation time of our last ground-based image on November 15.24, 7.3×10^9 kg, when the comet was at 0.61 AU. The start of the significant mass loss is at $r_h = 0.36$ AU pre-perihelion, where, after a short maximum burst, the activity continues at a high rate of 1.7×10^5 kg s^{-1}, until the observation date, November 28.07. The minimum particle sizes are rather small, ranging from about 1 μm to 0.1 μm during the peak activity, with the largest particles being ejected at ~10 m s^{-1}. The best fit image is shown in Figure 13(a), and a scan along the tail is compared to the observation in Figure 14(a). It must be noted that this strong production of particulate material at 0.36–0.08 AU is also accompanied by a strong reduction in the dust production rate at $r_h > 0.61$ AU in comparison with the derived loss rates from ground-based data at those heliocentric distances (see Figure 10(a)). Specifically, we must impose a reduction factor of at least 40 at $r_h > 0.61$ AU, otherwise the spike, which appears clearly in the northern branch of the tail in the Clear filter images (see Figure 4(a)), would appear markedly in these synthetic DeepRed images, contrary to the observations. An explanation of this on the light of particle sublimation is given in Section 4.2.1.

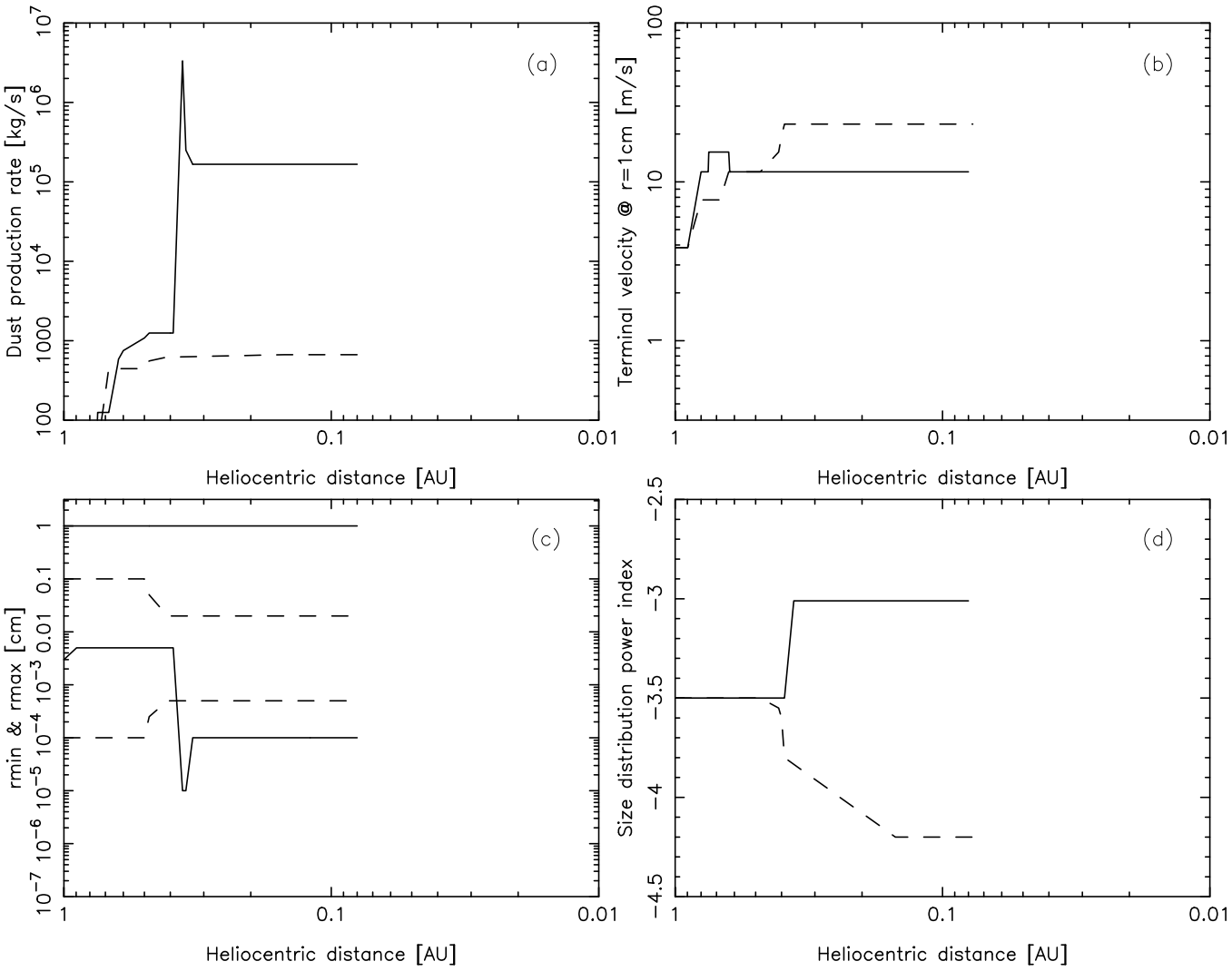

Figure 11. Pre-perihelion dust environment of the comet ISON from the selected DeepRed *SOHO* LASCO C3 images on 2013 November 28.07 (solid lines) and 28.62 (dashed lines). In panel (a), the dust production rate as a function of the heliocentric distance is displayed. Panel (b) shows the variation of the ejection velocity vs. heliocentric distance referred to a grain of 1 cm in radius. In panel (c), the maximum and minimum particle radii used in the model are displayed, and, in panel (d), the evolution of the power index of the size distribution.

The next image to fit was the DeepRed image taken on 2013 November 28.62 To fit this image, a considerable decrease in mass-loss rate in comparison with the November 28.07 image must be considered. In addition, the dust production must stop just after November 28.07, otherwise the region of the comet's heat would be much brighter than observed. Also, a notable variation in the range of particle size had to be introduced, in such a way that the distribution has become much more monodisperse (see Figure 11(c)). The dust mass contained in this tail is 7.6×10^8 kg, a factor of about 300 smaller than the mass on November 28.07. The resulting fit to the image, and a scan along both the observed and modeled tails, are shown in Figures 13(b) and 14(b). As in the case of the pre-perihelion DeepRed image on November 28.07, we imposed a strong reduction in the dust production rate at heliocentric distances of $r_h > 0.61$ AU of a factor of at least 40 (Figure 11(a)), with respect to the production rate derived from ground-based data at those heliocentric distances (Figure 10(a)), for the same reason: the spike that is clearly seen in the Clear filter image (see Figure 4(b)), which corresponds to dust ejected much earlier in the orbital path, would appear clearly in the synthetic DeepRed image of November 28.62, unless this reduction is applied. The spike only appears in a high-contrast display, such as shown in Figure 13(e), when that reduction to the dust production rate is performed.

The two post-perihelion images analyzed were taken at phase angles of 121°.1 and 127°.8 on November 29.28 and 30.21, respectively. As a consequence, a correction for the forward-scattered brightness, in a similar way as we did for the early images and Afρ data for phase angles close to backscattering, must be performed. We followed the parameterization of Marcus (2007), also used by Knight et al. (2010), for an intermediate dust-to-gas ratio of 0.52. Then, to take into account the cometary phase curve, and putting the data at the brightness level of the 30° phase angle, as for the ground-based images and Afρ data, the images on November 29.28 and 30.21 are corrected by 0.50 and 0.75 mag, respectively. Both post-perihelion observations reveal a bilobed -shaped tail, with some material in between. The dust parameters of the best fits are displayed in Figure 12, while the best-fit images are compared to the observations in Figures 13(c) and (d), while scans along the images are displayed in Figures 14(c) and (d). As stated previously, the theoretical

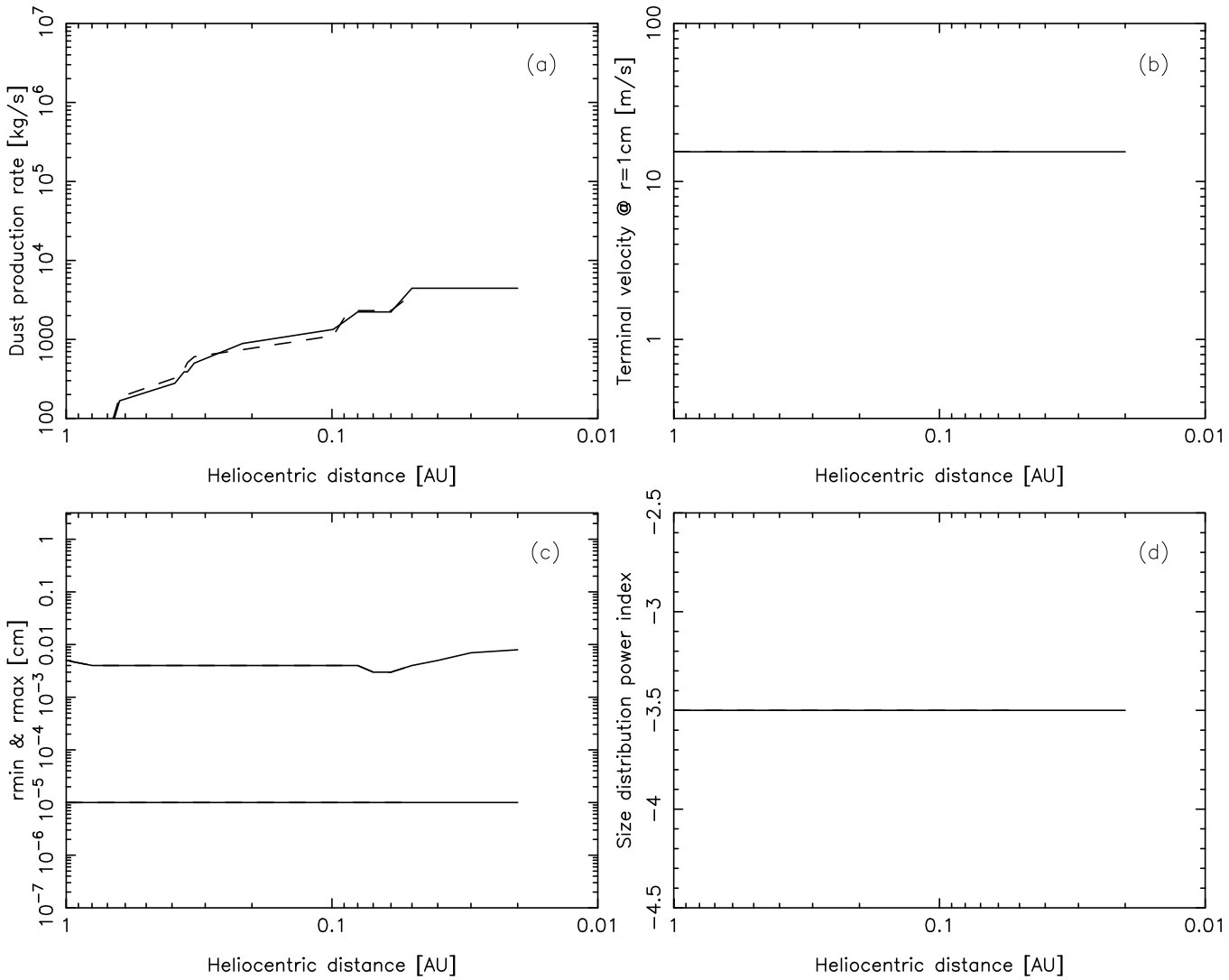

Figure 12. Post-perihelion dust environment of the comet ISON from the selected DeepRed (2013 November 29.28, solid lines) and Clear (2013 November 30.21, dashed lines) *SOHO* LASCO C3 images. In panel (a), the dust production rate as a function of the heliocentric distance is displayed. Panel (b) shows the variation of the ejection velocity vs. heliocentric distance referred to a grain of 1 cm in radius. In panel (c), the maximum and minimum particle radius used in the model are displayed, and, in panel (d), the evolution of the power index of the size distribution. Note that with the exception of panel (a), the dust environments from the analysis of both post-perihelion images are indistinguishable.

nucleus position is significantly outside the optocenter of these images. This is consistent with the fact that the comet ceases activity before perihelion, as confirmed by the model results. The dust parameters are the same for both post-perihelion images, except that the mass production stops at 0.02 AU for the November 29.28 image and at 0.05 AU for the November 30.21 image. This accounts for the difference in total dust mass released in the two observations, 8.1×10^8 kg and 6.7×10^8, respectively. It is also important to note is the very small size of the particles that constitute both tails in comparison with all previous images, being in the range 0.1–50 μm.

It must be noted that while an isotropic ejection pattern was compatible with the ejection scenario in the first of the two pre-perihelion images on November 28.07, in order to perform a good fit to the images on November 28.62, 29.28, and 30.21, an anisotropic ejection model had to be considered. Specifically, for those images (those displayed in Figures 13(b), (c), and (d)) the ejection pattern was characterized by $u_R = 0.7 + 0.3\,r_1$ and $u_\theta = 0.5 + 0.5\,r_2$ while the ejection component along the perpendicular to the orbit plane is isotropic, i.e., $u_z = 2\,r_3$–1, where r_1, r_2, and r_3 are random numbers in the (0, 1) interval. To show this, post-perihelion synthetic images built under the assumption of isotropic ejection are shown in Figure 15, where it can be seen that they not adequately reproduce the observed brightness pattern.

4.2.1. Particle Sublimation Near ISON Perihelion

To gain insight into the size variations that the particles might experience due to sublimation processes that have taken place during the ISON close approach to perihelion, we have calculated the evolution of the grain sizes for different cometary materials. We have specifically considered spherical grains of crystalline olivine, pyroxene glass, and glassy carbon as typical cometary materials. The rate of size decrease due to sublimation is governed by the Clausius–Clapeyron equation as (see, e.g., Mukai & Mukai 1973; Kimura et al. 2002)

$$\frac{dr}{dt} = -\frac{1}{\rho_p}\sqrt{\frac{M_r u}{2\pi k_B T}}\,p(T), \qquad (1)$$

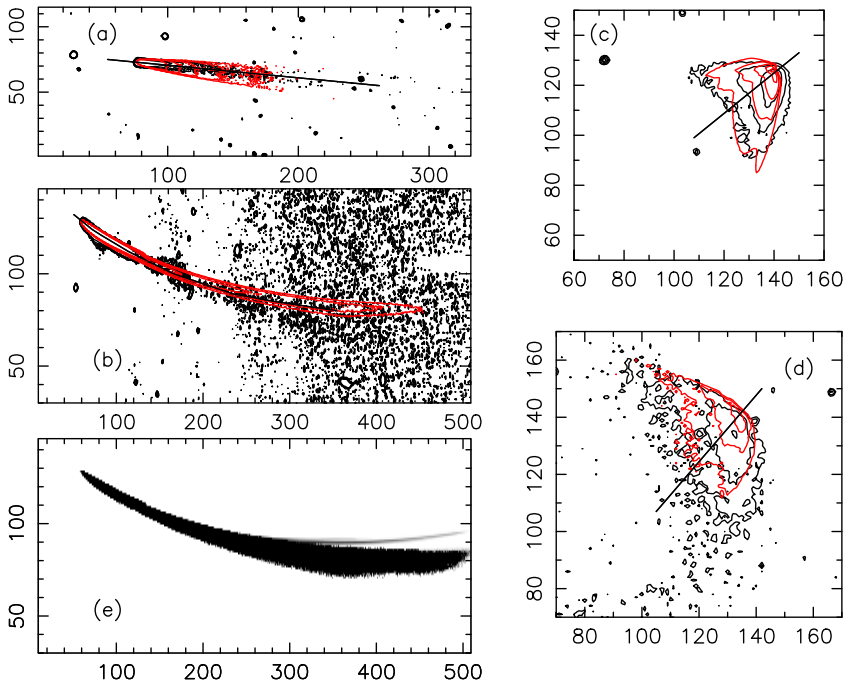

Figure 13. Panels (a)–(d): observed brightness isophotes (black contours) and modeled isophotes (red contours) for the analyzed *SOHO* LASCO C3 images. Panels (a), (b), (c), and (d) refer to the images on 2013 November 28.07, 28.63, 29.26, and 30.21, respectively (see Table 1). The black lines along the tails correspond to the brightness scans shown in Figure 14. Panel (e) shows a highly contrasted version of the model image on November 28.63 (panel (b)) intended to show the northern spike that is clearly seen in the Clear filter image (see Figure 4(b)), which is due to dust ejected much earlier in the ISON orbit.

(A color version of this figure is available in the online journal.)

where T is the temperature, ρ_p is the particle density, M_r is the molecular mass of the gas released in the sublimation process, $u = 1.66 \times 10^{-27}$ kg is the atomic mass unit, and k_B is the Boltzmann constant. The vapor pressure, $p(T)$, is given by

$$p(T) = \exp\left(-\frac{M_r u}{k_B T} L + b\right), \quad (2)$$

where L is the latent heat for sublimation, and b is a constant, which are obtained from evaporation experiments of the material involved.

The equilibrium temperature of the grains is computed from the balance between the energy absorbed and emitted using the equation (e.g., Hanner et al. 1997)

$$\frac{\pi r^2}{r_h^2} \int_0^\infty S(\lambda) Q_{\rm abs}(\lambda, r) d\lambda = 4\pi r^2 \int_0^\infty Q_{\rm abs}(\lambda, r) \pi B_\lambda(T(r)) d\lambda, \quad (3)$$

where $S(\lambda)$ is the solar flux at 1 AU, r_h is the heliocentric distance in AU, $B_\lambda(T(r))$ is the Planck function for grain temperature T, and $Q_{\rm abs}(\lambda, r)$ is the absorption efficiency of the grain of radius r at wavelength λ. The absorption efficiencies are computed for spherical grains by Mie theory, and are a function of the refractive index of the material. The refractive indices are taken from Edoh (1983) for glassy carbon, from Dorschner et al. (1995) for glassy pyroxene of composition $Mg_{0.5}Fe_{0.5}SiO_3$, and from Fabian et al. (2001), and Zeidler et al. (2011) for natural crystalline olivine in the mid-IR, and from unpublished data in the UV through the near-IR from the JENA database (http://www.astro.uni-jena.de/Laboratory/OCDB/crsilicates.html). The olivine refractive indices in the mid-IR from the three optical axes were averaged out.

The adopted values for the constants appearing in the sublimation equations are $b = 31.84$ (when MKS units are used), $L = 3.21\times10^6$ J kg^{-1}, $M_r = 169$, and $\rho_p = 3710$ kg m^{-3} for crystalline olivine, $b = 24.17$ (when MKS units are used), $L = 9.61\times10^6$ J kg^{-1}, $M_r = 60$ (see Kimura et al. 2002), and $\rho_p = 3200$ kg m^{-3} for pyroxene, and $b = 32.8$ (when MKS units are used), $L = 6.19\times10^7$ J kg^{-1}, $M_r = 12$, and $\rho_p = 2250$ kg m^{-3} for carbon. To obtain the evolution of the grain size for the different materials, we first compute the equilibrium temperature of the grains and the rate of change of the grain radius for different heliocentric distances and grain sizes. Then, we integrate Equation (1) taking into account, at each time step, the predicted heliocentric position of the comet ISON. Thus, the evolution of the grain size as a function of the heliocentric distance, for different initial grain radii and the three different compositions, is displayed in Figure 16.

The first immediate conclusion that can be drawn from Figure 16 is that grains of sizes $r \lesssim 10$ μm and of any of the studied compositions cannot survive ISON perihelion passage. In particular, crystalline olivine grains of any size will be completely vaporized at $r_h \leqslant 5$ $R_\odot$, so that grains of this composition will not survive. In contrast, pyroxene grains of sizes $r \gtrsim 100$ μm will survive, with some size reduction. Micrometer and submicrometer pyroxene grains will start to vaporize at $r_h \lesssim 10$ $R_\odot$. On the other hand, glassy carbon grains last longer than grains of the other substances, those of $r \lesssim 10$ μm being vaporized very close to perihelion, and those having $r \gtrsim 100$ μm surviving the perihelion passage with some size reduction.

From the pre-perihelion LASCO C3 image on November 28.07, we have inferred a large mass-loss rate in the 0.36–0.08 AU heliocentric distance range. Based on the extraordinary amount of dust mass contained in the tail, of

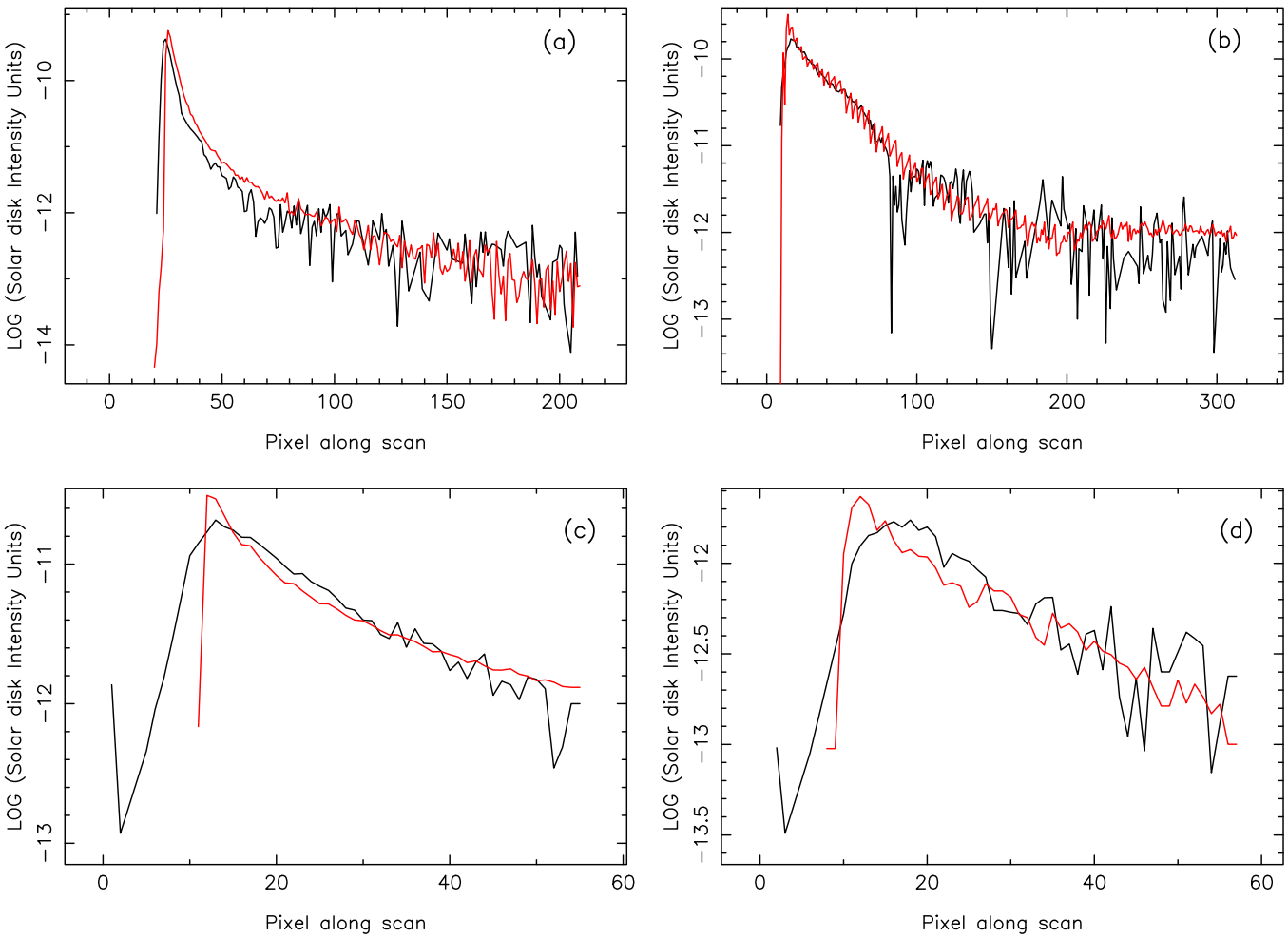

Figure 14. Brightness scans along the *SOHO* LASCO C3 images displayed in Figure 13. The black scans correspond to the observation, and the red scans to the model.

(A color version of this figure is available in the online journal.)

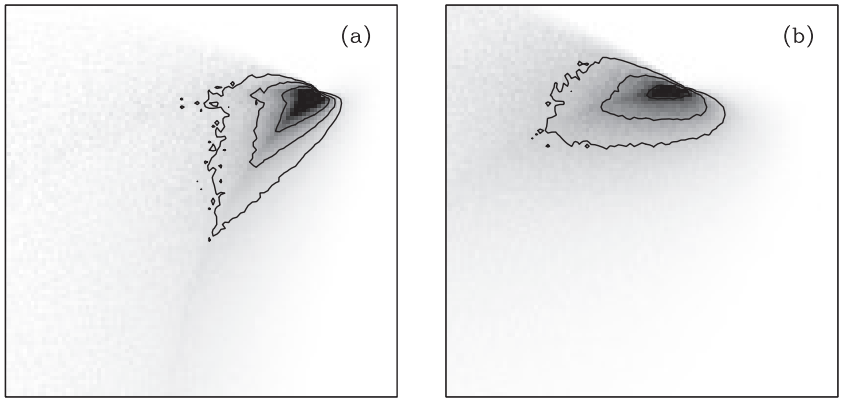

Figure 15. Synthetic images of ISON on 2013 November 29.28 (a) and 30.21 (b) under the assumption of isotropic emission.

2.3×10^{11} kg, we believe that most of the mass released is a consequence of a cataclysmic disruption of the nucleus, from whose interior a large amount of fresh material was released in the form of both ice and refractory material. This huge release of material is simultaneously accompanied by a reduction in dust production rate by a factor of at least 40 of that derived from ground-based data at $r_h > 0.61$ AU, otherwise the spike seen in the Clear filter images would show up markedly in the synthetic DeepRed image. The reason that strong reduction must be linked to the fact that the entire tail is within the LASCO C3 field of view, i.e., inside 32 solar radii or ~0.15 AU, so that particle sublimation has surely taken place (see Figure 16). During this strong ejection of material, it is interesting to note the narrow spike in dust production near 0.37 AU or 80 $R_\odot$, heliocentric distance at which the blackbody temperature is about 450 K, which is the sublimation temperature of most organics

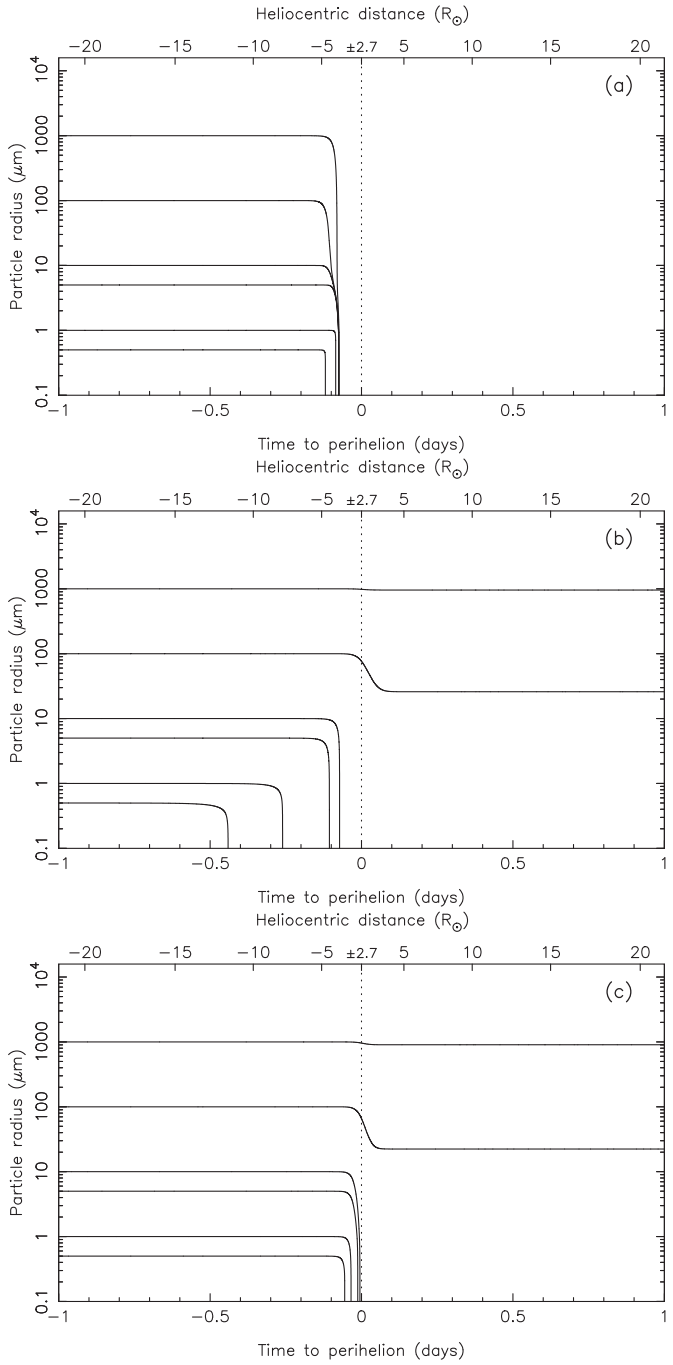

Figure 16. Evolution of grain size as a function of ISON heliocentric distance, for several initial radii and different materials: (a) crystalline olivine, (b) glassy pyroxene, and (c) carbon. For the source of the optical and sublimation constants for the different substances, see the text.

(Kouchi et al. 2002; Kimura et al. 2002). Then, if the equilibrium temperature of the grains is close to that of a blackbody, sublimation of the organic mantle covering the particles possibly takes place (Kimura et al. 2002). While the position of the spike corresponds to the heliocentric distance at which sublimation of organic compounds is expected, we cannot prove this solely from this data set.

Most of the large amount of material released in the 0.36 to 0.08 AU range is rapidly vaporized afterward as confirmed by the analysis of the November 28.62 DeepRed image, implying a strong reduction in dust mass production, mainly inward of 0.36 AU, as particle vaporization should be stronger for shorter heliocentric distances (see Figure 16). However, the total dust mass in the first post-perihelion tail on November 29.28 is approximately the same as in the post-perihelion November 28.62 tail. This would indicate that the dominant process in that time interval should be particle fragmentation, and not particle vaporization, in order to make mass conservation compatible with a decrease in grain size. It is possible that the smallest grains have undergone vaporization at distances $r_h \leqslant 5\ R_\odot$, and then the larger particles, which are essentially not vaporized, are suffering mostly fragmentation phenomena. This is consistent with the non-detection of ionized oxygen from the *Solar Dynamics Observatory* (Pesnell 2013).

Finally, the dust production rate profile corresponding to the last image analyzed on November 30.21 (the dashed line in Figure 12(a) stops at 0.05 AU (or 10.8 $R_\odot$), indicating that the material that makes the November 29.28 tail in the region 0.05–0.02 AU has been completely vaporized after undergoing the fragmentation phenomena.

5. CONCLUSIONS

We have performed a complete study of the dust environment evolution of the comet ISON by analyzing a series of images and Afρ data, spanning a period from after discovery until its almost complete vaporization a few days after perihelion. We use a Monte Carlo model to retrieve the dust parameters as a function of the heliocentric distance. The most important conclusions follow below.

The early Afρ and image data are consistent with ejection from an active area from a comet nucleus whose spinning axis has a large obliquity ($I = 70^\circ$), in agreement with the interpretation of *HST* observations of the comet by Li et al. (2013). The argument of the subsolar meridian at perihelion is found to be around ($\Phi = 270^\circ$; assuming prograde motion), and the nucleus would present a single and extended active area from 35° to 90° north. This configuration nicely fits the early images and Afρ data until approximately 200 days pre-perihelion, where the emission should vary from the mentioned active area on the northern hemisphere to become essentially isotropic afterward. The reason for that is unclear, although a plausible explanation is the propagation of a thermal wave into the nucleus that activate subsurface sublimation in areas that previously had been inactive.

The early Afρ data show a local maximum at approximately 350 days pre-perihelion which has been found to be coincident with a minimum phase angle of about 2°, showing the presence of backscattering enhancement, which has been corrected by a linear phase coefficient of $\kappa = 0.03$ mag deg^{-1}. However, a residual maximum still remains, even considering a larger κ. As a consequence, a coincidental outburst of activity cannot be ruled out.

The isotropic ejection model from approximately 200 days to perihelion to 13 days to perihelion is capable of fitting all the images and Afρ data in this interval, perfectly mimicking the minimum in the Afρ data found observationally 60 days before perihelion and the strong rise afterward. Comparing to the water production rate, we found a dust-to-gas ratio that generally decreases with increasing heliocentric distance, and a velocity ejection law that is close to a $1/r_h^2$ dependence.

The analysis of *SOHO* LASCO C3 2013 November 28.07 DeepRed images reveals that, assuming an initial nucleus of

$R_N = 500$ m with $\rho = 1000$ kg m^{-3}, at least half of the mass of the nucleus was vaporized when the comet was at about 17 $R_\odot$. At this time, based on the particle sublimation curves for different cometary materials, we conclude that the nucleus must have suffered a cataclysmic fragmentation releasing a large amount of material. The analysis of yet another pre-perihelion image on November 28.62 reveals that most of the material released was immediately vaporized after the catastrophic event, so that the nucleus itself probably disappeared at that time. The analysis of a post-perihelion LASCO C3 DeepRed image on November 29.28 reveals that the total mass has not changed with respect to the pre-perihelion November 28.62 image, while the particle size has decreased notably, which is compatible with fragmentation phenomena of the largest particles, but not with vaporization. In fact, for two analyzed compositions, pyroxene glass, and glassy carbon, particles of the size $r > 10$ μm could have survived ISON perihelion passage, experiencing only a small variation in size.

The total mass contained in the last LASCO C3 post-perihelion image analyzed, the surviving ISON material, is just 6.7×10^8 kg, or a sphere of 54 m in radius with a density of 1000 kg m^{-3}. This surviving dust is populated by small particles in the size range 0.1–50 μm, the final product of profuse vaporization and particle fragmentation process.

We thank an anonymous referee for the critical reviewing of the manuscript and constructive comments that helped to improve the paper.

We are grateful to Bernhard Fleck, who made the *SOHO* LASCO C3 images used in this paper available to us.

This work is partially based on observations collected at the Centro Astronómico Hispano Alemán (CAHA) at Calar Alto, operated jointly by the Max-Planck Institut für Astronomie and the Instituto de Astrofísica de Andalucía (CSIC), and on observations made at the 0.90 m and 1.52 m of Sierra Nevada Observatory, operated by the Instituto de Astrofísica de Andalucía (CSIC).

This work was supported by contracts AYA2012-39691-C02-01 and AYA2011-30106-C02-01 (Ministerio de Economía y Competitividad) and FQM-4555 (Junta de Andalucía).

Facilities: OSN:1.5m, OSN:0.9m, CAO:2.2m, CAO:1.2m, SOHO

REFERENCES

Agúndez, M., Biver, N., Santos-Sanz, P., et al. 2014, A&A, 564, L2
Biver, N., Agúndez, M., Santos-Sanz, P., et al. 2013, CBET, 3711, 2
Boehnhardt, H., Tubiana, C., Oklay, N., et al. 2013, CBET, 3715, 1
Combi, M. R., Fougere, N., Mäkinen, J. T. T., et al. 2014, ApJL, 788, L7
Crifo, J. F., & Rodionov, A. V. 1997, Icar, 129, 72
Domingo, V., Fleck, B., & Poland, A. I. 1995, SoPh, 162, 1
Dorschner, J., Begemann, B., Henning, T., et al. 1995, A&A, 300, 503
Draine, B. T., & Flatau, P. J. 1994, JOSAA, 11, 1491
Edoh, O. 1983, PhD thesis, Univ. Arizona, Tucson
Fabian, D., Henning, T., Jäger, C., et al. 2001, A&A, 378, 228
Fulle, M. 1989, A&A, 217, 283
Fulle, M., Colangeli, L., Agarwal, J., et al. 2010, A&A, 522, 63
Fulle, M., Molaro, P., Buzzi, L., et al. 2013, ApJ, 771, 21
Hanner, M. S., Gehrz, R. D., Harker, D. E., et al. 1997, EM&P, 79, 247
Jorda, L. J., Crovisier, J., & Green, D. W. E. 2008, LPICo, 1405, 8046
Kimura, H., Mann, I., Biesecker, D. A., & Jessberger, E. K. 2002, Icar, 159, 529
Knight, M. M., A'Hearn, M. F., Biesecker, D. A., et al. 2010, AJ, 139, 926
Knight, M. M., & Battams, K. 2014, ApJL, 782, L37
Kouchi, A., Kudo, T., Nakano, H., et al. 2002, ApJL, 566, L121
Li, J.-Y., Kelley, M. S., Knight, M. M., et al. 2013, ApJL, 779, L3
Marcus, J. N. 2007, ICQ, 29, 39
Meech, K. J., & Jewitt, D. C. 1987, A&A, 187, 585
Moreno, F., Cabrera-Lavers, A., Vaduvescu, O., et al. 2013, ApJL, 770, L30
Moreno, F., Pozuelos, F., Aceituno, F., et al. 2012, ApJ, 752, 136
Morrill, J. S., Korendyke, C. M., Brueckner, G. E., et al. 2006, SoPh, 233, 331
Mukai, T., & Mukai, S. 1973, PASJ, 25, 481
Nevski, V., & Novichonok, A. 2012, CBET, 3238
Opitom, C., Jehin, E., Manfroid, J., & Gillon, M. 2013, CBET, 3711, 3
Pesnell, D. 2013, ISON Observer's Workshop Follow-up Meeting, "SDO Observations of Comet ISON," Johns Hopkins Applied Physics Laboratory, 2013 December 6
Sekanina, Z. 1981, AREPS, 9, 113
Watanabe, J., Kawakita, H., Furusho, R., et al. 2003, ApJ, 585, 159
Whipple, F. 1951, ApJ, 113, 464
Wilson, J. K., Baumgardner, J., & Mendillo, M. 1998, GeoRL, 25, 225
Zeidler, S., Posch, Th., Mutschke, H., et al. 2011, A&A, 526, A68

4.2 Unpublished results

In this section we report some results which have not been published yet, but which are being considered for publication shortly. These results are related to outbursts suffered by two SPCs: 217P/Linear and P/2010 H2 (hereafter 217P and Vales). Outbursts are short duration events which increase the comet brightness by several magnitudes as a consequence of a massive dust release from the nucleus. The mechanisms which drive these events are not completely understood, although some theories are being put forward. In the first Chapter, subsection 1.5, we introduced these events in detail as well as the current theories about their triggering mechanisms.

Both comets are JFCs with perihelion distances and orbital periods of $q = 1.22$ AU and $P = 7.83$ yr in the case of 217P, and $q = 3.10$ AU and $P = 7.56$ yr in the case of Vales. They suffered the outbursts some days after their last perihelion passage in 2009 September 8th (217P), and 2010 March 9th (Vales).

Sarugaku et al. (2010) studied the outburst of 217P, using optical images taken with the Kiso 105 cm Schmind Telescope which captured the day-by-day variation of the dust environment during the event (see 1.7). On the other hand, comet Vales was discovered as a consequence of its outburst, when it reached about 8-9 mag, appearing suddenly in the sky. However, no studies of that event have been published yet. Thus, our purpose is to determine the dust parameters which best describe the dust environment of these objects before, during, and after the outbursts, and compare them with previous results for 217P and others available, such as the case of 17P/Holmes (see e.g. Moreno et al. 2008; Ishiguro et al. 2013). In addition, we obtain the total amount of dust emitted during the explosions and their duration.

To perform this task we used optical images taken at Sierra Nevada Observatory (see Fig. 4.1) and $Af\rho$ measurements as a function of the heliocentric distance, provided by the amateur astronomical association *Cometas-Obs*. The image reduction process, as well as the Monte Carlo model used to fit the observations, have already been explained in each appended paper of the previous section, and will not be repeated here.

217P/Linear

This comet suffered an outburst on October 13, 2010. In our study we have one observation $\sim$ 60 days after the outburst, and 215 $Af\rho$ measurements provided by *Comets-Obs* which span $\sim$ 290 days pre- and post-perihelion. From our model we find that the comet started emitting dust at $\sim$ 2.5 AU inbound, and the activity increased little by little until perihelion. The rest of the dust parameters, i.e., ejection velocities and size distribution of particles, display the same trend. The current knowledge of cometary properties establishes the bulk density around $\rho = 600$ kg m^{-3} (see e.g. Davidsson & Gutiérrez 2004; A'Hearn et al. 2005). The ejection velocity at a distance of $R \sim 20R_N$, where the gas drag vanishes, must overcome the escape velocity, which is given by $v_{esc} = \sqrt{2GMR^{-1}}$, and if we assume a spherical shaped nucleus, the escape velocity is $v_{esc} = R_N\sqrt{(2/15)G\pi\rho}$. Due to the lack of nucleus size estimates, we considered the minimum particle velocity determined in the model as $v_{esc} \sim v_{min}$. In this way, we could estimate an upper limit of the nucleus radius. In our case, the terminal velocity for the largest particles at 2.5 AU, were $v_{min} = 50$ cm s^{-1}, so we can conclude that the upper size of the nucleus is roughly 3.8 km.

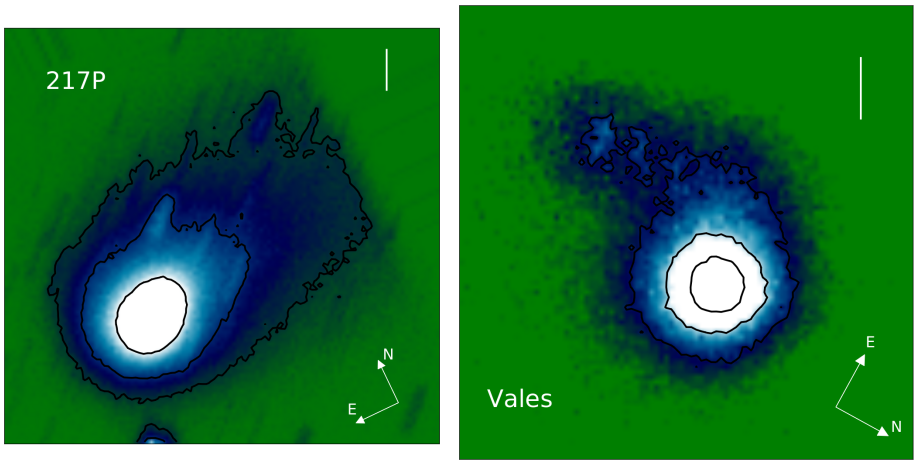

Figure 4.1: Observations carried out at Sierra Nevada Observatory in Granada, using a CCD camera at the 1.52 m telescope. Left panel corresponds to comet 217P on December 12, 2009 ($\sim$ 60 days after the outburst). The isophotes levels are 0.50×10^{-13}, 0.22×10^{-13}, 1.00×10^{-14} SDU. Right panel corresponds to comet Vales on June 3, 2010 ($\sim$ 51 days after the outburst). The isophote levels are 1.50×10^{-13}, 1.00×10^{-13}, 0.50×10^{-13}, and 0.22×10^{-13} SDU. In both cases the orientation is given and the vertical bars correspond to 10^4km in the sky. Table 4.1 shows the log of the observations.

Table 4.1: Log of observations

Comet	Observation Date (UT)	Days from perihelion	r_h (AU)	Δ (AU)	Resolution (km pixel^{-1})	Phase Angle (°)	$Af\rho$ (cm^{-1})	Num. of *Cometas-Obs* observations
217P/LINEAR	2009 Dec 12 02:15	80.5	1.684	0.732	976.9	334.4	80	215
P/2010 H2 (Vales)	2010 Jan 3 23:45	86.7	3.129	2.463	822.1	118.8	166	112

Note. Both comets were observed post-perihelion, and after the outbursts.

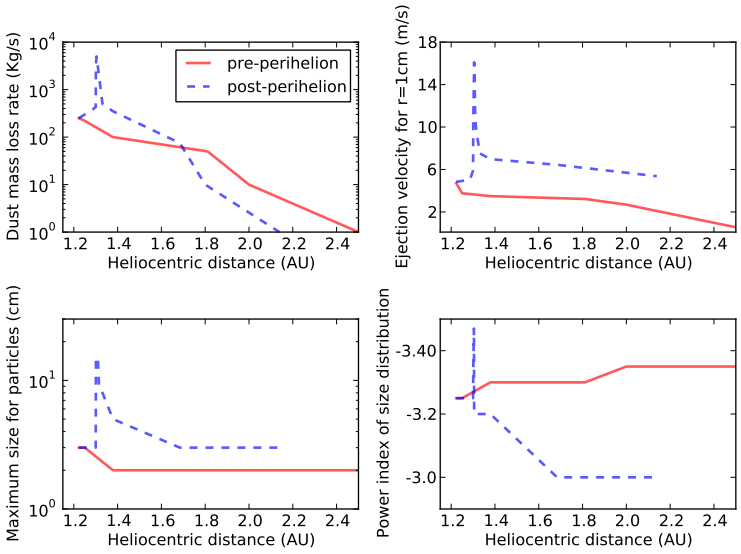

Figure 4.2: 217P dust parameters derived from the model which best fits the observations. All parameters are given as a function of the heliocentric distance. From top to bottom and left to right the panels are: (a) Dust mass loss rate [kg s^{-1}]; (b) Ejection velocities for r=1 cm glassy carbon spherical particles [m/s]; (c) Maximum size of the particles [cm]; (d) Power index of the size distribution δ. In all cases the solid red line corresponds to pre-perihelion and the dashed blue line to post-perihelion.

In Fig. 4.2, the dust parameters as a function of the heliocentric distance are shown. In all cases, we can see a remarkable increase at $r = 1.301$ AU post-perihelion. This event corresponds to the outburst on October 13. From October 15, the dust parameters started to decrease. During the outburst, the peak dust production rate was 5100 kg s^{-1}. The peak ejection velocity for $r = 1$ cm particles reached a value of $v_{ejec} = 16$ m s^{-1} and the maximum size of particles was $r = 15$ cm, while the minimum size was fixed as constant with value of 1 μm. The power of the size distribution reached the value of $\alpha \sim -3.6$. We established that the onset of the event was on October 13, and its duration was roughly 45 h. During that time, the total mass ejected was $M_{outb} \sim 3.2 \times 10^8$ kg. The comet emission pattern is concluded to be isotropic for the whole study. The total dust production was 3.2×10^9 kg. In Fig 4.3 we present the comparison of the model with the observational data, where the agreement between them is remarkable.

P/2010 H2 (Vales)

Vales comet appeared suddenly in the sky on April 16 , 2010. There have been no reports on its general properties or on the outburst suffered. From our model, we infer that the comet had a huge explosion on April 14, which lasted until April 18. After that date, the comet faded away until its disappearance. Thus, our data correspond to one observation night carried out at 1.52 m telescope at the OSN, and 112 measurements of the $Af\rho$ parameter provided by *Cometas-Obs*, which cover from the onset of activity until $\sim$ 52 days later.

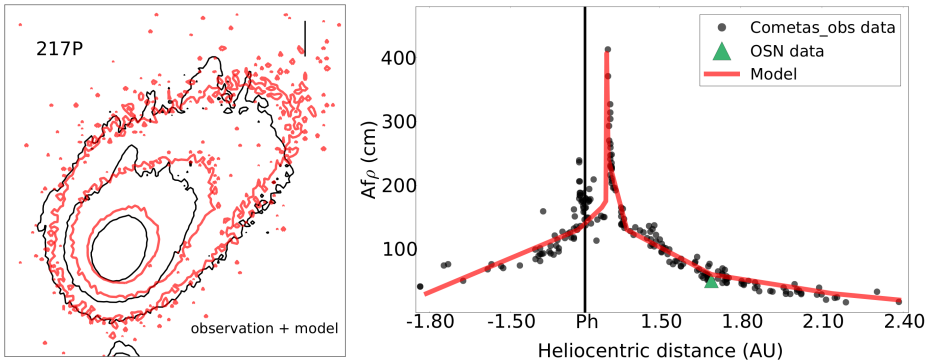

Figure 4.3: Comparison between model and observations of comet 217P/Linear. Left panel: Isophote field on December 12, 2009. The contours levels are 0.50×10^{-13}, 0.22×10^{-13}, and 1.00×10^{-14} SDU. The black contours correspond to the OSN observation, and the red contours to the model. The vertical bar corresponds to 10^4 km in the sky. Right panel: $Af\rho$ versus heliocentric distance. The black dots correspond to the *Cometas-Obs* measurements and the green triangle is the OSN datum, which corresponds to the observation day. The red line is the model. Both observations and model refer to $\rho = 10^4$ km.

From the analysis of this observational information we infer that the dust loss rate reached its peak at 35×10^3 kg s^{-1} with an ejection velocity for $r = 1$ cm particles of 10 m s^{-1}. In addition, the maximum size of particles during the event was found to be $r = 10$ cm, and the power index of the size distribution was in the range of -3.0-(-3.5). The total duration of the outburst was roughly 120 h. During that period, the total ejected dust was found to be 8.5×10^9 kg, which indicates the strength of the event. In Fig 4.4 the evolution of the dust parameters during the outburst as a function of the heliocentric distance are shown, and in Fig. 4.5, a comparison between the observation and the model is displayed.

Discussion

The outburst of comet 217P was reported by Sarugaku et al. (2010), where the authors imaged the comet day-by-day from October 11 to October 17. From their analysis they concluded that the total dust emitted was in the range of $10^6 - 10^9$ kg depending on the size of the particles, with minimum size of 3μm and maximum size up to 12 cm. These values agree with our estimates. In addition, they are comparable to the small outburst characterized by us in paper III, where the total dust emitted by two outbursts was in the range of $3 - 9 \times 10^8$ kg. These outbursts are larger than the ones reported by Belton et al. (2008) in his studies of comet 9P/Temple 1. The authors observed at least 10 events in the range of $6 - 30 \times 10^4$ kg and established a relationship between those mini-outbursts and some features observed on the surface during the Deep Impact mission (see e.g. Veverka et al. 2013; A'Hearn et al. 2005; Thomas et al. 2013).

In the case of comet Vales, there are no previous reports on its outburst. The total dust ejected was 8.5×10^9 kg. This value is comparable to the results obtained by some authors of comet 29P/S-W, whose outbursts reach values in the range of $10^8 - 10^{10}$ kg (see e.g. Moreno 2009; Sekanina

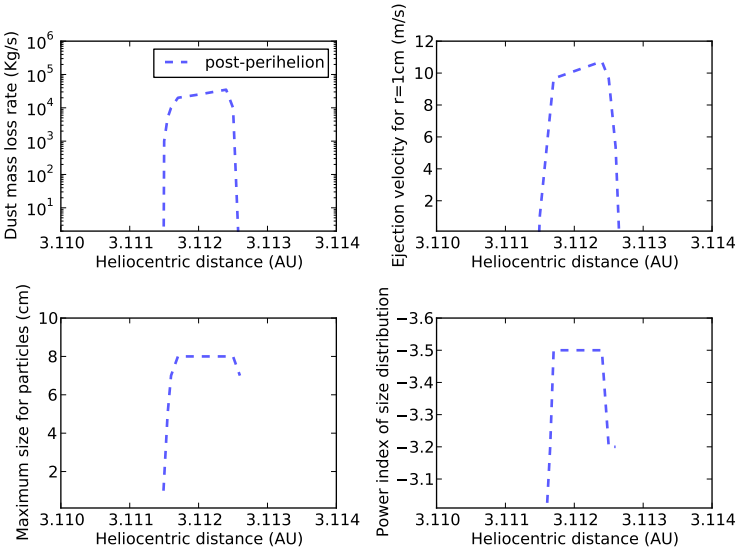

Figure 4.4: Dust environment for comet Vales derived from the Monte Carlo model. All parameters are given as a function of the heliocentric distance. From top to bottom and left to right the panels are: (a) Dust mass loss rate [kg s^{-1}]; (b) Ejection velocities for particles of r=1 cm glassy carbon spheres [m/s]; (c) Maximum size of the particles [cm]; (d) Power index of the size distribution δ. In all cases the dashed red line corresponds to post-perihelion.

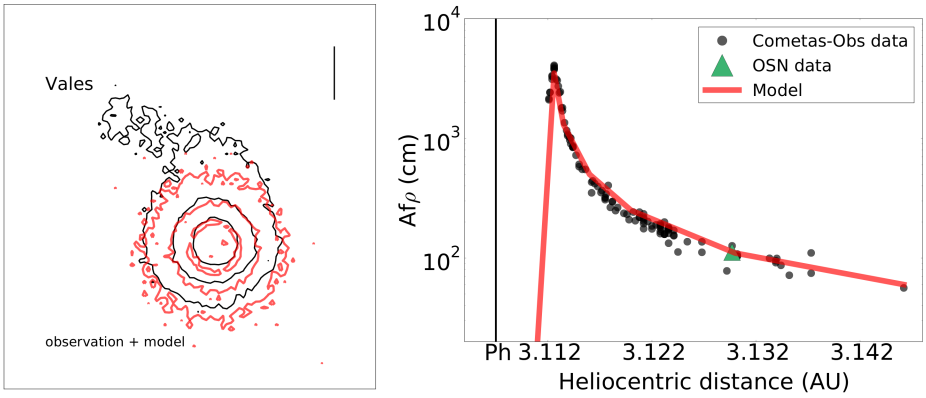

Figure 4.5: Comparison between model and observations of comet P/2010 H2 (Vales). Left panel: Isophote field on June 3, 2010. The contours levels are 0.85×10^{-13}, 0.45×10^{-13}, and 0.20×10^{-13} SDU. The black contours correspond to the OSN observation, and the red contours to the model. The vertical bar corresponds to 10^4 km on the sky. Right panel: $Af\rho$ versus heliocentric distance. The black dots correspond to the *Cometas-Obs* measurements and the green triangle is the OSN datum, which corresponds to the observation date. The red line is the model. Both observations and the model refer to $\rho = 10^4$ km.

2008; Hosek et al. 2013). However, these strong values from comet Vales and 29P/S-W are far from the breathtaking outburst suffered by comet 17P/Holmes (see Fig. 1.8). This comet experienced a massive dust release from its nucleus in the range of 10^{10}-10^{12} kg (see e.g. Moreno et al. 2008; Sekanina 2008; Li et al. 2011), with expansion velocities of 9-250 m s^{-1} for particles with sizes of 2-200 μm (Reach et al. 2010). It was estimated that the total mass ejected corresponded with $\sim 3-9\%$ of its nuclear mass (Boissier et al. 2012), and produced the ejection of large chunks in the range of 10-100 m (Stevenson et al. 2010).

Chapter 5

Future work

In this Chapter, we summarize some ongoing projects which were not finished at the time this thesis dissertation went to print. These projects, are presented according to the comet family involved, as we did before in the results section (Chapter 4).

Regarding the SPCs, we have planned a long-term study of comet 67P/Churyumov-Gerasimenko. This comet is of special interest as a target of the Rosetta mission, which will arrive at the comet in August-September 2014. We will make an extensive characterization of this target and will compare the results with those obtained for other targets of this family, presented in Chapter 4. There are planned observations from the OSN and other telescopes, and systematic measure of the $Af\rho$ parameter from the amateur association *Cometas-Obs*. The idea is to compare these data with the *in situ* data derived from Rosetta Mission.

In the case of the MBCs, due to their unpredictable activation times, we have started a target-of-opportunity (ToO) observation campaign at the OSN and at the GTC telescope (Canary Islands, Spain) in a IAA-IAC collaboration. An example of this, was the report of the first observed asteroid nucleus fragmentation, in MBC P/2013 R3 (Catalina-PanStarrs) (Licandro et al. 2013) (see Fig 5.1).

Some projects are focused on LPCs, particularly on comet C/2013 A1 (Siding Spring) which will have a close encounter with Mars (~40 Martian radii) on October 18, 2014 (see Fig. 5.8. We have obtained observation time for this comet from CASLEO (Complejo Astronómico El Leoncito) (Argentina) from July to September 2014, in collaboration with R. Gil-Hutton. This is an important event in terms of the accretion of water and organic materials on the planet. Although approaches are more common than direct impacts, once each $\sim 10^8$ yr (Stokes & Yeomans 2003), they are still rare. The event will be followed by a number of international groups (Ye & Hui 2014; Tricarico et al. 2014; Farnocchia et al. 2014). The ground-based observation window is from June to November, 2014, and only from the southern hemisphere. We will use the 2.15 m telescope (Jorge Sahade), for 9 nights. In addition, we have planned a monitoring of this event with *Cometas-Obs*, who have some observers in Australia.

Another project on this family will be the characterization of a sample of LPCs. These comets, namely C/2009 P1 (Garradd), P/2011 L4 (PanStarrs), and P/2012 F6 (Lemmon), have already been observed at the 1.52 m telescope at the Sierra Nevada Observatory, and we also have available $Af\rho$

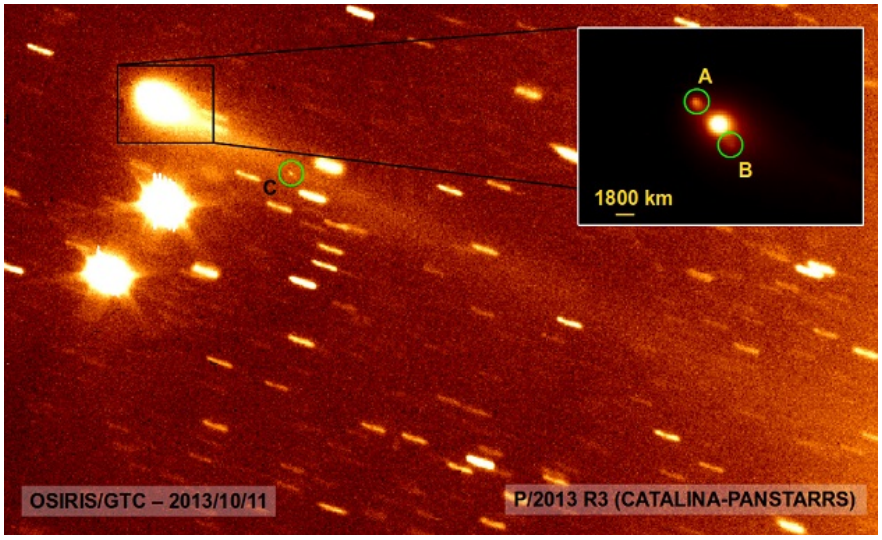

Figure 5.1: The MBC P/2013 R3 (Catalina-Panstarrs) obtained at GTC telescope on October 11th, 2013. The green circles mark the three fragments detected: A, B and C.

measurements from *Cometas-Obs*. C/2009 P1 (Garradd) has one of the highest dust-to-gas ratios ever observed, as in the case of C/1995 O1 (Hale-Bopp). Some observations at the OSN, and the $Af\rho$ curve are shown in Figs. 5.2, and 5.3. C/2011 L4 (PanStarrs) displayed asymmetric activity around perihelion, and became one of the most active targets in recent years (see e.g. Combi et al. 2014; Yang et al. 2014). The OSN observations are shown in Fig. 5.4, and the $Af\rho$ measurements are presented in Fig. 5.5. Comet C/2012 F6 (Lemmon) had the peculiarity of having a heterogeneous nucleus, due to the normal HCN, CH_4, and CO abundances, but enhanced H_2CO abundance(see e.g. Combi et al. 2014; Paganini et al. 2014). In Fig. 5.6 and 5.7, the OSN observations and the $Af\rho$ curve as a function of the time to perihelion are shown.

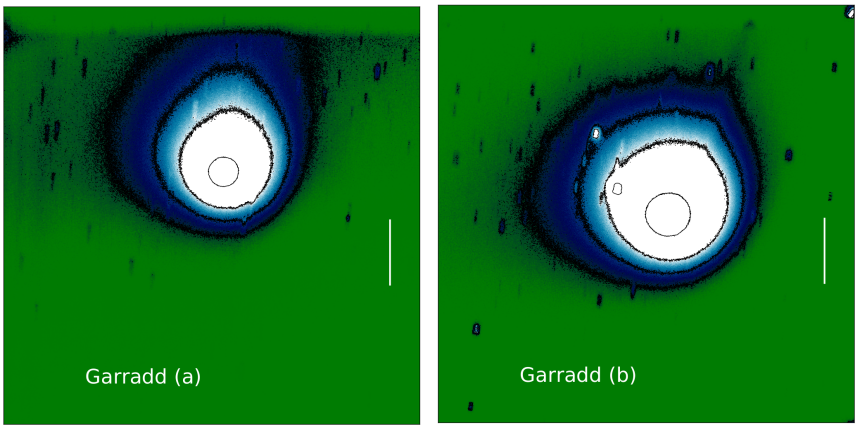

Figure 5.2: C/2009 P1 (Garradd) observations obtained using a CCD camera at the 1.52m OSN telescope, in Granada, Spain. (a) January 3, 2013, and (b) January 6, 2013. Both images correspond to r_h = 1.56 AU, Δ = 1.90 AU, and a pixel size of 633.9 km. The isophote levels, in Solar Disk Units (SDU), are 2.0×10^{-12}, 0.5×10^{-12}, 0.25×10^{-12}, and 0.1×10^{-12}. North is up and East is left. The vertical bars correspond to 10^6 km in the sky.

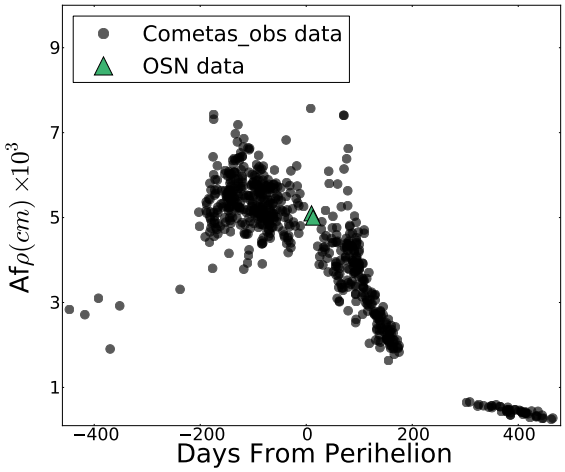

Figure 5.3: C/2009 P1 (Garradd). $Af\rho$ versus time to perihelion. The black dots correspond to *Cometas-Obs* data, and the green triangles are the OSN observations presented in Fig. 5.2. These observations are refered to $\rho = 10^4$ km.

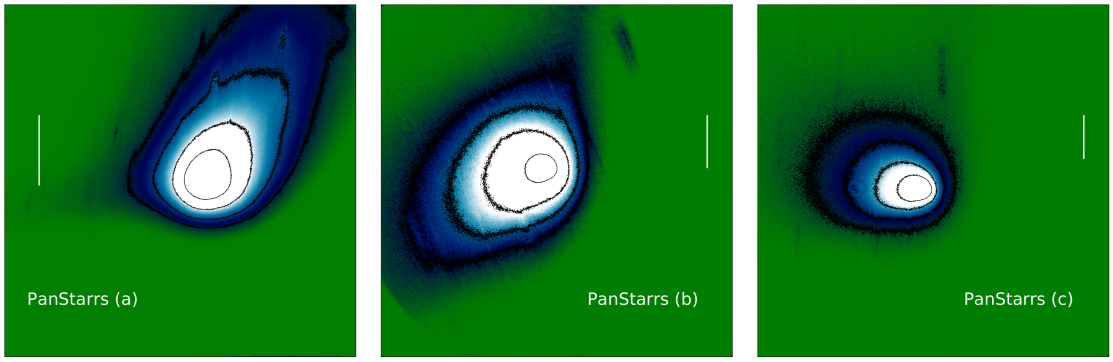

Figure 5.4: As Fig. 5.2 but for the comet C/2011 L4 (PanStarrs). (a) May 1, 2013, r_h = 1.31 AU, Δ = 1.53 AU, and pixel size of 510.4 km. The isophote levels are 2.0×10^{-12}, 1.0×10^{-12}, 0.5×10^{-12}, and 0.25×10^{-12} SDU. (b) June 13, 2013, r_h = 2.04 AU, Δ = 2.01 AU, and pixel size of 670.6 km. The isophote levels are 0.5×10^{-12}, 0.15×10^{-12}, 0.75×10^{-13}, and 0.40×10^{-13} SDU. (c) July 8, 2013, r_h = 2.42 AU, Δ = 2.40 AU, and a pixel size of 807.4 km. The isophote levels are 2.0×10^{-13}, 1.0×10^{-13}, 0.5×10^{-13}, and 0.25×10^{-13} SDU.

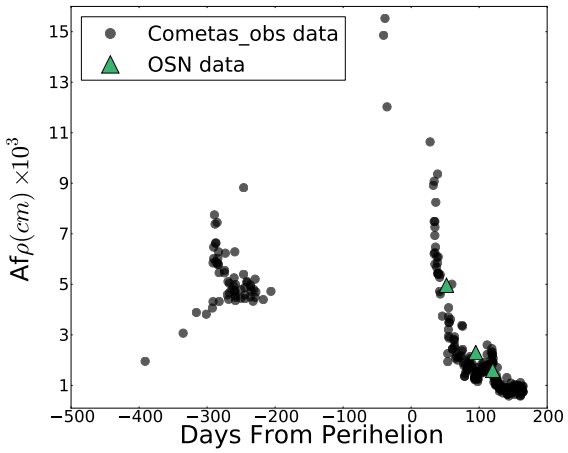

Figure 5.5: As Fig. 5.3 but for the comet C/2011 L4 (PanStarrs).

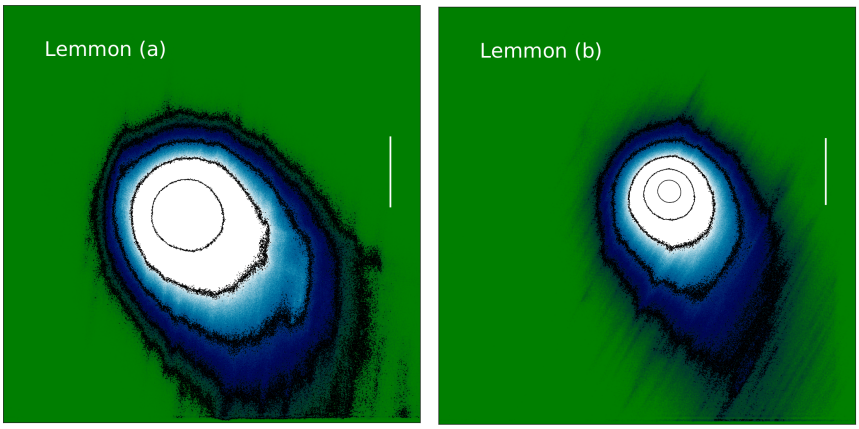

Figure 5.6: As Fig. 5.2 but for the comet C/2012 F6 (Lemmon). (a) June 14, 2013, r_h = 1.64 AU, Δ = 1.77 AU, and pixel size of 590.5 km. (b) July 9, 2013, with r_h = 1.99 AU, Δ = 1.87 AU, and pixel size of 623.9 km. In both dates the isophote levels are 5.0×10^{-13}, 2.0×10^{-13}, 1.0×10^{-13}, 0.5×10^{-13}, and 0.25×10^{-13} SDU.

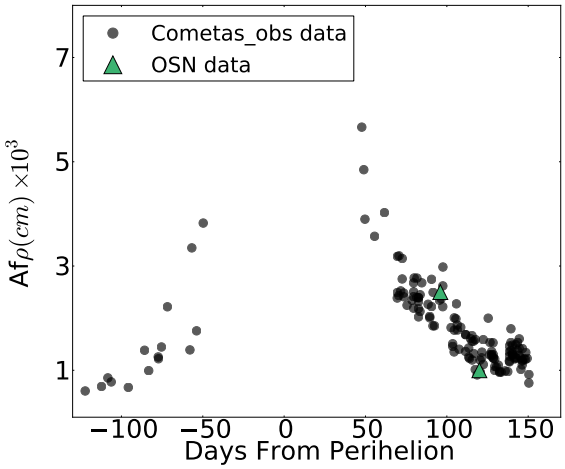

Figure 5.7: As Fig. 5.3 but for the comet C/2012 F6 (Lemmon).

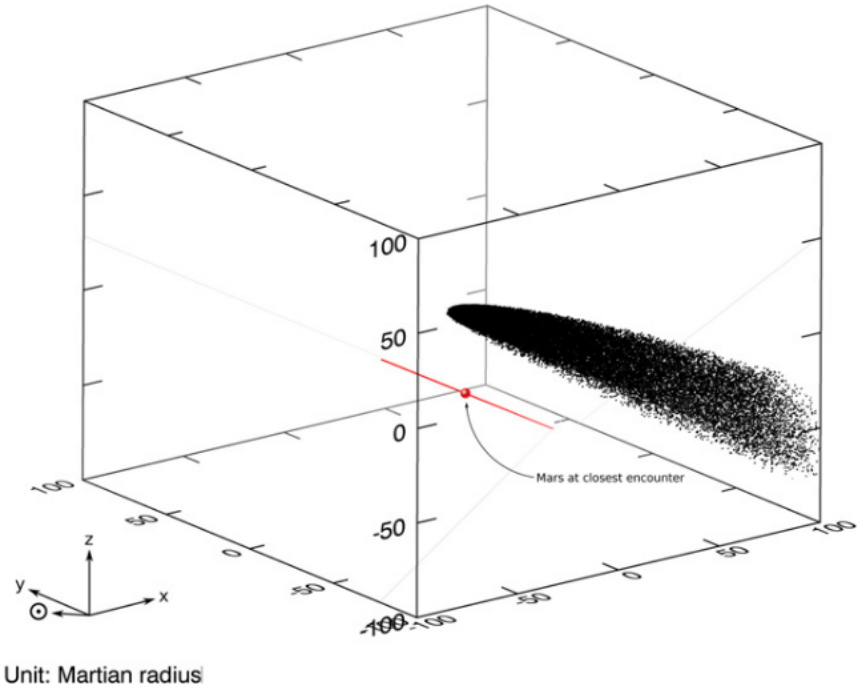

Figure 5.8: Close approach between Mars and the LPC C/2013 A1 (Siding-Spring). In the graph, 1 unit equals 1 Martian radius. Extracted from Ye & Hui (2014).

Chapter 6

Summary & Conclusions

In this Ph.D. thesis, we have discussed the dust environment of comets of different families, as a function of the heliocentric distance. In addition, for the SPCs, we have presented dynamical analyses. In this section, we give a short summary of the studies done and its conclusions.

- In papers I, II, and III we report on the dust analysis and dynamical studies of a sample of ten SPCs. These comets are: 22P/Kopff, 30P/Rienmuth 1, 78P/Gehrels 2, 81P/Wild 2, 103P/Hartley 2, 115P/Maury, 118P/Shoemaker-Levy 4, 123P/West-Hartley, 157P/Tritton, 185P/Petriew, and P/2011 W2 (Rinner). In these papers, we present an accurate characterization of the dust parameters which best describe the dust environment of the comets during a significant orbital arc around their perihelion passages. These parameters are: dust loss rates, size distribution functions of the particles, ejection velocities, and the emission patterns. To this end, we use our Monte Carlo dust tail code (e.g. Moreno et al. 2012). In addition, using the numerical integrator Mercury 6.2 developed by Chambers (1999), we have determined the dynamical history of each comet, in order to identify the solar system regions visited and the time spent there, for each comet. From these two different analyses, we relate the annual dust production rate with the time spent in the region of JFCs for all comets. The main result obtained, is that the highly active comets are also the youngest ones with age in the range of 40-600 yr in the Jupiter Family region.

- The work concerning MBCs is presented in papers IV and V. In these papers, the comets studied are P/2012 T1 (PANSTARRS) and P/2013 P5 (PANSTARRS). We present a characterization of the dust environment following the steps described in chapter 3. The mechanisms which drive the activity of these objects, and the MBC population in general, are still unclear. In the case of the P/2012 T1, the dust ejection was sustained over time, when the comet was near to perihelion, and we inferred that the activity was not produced by any impulsive event, the most likely driver being the sublimation of ices. The anisotropic ejection pattern obtained is in remarkable agreement with the one found for the MBC P/La Sagra (Moreno et al. 2011a), and agrees with the seasonally driven behavior also found in the case of 176P by Hsieh et al. (2011). We concluded that if this behavior is confirmed in

the next perihelion passage or if it is found in other MBCs, it would then have important consequences for the evolution and nature of these objects. In the case of the MBC P/2013 P5, which displayed a multi-tailed pattern, the rotational disruption was confirmed as the most likely mechanism. This produced an intermittent dust mass loss, which caused the complex tail brightness observed at different epochs.

- In paper VI, we report an extensive study of the dust environment evolution of comet C/2012 S1 (ISON). The observational data covered the period from right after its discovery, at ~ -6.2 AU, until its almost complete disintegration a few days after perihelion. In the first period, the ejection of dust was produced by an active area located in the Northern hemisphere until $\sim$ 200 days to perihelion. Then, the emission became isotropic until 13 days to perihelion. We found a clear correlation between the water and dust production rates during the approach, and a velocity ejection law close to a $1/r_h^2$ dependence. When the comet was near perihelion, it was monitored by *SOHO*. From the analysis of *SOHO LASCO C3* images, we inferred that the large mass loss rate observed between 77 and $17R_\odot$ was due to a cataclysmic disruption of the nucleus, releasing fresh material which contained ices that were rapidly vaporized. Thus, at least half of the mass of the nucleus was vaporized. In addition, based on the particle sublimation curves for different cometary materials, we concluded that at $\sim 5R_\odot$, small particles ($r \lesssim 10\mu$m) were vaporized. However, the total dust mass in the tail before and after perihelion passage, was approximately the same, while the particle size decreased notably. This suggests that the dominant process at that time was particle fragmentation, and not particle vaporization. The final surviving post-perihelion dust cloud was populated by tiny particles with the size range 0.1-50 μm, with a mass of only $\sim 6.7 \times 10^8$ kg.

- In addition to the appended papers, we have presented some results which have not been published yet. These refer to the outbursts suffered by comets 217P/Linear and P/2010 H2 (Vales). From these studies we obtained the dust environment before, during and after the outbursts. In the case of 217P, the observational data cover most of the orbit. We inferred that the total dust mass released from the nucleus during the explosion was 3.2×10^8 kg and the duration was $\sim$ 45 h. These results agree with previous studies available for this comet (Sarugaku et al. 2010). On the other hand, comet Vales outburst was far more intense. The total mass released from the nucleus was 8.5×10^9 kg, and the duration $\sim$ 120 h. Therefore, we concluded that the outburst of 217P was a small event, similar to the ones suffered by 81P/Wild 2, reported in paper III, but larger than the mini-outbursts suffered by 9P/Temple 1 in the range of $6 - 30 \times 10^4$ kg (Belton et al. 2013). The outburst of Vales was close to the values reached by 29P/S-W erratic outbursts, with values of $10^8 - 10^{10}$ kg (see e.g. Moreno 2009; Hosek et al. 2013). However, both outbursts are far away from the huge outburst of 17P/Holmes which reached values in the range of $10^{10} - 10^{12}$ kg (see e.g. Moreno et al. 2008; Li et al. 2011).

- In chapter 5, an outline of future studies is presented, in connection with each comet family. In relation to SPCs, we are planning to monitor and study the Rosetta target 67P/C-G in real time during the next observation campaigns. In the case of MBCs, we are continuing with

the ToO programme and the IAA-IAC collaboration, to monitor these objects as soon as they become activated. Finally, in the case of the LPCs, we have already observed some comets, which are ready to be analyzed, and, in addition, we are involved in a IAA-CASLEO project to study the close approach of comet Siding Spring to Mars.

Bibliography

A'Hearn, M. F., Belton, M. J. S., Delamere, W. A., et al. 2011, Science, 332, 1396

A'Hearn, M. F., Belton, M. J. S., Delamere, W. A., et al. 2005, Science, 310, 258

A'Hearn, M. F., Schleicher, D. G., Millis, R. L., Feldman, P. D., & Thompson, D. T. 1984, AJ, 89, 579

Anderson, J. D., Esposito, P. B., Martin, W., Thornton, C. L., & Muhleman, D. O. 1975, ApJ, 200, 221

Belton, M. J. S., Feldman, P. D., A'Hearn, M. F., & Carcich, B. 2008, Icarus, 198, 189

Belton, M. J. S., Thomas, P., Carcich, B., et al. 2013, Icarus, 222, 477

Bessel, F. W. 1836, Astronomische Nachrichten, 13, 185

Bibring, J.-P., Rosenbauer, H., Boehnhardt, H., et al. 2007, Space Sci. Rev., 128, 205

Biermann, L. 1951, ZAp, 29, 274

Biermann, L. 1978, in Astronomical Papers Dedicated to Bengt Stromgren, ed. A. Reiz & T. Andersen, 327–336

Bobrovnikoff, N. T. 1954, AJ, 59, 356

Boissier, J., Bockelée-Morvan, D., Biver, N., et al. 2012, A&A, 542, A73

Bradley, J., Hariot, T., & Rigaud, S. P. 1833, Supplement to Dr. Bradley's Miscellaneous works; with an account of Harriot's astronomical papers.

Brownlee, D. E. 1981, in Comets and the Origin of Life, ed. C. Ponnamperuma, 63–70

Burns, J. A., Lamy, P. L., & Soter, S. 1979, Icarus, 40, 1

Byl, J. 1983, Moon and Planets, 29, 121

Byl, J. 1986, Earth Moon and Planets, 36, 263

Carrington, R. C. 1859, MNRAS, 20, 13

Chambers, J. E. 1999, MNRAS, 304, 793

Clube, S. V. M. & Napier, W. M. 1982, QJRAS, 23, 45

Colangeli, L., Lopez-Moreno, J. J., Palumbo, P., et al. 2007, Space Sci. Rev., 128, 803

Combi, M. R., Bertaux, J.-L., Quémerais, E., et al. 2014, AJ, 147, 126

Crifo, J. F. 1995, ApJ, 445, 470

Crovisier, J., Brooke, T. Y., Leech, K., et al. 2000, Thermal Emission Spectroscopy and Analysis of Dust, Disks, and Regoliths, 196, 109

Davidsson, B. J. R. & Gutiérrez, P. J. 2004, in Bulletin of the American Astronomical Society, Vol. 36, AAS/Division for Planetary Sciences Meeting Abstracts #36, 1118

de León, J., Duffard, R., Lara, L. M., & Lin, Z.-Y. 2011, A&A, 527, A42

Delsemme, A. H. 1987, A&A, 187, 913

Delsemme, A. H. & Miller, D. C. 1971, Planet. Space Sci., 19, 1229

Dones, L., Levison, H. F., Duncan, M. J., & Weissman, P. R. 2005, Icarus (in press)

Dones, L., Weissman, P. R., Levison, H. F., & Duncan, M. J. 2004, Oort cloud formation and dynamics, ed. G. W. Kronk, 153–174

Duncan, M., Quinn, T., & Tremaine, S. 1988, ApJ, 328, L69

Duncan, M. J. & Levison, H. F. 1997, Science, 276, 1670

Edgeworth, K. E. 1949, MNRAS, 109, 600

Edoh, O. 1983, Univ. Arizona

Espinasse, S., Klinger, J., Ritz, C., & Schmitt, B. 1991, Icarus, 92, 350

Everhart, E. 1974, Celestial Mechanics, 10, 35

Farnham, T. L., Wellnitz, D. D., Hampton, D. L., et al. 2007, Icarus, 187, 26

Farnocchia, D., Chesley, S. R., Chodas, P. W., et al. 2014, ArXiv e-prints

Fernandez, J. A. 1980, MNRAS, 192, 481

Fernández, J. A. 1990, in Asteroids, Comets, Meteors III, ed. C. I. Lagerkvist, H. Rickman, & B. A. Lindblad, 309

Fernández, J. A. 2005, Dynamics of LP comets entering the inner planetary region, ed. W. B. Burton, Vol. 328 (Springer), 77–102

Filonenko, V. S. & Churyumov, K. I. 2009, in Deep Impact as a World Observatory Event: Synergies in Space, Time, and Wavelength, ed. H. U. Käufl & C. Sterken, 73

Finson, M. J. & Probstein, R. F. 1968a, ApJ, 154, 327

Finson, M. L. & Probstein, R. F. 1968b, ApJ, 154, 353

Fulle, M. 1987, A&A, 171, 327

Fulle, M. 1989, A&A, 217, 283

Fulle, M. 2000, Icarus, 145, 239

Fulle, M. 2004, Motion of cometary dust, ed. M. C. Festou, H. U. Keller, & H. A. Weaver, 565–575

Fulle, M., Colangeli, L., Agarwal, J., et al. 2010, A&A, 522, A63

Gehrz, R. D. & Ney, E. P. 1992, Icarus, 100, 162

González, M. 2012, PhD thesis, Universidad de Granada-Instituto de Astrofísica de Andalucía-CSIC

González, M., Gutiérrez, P. J., Lara, L. M., & Rodrigo, R. 2008, A&A, 486, 331

Green, S. F., McDonnell, J. A. M., Perry, C. H., Nappo, S., & Zarnecki, J. C. 1987, in ESA Special Publication, Vol. 278, Diversity and Similarity of Comets, ed. E. J. Rolfe & B. Battrick, 379–384

Gronkowski, P. 2007, Astronomische Nachrichten, 328, 126

Gutiérrez, P. J., Ortiz, J. L., Rodrigo, R., & López-Moreno, J. J. 2000, A&A, 355, 809

Hanner, M. S., Giese, R. H., Weiss, K., & Zerull, R. 1981, A&A, 104, 42

Hanner, M. S., Lynch, D. K., Russell, R. W., et al. 1996, Icarus, 124, 344

Hanner, M. S. & Newburn, R. L. 1989, AJ, 97, 254

Harmon, J. K., Nolan, M. C., Howell, E. S., Giorgini, J. D., & Taylor, P. A. 2011, ApJ, 734, L2

Harrington, R. S. 1985, Icarus, 61, 60

Heisler, J. 1990, Icarus, 88, 104

Heisler, J. & Tremaine, S. 1986, Icarus, 65, 13

Hilchenbach, M. 2013, AGU Fall Meeting Abstracts, A1754

Hillman, Y. & Prialnik, D. 2012, Icarus, 221, 147

Hills, J. G. 1981, AJ, 86, 1730

Hoffmeister, C. 1943, ZAp, 22, 265

Horner, J., Evans, N. W., Bailey, M. E., & Asher, D. J. 2003, MNRAS, 343, 1057

Hörz, F., Bastien, R., Borg, J., et al. 2006, Science, 314, 1716

Hosek, J. M. W., Blaauw, R. C., Cooke, W. J., & Suggs, R. M. 2013, AJ, 145, 122

Hsieh, H. H., Ishiguro, M., Lacerda, P., & Jewitt, D. 2011, AJ, 142, 29

Hsieh, H. H. & Jewitt, D. 2006, Science, 312, 561

Hsieh, H. H., Jewitt, D. C., & Fernández, Y. R. 2004, AJ, 127, 2997

Hughes, D. W. 1990, QJRAS, 31, 69

Hut, P. & Tremaine, S. 1985, AJ, 90, 1548

Ishiguro, M., Kim, Y., Kim, J., et al. 2013, ApJ, 778, 19

Jewitt, D., Agarwal, J., Weaver, H., Mutchler, M., & Larson, S. 2013, ApJ, 778, L21

Jewitt, D. & Luu, J. 1993, Nature, 362, 730

Jockers, K. 1997, Earth Moon and Planets, 79, 221

Keller, H. U., Barbieri, C., Koschny, D., et al. 2010, Science, 327, 190

Keller, H. U., Barbieri, C., Lamy, P., et al. 2007, Space Sci. Rev., 128, 433

Keller, H. U., Kramm, R., & Thomas, N. 1988, Nature, 331, 227

Klinger, J. 1980, Science, 209, 271

Klinger, J. 1991, in Astrophysics and Space Science Library, Vol. 167, IAU Colloq. 116: Comets in the post-Halley era, ed. J. R. L. Newburn, M. Neugebauer, & J. Rahe, 227–241

Kolokolova, L., Hanner, M. S., Levasseur-Regourd, A.-C., & Gustafson, B. Å. S. 2004, Physical properties of cometary dust from light scattering and thermal emission, ed. G. W. Kronk, 577–604

Kuiper, G. P. 1951, in 50th Anniversary of the Yerkes Observatory and Half a Century of Progress in Astrophysics, ed. J. A. Hynek, 357

Lacerda, P. 2013, MNRAS, 428, 1818

Langevin, Y., Kissel, J., Bertaux, J.-L., & Chassefiere, E. 1987, A&A, 187, 761

Levison, H. F. 1996, in Astronomical Society of the Pacific Conference Series, Vol. 107, Completing the Inventory of the Solar System, ed. T. Rettig & J. M. Hahn, 173–191

Levison, H. F. & Duncan, M. J. 1994, Icarus, 108, 18

Levison, H. F. & Duncan, M. J. 1997, Icarus, 127, 13

Li, J., Jewitt, D., Clover, J. M., & Jackson, B. V. 2011, ApJ, 728, 31

Licandro, J., Moreno, F., Cabrera-Lavers, A., et al. 2013, Central Bureau Electronic Telegrams, 3679, 1

Marsden, B. G., Sekanina, Z., & Yeomans, D. K. 1973, AJ, 78, 211

Mazets, E. P., Aptekar, R. L., Golenetskii, S. V., et al. 1986, Nature, 321, 276

McDonnell, J. A. M., Evans, G. C., Evans, S. T., et al. 1987, A&A, 187, 719

Meech, K. J. & Jewitt, D. C. 1987, A&A, 187, 585

Miles, R. 2007, ArXiv e-prints

Millis, R. L., Ahearn, M. F., & Thompson, D. T. 1982, AJ, 87, 1310

Min, M., Hovenier, J. W., de Koter, A., Waters, L. B. F. M., & Dominik, C. 2005, Icarus, 179, 158

Moreno, F. 2009, ApJS, 183, 33

Moreno, F., Lara, L. M., Licandro, J., et al. 2011a, ApJ, 738, L16

Moreno, F., Licandro, J., Álvarez-Iglesias, C., Cabrera-Lavers, A., & Pozuelos, F. 2014, ApJ, 781, 118

Moreno, F., Licandro, J., Ortiz, J. L., et al. 2011b, ApJ, 738, 130

Moreno, F., Muñoz, O., Vilaplana, R., & Molina, A. 2003, ApJ, 595, 522

Moreno, F., Ortiz, J. L., Santos-Sanz, P., et al. 2008, ApJ, 677, L63

Moreno, F., Pozuelos, F., Aceituno, F., et al. 2012, ApJ, 752, 136

Ney, E. P. 1982, in IAU Colloq. 61: Comet Discoveries, Statistics, and Observational Selection, ed. L. L. Wilkening, 323–340

Ney, E. P. & Merrill, K. M. 1976, Science, 194, 1051

Oort, J. H. 1950, Bull. Astron. Inst. Netherlands, 11, 91

Paganini, L., DiSanti, M. A., Mumma, M. J., et al. 2014, AJ, 147, 15

Prialnik, D., A'Hearn, M. F., & Meech, K. J. 2008, MNRAS, 388, L20

Reach, W. T., Vaubaillon, J., Lisse, C. M., Holloway, M., & Rho, J. 2010, Icarus, 208, 276

Richter, N. 1941, Astronomische Nachrichten, 271, 207

Sarugaku, Y., Ishiguro, M., Ueno, M., Usui, F., & Watanabe, J. 2010, ApJ, 724, L118

Sekanina, Z. 1981, Annual Review of Earth and Planetary Sciences, 9, 113

Sekanina, Z. 2008, International Comet Quarterly, 30, 3

Sinding, E. 1937, Astronomische Nachrichten, 261, 457

Sitarski, G. 1983, Acta Astron., 33, 295

Sitarski, G. 1992, AJ, 104, 1226

Smoluchowski, R. 1981, ApJ, 244, L31

Snodgrass, C. & Castalia mission science Team. 2013, in AAS/Division for Planetary Sciences Meeting Abstracts, Vol. 45, AAS/Division for Planetary Sciences Meeting Abstracts, #211.21

Stern, S. A., Parker, J. W., Feldman, P. D., et al. 2011, AJ, 141, 199

Stevenson, R., Kleyna, J., & Jewitt, D. 2010, AJ, 139, 2230

Stoer, J. & Bulirsch, R. 1980, Introduction to Numerical Analysis, ed. N. Y. Springer, 443,460

Stokes, G. H. & Yeomans, D. K. 2003, AGU Fall Meeting Abstracts

Stroemgren, E. 1947, Publikationer og mindre Meddeler fra Kobenhavns Observatorium, 144, 1

Thomas, N., Keller, H. U., Arijs, E., et al. 1998, Advances in Space Research, 21, 1505

Thomas, P., A'Hearn, M., Belton, M. J. S., et al. 2013, Icarus, 222, 453

Tokunaga, A. T., Golisch, W. F., Griep, D. M., Kaminski, C. D., & Hanner, M. S. 1986, AJ, 92, 1183

Torbett, M. V. 1989, AJ, 98, 1477

Tricarico, P., Samarasinha, N. H., Sykes, M. V., et al. 2014, ApJ, 787, L35

Trigo-Rodríguez, J. M., García-Hernández, D. A., Sánchez, A., et al. 2010, MNRAS, 409, 1682

van de Hulst, H. C. 1957, Light Scattering by Small Particles

van Woerkom, A. J. J. 1948, Bull. Astron. Inst. Netherlands, 10, 445

Veverka, J., Klaasen, K., A'Hearn, M., et al. 2013, Icarus, 222, 424

Weissman, P. R. 1980, Nature, 288, 242

Weissman, P. R. 1996, in Astronomical Society of the Pacific Conference Series, Vol. 107, Completing the Inventory of the Solar System, ed. T. Rettig & J. M. Hahn, 265–288

Whipple, F. L. 1950, ApJ, 111, 375

Whipple, F. L. 1951, ApJ, 113, 464

Whitney, C. 1955, ApJ, 122, 190

Yang, B., Keane, J., Meech, K., Owen, T., & Wainscoat, R. 2014, ApJ, 784, L23

Ye, Q.-Z. & Hui, M.-T. 2014, ApJ, 787, 115